

**Study for the wide-angle  
air Cherenkov detector H<sub>i</sub>SCORE  
and  
time gradient event reconstruction  
for the H.E.S.S. experiment**

**Dissertation zur Erlangung des Doktorgrades  
des Department Physik der Universität Hamburg**

**vorgelegt von**

**Daniel Hampf**

**aus Recife (Brasilien)**

**Hamburg 2012**

Gutachter der Dissertation: Prof. Dr. Dieter Horns  
Prof. Dr. Bruce Dawson

Gutachter der Disputation: Prof. Dr. Erika Garutti  
Dr. Axel Lindner

Datum der Disputation: 22.05.2012

Vorsitzender des Prüfungsausschusses: Dr. Georg Steinbrück

Vorsitzender des Promotionsausschusses: Prof. Dr. Peter Hauschildt

Dekan der MIN Fakultät: Prof. Dr. Heinrich Graener

*If I can see any further, it is only  
because I am standing on the  
shoulders of giants.*

after Bernard of Chartres

Dedicated to the memory of the countless men and women who throughout the centuries have devoted their lives to the quest for truth, the advancement of reason and the fight against ignorance. Only the pursuit of enlightenment has enabled humankind to rise above the received conventions of existence, into the boundless space of intellect.

## Abstract

This thesis presents efforts to extend the range of astronomical gamma-ray observations to the ultra high energy regime, i.e. to energies above  $3 \times 10^{13}$  eV. Current gamma-ray instruments like the H.E.S.S. Cherenkov telescope array have limited sensitivity towards those energies, since the flux of gamma-ray sources is extremely small in this regime and not enough events can be detected with the available effective areas.

It is shown that the potential of H.E.S.S. for the observation at ultra high energies can be improved by utilising the data on the time evolution of the recorded Cherenkov light images. Essentially this becomes possible since the timing data offers an additional, rather robust method for the core position and direction reconstruction of events with large core distances. The potential of this method is quantified using air shower and detector simulations along with a newly developed event reconstruction algorithm. Additionally, the use of time information is tested on real H.E.S.S. data.

While the timing data analysis can improve the performance of current gamma-ray instruments towards the high energy end of their sensitivity range to a certain extent, opening up the window to ultra high energy gamma-ray observations will only be possible with dedicated instruments. To that end, a new gamma-ray observatory with a very large effective area is proposed. A study of this new detector, called H<sub>i</sub>SCORE, is presented.

The H<sub>i</sub>SCORE design is based on an array of wide-angle, non-imaging Cherenkov light detectors, spaced more than hundred metres apart from each other. The Cherenkov light front is sampled by photomultipliers and a fast readout system. Due to a cost-effective design of the detector stations and the large inter-station spacing it becomes feasible to equip an area of  $10\text{ km}^2$  to  $100\text{ km}^2$  at a reasonable effort.

It is shown in this thesis that despite the large inter-station spacing and thus the low number of data channels a decent event reconstruction is possible using a specifically developed algorithm. The resolution of the direction and energy reconstruction is comparable to current gamma-ray observatories. The energy range between  $5 \times 10^{13}$  eV and  $10^{16}$  eV is ideally suited to complement the currently possible gamma-ray observations. The expected sensitivity is sufficient to study in detail the ultra high energy continuation of the energy spectra of currently known sources, and to search for the – yet undiscovered – Galactic objects that accelerate cosmic rays to energies above  $10^{15}$  eV (pevatrons). Additionally, the H<sub>i</sub>SCORE detector offers possibilities for cosmic ray and, indirectly, particle physics measurements.

Additionally, the question of a suitable deployment site for the detector is discussed. Several possible locations are examined using a pre-defined set of criteria. Special focus is given to the visible sky region and to the night sky brightness at the site. One candidate site, the Fowler's Gap research station in New South Wales, Australia, has been visited for closer examination, and the night sky brightness on site has been characterised using dedicated measurements.

## Zusammenfassung

In dieser Arbeit werden Möglichkeiten untersucht, die Beobachtungen von kosmischer Gammastrahlung auf den Energiebereich jenseits von  $3 \times 10^{13}$  eV (ultrahohe Energien) auszudehnen. Zur Zeit existierende Experimente, wie das H.E.S.S. Cherenkov Teleskop System, haben bei diesen Energien nur eine begrenzte Sensitivität, da der Gammastrahlungsfluss in diesem Bereich sehr gering ist und mit den verfügbaren effektiven Flächen nicht genügend Ereignisse detektiert werden können.

Es wird gezeigt, dass das Potenzial des H.E.S.S. Experiments für die Beobachtung bei ultrahohen Energien verbessert werden kann, wenn die Informationen aus der Zeitentwicklung des Cherenkovlichts ebenfalls ausgewertet werden. Im Wesentlichen ist dies möglich, da die Zeitinformation eine zusätzliche, robuste Methode zur Bestimmung des Kernorts und der Herkunftsrichtung, insbesondere für Ereignisse, die weit entfernt von den Teleskopen auftreten, bietet. Das Potenzial dieser Methode wird mit Hilfe einer Luftschauer- und Detektorsimulation und einem neuen Algorithmus zur Ereignisrekonstruktion untersucht. Zusätzlich wird die Zeitanalyse an echten H.E.S.S. Daten getestet.

Für sensitive Beobachtungen bei ultrahohen Energien sind jedoch neue, dedizierte Instrumente mit viel größeren effektiven Flächen notwendig. Eine Studie für ein solches Experiment, den H<sub>i</sub>SCORE Detektor, wird vorgestellt.

Das H<sub>i</sub>SCORE Design beruht auf einem Feld aus nichtabbildenden Weitwinkel-Cherenkovdetektoren mit einem Stationsabstand von mehr als hundert Metern. Die Cherenkovlichtfront wird durch Photomultiplier und eine schnelle Ausleseelektronik aufgenommen. Durch die kostengünstige Bauweise der Detektorstationen und den großen Abstand zwischen den Stationen ist die Instrumentierung einer Fläche von 10 km<sup>2</sup> bis 100 km<sup>2</sup> realisierbar.

In dieser Arbeit wird gezeigt, dass trotz des großen Stationsabstandes und der daraus resultierenden geringen Anzahl an Datenkanälen eine gute Ereignisrekonstruktion möglich ist. Mit einem speziell entwickelten Rekonstruktionsalgorithmus wird eine Winkel- und Energieauflösung erreicht, die vergleichbar mit jener heutiger Systeme für geringere Energien ist. Durch den Energiebereich von  $5 \times 10^{13}$  eV bis  $10^{16}$  eV ist der Detektor ideal geeignet, um die heutzutage möglichen Messungen zu ultrahohen Energien zu erweitern. Die erwartete Sensitivität ist ausreichend, um die Fortsetzung der bisher bekannten Energiespektren von Gammaquellen zu ultrahohen Energien zu untersuchen, und um nach den bisher unentdeckten galaktischen Objekten zu suchen, die die Teilchen der geladenen kosmischen Strahlung auf Energien von über  $10^{15}$  eV beschleunigen (Pevatrons). Zusätzlich ermöglicht der H<sub>i</sub>SCORE Detektor die Messung der geladenen kosmischen Strahlung und, indirekt, Untersuchungen aus dem Bereich der Teilchenphysik.

Schließlich wird die Suche nach einem passenden Standort für den Detektor thematisiert. Verschiedene mögliche Standorte werden nach bestimmten Kriterien betrachtet. Ein besonderes Augenmerk liegt auf der beobachtbaren Himmelsregion und auf der Resthelligkeit des Nachthimmels. Ein möglicher Standort, die Forschungsstation Fowler's Gap in New South Wales (Australien), wurde für genauere Untersuchungen besucht, und die Nachthimmelshelligkeit vor Ort wurde mit Hilfe von Messungen charakterisiert.



# Acknowledgements

## Frequently used software tools and websites

This chapter acknowledges the most important software tools used during the work on this thesis. As most of these tools are freeware / open source, I would like to thank all the authors who devote their time and money to the development and distribution of these programmes.

- Linux in all its variations
- kile for writing  $\LaTeX$
- Gnuplot for plots and figures
- xfig for schematics and illustrations
- gimp for image file type conversions and image manipulation
- python, including the modules given in appendix A.8
- LabView for the hardware control during the NSB measurements
- CORSIKA for air shower simulations
- sim\_telarray for the H.E.S.S. simulations

The same is true for the many websites and forums that helped me so often with technical problems. An exhaustive collection is obviously impossible, so let me mention only the most frequently used:

- [www.dict.cc](http://www.dict.cc) and [dict.leo.org](http://dict.leo.org) for help with my English
- [www.wikipedia.org](http://www.wikipedia.org) for knowing an answer to (almost) everything
- [www.google.de](http://www.google.de) for finding answers to everything else
- [adsabs.harvard.edu](http://adsabs.harvard.edu) for its fantastic paper database
- [arxiv.org](http://arxiv.org) for bringing us a long way towards Open Access of scientific information

## Financial support

I would like to acknowledge the financial support the German Federal Ministry of Education and Research, BMBF (contract number 05A08GU1), as well as the German Academic Exchange Service (DAAD) for its support of the field studies in Australia under the “Kurzstipendium für Doktoranden” scheme.

## Personal acknowledgements

I would like to thank my supervisor Dieter Horns for giving me the opportunity to work on this magnificent project, for the freedom to pursue the project my way and for giving me all support a PhD student could possibly dream of to develop my own scientific standing.

A special thanks goes to my unshakable project coordinator and office mate Martin Tluczykont, who was an inspiring teacher and fantastic partner in our joint efforts to get the H<sub>i</sub>SCORE project off the ground. His humour and encouragement made my PhD time a very pleasant one.

Along the same line, I would like to thank all the members of the astrophysics group in Hamburg, who have shared their days with me and who have helped me with so many small and big things during the years. In particular this goes to Martin Raue, who was always there when I needed him and who could always help me find my way back onto the track when I was lost. Furthermore I'd like to thank Milton Fernandes for our enlightening discussions about the H.E.S.S. software and ROOT, Max Kastendieck for his help with all sorts of odd Linux problems, and Tanja Kneiske for providing me with all the books on astrophysics and air showers. A special thanks also goes to all further members of the H<sub>i</sub>SCORE team who I had the pleasure to work with.

I would like to thank Dieter Horns, Martin Tluczykont and Martin Raue especially for proof-reading my thesis and giving valuable comments. For patient help with my questions about English grammar and phrasing and their excellent suggestions, I'd like to thank Nelly Nguyen, Peter Kolarz and Juliane John.

Further thanks goes to the staff behind the scenes, the mind-boggling Rainer Peter Feller and his team, our always helpful secretary Magdalena Hack and the teams from the electronic and mechanical workshops. In particular this goes to Stefan Fleig and his team for building all the excellent equipment we used for our studies. I would also like to acknowledge the very friendly help of Jochen Ebert with the transmission and reflectivity measurements.

Maybe the greatest phase of my PhD time I spent at the University of Adelaide, and this is largely due to the fantastic people I met there: Gavin Rowell, who helped me endlessly with all the organisational stuff and the field trips and who always guided me safely through my project. Neville Wild, who taught me so much about electronics and so much more, and whose gentle character cheered up so many of my days. Bruce Dawson, for our memorable discussions about physics and the universe and the rest, and for daringly accepting to review my thesis. Victor Stamatescu, who not only provided me with unprecedented insights to air shower physics, but who also became a friend at the other end of the world and guided me behind the scenes of Adelaide. Tristan Sudholz, who was a cheerful companion during the long observation nights in the outback, and who helped me a lot with the practical aspects of the measurements. Ramona Adorjan, the most competent computer specialist I ever met in my life. Furthermore, I would like to thank Roger Clay, Andrew Smith and Paddy McGee for helpful hints and discussions about photomultipliers, telescopes and the celestial coordinate system. And of course the unrivalled Greg Thornton for sharing with me his cloud cover maps and well, for just being there.

Finally I'd like to thank all my friends and family, and my dear Sara, for their great inspiration, motivation, love and support. Without them, none of this would have happened.

# Contents

<b>1</b>	<b>Introduction</b>	<b>13</b>
<b>2</b>	<b>Cosmic rays and gamma-ray astronomy</b>	<b>15</b>
2.1	Cosmic rays . . . . .	15
2.2	Sources of cosmic rays . . . . .	18
2.3	Gamma-ray astronomy . . . . .	20
2.3.1	Very high energy gamma-ray astronomy . . . . .	20
2.3.2	Ultra high energy gamma-ray astronomy . . . . .	22
2.4	Experimental techniques in cosmic ray physics and gamma-ray astronomy . . . . .	24
2.4.1	Satellite experiments . . . . .	25
2.4.2	Extensive air showers . . . . .	25
2.4.3	Air shower arrays . . . . .	29
2.4.4	Cherenkov light from extensive air showers . . . . .	30
2.4.5	Imaging Cherenkov detectors . . . . .	32
2.4.6	Wide-angle, non-imaging Cherenkov detectors . . . . .	34
<b>3</b>	<b>Sampling mode event reconstruction for the H.E.S.S. experiment</b>	<b>37</b>
3.1	The H.E.S.S. experiment . . . . .	37
3.2	Standard event reconstruction . . . . .	39
3.2.1	Image processing . . . . .	40
3.2.2	Stereo reconstruction of shower core position and particle direction . . . . .	42
3.2.3	Energy reconstruction and gamma hadron separation . . . . .	43
3.2.4	Background calculation and source detection . . . . .	45
3.3	Event reconstruction using sampling mode information . . . . .	45
3.3.1	Using the time gradient as distance estimator . . . . .	47
3.3.2	Implementation of the time gradient analysis . . . . .	48
3.3.3	New core position and direction reconstruction . . . . .	50
3.4	Software framework . . . . .	50
3.4.1	Event simulation . . . . .	52
3.4.2	Standard H.E.S.S. software . . . . .	54
3.4.3	New sampling mode analysis . . . . .	54
3.5	Simulated performance of the time gradient reconstruction . . . . .	55
3.5.1	Standard nominal distance cut . . . . .	56
3.5.2	Extended nominal distance cut . . . . .	56
3.5.3	Energy reconstruction . . . . .	58
3.6	Sampling mode data taken with the H.E.S.S. experiment . . . . .	61
3.6.1	Run summary . . . . .	61
3.6.2	Data rate . . . . .	61
3.6.3	Telescope performance . . . . .	62
3.6.4	Position of the peak time . . . . .	62
3.6.5	Time offsets between channels . . . . .	64

## Contents

3.6.6	Pedestal gradient . . . . .	64
3.7	Analysis and results of sampling mode data . . . . .	66
3.7.1	The Crab Nebula . . . . .	66
3.7.2	Standard analysis . . . . .	67
3.7.3	Sampling mode analysis with standard nominal distance cut . . . . .	69
3.7.4	Sampling mode analysis with extended nominal distance cut . . . . .	71
3.8	Summary and Outlook . . . . .	73
<b>4</b>	<b>The H<sub>i</sub>SCORE experiment</b>	<b>75</b>
4.1	Scientific goals and detector concept . . . . .	75
4.2	Development of a detector station prototype . . . . .	77
4.2.1	Mechanical set-up . . . . .	77
4.2.2	The Winston cone light concentrator . . . . .	79
4.2.3	Electronic set-up . . . . .	85
4.3	Ideas for time synchronisation . . . . .	89
4.4	Concluding remarks and outlook . . . . .	90
<b>5</b>	<b>H<sub>i</sub>SCORE simulations and event reconstruction</b>	<b>93</b>
5.1	Overview . . . . .	93
5.2	Night sky brightness simulation . . . . .	95
5.3	Detector simulation sim_score . . . . .	100
5.4	Event reconstruction . . . . .	102
5.4.1	Signal pre-processing . . . . .	104
5.4.2	Shower core position . . . . .	105
5.4.3	Direction of origin . . . . .	106
5.4.4	Particle energy . . . . .	113
5.4.5	Vertical position of the shower maximum . . . . .	117
5.5	Particle separation . . . . .	129
5.5.1	Separation using depth reconstruction bias . . . . .	130
5.5.2	Separation using depth versus energy . . . . .	130
5.5.3	Separation using signal rise times . . . . .	131
5.5.4	Other methods . . . . .	133
5.5.5	Performance of gamma hadron separation . . . . .	135
5.5.6	Determination of hadron mass . . . . .	140
5.6	Detector acceptance and sensitivity to gamma-ray sources . . . . .	140
5.6.1	Angular and spatial acceptance . . . . .	140
5.6.2	Effective areas . . . . .	142
5.6.3	Event rates . . . . .	144
5.6.4	Sensitivity . . . . .	145
5.7	Options to lower the energy threshold . . . . .	147
5.8	Concluding remarks . . . . .	149
<b>6</b>	<b>Site evaluation</b>	<b>151</b>
6.1	Criteria for a suitable detector site . . . . .	151
6.1.1	Field of view and potential gamma-ray sources . . . . .	151
6.1.2	Weather conditions . . . . .	151
6.1.3	Darkness . . . . .	152
6.1.4	Infrastructure and geographical conditions . . . . .	153
6.1.5	Safety and sustainability . . . . .	154

6.2	Possible detector sites . . . . .	154
6.2.1	Fowler’s Gap research station . . . . .	155
6.2.2	TUNKA site . . . . .	156
6.2.3	Pierre Auger Observatory site . . . . .	156
6.2.4	Other options . . . . .	157
6.3	Simulated field of view . . . . .	157
6.4	Night sky brightness measurement at Fowler’s Gap . . . . .	160
6.4.1	The instrument and its calibration . . . . .	161
6.4.2	Data evaluation . . . . .	163
6.4.3	Brightness levels at Fowler’s Gap . . . . .	166
6.4.4	Expected noise level in the $H_i$ SCORE detector channels . . . . .	167
6.4.5	Spectral composition of the night sky brightness . . . . .	170
6.4.6	The use of filters to suppress night sky brightness . . . . .	172
6.5	Concluding remarks . . . . .	173
<b>7</b>	<b>Conclusion &amp; Outlook</b>	<b>175</b>
7.1	Time gradient event reconstruction for the H.E.S.S. experiment . . . . .	175
7.2	The wide-angle, non-imaging air Cherenkov detector $H_i$ SCORE . . . . .	176
	<b>Appendices</b>	<b>181</b>
<b>A</b>	<b>Software developed for this work</b>	<b>181</b>
A.1	H.E.S.S. event reconstruction . . . . .	181
A.2	Ray tracing algorithm . . . . .	183
A.3	NSB simulation and trigger rate calculation . . . . .	184
A.4	$H_i$ SCORE event reconstruction . . . . .	184
A.5	$H_i$ SCORE sensitivity calculation . . . . .	187
A.6	$H_i$ SCORE source exposure calculation and display . . . . .	187
A.7	LabView VI for NSB measurement . . . . .	188
A.8	Reference list of needed python modules . . . . .	188
<b>B</b>	<b>Tabulated results of <math>H_i</math>SCORE event reconstruction</b>	<b>189</b>
<b>C</b>	<b>Additional information on Fowler’s Gap</b>	<b>191</b>
<b>D</b>	<b>Angular acceptance of a tube</b>	<b>193</b>
<b>E</b>	<b>Datasheets</b>	<b>195</b>
	<b>Bibliography</b>	<b>203</b>
	<b>List of publications</b>	<b>219</b>

## *Contents*

# 1 Introduction

The systematic observation of celestial objects has begun more than 5000 years ago, and has triggered or influenced many advances in civilisation from calendar systems to ocean navigation, as well as many philosophical discourses like the controversy about the position of Earth and humankind in the universe. Stars and planets have been observed and catalogued since the ancient era, and some of the concepts developed in that time are still in use today, e.g. the magnitude scale. The invention of the telescope in the 17<sup>th</sup> century allowed a far deeper view into the universe, making the discovery of much fainter and much more distant objects possible. Finally, in the 20<sup>th</sup> century it became possible to greatly enrich the exploration of the universe with observations of electromagnetic radiation at other wavelengths than those of visible light, e.g. radio, infrared, UV, X-rays and gamma-rays, and of other messenger particles such as charged cosmic rays and neutrinos. With that the window to the *non-thermal universe* opened, as these broadband observations can be used to study non-thermal processes such as the acceleration of particles in the extreme conditions near objects like pulsars, black holes or shell-type supernova remnants.

One of the newest fields in this context is ground-based gamma astronomy, which deals with the observation of electromagnetic radiation with photon energies<sup>1</sup> above about 30 GeV, corresponding to wavelengths shorter than  $4 \times 10^{-17}$  m. Since the atmosphere is not transparent for photons at these energies, an indirect technique is used: The highly energetic photons interact with air molecules and initiate a cascade of secondary particles (*air shower*). These secondary particles have velocities larger than the speed of light in air, which causes them to emit Cherenkov light, that is in turn detected with telescopes or other light detectors on the ground (see e.g. Hinton [2009] for a review). One of the particular strengths of this technique is that the effective area of the detector is far greater than the instrumented area, since a single telescope can detect air showers within a radius of up to a few hundred metres. This way, effective areas of  $10^5$  m<sup>2</sup> can be achieved with current experiments, which makes the detection of very weak fluxes (less than  $10^{-8}$  photons per second and square metre) possible [Aharonian *et al.*, 2008b].

So far, ground-based gamma-ray astronomy has focused mainly on the very high energy regime (VHE,  $30 \text{ GeV} \lesssim E \lesssim 30 \text{ TeV}$ ). About one hundred sources of emission have been detected by mid 2011, among them Galactic sources such as pulsar wind nebulae and shell-type supernova remnants as well as extragalactic sources such as Active Galactic Nuclei [Wakely and Horan, 2011]. The energy spectrum, the time evolution of the emission (for variable sources), and the morphology (for extended sources) are used to derive a wealth of new information about these objects [Horns, 2008].

However, current detector systems are not sensitive enough to detect gamma-ray sources at even higher energies, in the ultra high energy domain (UHE,  $E \gtrsim 30 \text{ TeV}$ ). Photon fluxes of currently known sources decrease with energy following a power law (mostly with an index  $\Gamma < -2$ ), and beyond a few ten TeV the fluxes of almost all sources are too weak to be detected with the effective areas of current detectors. While a cut-off in the energy spectrum has been detected in some sources, other spectra extend without a change in slope up to the end of the sensitive range of current instruments, and it is unknown how far these spectra continue. From charged cosmic ray measurements there is (indirect) evidence that some sources should also emit gamma-rays up to larger energies than currently measured, and the discovery of sources with UHE gamma-ray emission would have a great impact on the search for the sources of charged cosmic rays [Gabici and Aharonian, 2007; Rowell *et al.*, 2008; Tluczykont *et al.*, 2012b]. In chapter 2 of this work, the current

---

<sup>1</sup>In this thesis, energies are usually given in electronvolt, using the SI unit prefix system (see table 2.1 on page 17) for large numbers

## 1 Introduction

status of the field of gamma-ray astronomy is lined out in the context of its benefit for the exploration of the non-thermal universe, with a special emphasis on the potential of observations in the UHE regime.

The High Energy Stereoscopic System (H.E.S.S.), a system of four imaging Cherenkov telescopes located in the Khomas Highlands in Namibia, is a sensitive instrument for gamma-ray astronomy in the VHE domain [Hinton, 2004; Aharonian *et al.*, 2006c]. Due to the stereoscopic view of the air shower the event reconstruction, i.e. the calculation of the particle properties such as energy and direction of origin from the measured signals, achieves great accuracy. Usually, only static images of the Cherenkov light are used for the event reconstruction, however even more information about the event can be gained from the time evolution of the image [Heß *et al.*, 1999; Aliu *et al.*, 2009; Stamatescu *et al.*, 2011]. While the time evolution can be recorded with the H.E.S.S. hardware, it is not used for event reconstruction so far. Chapter 3 of this work presents a new event reconstruction that makes use of the timing information, with the ultimate goal of improving the sensitivity of the H.E.S.S. experiment near the high energy end of its sensitivity range. The new method is tested both on simulated and actual observational data.

While it is possible to increase the performance of current experiments at multi-TeV energies to some extent, new detector systems with larger effective areas will be needed for a detailed study of the gamma-ray sky at ultra high energies. In chapter 4 of this work, the wide-angle, non-imaging air Cherenkov detector array H<sub>i</sub>SCORE is presented as a new concept specifically designed for gamma-ray observations in the UHE regime. In the standard configuration, the detector stations will be spaced at a distance of 150m ( $\sim 49$  stations per km<sup>2</sup>) and have a light sensitive area of 0.5m<sup>2</sup> each. The simple, inexpensive design of the detector stations and the large spacing between them make the instrumentation of an area between 10km<sup>2</sup> and 100km<sup>2</sup> feasible. With such a large effective area, an unprecedented sensitivity in the UHE regime can be achieved. The expected sensitivity will allow to study the ultra high energy part of the spectra of many currently known sources, and may lead to the discovery of new sources in the UHE regime. As one part of the design study, a prototype detector station has been developed, which is introduced as well in this chapter.

One of the main challenges of such an detector is the accurate reconstruction of the event parameters. Previous non-imaging Cherenkov detectors have used a much denser spacing of detector stations (e.g. 30m in the case of the AIROBICC experiment), which allowed them to study the properties of the Cherenkov light in more detail [Arqueros *et al.*, 1996; Lindner, 1998; Fowler *et al.*, 2001]. Therefore, a dedicated H<sub>i</sub>SCORE event reconstruction has been developed for this study, which will be presented in chapter 5. It incorporates approaches used in previous detectors, adapted for a large spacing, and introduces some new techniques. Together with air shower simulations using CORSIKA [Heck *et al.*, 1998], and the detector simulation `sim_score`, this event reconstruction algorithm is used to calculate the performance of the detector in terms of angular and energy resolution, and its sensitivity to gamma-ray point sources. Additionally, the impact of the detector altitude and the station spacing on the energy threshold is discussed in this chapter.

Chapter 6 deals with the selection of a suitable site for the detector. The visible regions of the sky and the exposure times are simulated for detector locations on the northern hemisphere and southern hemisphere of Earth. A more in-depth search for a suitable site was conducted in Australia. Since the light of night sky brightness is the major source of noise in a wide-angle Cherenkov detector like H<sub>i</sub>SCORE, it is important to find a site with very low night sky brightness and no artificial light pollution. Therefore, the study of one particular candidate site in New South Wales, Australia, also included a detailed measurement of the night sky brightness.

In conclusion, this thesis presents an experimental approach to open up a new window in the electromagnetic spectrum, the ultra high energy gamma-ray regime, which will hopefully, over time, greatly enrich our knowledge of the non-thermal universe.

## 2 Cosmic rays and gamma-ray astronomy

In this chapter the context of this work in high energy astrophysics will be given. In section 2.1 the current knowledge about cosmic rays will be summarised, starting from measured quantities like the all-particle spectrum, the composition and the (an-)isotropy, leading to a discussion about possible sources of the cosmic rays in section 2.2. In section 2.3 the use of gamma-rays as tracers for cosmic ray acceleration will be discussed, reviewing current results and sketching the potential of future experiments, with a special focus on the ultra high energy regime. Other applications of very high energy and ultra high energy gamma-ray astronomy will also be included, motivating the work on the improvement of the H.E.S.S. analysis near its high energy end as well as the development of the H<sub>i</sub>SCORE detector concept presented in the main part of this thesis. In the final section 2.4, experimental techniques used in cosmic ray physics and gamma-ray astronomy will be introduced, with a focus on the air-Cherenkov technique that is used in both H.E.S.S. and H<sub>i</sub>SCORE. A more detailed description of these two experiments will be postponed to the respective chapters 3 (H.E.S.S.) and 4 (H<sub>i</sub>SCORE).

### 2.1 Cosmic rays

Cosmic rays are highly energetic particles that hit the atmosphere of the Earth, first detected in balloon flight experiments by Victor Hess in 1912 [Hess, 1912]. Since then they have been studied in great detail, and are still subject of many experiments and theoretical works today. The majority of cosmic ray particles are protons, however, atomic nuclei of all other elements are found as well. While these *hadronic cosmic rays* make up the majority of all cosmic rays seen at Earth, there are also *leptonic cosmic rays*, mainly electrons. In a wider sense, high energy photons (gamma-rays) and cosmic neutrinos can also be seen as cosmic rays, however, in this thesis the term “cosmic rays” will be used exclusively for *charged* cosmic rays.

**Energy spectrum** The rate of cosmic rays seen on Earth decreases rapidly with energy. About one particle arrives per second and square metre with an energy above 300 GeV. At 100 TeV, the rate has decreased to  $7 \times 10^{-5} \text{ m}^{-2} \text{ s}^{-1}$ , and at 100 PeV only about one particle arrives every two hours per square *kilometre*.

The energy spectrum of hadronic cosmic rays as known today is shown in figure 2.1. It follows a power law ( $\frac{dN}{dE} \propto E^\Gamma$ ) over many decades in energy with only slight changes in the index: At the energy of about 4.5 PeV (“the knee“) the spectrum steepens from  $\Gamma \approx -2.7$  to  $\Gamma \approx -3.1$ , a further (slight) steepening is observed at about 400 PeV (“second knee“) [Blümer *et al.*, 2009].

The change of slope at the knee is often explained with a change of the composition of cosmic rays [Hillas, 2006]. The total population of measured cosmic rays is made up by contributions from different particles, that may extend to different maximum energies. The knee can then be interpreted as a sign for the maximum energy of the most abundant cosmic ray component, the protons, while the second knee marks the end of the iron component [Hörandel, 2003; Apel *et al.*, 2011]. This is discussed in more detail in section 5.6.4, where the cosmic ray flux is modelled using these assumptions. Other origins of the knee have been discussed in literature, e.g. a local source of cosmic rays that dominates the spectrum [Erlykin and Wolfendale, 1997]. It has also been suggested that the observed change of slope is not a feature of the actual cosmic ray spectrum, but due to yet unknown channels in the air shower development [Dixit *et al.*, 2010].

It is generally assumed that the cosmic rays up to about  $10^{17}$  eV or  $10^{18}$  eV are mainly of Galactic origin. Above these energies, an extra-galactic component takes over, causing a flattening of the all-particle spec-

## 2 Cosmic rays and gamma-ray astronomy

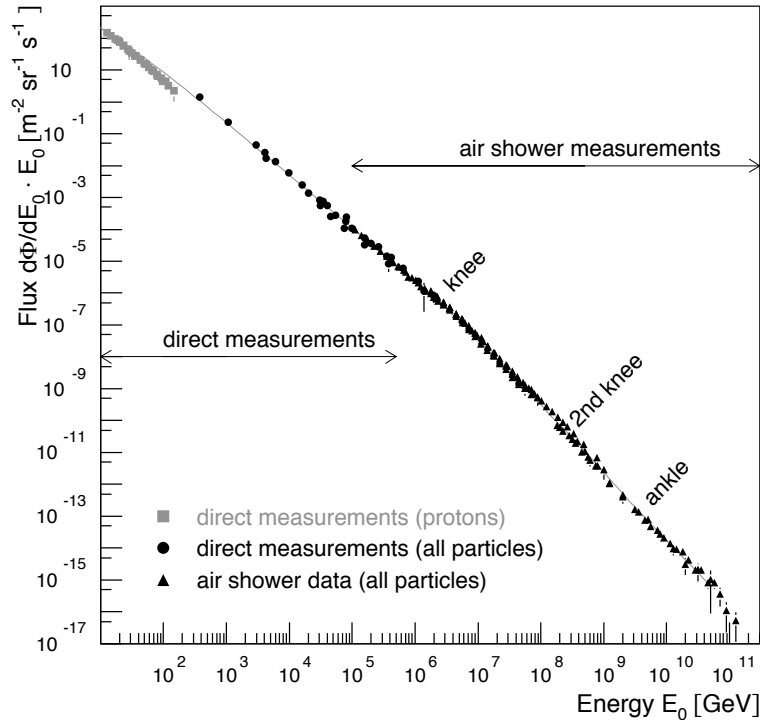


Figure 2.1: Cosmic ray energy spectrum as discussed in section 2.1. The direct and indirect (air shower) measurement techniques are discussed in section 2.4 [Blümer *et al.*, 2009].

trum at the "ankle" [Bird *et al.*, 1994; Wibig and Wolfendale, 2008]. Above the ankle, uncertainties in the experimental results are large, due mainly to the very low flux, but also to the uncertainty in the hadronic interaction models used in the Monte Carlo simulations of air showers at these energies. Nevertheless, particles with energies exceeding  $10^{20}$  eV have been observed with several large area experiments, e.g. the Fly's Eye detector [Bird *et al.*, 1994], HiRes [The High Resolution Fly's Eye Collaboration, 2009], and the Pierre Auger Observatory [Abraham *et al.*, 2010b]. Another steepening of the spectrum is clearly visible around  $10^{19.5}$  eV, which can be interpreted as evidence for the GZK cut-off. This cut-off, first predicted by Greisen, Zatsepin and Kuz'min in 1966, is caused by the strong interaction of particles above  $5 \times 10^{19}$  eV with the cosmic microwave background, which leads to a significant energy loss of particles above this energy [Greisen, 1966; Zatsepin and Kuz'min, 1966].

**Composition** The measured abundances of elements in cosmic rays at energies around 1 GeV/nucleon are shown in figure 2.2, together with the abundances of elements in the solar system. While the general shape of the distributions is similar, some elements are more abundant in cosmic rays, such as Lithium, Beryllium and Boron, some elements below  $Z = 26$  (iron) and below  $Z = 82$  (lead). These elements are assumed to be produced in interactions of cosmic rays with interstellar medium and are therefore referred to as secondary particles [Blümer *et al.*, 2009]. For some of the lighter elements individual spectra have been measured, which can be used to calculate the propagation length, see e.g. Aguilar *et al.* [2010].

At higher energies it gets more difficult to distinguish particles, since due to the lower flux only indirect (air shower) measurements are possible. In this regime, it is usually only possible to derive a mean mass of the particles using the average air shower depth and the ratio of muons to electrons, as will be discussed in more detail in section 2.4.2. The majority of measurements seem to indicate that the mean mass is increasing with energy up to  $10^{19}$  eV [Blümer *et al.*, 2009]. Above this energy, measurements from the Pierre Auger Observatory and from HiRes seem to contradict each other, the former claiming a composition dominated

Prefix	Symbol	Value
kilo-	k	$10^3$
Mega-	M	$10^6$
Giga-	G	$10^9$
Tera-	T	$10^{12}$
Peta-	P	$10^{15}$
Exa-	E	$10^{18}$

Table 2.1: SI unit prefixes commonly used in this thesis.

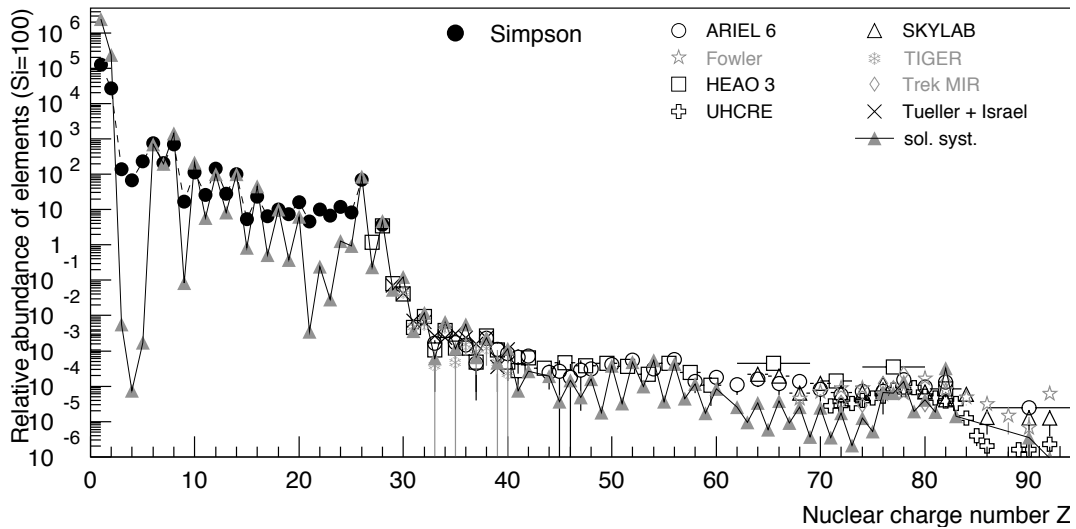


Figure 2.2: The abundances of individual elements in cosmic rays at an energy of 1 GeV/nucleon, normalised to Si ( $Z = 14$ ). Different markers represent measurements from different experiments. For reference, the abundances of elements in the solar system are shown with grey triangles [Blümer *et al.*, 2009].

by iron [Abraham *et al.*, 2010a], the latter one dominated by protons [Abbasi *et al.*, 2010b].

**Arrival directions** Generally, the flux of cosmic rays in the Galaxy is nearly isotropic, as the charged particles are deflected in interstellar magnetic fields. The effect of these fields can be estimated using the relativistic Larmor radius

$$r = \frac{E/c}{|q|B} \quad (2.1)$$

With a magnetic field of  $B = 5 \mu\text{G}$  [Battaner *et al.*, 2009] a PeV proton has a gyroradius of about 0.2 pc, which means that it is not possible to relate the arrival direction of such a cosmic ray particle to its origin for sources outside the vicinity of our solar system.

Nevertheless, small anisotropies in the TeV energy range have been found by various experiments, e.g. MILAGRO (Abdo *et al.* [2008], see figure 2.3), TIBET [Amenomori *et al.*, 2006] and IceCube [Abbasi *et al.*, 2010a]. These can be explained with special field configurations of the local magnetic field that focuses the isotropic cosmic ray flux [Battaner *et al.*, 2009], or "magnetic mirrors" that guide cosmic rays from a nearby source to the solar system [Drury and Aharonian, 2008]. However, it is not possible to identify specific sources of cosmic rays from these data.

The case is different for particles at energies above the GZK cut-off: Due to the strong energy losses

## 2 Cosmic rays and gamma-ray astronomy

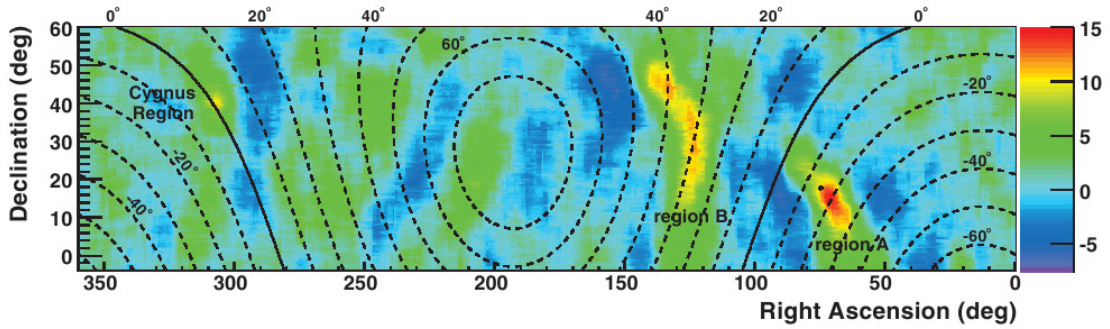


Figure 2.3: Colour map of significances of the cosmic ray anisotropies discussed in section 2.1, as seen by MILAGRO. Significant excesses can be seen in the Cygnus region and the two large regions A and B. The solid line indicates the Galactic plane and the dashed lines the Galactic latitude in  $10^\circ$  steps. The fractional excess is  $6 \times 10^{-4}$  in region A and  $4 \times 10^{-4}$  in region B [Abdo *et al.*, 2008].

above this limit particles at these energies are expected to originate mainly from relatively nearby sources, while at the same time their deflection in magnetic fields is relatively low (see equation 2.1). Therefore the distribution of their arrival directions may show indications of possible sources, depending on their composition, the propagation models and the configuration and strength of the extra-galactic magnetic fields. The Pierre Auger Observatory has detected 69 events at energies above 55 EeV (up to December 2009) and finds a slight correlation with nearby Active Galactic Nuclei (AGN) from the VCV catalogue [Véron-Cetty and Véron, 2006], as well as an overdensity in a circle of  $18^\circ$  around Centaurus A [Abreu *et al.*, 2010]. However, the present results are not yet significant enough to identify cosmic ray accelerators [Giacinti *et al.*, 2011].

So far, only hadronic cosmic rays have been discussed. Beside these there are also leptonic cosmic rays, consisting mainly of electrons. Electrons have a much shorter propagation length than hadronic cosmic rays, as they suffer substantial energy losses due to synchrotron radiation in interstellar magnetic fields. It is therefore assumed that the electrons arriving at Earth are mostly originating from one or a few nearby sources, are produced in secondary processes during the propagation, or in self-annihilation or decay processes of dark matter [Kobayashi *et al.*, 2004; Bergström *et al.*, 2009; Lineros, 2011]. The observed flux level of leptonic cosmic rays is two to three orders of magnitudes below that of hadronic cosmic rays, which is mainly due to their shorter propagation length. Near the sources, leptonic cosmic rays can play an important role, as will be discussed in sections 2.2 and 2.3.

### 2.2 Sources of cosmic rays

The shape of the energy spectrum as well as the high energies of the observed cosmic rays indicate a non-thermal acceleration process. A model to explain the acceleration has been first suggested by Enrico Fermi [Fermi, 1949] and is known as *Fermi first order acceleration* or diffusive shock acceleration today. In this model the particles pass through a shock-front many times, gaining energy at each cycle. The energy gain at each cycle is proportional to the energy of the particle, while there is a constant probability that the particle remains downstream and does not return to the shock-front. If the characteristic times of acceleration and escape are  $\tau_{acc}$  and  $\tau_{esc}$ , the resulting overall energy spectrum of the particles is [Blandford and Eichler, 1987]:

$$\frac{dN}{dE} \propto E^{-(1+\tau_{acc}/\tau_{esc})} \quad (2.2)$$

This agrees very well to the observation that the cosmic ray energy spectrum follows a power law.

It is however not clear at this point where in the universe cosmic rays are accelerated. Many authors have argued that supernova remnants (SNRs) are good sites for Fermi acceleration and that the energy density of Galactic cosmic rays can be produced by a few supernovae per century (see e.g. Blasi [2010] for a recent review). The models predict a source spectrum proportional to  $E^{-2.1}$ , which is altered to the observed  $E^{-2.7}$  along the way as the trapping time for cosmic rays in the Galaxy is estimated to be proportional to  $E^{-0.6}$  [Hillas, 2005]. However, there are several problems with the assumption that SNRs are responsible for the bulk of cosmic rays observed, the most important being that most SNR theories predict a maximum particle energy of no more than 10 to 100 TeV  $\times Z$  [Lagage and Cesarsky, 1983], clearly in disagreement with the idea that cosmic rays at least up to the knee at 4.5 PeV  $\times Z$  are of Galactic origin. Lucek and Bell [2000] have developed a model that can amplify the particle energies in SNRs, and evidence for this was reported to be seen in X-ray observations of Uchiyama *et al.* [2007].

Butt [2009] argues that isolated SNRs are not likely to be the source of the bulk of cosmic rays and that superbubbles filled with a large number of very massive, short-lived O and B stars and their corresponding supernovae are better suited to produce the amount of cosmic rays seen. Völk and Zirakashvili [2004] suggest that cosmic rays up to the knee energy can also be produced by Slipping Interaction Regions of the Galactic Wind. In summary, even though there is some (indirect) evidence for cosmic ray acceleration at SNRs, it remains largely uncertain what objects are the main contributors to the observed large number of Galactic cosmic rays.

In the domain of extra-galactic cosmic rays, the main problem is of another type. Since cosmic rays up to energies of above  $10^{20}$  eV have been observed, there must exist accelerators with the ability to accelerate particles to at least these energies. Since the particles have to be confined magnetically within the boundaries of the accelerating object, the product of its size and its magnetic field must be large, and only few known astrophysical objects satisfy this requirement. So far, Active Galactic Nuclei (AGN) seem to be the most promising candidate for this.

Overall it can be seen that the study of cosmic rays alone is not sufficient to identify their sources and to understand their generation in detail. However, two other messenger particles can be used to examine the high energy sky: High energy neutrinos and gamma photons. Both are produced in the vicinity of cosmic ray accelerators and can be used to pinpoint these accelerators since they are not affected by magnetic or electric fields.

Several large detector systems exist today for the detection of high energy neutrinos, e.g. the IceCube detector, but no signal of cosmic neutrinos could be detected so far [Abbasi *et al.*, 2011]. It is believed that a supernova in our galaxy or in a galaxy of the local group will produce a neutrino flux high enough to be detected in current instruments, but none has been observed by any instrument. A recent analysis of IceCube data up to May 2009 searching for emission from other candidate sources such as starburst galaxies, clusters of galaxies or sources seen by gamma-ray instruments has produced only upper limits. The sensitivity of the IceCube detector will however improve with the completion of the array and possible extensions [Abbasi *et al.*, 2011]. The only neutrinos from an astrophysical source that have been detected to this day – apart from solar neutrinos – originate from the supernova 1987A in the Large Magellanic Cloud (see Krivosheina [2004] for a review). However, these neutrinos had energies in the MeV regime and were not connected to non-thermal processes.

On the other hand, more than hundred sources of very high energy gamma-ray emission have been detected so far, and some of these sources show evidence for cosmic ray acceleration. The next section introduces the field of gamma-ray astronomy and discusses its potential to contribute to the solution of the question of the origin of cosmic rays.

## 2 Cosmic rays and gamma-ray astronomy

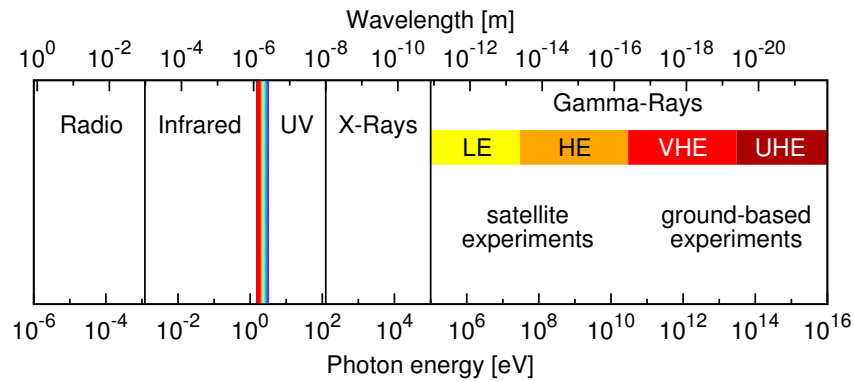


Figure 2.4: Energy bands in modern astronomy from radio to gamma-rays. The visible regime is indicated by the rainbow colours at about 1 eV. The energy bands of gamma-ray astronomy are: Low energy (LE), high energy (HE), very high energy (VHE) and ultra high energy (UHE).

### 2.3 Gamma-ray astronomy

For many centuries astronomy was limited to observations of the visible region of the electromagnetic spectrum. It was only in the 20<sup>th</sup> century that technological advances made observations of light at other wavelengths possible. Since then, astronomy has expanded to radio, infrared, UV, X-ray and the wide range of gamma energies (see figure 2.4). As the atmosphere is opaque for most of these frequencies (gamma, X-ray, UV and partly infrared), these observations are done with experiments in space. The only windows in the atmosphere for electromagnetic radiation are in the radio and the narrow visible light band. However, at high photon energies (starting from about 30 GeV) it is possible again to detect radiation from the ground — indirectly, by detecting the extensive air showers produced by these highly energetic photons (see section 2.4).

The gamma-ray domain is usually sub-divided into several energy regimes [Aharonian, 2004]:

- Low energy (LE): up to 30 MeV
- High energy (HE): 30 MeV to 30 GeV
- Very high energy (VHE): 30 GeV to 30 TeV
- Ultra high energy (UHE): Above 30 TeV

The low and the high energy regime are accessible only for space instruments, while the very high energy and ultra high energy regime are exclusively covered by ground-based experiments, with a small overlap of the techniques between 10 to 100 GeV (see section 2.4). The focus of this thesis is on the latter two, and this section will give an introduction into the rapidly developing field of very high energy gamma-ray astronomy and motivate the expansion to the — yet poorly covered — ultra high energies.

#### 2.3.1 Very high energy gamma-ray astronomy

In the last two decades, very high energy (VHE) gamma-ray astronomy has been established as a new field in astronomy, mainly using imaging air Cherenkov telescopes (see section 2.4.5) that cover the photon energy range from about 30 GeV to about 100 TeV. At the low energies, the limit is set by the faintest Cherenkov light signal that can still be seen against the residual light present even during dark, moonless nights, and large telescope mirror areas are needed to achieve a low energy threshold. Additionally, large shower fluctuations make the reconstruction of events at low energies difficult, and the strong cosmic ray

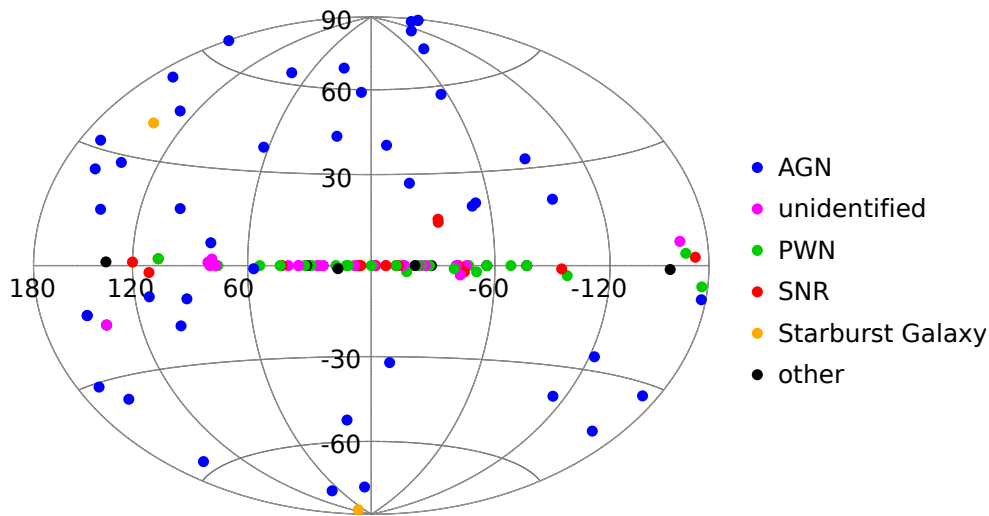


Figure 2.5: Currently known sources of VHE gamma-ray emission (June 2011), colour coded according to the source type, in Galactic coordinates. AGN are Active Galactic Nuclei (all types), PWN are pulsar wind nebulae and SNR are supernova remnants (all types). Dark sources, i.e. sources with no counterpart in any other wavelength band, have been included under "unidentified". Source list is taken from Wakely and Horan [2011].

electron flux below 100 GeV poses a major source of background. At the high energy end the limit is given by the decreasing gamma photon flux. Large effective areas and long exposure times per source are needed to collect enough photons at energies above 10 TeV. The maximum energy to which a particular gamma-ray spectrum can be measured with a given instrument depends on the slope of the spectrum and the absolute flux.

About one hundred sources of VHE gamma-ray emission have been found so far, some with clear counterparts in other wavelength regimes, some without (see figure 2.5). About two thirds of the sources are Galactic, among them supernova remnants (SNRs), pulsar wind nebula (PWN), X-ray binaries and stellar clusters. The "dark" sources, where no counterpart has been found so far in any other wavelength, make up a significant number, and understanding these sources remains an open challenge for the field (see e.g. Aharonian *et al.* [2008a]; Tibolla *et al.* [2009]).

With the angular resolution of Cherenkov telescope systems of about  $0.1^\circ$ , spatial features of many extended (Galactic) sources can be resolved. Among the most prominent discoveries are the shell-type supernova remnants, where the ring structure seen in other wavelength bands can also be seen in gamma-rays, e.g. SN 1006 [Acero *et al.*, 2010a] or RX J0852.0-4622 (Vela Junior, shown in figure 2.6).

One of the key science objectives of VHE gamma-ray astronomy is the search for the sources of cosmic rays [Drury *et al.*, 1994]. While a gamma-ray signal from an astronomical source is a clear indication for particle acceleration at this object, it is not straightforward to uniquely identify this object as a source of *hadronic* cosmic rays, since gamma-rays can be produced efficiently either by hadronic or leptonic particles. In the hadronic scenario, neutral pions are produced in collisions of highly energetic hadronic particles with the interstellar medium, and gamma-rays are created as the pions decay. In the leptonic scenario, the gamma-rays are produced by the inverse Compton effect, in which the energy of the electron is transferred to a low energy photon, e.g. a cosmic microwave photon or a thermal photon from a nearby star. In a dense surrounding medium the electrons can also produce gamma-rays through non-thermal bremsstrahlung [Aharonian, 2004].

To overcome this ambiguity observations in different energy bands from radio wavelengths to gamma-rays are combined in a broadband spectral energy distribution and compared with models of the emission.

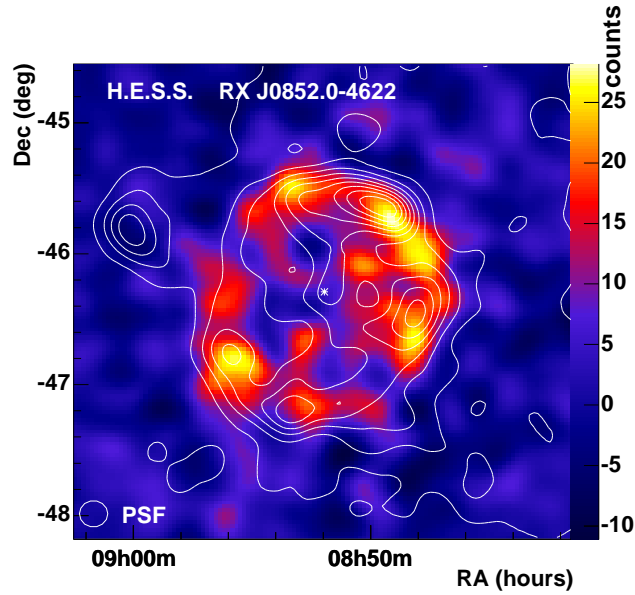


Figure 2.6: SNR RX J0852.0-4622 (Vela Junior) as seen in gamma-rays by H.E.S.S., with overlaid contours from X-ray observations by ROSAT [Aharonian *et al.*, 2005c].

This has been used, for example, to examine the acceleration processes in the SNR RX 1713.7-3946, which was identified by VHE observations as a good cosmic ray source candidate [Aharonian *et al.*, 2006a]. In this case, both the observations in the X-ray as well as in the HE gamma regime indicate that hadronic acceleration is unlikely to occur [Ellison *et al.*, 2010] or at least to dominate [Abdo *et al.*, 2011a]. In many cases, however, the source of the VHE gamma-ray emission cannot be identified unambiguously, as the model-dependency in the interpretation of multi-wavelength data often introduces large uncertainties.

Although gamma-ray astronomy in the VHE band has produced a wealth of new information and greatly increased our knowledge about the non-thermal universe, some questions remain, e.g. about the nature of the dark sources. It is especially remarkable that despite the discovery of a great number of cosmic ray source candidates, a conclusive picture about the origin of cosmic rays has still not been achieved. Specifically, current observations cannot answer the question about what sources are responsible for the acceleration of cosmic rays up to PeV energies, and for many sources the emission scenario (leptonic or hadronic) remains uncertain. As outlined in the following subsection, extending the range of gamma-ray observations to higher energies may help to answer those questions.

### 2.3.2 Ultra high energy gamma-ray astronomy

As discussed in section 2.2, it is expected that the Galaxy contains objects that can accelerate cosmic rays up to energies of above  $10^{17}$  eV ("PeVatrons"), although uncertainty remains about the nature of these objects. Due to the kinematics in the hadronic scenario of cosmic ray acceleration, these objects should also be emitters of gamma-rays up to energies of several 100 TeV [Gabici and Aharonian, 2007], and gamma-ray observations at ultra high energies should lead to unambiguous identification of these PeVatrons.

Up to now, no gamma-ray source could be established above 100 TeV, mainly due to the insufficient effective areas of current gamma-ray observatories. There exists, however, a large number of (mainly Galactic) gamma-ray sources where no cut-off in the energy spectrum was found in the sensitivity range of current instruments, and it is very well possible that these sources emit gamma-rays with energies much higher than detected so far. A few sources of gamma-ray emission at multi-TeV energies, at the transition from VHE to UHE, have been detected by H.E.S.S., either because of their relatively strong fluxes or very long

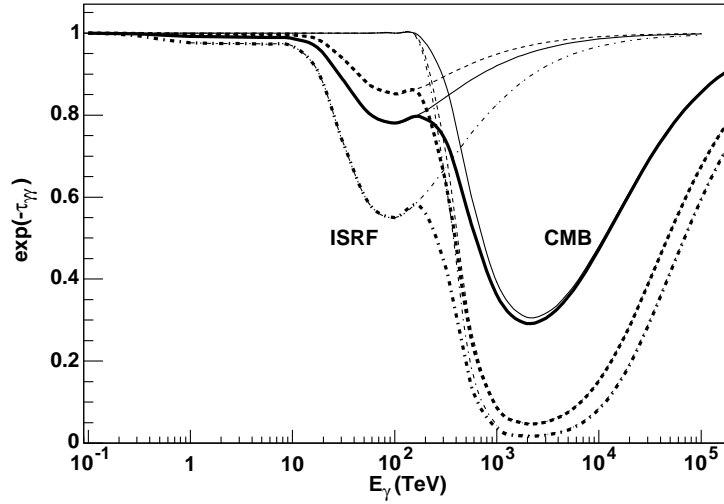


Figure 2.7: Transmittance of gamma-rays  $T = \exp(-\tau_{\gamma\gamma})$  versus gamma-ray energy  $E_{\gamma}$  [Moskalenko *et al.*, 2006]. The thick lines show the total absorption, while the thin lines show the contributions by ISRF and CMB. The three different line styles refer to different positions of the source in the Galaxy: Solid lines – Near the Galactic Centre (GC); dashed lines – At 20 kpc from the GC, perpendicular to the line from the sun to the GC; dash-dotted lines – At 20 kpc behind the GC.

observation times. Among them are several SNRs, e.g. RX J0852.0-4622 [Aharonian *et al.*, 2007] and the aforementioned RX 1713.7-3946, and pulsar wind nebulae, e.g. MSH 15-52 [Aharonian *et al.*, 2005a] or Vela X [Aharonian *et al.*, 2006b]. The MILAGRO observatory (see section 2.4.3) has also found a number of sources in the multi-TeV energy range [Abdo *et al.*, 2009]. Their spectrum of the Crab Nebula contains data points up to 100 TeV, albeit with a low significance [Hüntemeyer and Milagro Calibration, 2010].

Dedicated observations in the multi-TeV to UHE regime have been proposed by different authors for various reasons. Detections of sources in the UHE regime would not only help to explain the acceleration of Galactic cosmic rays up to PeV energies, the shape of the spectrum at these energies could also be used to distinguish between leptonic and hadronic accelerators. The Klein-Nishina effect, i.e. the decreasing cross-section for the inverse Compton effect at ultra high energies, and the radiative synchrotron energy losses of a primary electron population in magnetised post-shock environments, should lead to a clear drop in the gamma-ray spectrum in the UHE regime, if the acceleration mechanism is mainly leptonic [Rowell *et al.*, 2008]. Measuring the energy spectra of sources up to the UHE regime can therefore help to resolve ambiguities between the leptonic and hadronic emission scenarios.

Giant molecular clouds have also been proposed as possible sources of UHE gamma photons, being tracers of nearby supernovae. While the supernovae can only accelerate particles to the highest possible energies for a short time after the initial explosion, and are therefore hard to detect, the particles may produce a visible UHE signal upon interaction with matter in a nearby giant molecular cloud for a much longer time [Gabici and Aharonian, 2007]. Apart from that, the few known young supernovae in the Galaxy or its vicinity, e.g. SN 1987A in the Large Magellanic Cloud, are also interesting candidates for UHE gamma-ray emission. It has also been suggested that UHE gamma-rays may be seen from the direction of the local supercluster [Kneiske *et al.*, 2009].

It is known that the absorption of gamma-rays by the interstellar radiation field (ISRF) and the cosmic microwave background (CMB) becomes stronger at higher energies, leading to a steeper energy spectrum. Depending on the position of the source, this may become an obstacle for observations in the ultra high energy regime. Figure 2.7 shows the transmittance of gamma-rays versus the energy as simulated by Moskalenko *et al.* [2006]. In this, the transmittance  $T$  is defined as the fraction of photons not absorbed and calculated

## 2 Cosmic rays and gamma-ray astronomy

from the optical depth  $\tau_{\gamma\gamma}$  by  $T = \exp(-\tau_{\gamma\gamma})$ . For a source near the Galactic Centre, the absorption is about 23% at 100 TeV and increases to about 65% at 1 PeV. It is significantly greater for sources further away, and can become as strong as 95% at 1 PeV for a source at the other end of the Galaxy, 20 kpc behind the Galactic Centre. It seems however, that the observation of gamma-rays at least in the 100 TeV region is not severely complicated by absorption effects. As an interesting side-effect an estimation of the distance to a gamma-ray source may be possible from the spectrum, assuming that the source spectrum itself can be modelled with sufficient certainty [Tluczykont *et al.*, 2009b].

For extragalactic sources, the absorption in the UHE regime is considerable due to the longer path the photons have to travel through the ISRF and the CMB [Hauser and Dwek, 2001; Kneiske and Dole, 2008; Raue and Mazin, 2010], which makes the detection of UHE gamma-ray signals from extra-galactic sources unlikely. On the other hand, current results from Cherenkov telescopes indicate that the gamma-ray absorption for distant sources may be weaker than commonly assumed [Horns and Meyer, 2012]. Likewise, UHE gamma-ray signals from extra-galactic sources – if detected – may raise interesting questions about the transparency models of the universe, or hint at new physics.

### 2.4 Experimental techniques in cosmic ray physics and gamma-ray astronomy

Generally, similar detection techniques are used in both cosmic ray physics and gamma-ray astronomy. At lower energies, the particles are detected *directly* by particle detectors on board of satellites in space, while at higher energies *indirect*, ground-based techniques are used. The transition from space to ground-based experiments in gamma-ray astronomy occurs at energies of about 10 to 100 GeV, with a small overlap of space-based and ground-based experiments. Above these energies the flux of gamma-ray sources becomes too weak to detect enough photons in the relatively small spaceborne detectors (effective area  $O(1 \text{ m}^2)$ ), while on the other hand the photon energy becomes high enough to produce extensive air showers detectable by ground-based detectors. In cosmic ray physics, direct experiments are possible up to 100 TeV due to the higher flux, but nevertheless air shower experiments have about the same energy threshold as for gamma-rays, thus giving a much larger overlap (see figure 2.1).

All gamma-ray detectors are also sensitive to charged cosmic rays, and methods of discrimination between the two are essential in order to enable observations of gamma-ray sources against the much higher, isotropic flux of charged cosmic rays.

The following sections will give an overview of space-based and different types of ground-based detection techniques and introduce some experiments, with the focus on Cherenkov detectors for gamma-ray astronomy, as the work described in this thesis is set in this field. Section 2.4.1 will briefly introduce satellite experiments for gamma-rays and charged cosmic rays, while the remaining sections will deal with ground-based experiments. Section 2.4.2 starts with an introduction to extensive air showers, which can be detected directly with air shower arrays (section 2.4.3), historically the first ground-based cosmic ray detectors and still widely used today. Section 2.4.4 deals with Cherenkov light that is produced by extensive air showers and can be also used for their detection. Section 2.4.5 covers the imaging Cherenkov technique which was the great breakthrough in ground-based gamma-ray astronomy and which is used by almost all current instruments in the field. The final section 2.4.6 introduces the non-imaging Cherenkov technique, which is used today in several cosmic ray experiments, but also has a potential for gamma-ray astronomy, as will be shown.

It should be noted at this point that some other important techniques in the field will not be discussed, as they are not closely related to the main topic of this thesis. Among these are the fluorescence detection of air showers, which is used especially for cosmic ray physics at the highest energies, e.g. by telescopes in the Pierre Auger Observatory [Abraham *et al.*, 2004] or Telescope Array [Ogio *et al.*, 2005], or the measurement of radio signals emitted by charged particles in the influence of the terrestrial magnetic field, e.g. by LOPES

[Hörandel *et al.*, 2011].

### 2.4.1 Satellite experiments

Satellite detectors for high energy gamma-rays work in a similar way as particle detectors on Earth. Current instruments like AGILE [Tavani *et al.*, 2009] and FERMI [Atwood *et al.*, 2009] detect gamma photons by tracking their conversions into  $e^+/e^-$  pairs with a segmented silicon strip detector. A subsequent calorimeter is used to accurately reconstruct the energy of the particle and to help with the particle identification. Charged particles are rejected using an anticoincidence system, consisting of a shield of plastic scintillators around the detector.

Satellite experiments work in continuous operation, unaffected by the day-and-night cycle and weather conditions. Together with a large field of view (e.g. about 2.4sr for FERMI) this leads to a high exposure survey of the whole sky, albeit with a small effective area compared to ground-based experiments. The energy range of satellite detectors usually extends up to about 100GeV, a limit posed by the effective areas and the maximum energies that can be measured reliably within the magnetic calorimeter of a space-based experiment.

Besides the combined gamma-ray and cosmic ray experiments there are also detectors optimised for cosmic ray measurements only, often with a focus on particle separation and detection of antiparticles. The PAMELA experiment has found a significant excess of positrons compared to the models that expect all positrons to be secondary, i.e. to be produced from primary cosmic rays during the propagation. This can be explained by a primary source for positrons nearby, or the decay of dark matter [Adriani *et al.*, 2009]. In the case of antiprotons, no deviation from the expected pure secondary production was found by PAMELA [Adriani *et al.*, 2010]. Recently the AMS-02 detector was installed on the International Space Station, offering an unprecedented sensitivity to antimatter in cosmic rays and probing the existence of primordial antimatter in the universe [Zuccon, 2009].

### 2.4.2 Extensive air showers

If a highly energetic particle (either charged cosmic ray or gamma photon) hits the atmosphere, it interacts with the air molecules and produces secondary particles. The average height of the first interaction is determined by the cross-section and depends on the energy and the nature of the primary particle. The secondary particles produce new particles through various processes, thus initiating a particle cascade called *extensive air shower (EAS)*.

**Composition of air showers** Generally, an air shower consists of a hadronic, an electromagnetic and a muonic component (see figure 2.8). The hadronic component consists mainly of neutral and charged pions, which are formed in strong interactions upon collisions of hadronic particles with air molecules. After a very short lifetime of about  $10^{-16}$  s (already taking into account the time dilation caused by their relativistic velocities) the neutral pions decay into two photons, which feed the electromagnetic component. The mean lifetime of the charged pions is considerably longer ( $> 10^{-7}$  s), therefore they contribute to the hadronic cascade, before they eventually decay into muons [Grieder, 2001].

The electromagnetic component consists mainly electrons ( $e^+$  and  $e^-$ ) and gamma photons. The secondary electrons produce highly energetic photons through bremsstrahlung, which in turn produce new  $e^+$  and  $e^-$  through pair production, thus sustaining the electromagnetic cascade. The average energy of the secondary particles decreases with height due to further reactions and inelastic scattering. The energy losses due to bremsstrahlung decrease strongly with energy, and below a critical energy  $E_c$  the electrons lose more energy to ionisation processes than to bremsstrahlung. In this case, no new particles are produced, and eventually the electromagnetic cascade dies out. The critical energy for electrons can be approximated by

## 2 Cosmic rays and gamma-ray astronomy

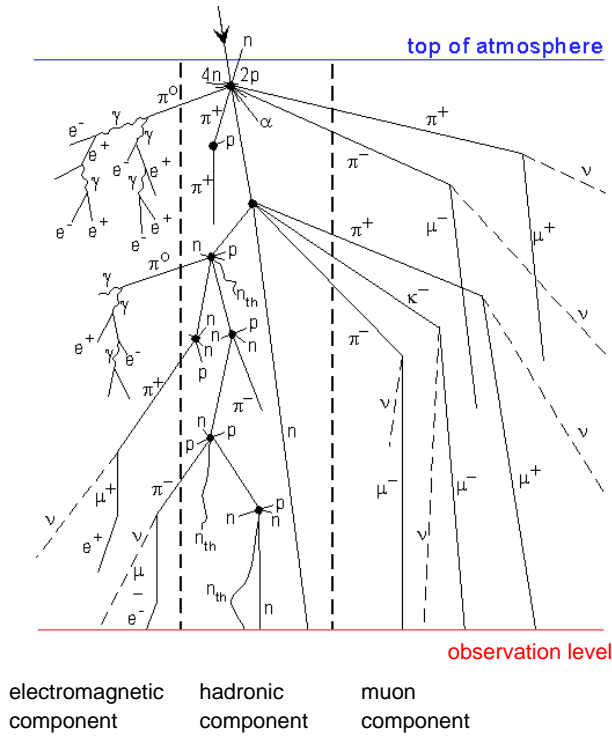


Figure 2.8: Schematic illustration of a hadronic air shower, split up to the three components discussed in the text (modified from Clay and Dawson [1997]; Gosse [2001]; Grieder [2001]).

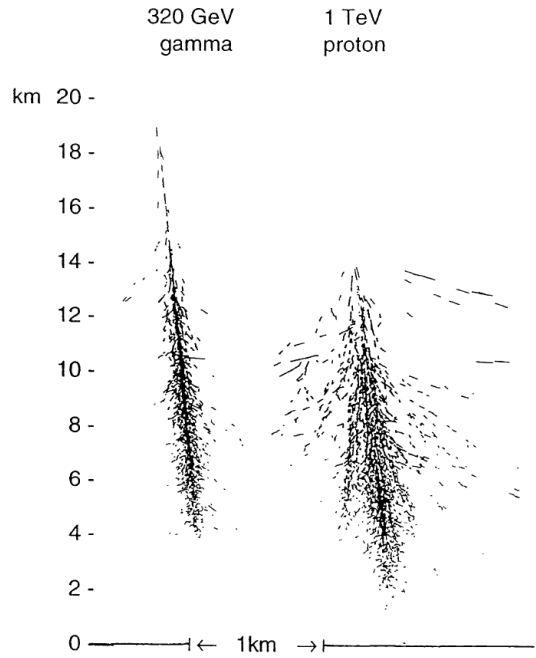


Figure 2.9: Illustrative comparison of air showers induced by a gamma photon and a proton primary. The lateral scale is exaggerated by a factor of five for better visibility [Hillas, 1996].

[Berger and Seltzer, 1964]

$$E_c = \frac{800}{Z + 1.2} [\text{MeV}] \quad (2.3)$$

where  $Z$  is the charge number of the respective air molecule. Effectively, it amounts to about 84.2 MeV for electrons in air at standard conditions [Grieder, 2001].

The muonic component is fed mainly from the hadronic cascade. Muons have a lifetime of about  $2.2 \times 10^{-6}$  s, but due to the time dilation most of them reach the ground, while a few decay into an electron, a neutrino and an anti-neutrino.

**Differences between hadronic and photonic primaries** Hadronic primary particles initiate a hadronic cascade from their first interaction, with the electromagnetic cascade starting from the first decaying neutral pions almost directly after (this case is shown in figure 2.8). In the case of a primary electron (not considered further here) or gamma photon, the electromagnetic cascade is started first, either with the generation of bremsstrahlung (electron primary) or pair production (photon primary). In this case, the hadronic component sets on only later, and is much weaker.

Extensive air showers from hadronic and photonic origin also differ in their lateral shape: The electromagnetic cascade is usually concentrated close to the shower axis, while the hadronic cascade fans out further through sub-showers with large transversal momentum (see figure 2.9). These differences can also be used for gamma hadron separation if they can be detected by the experiment. In imaging Cherenkov telescopes, hadronic events appear as a wider, more scattered image in the camera, which provides a powerful

## 2.4 Experimental techniques in cosmic ray physics and gamma-ray astronomy

method to discriminate cosmic rays from gamma-rays in these experiments (see e.g. Hillas [1985, 1996] and discussions in sections 2.4.5 and 3.2).

**Longitudinal development** Figure 2.10 shows the longitudinal developments of the three components in an air shower for different primary particles. In all cases secondary gamma photons and electrons (i.e. the electromagnetic component) are the most numerous particles. The hadronic and muonic components are stronger for proton and iron induced showers than for gamma-ray induced showers, nevertheless contain still less particles than the electromagnetic component. At the same primary energy, protons produce slightly fewer electrons than gamma primaries, and iron nuclei produce even fewer. This causes a particle-dependent shift of the reconstructed energy in experiments that are sensitive only to the electron component or the total number of charged particles, such as Cherenkov detectors. As the electromagnetic component is the strongest one in the air shower, its maximum also defines the global *shower maximum*, i.e. the point at which the air shower has reached the largest number of particles. It is slightly higher in the atmosphere for protons than for gammas, and significantly higher for iron primaries, but is also proportional to the logarithm of the primary energy.

**A simple air shower model** This behaviour can be explained with a simple shower model introduced by Heitler [1944], that assumes that the number of air shower particles doubles exactly after every characteristic length  $\lambda$ . The number of particles at the depth<sup>1</sup>  $X$  is then given by

$$N(X) = 2^{X/\lambda} \quad (2.4)$$

If the energy of a particle is split up exactly equally between the two newly generated particles at each interaction point, and no energy is lost to other processes, the energy of each particle is  $E_p = E_0/N$ , with  $E_0$  as the primary particle energy and  $N$  the number of particles currently in the shower. If this energy falls below the critical value  $E_c$ , no new particles are generated and the maximum number of particles (i.e. the number of particles at the shower maximum) is given by

$$N_{max} = \frac{E_0}{E_c} \quad (2.5)$$

Combined with equation 2.4 this predicts the shower maximum at a depth of

$$X_{max} = \frac{\lambda}{\ln(2)} \ln\left(\frac{E_0}{E_c}\right) \quad (2.6)$$

In this simple model, particles with more than one nucleon are treated as a superposition of individual particles. If the nucleus contains  $A$  nucleons, each one triggers an air shower with an energy of  $E_0/A$ . In this case, the depth of the maximum is at

$$X_{max} = \frac{\lambda}{\ln(2)} \ln\left(\frac{E_0}{A E_c}\right) \quad (2.7)$$

The model therefore correctly predicts the logarithmic dependence of the shower depth on the energy, as well as the smaller depth for heavier particles. However, complex simulations that take into account the particle and energy dependencies of the interaction lengths, the energy distributions between generated particles and other important factors, show that the difference in shower depth between hadrons of different mass is overestimated by this model. The results from such simulations are presented in section 5.4.5.

<sup>1</sup>In air shower physics the vertical position is usually given by the atmospheric depth in  $\text{g}/\text{cm}^2$ , which can be seen as the air column that has been traversed by the shower so far. The relation between atmospheric depth and the height above sea level depends on the atmospheric conditions, which is taken into account in the simulations by using different empiric atmospheric models. Thus, the relation between depth and height implied in figure 2.10 is to be seen as rough approximation.

2 Cosmic rays and gamma-ray astronomy

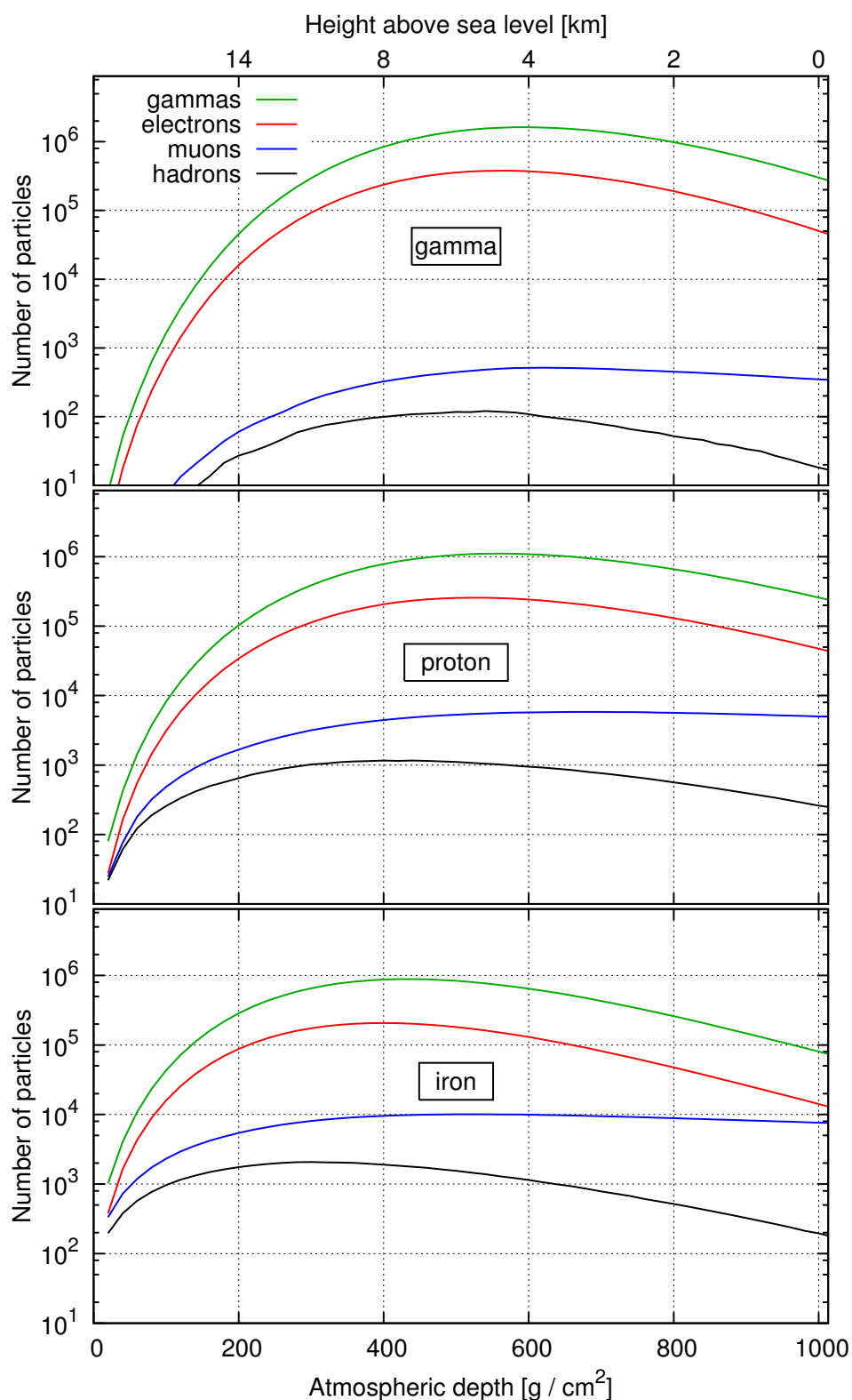


Figure 2.10: Numbers of different particle species at different heights in an air shower, shown for gamma (top), proton (middle) and iron (bottom) primaries. Electrons are  $e^+$  and  $e^-$ , muons are  $\mu^+$  and  $\mu^-$ . All plots show an average of 100 simulated vertical showers with 500 TeV primary energy. Simulations were done with CORSIKA 6.735 [Heck *et al.*, 1998].

## 2.4 Experimental techniques in cosmic ray physics and gamma-ray astronomy

Equation 2.5 also shows that the total number of (relativistic) particles in the air shower is expected to be roughly proportional to the primary energy, thus it can be used in the energy reconstruction.

If the energy of the particle can be accurately estimated, the difference of the average shower depth can be used to estimate the mass of a detected particle. The use of this method is discussed in more detail in section 5.5 for the case of the H<sub>i</sub>SCORE experiment. Another method to discriminate between the particles is the independent detection of the electronic and muonic components with respective detectors at the observation level. A high  $N_\mu$  to  $N_e$  ratio implies a heavier primary particle, a very low ratio a gamma primary.

**EAS simulations** In order to develop air shower detectors and interpret their measurements, it is very important to have an accurate air shower simulation that takes into account all possible reactions to the best knowledge. CORSIKA [Heck *et al.*, 1998] is a sophisticated and powerful air shower simulation package, which was developed in the framework of the KASCADE experiment and is today widely used in the field. All simulations presented in this thesis are done using CORSIKA version 6.735 with the QGSJET module [Kalmykov *et al.*, 1997] for high energy hadronic interactions, the GHEISHA module [Fesefeldt, 1985] for lower energies, and EGS4 for the electromagnetic component. It provides detailed outputs of the particle populations at different heights (as shown in figure 2.10) and at the ground, the energy losses and the arrival times of particles. The additional IACT package calculates the Cherenkov light generated by the relativistic particles in the air shower and is used for the simulation of both imaging Cherenkov telescopes (see section 2.4.5) and wide-angle Cherenkov detectors (section 2.4.6). Its output is used as input for the detector simulations `sim_telarray` for H.E.S.S. (see chapter 3) and `sim_score` for the H<sub>i</sub>SCORE experiment (see chapters 4 and 5).

### 2.4.3 Air shower arrays

Present day air shower experiments measure the cascade of secondary particles usually with scintillation or water Cherenkov detectors. In both cases all charged particles at observation level produce light signals in the detector that are read out with photomultipliers. Some experiments use additional muon detectors to gain information about the nature of the primary particle, e.g. the HEGRA detector [Just *et al.*, 1993] or KASCADE. With its good area coverage the KASCADE experiment is especially sensitive to the composition of cosmic rays [Hörandel *et al.*, 2006]. The largest detector using scintillation detectors was the AGASA array [Agasa Collaboration, 2006] with 111 detector station distributed over 100 km<sup>2</sup>, that detected cosmic rays up to above 10<sup>20</sup> eV. The largest detector ever build is the Pierre Auger Observatory in Argentina [Zavrtanik and Pierre Auger Collaboration, 2011] with an effective area of about 3000 km<sup>2</sup>, using water Cherenkov detectors and fluorescence telescopes. Only with such a large area it became possible to make the detailed study of the cosmic ray energy spectrum and the arrival directions of particles at energies above the GZK cut-off that has been mentioned in section 2.1.

Though all air shower detectors are in principle sensitive also to gamma-rays, it was only recently that the first gamma-ray sources could be detected by the air shower experiments MILAGRO, Tibet AS array and ARGO-YBJ. The main requirements for the successful detection are a low energy threshold and good angular resolution. MILAGRO [Atkins *et al.*, 2005] was a water Cherenkov detector with a large pool of 60 m × 80 m × 8 m surrounded by a sparse 200 m × 200 m array of 175 smaller outrigger stations, located at an altitude of 2630 m in New Mexico, USA. Due to its high elevation it achieves a gamma-ray threshold of about 1 TeV. It has observed gamma-ray emission in the TeV range from a couple of sources, including 14 sources also seen by the FERMI satellite in the high-energy band [Abdo *et al.*, 2009], and from the Cygnus region [Abdo *et al.*, 2007]. The Tibet air shower array consists of currently 533 plastic scintillator detectors covering an area of 22,050 m<sup>2</sup> and is located in Tibet, China, at an altitude of 4300 m. Seven spots of emission could be detected in a search for counterparts of 27 FERMI sources with a significance of greater than 2σ. The Crab Nebula is seen with a significance of 6.9σ [Amenomori *et al.*, 2010]. The ARGO-YBJ detector, located in Tibet as well, uses Resistive Plate Chambers to detect air showers and covers an area

## 2 Cosmic rays and gamma-ray astronomy

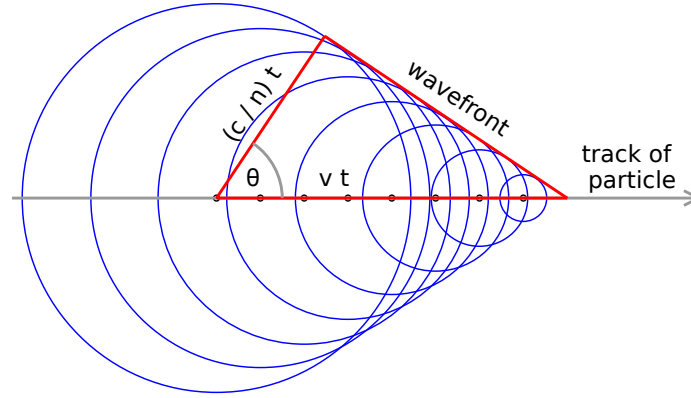


Figure 2.11: The Cherenkov light front is produced by constructive interference of individual waves emitted along the track of the charged particle.

of about  $10,000\text{m}^2$  [Aielli *et al.*, 2006]. Up to 2011, four previously known sources of VHE gamma-ray emission, including the Crab Nebula and Mrk 421, could be seen with ARGO-YBJ with more than  $5\sigma$  [Cao *et al.*, 2011].

Currently, the new gamma-ray air shower detector HAWC is constructed in the Sierra Negra, Mexico, at an altitude of 4100m [Goodman and HAWC Collaboration, 2010]. It consists of an array a medium-sized water tanks (4.6m deep, 5 m across), each one equipped with one large photomultiplier. Due to its higher altitude and larger instrumented area it is expected to be about 10 to 15 times more sensitive to gamma-ray sources than MILAGRO.

At higher energies, upper limits on the gamma-ray flux have been established, e.g. by the KASCADE experiment for point sources at 300TeV [Antoni *et al.*, 2004], and the Pierre Auger Observatory for a diffuse gamma-ray flux above  $10^{18}\text{eV}$  [Abraham *et al.*, 2009; Scherini and the Pierre Auger Collaboration, 2011].

One of the main drawbacks of air shower arrays is their relatively high threshold and their low energy resolution, both due to the low number of secondary particles that reach the ground. Setting up the detector at high altitudes, close to the shower maximum, can partly offset this disadvantage (see figure 2.10). On the other hand, relativistic particles at all stages of the air shower emit Cherenkov light. The number of Cherenkov photons at the ground is many orders of magnitude larger than the number of particles, and the Cherenkov light contains – in principle – information about all stages of the air shower. It can be detected with fast light sensitive detectors on the ground and used to reconstruct the properties of the air shower, as will be explained in the following subsection.

### 2.4.4 Cherenkov light from extensive air showers

Cherenkov light is emitted if charged particles move through a dielectric medium with a speed faster than the speed of light in the medium, i.e. if

$$v > \frac{c}{n} \Leftrightarrow \frac{v}{c} > \frac{1}{n} \quad (2.8)$$

with  $n$  being the refractive index of the material. The charged particle polarises the molecules of the ambient medium for a brief moment while passing by, producing small dipoles. Each of the moving dipoles generates electromagnetic radiation. If the Cherenkov condition 2.8 is true, the individual waves produced along the way form a constructive interference (see figure 2.11). The angle of emission is given by

$$\cos(\theta) = \frac{c}{nv} = \frac{1}{n\beta} \quad (2.9)$$

## 2.4 Experimental techniques in cosmic ray physics and gamma-ray astronomy

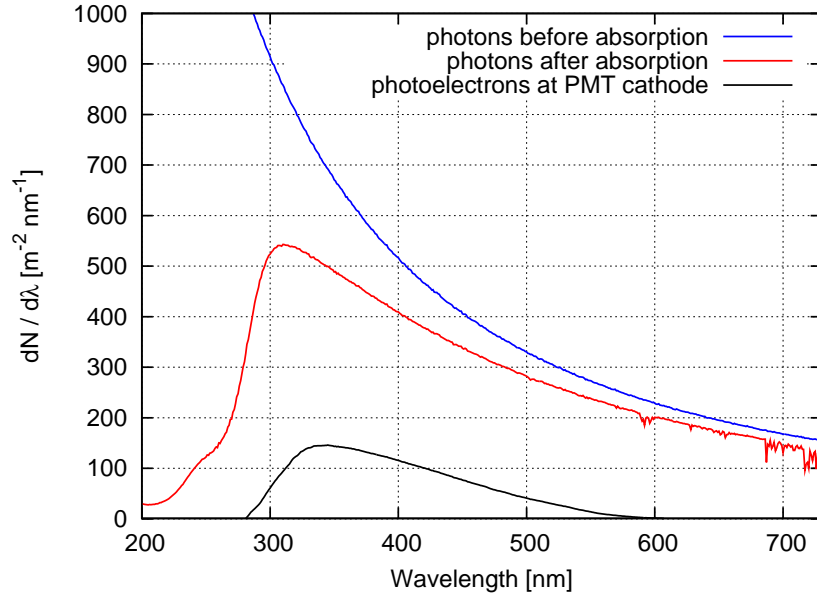


Figure 2.12: The spectrum of Cherenkov light from 750 TeV gamma-ray events before and after atmospheric absorption, and after taking into account the wavelength-dependent quantum efficiency of the detector. The emission spectrum is taken from CORSIKA simulations, absorption is done using MODTRAN [Kneizys *et al.*, 1996] and the quantum efficiency of the PMT is modelled using the values given in the data sheet of the Electron Tubes PMT 9352KB, one candidate photomultiplier for the H<sub>i</sub>SCORE experiment (see appendix E).

The minimal energy that a relativistic particle must have to emit Cherenkov radiation is given by

$$\frac{E_{th}}{m_0 c^2} = \frac{1}{\sqrt{1 - (v/c)^2}} \stackrel{!}{=} \frac{1}{\sqrt{1 - (1/n)^2}} \quad (2.10)$$

Air Cherenkov detectors utilise the fact that most of the secondary particles in an air shower fulfil the Cherenkov condition and emit Cherenkov light. Since the refractive index of air varies with pressure, the energy threshold and the emission angle of Cherenkov light in air depend on altitude and the atmospheric conditions. For a typical atmosphere [US Standard Atmosphere, 1976] the refractive index is about  $n = 1.00011$  at a typical height of an air shower maximum at 8km, which gives an energy threshold of  $E_{th} = 67m_0c^2$  (about 34MeV for electrons and 7GeV for muons) and an emission angle of  $\theta = 0.85^\circ$  (assuming  $\beta = 1$ ).

The Cherenkov light spectrum of a singly charged particle is given by

$$\frac{dN}{dx d\lambda} = 2\pi\alpha \left( 1 - \frac{1}{(\beta n(\lambda))^2} \right) \frac{1}{\lambda^2} \quad (2.11)$$

where  $\alpha \approx 1/137$  is the fine structure constant and  $n(\lambda)$  the wavelength dependent refractive index of the ambient material. In the visible light regime  $n(\lambda)$  is roughly constant and the Cherenkov light spectrum follows a  $\lambda^{-2}$  dependence, making Cherenkov light appear blue. In the UV regime, the refractive index becomes smaller than 1, making Cherenkov emission impossible and preventing an "infinite" total amount of Cherenkov radiation.

The spectrum seen with atmospheric Cherenkov detectors is a product of the emission spectrum and the atmospheric transmission between the emission and the observation altitude. Figure 2.12 shows the spectrum of Cherenkov light before and after atmospheric absorption (assuming a sea level detector altitude),

## 2 Cosmic rays and gamma-ray astronomy

and after taking into account the wavelength-dependent sensitivity of the detector, for an average of 50 gamma-ray showers of 750 TeV primary energy. Since the absorption is stronger at shorter wavelengths, the ratio of intensities at short and long wavelengths may be used for estimation of the emission height. This will be discussed in more detail in section 5.4.5.

The typical duration of a Cherenkov signal from an air shower is between a few nanoseconds near the shower core up to about 40 ns a few hundred metres away from the core (see also figure 5.29 in section 5.4.5). A primary particle of 1 TeV energy results in a Cherenkov photon density of about 100 photons per  $\text{m}^2$  [Hinton, 2009]. On the other hand, the brightness of the night sky is at least  $2 \times 10^{12}$  photons/(s sr  $\text{m}^2$ ) (see section 6.4). This defines the main requirements for detectors of Cherenkov light: Large light collection areas to achieve a good signal to noise ratio and fast photosensors and electronics with nanosecond resolution. If the Cherenkov detectors are to be used for gamma-ray astronomy, another important point is the identification of events caused by gamma-ray events against the large background of cosmic ray events.

### 2.4.5 Imaging Cherenkov detectors

Imaging air Cherenkov telescopes (IACTs) collect the Cherenkov light from an extensive air shower with a segmented mirror and focus it on a camera consisting of an array of photomultipliers. The position and shape of the air shower image in the camera carries important information about the event that can be used to reconstruct its direction, energy, depth of maximum and the nature of the primary particle. One of the most important features of the imaging technique is the very good suppression of hadronic cosmic rays: The larger transversal momentum of hadronic air showers leads to broader shower images, and a cut on the image width, suggested first by Hillas [1985], has proven to be very successful in the gamma hadron separation. The event reconstruction technique for imaging air Cherenkov telescopes, including the gamma hadron separation, will be explained in more detail for the H.E.S.S. system in section 3.2.

**Early systems** The first experiment that made successful use of Cherenkov imaging was the Whipple telescope that could for the first time establish a source of VHE gamma-ray emission with a significance of more than  $5\sigma$ : The Crab Nebula [Weekes *et al.*, 1989]. Although the camera contained only 37 pixels, thus producing rather coarse images of the showers, about 98% of the cosmic ray events could be suppressed. The 10 m optical reflector and the observation altitude of 2300 m allowed for an energy threshold of 700 GeV.

In the 1990s many improvements of the technique were developed and implemented in systems like HEGRA at La Palma [Daum *et al.*, 1997] and CANGAROO in Australia [Hara *et al.*, 1993]. One of the main new achievements was the development of the stereoscopic technique: Two or more telescopes were placed at a distance of around hundred metres to each other, so that events could be viewed from different angles, which greatly enhanced the accuracy of the direction and energy reconstruction [Kohnle *et al.*, 1996; Hofmann *et al.*, 1999].

**Current instruments** In the first decade of the 21<sup>st</sup> century the "third generation" of Cherenkov telescopes was being put into operation with H.E.S.S., MAGIC, and VERITAS. H.E.S.S. is a stereoscopic system of four imaging Cherenkov telescopes located in the Khomas highlands in Namibia. Each telescope has a mirror size of  $107 \text{ m}^2$  and a camera with 960 pixels. It achieves an energy threshold of about 100 GeV and can detect a source with flux of the same strength as the Crab Nebula in 30 s (as compared to several ten hours needed in the original detection by Whipple). It is the only current major instrument on the southern hemisphere and thus with a view of the inner Galactic region, and one of its key science missions, a survey of the Galactic plane, resulted in the discovery of dozens of new Galactic sources [Aharonian *et al.*, 2005b; Chaves and the H.E.S.S. Collaboration, 2009]. The H.E.S.S. experiment will be described in more detail in section 3.1.

The MAGIC telescope has a mirror area of  $236 \text{ m}^2$ , making it the largest Cherenkov telescope built so far [Doro *et al.*, 2008]. It achieves the very low threshold of 25 GeV, which leads to a significant overlap with

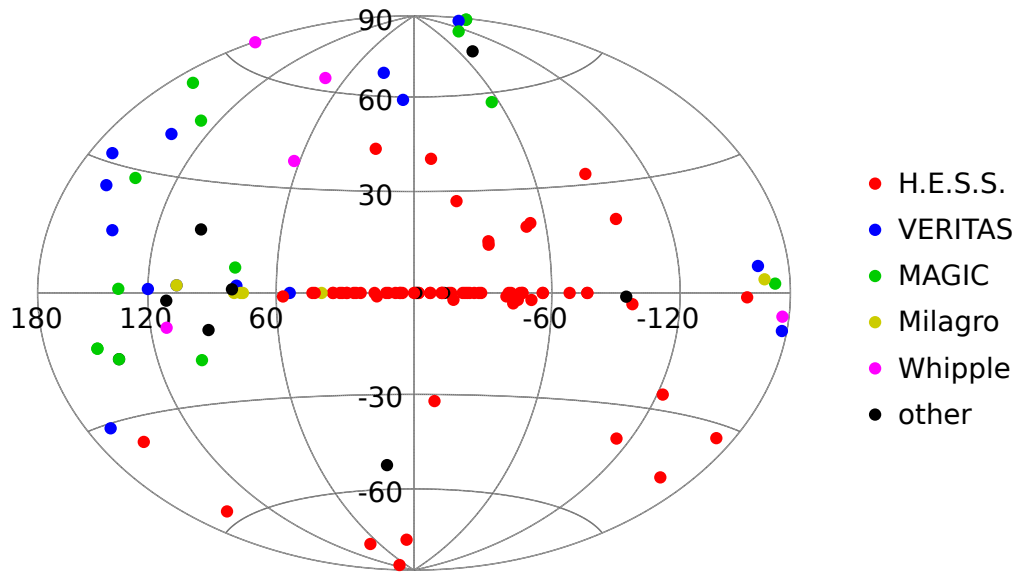


Figure 2.13: Currently known VHE gamma-ray sources (June 2011), colour coded by the discovering instruments, in Galactic coordinates. List of sources and instruments taken from Wakely and Horan [2011].

current space-based experiments. With this low threshold it was possible for the first time to detect the Crab *pulsar* with a ground based gamma-ray system [Aliu *et al.*, 2008]. It is also well suited for extra-galactic observations due to its location on the northern hemisphere and its low threshold, since the mean free path for gamma photons is longer at lower energies (see e.g. Hauser and Dwek [2001]). This led also to the detection of the furthest object seen so far by a Cherenkov telescope, the radio quasar 3C279, probing the transparency of the universe at very high energies [Albert *et al.*, 2008]. A second, almost identical telescope has been built at the site in order to allow stereoscopic observations. The new system is called MAGIC Phase II and has started operation in 2009 [Tridon *et al.*, 2010].

VERITAS is a four telescope system similar to H.E.S.S., located in Arizona, USA. The full array has started observations in 2007, with a scan of the Cygnus region, the search for dark matter and a survey of potential VHE gamma-ray sources (SNRs, pulsar wind nebulae and blazars) as its key science projects [Krennrich *et al.*, 2011].

Figure 2.13 shows a skymap with all currently detected sources, colour coded by the discovering experiments. It shows the great potential of discoveries in the inner Galactic region which could so far only be exploited by H.E.S.S.. It should be noted that many of the sources have been revisited and confirmed by other instruments than the discovering one, usually leading to additional scientific data like an improved energy spectrum, better spatial resolution or new data on the source variability.

**Outlook** Meanwhile, the next generation of Cherenkov telescope systems is already being developed. The design goal of the Cherenkov Telescope Array (CTA) is an improvement in sensitivity of at least a factor of ten compared to current instruments, and an energy range from a few ten GeV up to beyond 100 TeV. It is foreseen to set up two arrays, a larger one in the southern hemisphere with a focus on Galactic gamma-ray astronomy and a smaller one in the northern hemisphere, dedicated mainly to the observation of extra-galactic sources. Each detector array will consist of several ten telescopes of different sizes, with a few large telescopes for observations at lower energies end and several smaller ones with a larger spacing and large field of view for higher energies [CTA Consortium, 2010].

Beside this collaborative world-wide effort for a new all-round instrument there are several initiatives for smaller, more specialised instruments. The DWARF project aims at a continuous monitoring of several

## 2 Cosmic rays and gamma-ray astronomy

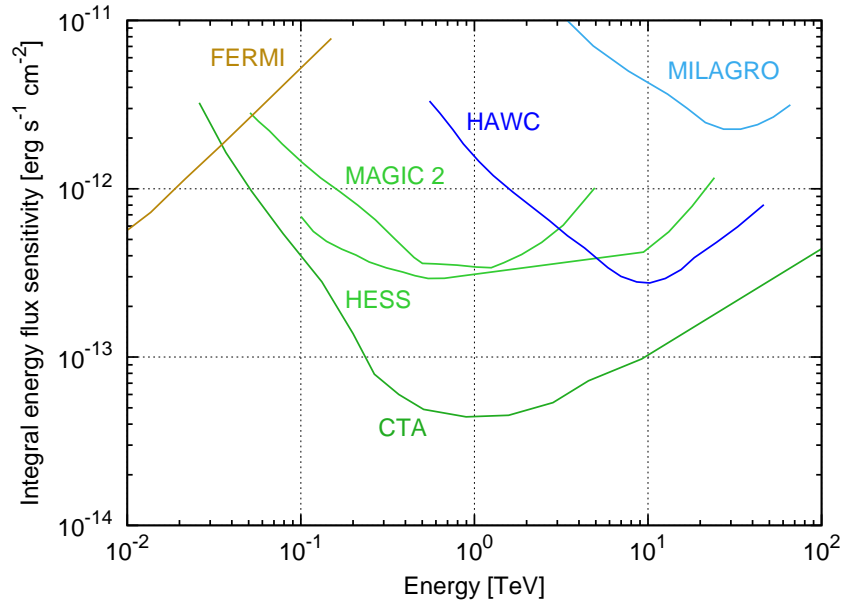


Figure 2.14: Sensitivity to gamma-ray point sources of selected current and planned gamma-ray observatories as described in section 2.4. Assumed observation times are 50 hours per source for Cherenkov telescopes and 5 year survey mode for FERMI, MILAGRO and HAWC. References: Atwood *et al.* [2009], Tridon *et al.* [2010], Actis *et al.* [2011], Aharonian *et al.* [2006c], Aharonian *et al.* [2008b]

bright, variable blazars with a world-wide network of moderate-sized Cherenkov telescopes, partly by re-viving decommissioned telescopes e.g. from the HEGRA experiment [Backes *et al.*, 2009]. This goes along with the FACT project that plans to outfit one of the old HEGRA telescopes with a new type of camera, using G-APDs instead of the conventional photomultipliers [Anderhub *et al.*, 2011]. If successful, this might also influence the camera development for the CTA project. A dedicated Cherenkov telescope array for the upper TeV range, called TenTen, has been suggested by an Australian group [Rowell *et al.*, 2008]. With a modest mirror size of  $23.8\text{ m}^2$ , but a large spacing between the telescopes, a large field of view of the cameras and the use of advanced event reconstruction techniques using the time information of the images a very good sensitivity can be achieved in the 1 TeV to 100 TeV range. Some event reconstruction techniques developed for the TenTen project are picked up and adapted for H.E.S.S. and H<sub>i</sub>SCORE in sections 3.2 and 5.4, respectively. On the other hand, the 5@5 concept aims at an extension of ground-based gamma-ray observations to low GeV energies, using a small array of large Cherenkov telescopes at a high altitude ( $\sim 5\text{ km}$ ) [Aharonian *et al.*, 2001].

One of the main performance figures of gamma-ray instruments is its point source sensitivity, defined as the minimal flux needed for a definite detection of the source within a certain time. For such a definite detection an excess of  $5\sigma$  above the background of cosmic rays is required, along with a minimum of 50 excess events. A good sensitivity is achieved by a large effective area to collect as many gamma events as possible, and a good discrimination between gamma photons and cosmic rays. A good angular resolution also contributes, since it reduces the area over which the emission from a point source is spread out and thus the number of background events within the source region. Figure 2.14 shows the sensitivity of some current and planned instruments for gamma-ray astronomy.

### 2.4.6 Wide-angle, non-imaging Cherenkov detectors

Another approach to detect atmospheric Cherenkov light of EAS are wide-angle detectors. These experiments consist of arrays of non-imaging light detectors, typically with light collecting areas below  $1\text{ m}^2$  per

## 2.4 Experimental techniques in cosmic ray physics and gamma-ray astronomy

station. Each station contains one or a few photomultipliers pointed towards zenith, and in some cases light concentrators to increase the light sensitive area. In contrast to imaging Cherenkov telescopes, no image of the shower is obtained, and the event reconstruction is done by Cherenkov light wavefront sampling: Every detector in the Cherenkov light pool records a Cherenkov light flash, and the relative timing of the recorded signals, their amplitude and their shape is used to reconstruct the properties of the primary particle.

These experiments have several advantages over imaging Cherenkov telescopes: With their wide field of view they continuously survey a large portion of the sky, which leads to an unbiased search for sources and a long exposure time for every possible source. The field of view is also very well suited for the study of extended emission regions, that may be larger than the field of view of imaging telescopes. Arrays of non-imaging detectors can also cover large areas on the ground at reasonable effort, thus providing large effective areas and making them the ideal instruments for the study of the very weak fluxes in the ultra high energy domain. Their drawbacks are a higher energy threshold (due to their smaller light collection area) and less potential for particle identification, especially the separation of gamma photons from cosmic rays.

Wide-angle Cherenkov detectors have been developed and used for a long time mainly for the study of charged cosmic rays. Early examples are the Yakutsk experiment [Dyakonov *et al.*, 1973] and the Buckland park detector in Australia [Kuhlmann *et al.*, 1977]. More recent examples are the BLANCA [Fowler *et al.*, 2001] and the TUNKA [Budnev *et al.*, 2009] experiments, the latter still being operational, with its main focus on measurements of the cosmic ray spectrum and composition in the knee region. The new combined air shower and wide-angle Cherenkov detector array BASJE is currently being set up in Bolivia at an altitude of 5200m, with similar science objectives as TUNKA [Tsunesada *et al.*, 2009].

Additionally, also some non-imaging detectors with a small field of view (i.e. not wide-angle) have been built. Several groups used heliostats from solar power plants or research facilities to achieve a large collection area for Cherenkov light, which is directed to a PMT camera in a central tower. Events are reconstructed using wavefront sampling. Some examples of such detectors are CELESTE [Paré *et al.*, 2002], STACEE [Gingrich *et al.*, 2005] and GRAAL [Arqueros, 2003]. The energy range covered by these experiments is similar to the one of current imaging Cherenkov telescope systems (100GeV to a few TeV), however, the achieved sensitivity is not as good as with imaging systems (see e.g. de Naurois *et al.* [2002] for the CELESTE sensitivity). Another approach of a wavefront-sampling system with a small field of view is the HAGAR experiment in India, a system of seven non-imaging Cherenkov telescopes which started observations in 2008 [Britto *et al.*, 2011].

So far, the only wide-angle detector specifically designed for gamma-ray astronomy has been the AIRO-BICC instrument built by the HEGRA collaboration and used in conjunction with the HEGRA air shower array [Karle *et al.*, 1995]. Its accurate timing provided a good angular resolution, its high altitude of 2200m and dense station spacing of 30m an energy threshold below 30TeV, thus ensuring the two main requirements for gamma-ray detection. However, its total instrumented area of only  $3 \times 10^4 \text{ m}^2$  was too small to achieve the necessary sensitivity, and no gamma-ray source could be detected. Nevertheless, some important new event reconstruction techniques were developed that were later picked up by other experiments, e.g. the reconstruction of shower cores outside of the array using signal widths developed by Henke [1994] has been successfully adopted by the TUNKA collaboration to increase the effective area of their detector.

In chapter 4 of this thesis the concept of a new wide-angle, non-imaging Cherenkov detector for gamma-ray astronomy is presented. The H<sub>i</sub>SCORE detector will feature a much larger total effective area than any other atmospheric Cherenkov detector so far, combined with an angular resolution and energy threshold comparable to AIROBICC. The large effective area becomes feasible by an inter-station spacing of more than hundred metres and a simple and inexpensive design of the individual stations, which will operate independently with their own power supply and a wireless data transmission system. One possible implementation is an array with a detector spacing of 150m, which allows to cover an area of 10km<sup>2</sup> with only 480 stations. The large spacing requires advanced event reconstruction techniques, since only very limited information about the air shower is available. It will be shown in chapter 5 that despite the considerably larger station spacing the resolution in the direction and energy reconstruction is comparable to the one

## *2 Cosmic rays and gamma-ray astronomy*

achieved by AIROBICC, and that a limited particle separation is also possible. This is achieved mainly by utilising the whole sampled photomultiplier signal in the analysis and by a four times larger light sensitive area per station. The sensitivity to gamma-ray point sources will be presented and the effect of different array layouts and observation altitudes is studied.

## 3 Sampling mode event reconstruction for the H.E.S.S. experiment

The H.E.S.S. experiment is a system of four imaging Cherenkov telescopes sensitive to gamma photons in the energy range from about 100 GeV to about 100 TeV. With its good sensitivity and location in the Khomas highlands in Namibia which allows a very good coverage of the inner region of our Galaxy it has helped to establish gamma-ray observations as an integral part of modern astronomy. With it, more than 70 sources of gamma-ray emission have been discovered and detailed results on the morphology, energy spectrum and temporal variability of many sources have been obtained. The experiment will be introduced in section 3.1.

In this work, a new event reconstruction algorithm for H.E.S.S., which makes use of the time development of the Cherenkov light image, is introduced. The time development is so far not used in the standard analysis, but preliminary results from this and other works indicate that it may be useful to improve the sensitivity of the instrument. In the study presented here the main focus is on the high energy end of the sensitivity range of H.E.S.S., i.e. at energies above a few TeV, where the sensitivity is limited by low event numbers. In section 3.2, the standard analysis of H.E.S.S., which is used as a reference, will be introduced, while the new approach will be presented in section 3.3.

To make use of the time information in the Cherenkov images, a new software framework has been implemented, which is introduced in section 3.4. It is then used together with an air shower and an experiment simulation to test the accuracy of the new reconstruction and compare it with the reference method (section 3.5).

To use the time information, the images must be recorded in *sampling mode*, in which the complete signal of each pixel is stored. This is not done by default in the H.E.S.S. experiment, but dedicated observations were carried out for 90 minutes in sampling mode in October 2009 for a test of the new reconstruction. The observations were directed towards the Crab Nebula, a prominent bright VHE gamma-ray source. The reconstruction introduced here is tested on the data, and results are presented in sections 3.6 and 3.7.

### 3.1 The H.E.S.S. experiment

The H.E.S.S. experiment (High Energy Stereoscopic System) consists of an array of four imaging Cherenkov telescopes, located at an altitude of 1800 m above sea level in Namibia ( $23^{\circ} 16' 18''$  S,  $16^{\circ} 30' 00''$  E) [Hinton, 2004]. The telescopes are positioned at the corners of a square with a side length of 120 m (see figure 3.1). The mirror surface of each telescope consists of 382 round mirrors with a diameter of 60 cm each, resulting in a total reflective area of  $107 \text{ m}^2$  per telescope (see figure 3.2). Each mirror can be adjusted independently using two remote controlled gear motors, and an automatic procedure is used to align all mirrors of the telescope [Cornils *et al.*, 2003].

The Cherenkov light is reflected and focused onto a camera of 960 photomultiplier tubes (PMTs), shown in figure 3.3. Each PMT has a field of view of  $0.16^{\circ}$ , and the field of view of the whole camera is about  $5^{\circ} \times 5^{\circ}$ . The signals are recorded by two analogue ring samplers per PMT (high and low gain) in 1 ns time bins over a period of 16 ns, using the same readout window for the whole camera. The signals are digitised by a computer in the camera casing before being sent to the central data acquisition system (DAQ). In standard mode, only the integral of each signal is transmitted, while in sampling mode all 16 time bins are stored, thus keeping the information about the signal shape and the relative timing of the signals in the camera (see section 3.3).

### 3 Sampling mode event reconstruction for the H.E.S.S. experiment

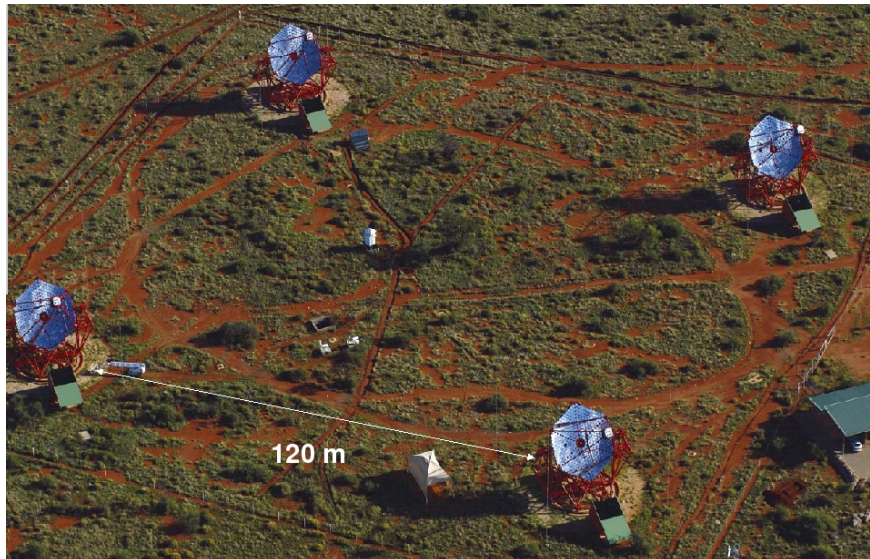


Figure 3.1: The H.E.S.S. array from above. The telescopes are located on a square with a side length of 120m [Plailly, 2006; Rowell, 2011].

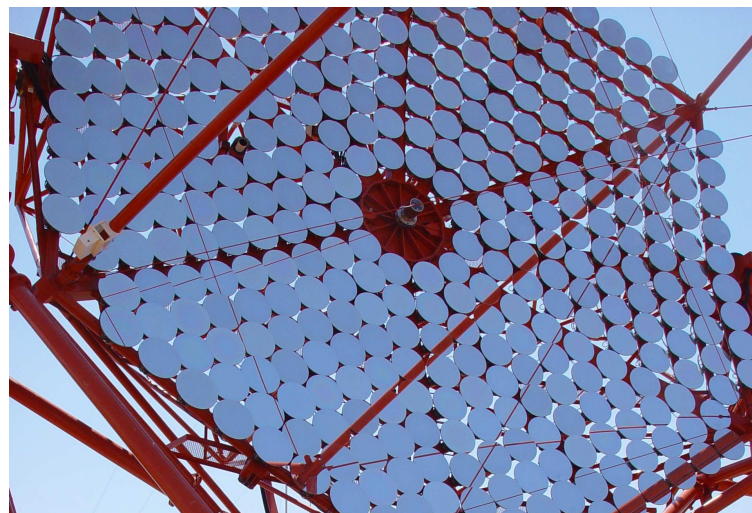


Figure 3.2: Mirror area of one of the H.E.S.S. telescopes [H.E.S.S. website, 2011]. Each mirror has a diameter of 60cm, the total area of the mirrors is  $107\text{m}^2$ .

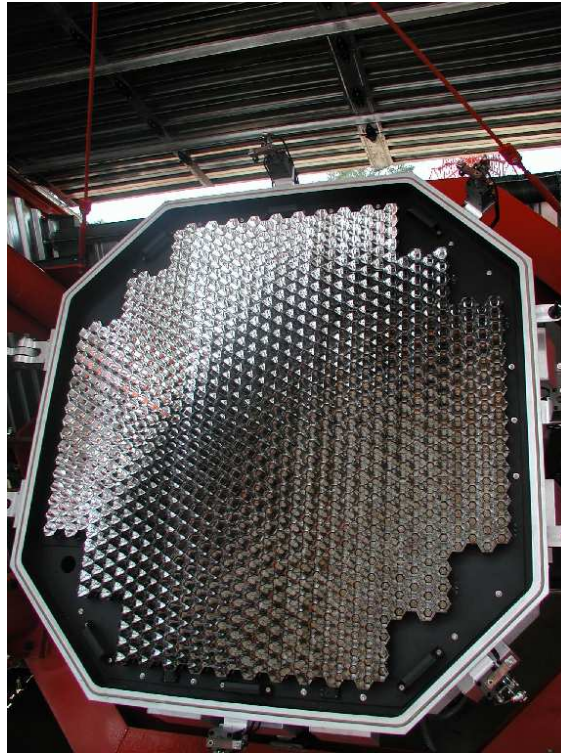


Figure 3.3: The H.E.S.S. camera with its 960 PMTs [Vincent *et al.*, 2003]. The camera is about 1.5 m across and has a field of view of about  $5^\circ \times 5^\circ$ .

The camera generates a telescope trigger if the signals of three PMTs in a sector (of 64 PMTs) are above a threshold of 4 photoelectrons each. The second level trigger asks for two telescope triggers within a timespan of 80 ns, thus suppressing accidental triggers from single muons [Funk *et al.*, 2004]. The system trigger rate is usually around 100 to 200 Hz (depending on the zenith angle) and is dominated by cosmic ray events, which can be suppressed only at a later stage, when the images of the telescopes are analysed (see section 3.2). A more detailed description of the H.E.S.S. experiment can be found in Aharonian *et al.* [2006c] and references therein.

Currently, the experiment is extended by a fifth telescope, called H.E.S.S. phase II. With its  $600\text{ m}^2$  mirror it will be the largest Cherenkov telescope ever built, and it is expected to lower the energy threshold of H.E.S.S. to at least 20 GeV. However, it will effectively operate as single telescope up to the threshold of the other four telescopes ( $\sim 100\text{ GeV}$ ), and a dedicated single telescope analysis is needed [Masbou *et al.*, 2009]. The time gradient reconstruction presented in section 3.3 may be a useful tool for this new reconstruction, however, this is not the topic of the presented work. It is currently expected that the new telescope will become operational in late 2012.

## 3.2 Standard event reconstruction

The algorithm which is used to derive the event parameters of interest from the data measured by the experiment is called *event reconstruction*. The main parameters to be reconstructed are the direction and the energy of the primary particle, and the type of the particle (photon, electron or hadron, possibly also mass or charge number of the hadron). A very important first step for the reconstruction of these parameters is the calculation of the position of the shower core, which is the intersection of the shower axis with the ground.

### 3 Sampling mode event reconstruction for the H.E.S.S. experiment

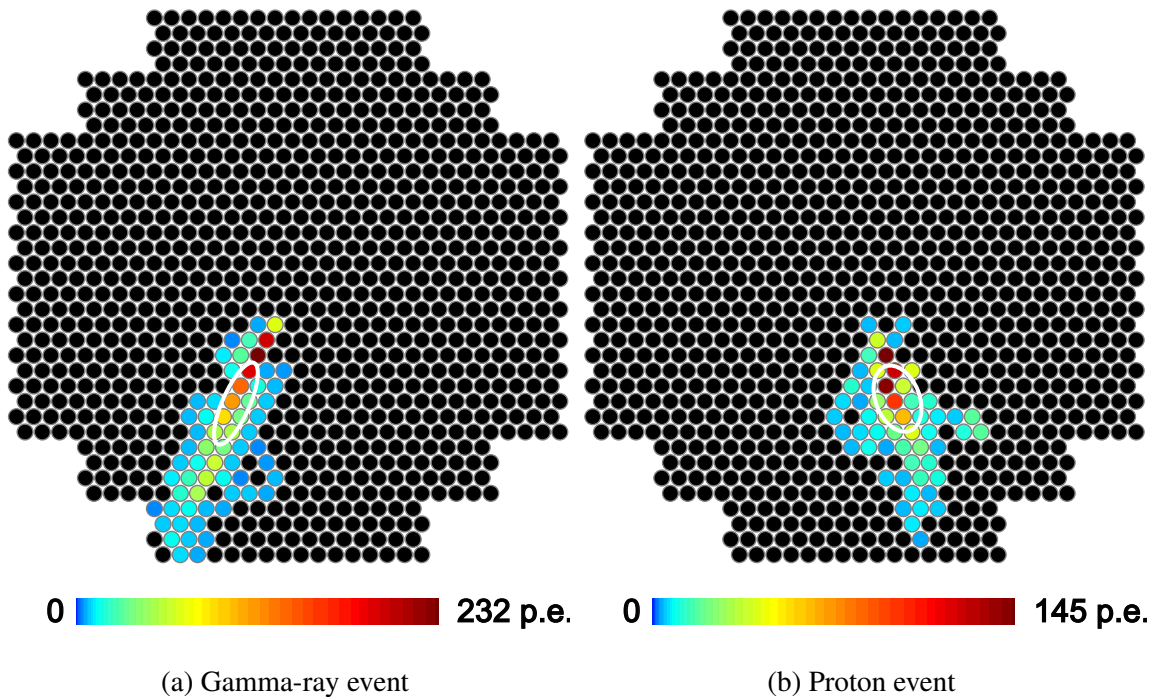


Figure 3.4: Colour coded intensity images of simulated events from a gamma-ray and a proton primary, after image cleaning. The events are selected to have similar energies ( $\sim 2.5$  TeV) and core distances ( $\sim 120$  m). The intensity is given in photoelectrons. Shown in white are the ellipses resulting from the Hillas parametrisation.

Another quantity used in the event reconstruction is the depth of the shower maximum, which is defined as the atmospheric depth at which the shower contains the largest number of relativistic particles (see also section 2.4.2). In the following, the individual steps of the event reconstruction for H.E.S.S. are explained.

Different approaches exist for the event reconstruction at Cherenkov telescope systems. The algorithms described in the following – Hillas formalism for image parametrisation, algorithm 1 stereo reconstruction – represent the de-facto standard of the field. They are relatively easy to implement and provide a robust way to derive all necessary event properties. The suppression of background, and thereby the sensitivity, can be improved by the use of more sophisticated analyses, usually incorporating a multivariate analysis of some image parameters (see e.g. Ohm *et al.* [2009]). These are not used here, since the primary goal of this study is to evaluate the benefit of the time gradient for the reconstruction, and the standard analysis provides a good reference for this.

#### 3.2.1 Image processing

**Image cleaning** The residual light present even during dark nights, the night sky brightness, adds fluctuations to all pixels and disturbs the calculation of the image parameters. Therefore, an *image cleaning* algorithm is applied as a first step, with the aim of retaining only pixels that contain Cherenkov light of the air shower. In the standard H.E.S.S. analysis, pixels need to have an amplitude of at least 10 photoelectrons and a next neighbour with at least 5 photoelectrons to be included in the further analysis. The next neighbour condition helps to eliminate bright fluctuations in single pixels.

**Image parameters** The Cherenkov light image of an air shower in the telescope camera can usually be described well by an ellipse (see figure 3.4). As will be explained below, its position, orientation, and shape are important parameters for the event reconstruction. The shape is parametrised as *width* and *length* and can be used to discriminate between gamma photons and the background of charged cosmic rays, as air showers of cosmic rays usually have a larger transversal spread and hence produce a wider image in the camera (see figures 3.4a and 3.4b). Another important quantity is the sum of pixel amplitudes, also called *image size*.

The ellipse parameters are usually calculated by the Hillas formalism [Hillas, 1985]. The ellipse centre is set by the centre of gravity of the pixel amplitudes, while the size, the orientation, the width and the length are calculated from the central moments of the image. If the pixel at the position  $(x, y)$  has the amplitude  $f(x, y)$ , the central moment  $\mu_{ij}$  is defined as

$$\mu_{ij} = \sum_x \sum_y (x - \bar{x})^i (y - \bar{y})^j f(x, y) \quad (3.1)$$

where  $\bar{x}$  and  $\bar{y}$  are the coordinates of the image centre of gravity. The size can then be written as  $\mu_{00}$ , which simply gives the sum over all pixels. The orientation of the ellipse is characterised by the angle of the major axis  $\alpha$  (relative to the coordinate system's x-axis), given by

$$\alpha = \frac{1}{2} \arctan \left( \frac{2\mu_{11}}{\mu_{20} - \mu_{02}} \right) \quad (3.2)$$

The width  $w$  and the length  $l$  of the ellipse are given by

$$w = \sqrt{\frac{\mu_{02} + \tan^2(\alpha)\mu_{20} - 2\tan(\alpha)\mu_{11}}{1 + \tan^2(\alpha)\mu_{00}}} \quad (3.3)$$

$$l = \sqrt{\frac{\mu_{20} + \tan^2(\alpha)\mu_{02} - 2\tan(\alpha)\mu_{11}}{1 + \tan^2(\alpha)\mu_{00}}} \quad (3.4)$$

**Quality cuts** Quality cuts are applied to the images in order to guarantee an accurate event reconstruction. Images that fail to pass the cut criteria are excluded from the event reconstruction, and the whole event is discarded if less than two images survive the cuts. In the standard set of parameters, the image size is required to be above 80 photoelectrons, and the centre of gravity must be no further than  $2^\circ$  away from the camera centre [Aharonian *et al.*, 2006c]. The second cut, also called *nominal distance cut*, is used to avoid the use of images that are cut off by the camera edge. Edge-affected images will have a centre of gravity that is systematically misreconstructed away from the camera edge and an orientation that may be significantly off the true axis (an example is shown in figure 3.10 in section 3.3.1). While the nominal distance cut helps to reduce the impact of these effects, it severely limits the effective area of the experiment, which is defined as

$$A_{eff} = \int_A \epsilon_{trigger}(\vec{r}) \epsilon_{cut}(\vec{r}) dA \quad (3.5)$$

where  $\epsilon_{trigger}(\vec{r})$  and  $\epsilon_{cut}(\vec{r})$  are the probabilities for an event at a given point on the ground  $\vec{r}$  to trigger and to survive the cuts. The integration area  $A$  is an (arbitrary) area which extends well beyond the area in which events can be detected. In general, the effective area is strongly energy dependent, since both  $\epsilon_{trigger}(\vec{r})$  and  $\epsilon_{cut}(\vec{r})$  change with energy. The trigger efficiency  $\epsilon_{trigger}(\vec{r})$  increases with energy, as more and more distant events are bright enough to produce usable images in the telescope cameras. However, it turns out that above about 10 TeV many of the distant events are discarded by the nominal distance cut, as they produce images close to the camera edge. The situation is additionally worsened as the average depth of the shower maxima increases with energy, which also increases the nominal distance in the image (see figure 3.6). In consequence, the probability  $\epsilon_{cut}(\vec{r})$  drops significantly above 10 TeV and limits the effective area of the experiment.

### 3 Sampling mode event reconstruction for the H.E.S.S. experiment

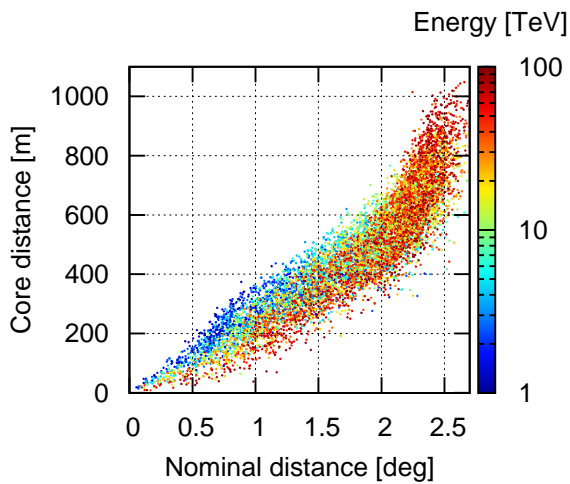


Figure 3.5: Correlation of the core distance (distance from the telescope to the shower core position) and the nominal distance (distance between the image centre of gravity and the camera centre) in the image, for simulated gamma-ray events at  $46.5^\circ$  zenith angle. The energy is shown in colour scale.

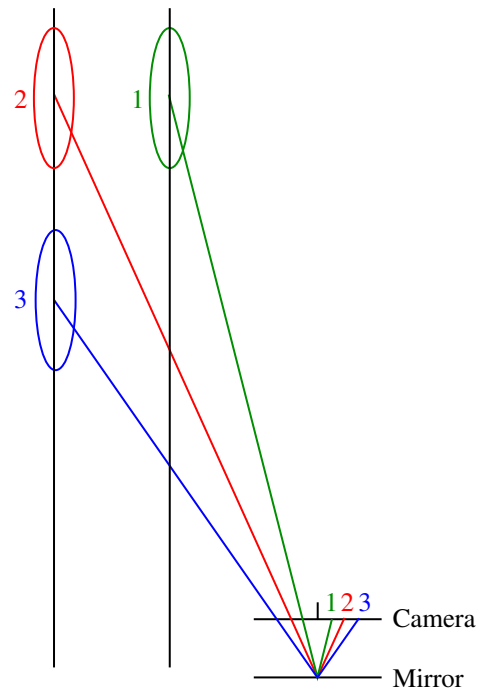


Figure 3.6: The light emitted from air showers with different core distances and shower depths is seen at different positions in the camera. The nominal distance increases with core distance (compare 1 and 2), but also with shower depth (compare 2 and 3). Adapted from Stamatescu [2010].

It will be shown that an event reconstruction using the sampling mode can handle edge-affected images better than the standard analysis and can be used to relax the nominal distance cut, recuperating events otherwise lost for the analysis. Nevertheless, to exploit the full potential of Cherenkov telescopes in the multi-TeV regime, a camera with a larger field of view would be necessary (see de La Calle Pérez and Biller [2006] for a detailed study).

#### 3.2.2 Stereo reconstruction of shower core position and particle direction

From the experience with the HEGRA telescopes it has been realised that the accuracy of the event reconstruction can be improved substantially if the image of the shower is viewed from more than one viewpoint, leading to the technique called *stereoscopy* [Kohnle *et al.*, 1996]. While the MAGIC collaboration has proven that a single telescope analysis can be used successfully, the upgrade to MAGIC phase 2 with a second large Cherenkov telescope promises a significant improvement in the sensitivity. Upon this upgrade, all major Cherenkov telescope systems now operate in stereo mode.

One of the main challenges in a single telescope analysis is the determination of the distance between the telescope and the shower core (*core distance*<sup>1</sup>). One possibility to estimate this distance is using the nominal distance, which correlates strongly with the distance to the shower core (see figure 3.5). However, it also depends on the depth of the the shower maximum, and is therefore a rather ambiguous distance estimator (see figure 3.6). The effect of the shower depth on the nominal distance can also be seen in figure 3.5: At the

<sup>1</sup>The same quantity is often also called “impact parameter”, however, in this thesis only the term “core distance” is used.

same core distance, events with a larger energy (and thereby larger shower depth) tend to appear at larger nominal distances.

The shape of the image can also be used as core distance estimator, as the images become narrower the further away the core is, but the shape depends also on the type of particle, and a cosmic ray event with a large core distance may look similar to a closer gamma-ray event. The same problem arises in the reconstruction of the particle direction, for which the source distance is needed (see figures 3.7 and 3.8).

If, however, more than one image of the shower is recorded, the different viewpoints can be used for a better reconstruction of the core and source distance. Various algorithms for this are described and compared in Hofmann *et al.* [1999]. The simplest of these algorithms, denoted algorithm 1 in that paper, is presented in the following and used as reference for the time gradient analysis presented in section 3.3.

For the determination of the core position, the major axes of the images (also called Hillas axes) are extended beyond the telescopes and their intersections are calculated (see figure 3.7). With four telescopes, up to six intersections are possible, if all telescopes have triggered. The core position is obtained as a weighted average of the intersections, with the weight depending on the image sizes and the stereo angle between the two intersecting axes. The size is used to give preference to larger images with higher amplitudes, as the Hillas axis will generally be better defined in these. In a given event, these images are usually from the telescopes nearer to the shower core. The stereo angle is used because images with similar orientations result in poorly defined, glancing intersections. The weight of the intersection between the axes from images  $A$  and  $B$  is calculated here as

$$\text{weight}_{AB} = (\text{size}_A + \text{size}_B)^2 \times \sin(\text{stereo angle}) \quad (3.6)$$

If the telescopes are not pointed towards zenith, the resulting core position is given in a rotated coordinate system that has its  $z$ -axis in parallel to the pointing direction of the telescopes (*shower frame*). To obtain the core position on the ground, it must be rotated back into the standard coordinate system. All calculations that involve the core distance, such as the reconstruction of the energy or the gamma hadron separation (see next subsection), are however usually done in the shower frame.

The direction of origin is reconstructed in a similar fashion: All camera images are transferred into a single coordinate system and the direction is obtained by the weighted average of the Hillas axes intersections in this coordinate system (see figure 3.8). The actual direction of origin of the particle is calculated by adding the reconstructed direction in the camera frame to the pointing direction of the telescopes. This direction is usually converted into equatorial coordinates, using the geographic location of the experiment and the exact time of the event.

A more sophisticated reconstruction algorithm, denoted algorithm 3 in Hofmann *et al.* [1999], takes into account a source distance predictor and estimates the core and source positions for each telescope, similar to a single telescope analysis. For each estimated position, an error ellipse is determined from comparison with Monte Carlo simulations. The final core and source position is then derived by combining the individual source positions, taking into account their estimated uncertainties. This algorithm is not used in the present work, however it gave some inspiration for the time gradient reconstruction presented in section 3.3. A detailed explanation of algorithm 3, including its application to a time gradient reconstruction, can be found in Stamatescu [2010].

### 3.2.3 Energy reconstruction and gamma hadron separation

As mentioned before, the *size* of a shower image depends on the particle's energy and the core distance. Once the core distance is known from the core position reconstruction, the energy can be reconstructed from the size using lookup tables generated with Monte Carlo simulations. The energy of a particle is estimated by taking the weighted average of all triggered telescopes, using the image size as weight.

Since the majority of detected events is of hadronic origin, an efficient discrimination of these hadronic events is important for a good sensitivity to gamma-rays. As mentioned before, cosmic rays usually produce a wider image in the camera due to the larger transversal spread of particles in the air shower. The observed

### 3 Sampling mode event reconstruction for the H.E.S.S. experiment

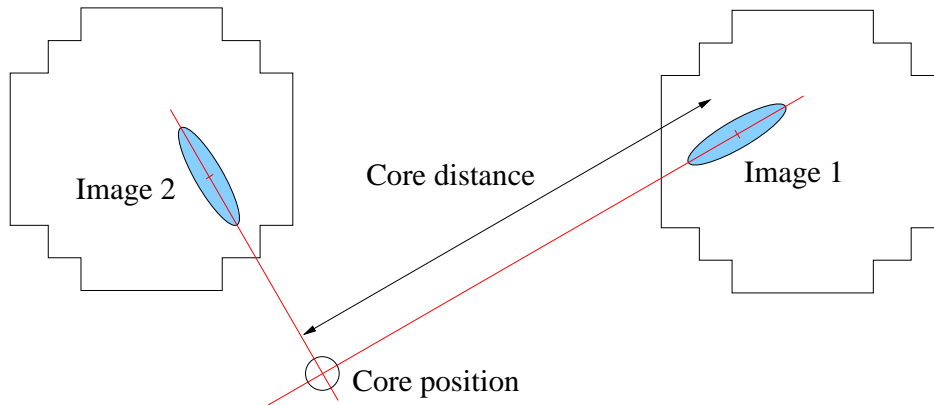


Figure 3.7: Illustration of core position reconstruction using algorithm 1 for the case of only two images. The core position is obtained by extending the Hillas axes from the telescopes and calculating their intersection. If only one image is available, the core distance has to be estimated from the image, which results in a larger uncertainty, especially at large core distances.

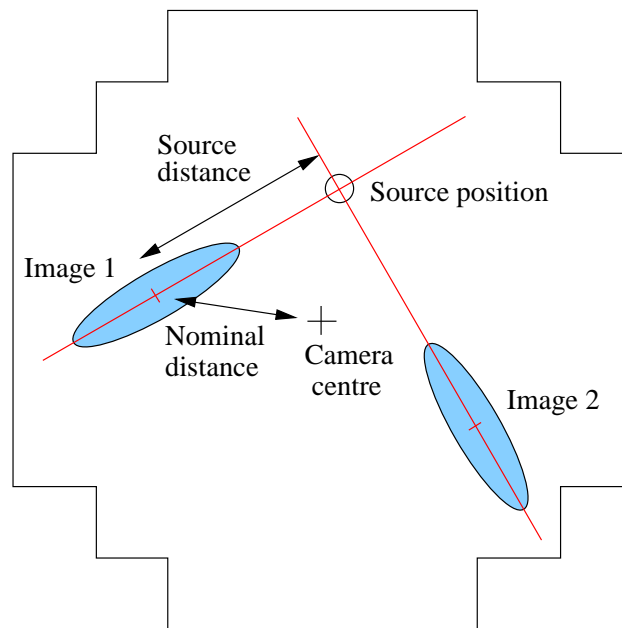


Figure 3.8: Illustration of the direction reconstruction using algorithm 1 for the case of two images. The direction is obtained by transforming the two images to the same camera frame and calculating the intersection between the Hillas axes. If only one image is available, the source distance needs to be estimated, e.g. from the image shape.

### 3.3 Event reconstruction using sampling mode information

width  $w_{obs}$  is compared to the width  $w_{MC}$  expected from Monte Carlo simulations for a gamma-ray shower with the given core distance and image size, and its scatter  $\sigma_{MC}$ , resulting in the scaled width  $w_{sc}$ :

$$w_{sc} = \frac{w_{obs} - w_{MC}}{\sigma_{MC}} \quad (3.7)$$

The average of these scaled widths over all triggered telescopes, called *mean scaled width*, is used as the primary particle separation parameter:

$$MSW = \frac{\sum w_{sc}}{N_{tel}} \quad (3.8)$$

For gamma-rays the distribution is centred around zero, while the distribution for cosmic rays peaks at a higher value. In the standard set of cut parameters, events with a MSW between -2 and 0.9 are accepted as gamma-rays [Aharonian *et al.*, 2006c].

#### 3.2.4 Background calculation and source detection

Even though the gamma-ray selection cuts eliminate a large fraction of cosmic ray events, the remaining sample usually still contains far more background than signal events, and a sophisticated analysis is needed to extract the spectrum, the skymap and – for variable sources – the lightcurve from the data. While the full coverage of this analysis is beyond the scope of this work, a few basic aspects will be needed to judge the results from the new analysis presented in the following. For simplicity, a point source will be assumed.

To test for the presence of a source, the  $\theta^2$  distributions of ON and OFF events can be used. In this,  $\theta$  is defined as the angular distance between the reconstructed direction and the test position in sky coordinates. The distribution of ON events is derived from a circular region around the expected source position, while the distribution of OFF events is derived from one or several background regions. Several alternatives exist for the position and shape of the OFF regions, all of which need to account for the decreasing acceptance of the camera with increasing distance from the camera centre (see also Berge *et al.* [2007]). The square of  $\theta$  is used in the distribution to obtain bins of approximately equal solid angle.

If a gamma-ray source is present, the  $\theta^2$  distribution of ON events will show an increase close to zero, while the background distributions should always be flat (for  $\theta$  values far smaller than the camera size). The source region is defined as a circular region around the source position, and all events outside of this region are discarded (“ $\theta^2$  cut”). The significance of the source detection is calculated by comparing the ON and OFF events that survive the  $\theta^2$  cut against the null hypothesis. The radius of the source region is usually adjusted to include as many gamma-ray events as possible while keeping the number of background events low. The best cut depends also on the signal to noise ratio: If the background level is low, a larger region including more events can be beneficial, while in a high background scenario a rather small source region is better suited.

A smaller number of background events in the source region leads to a better signal to noise ratio and thereby increases the sensitivity to a given gamma-ray flux. Apart from the gamma hadron separation, the background level also depends on the angular resolution of the instrument, as a better angular resolution concentrates the gamma-rays from a point source onto a smaller solid angle, thus making the definition of a smaller source region possible. The signal to noise ratio can also be improved by an increase of the effective area of the instrument, which leads to higher event numbers. It will be shown in the following section that using sampling mode data can help both to improve the angular resolution and increase the effective area, thereby improving the sensitivity of the instrument.

### 3.3 Event reconstruction using sampling mode information

In the standard analysis, only static images of the air shower are used. The H.E.S.S. telescopes are however also able to resolve the time structure of the Cherenkov light with a 1 ns resolution. While in standard mode

### 3 Sampling mode event reconstruction for the H.E.S.S. experiment

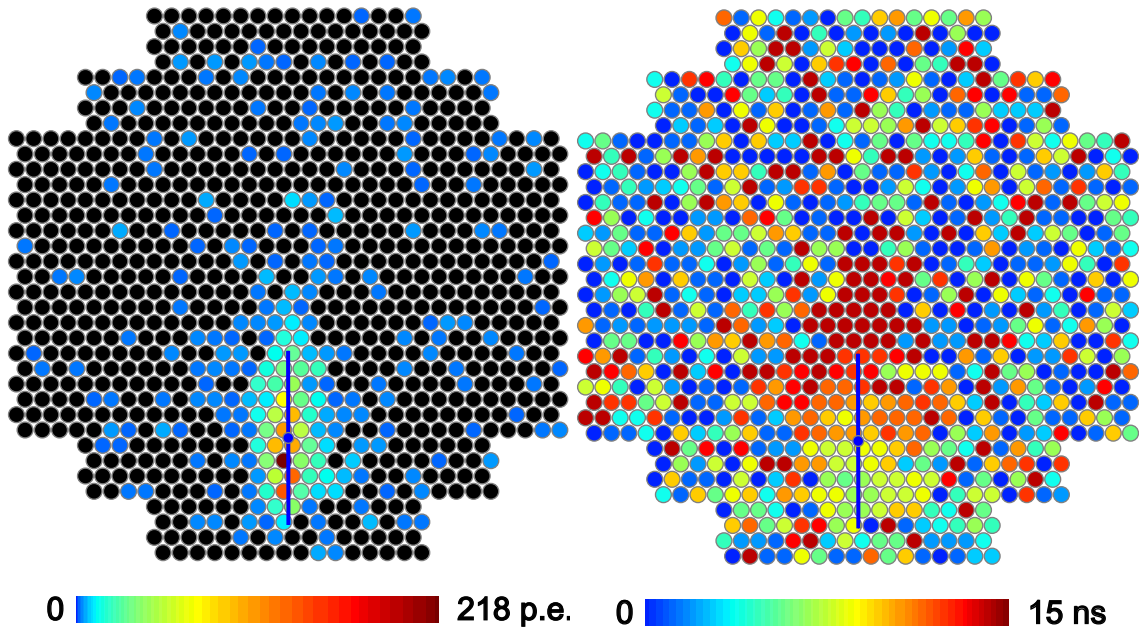


Figure 3.9: A camera image from the Crab Nebula observations (run 054367, event 4, telescope 1) colour coded in pixel amplitudes (left, in photoelectrons) and pixel peak times (right, in nanoseconds), before image cleaning. The Hillas axis and the centre of gravity of the image are shown in blue.

the 16 intensity values recorded by the 1 GHz analogue ring samplers are summed up before sending the data to the central DAQ, the individual entries are retained when the system is operated in sampling mode. So far, this mode is only used for tests and calibration, but not for usual observations. There are however indications that using the sampling mode data can lead to an improvement of the performance of Cherenkov telescope systems, as will be discussed below, which motivated some short test observations of the Crab Nebula in sampling mode in October 2009. The data from these observations will be presented in sections 3.6 and 3.7.

The sampling mode data can be used in various ways: Individual images of the 16 time bins can be produced, and the time evolution of the shower can be parametrised by the movement of the centre of gravity (direction and velocity) or the evolution of the image size, length and width. Another approach is to describe the properties of each pixel signal with quantities such as its amplitude, its peak time or mean time (centre of gravity of the pulse), and its duration. This opens a wealth of possibilities to derive additional information about the air shower, and it seems reasonable to assume that this information can help to improve the event reconstruction.

In this work, only the pixel peak times are used. Figure 3.9 shows a telescope image from the Crab Nebula dataset colour coded in intensity and in peak times, before image cleaning. Looking at the peak times, one can see that all neighbouring pixels that belong to the shower image have similar peak times, and it is easy for the eye to separate the shower pixels from the background with random peak pixel times. Image cleaning algorithms based on peak pixel times, possibly in connection with the standard intensity cleaning, can include more pixels with low intensity in the shower image while still rejecting noise pixels, and help to improve the reconstruction of weak images from large core distances or low energy events. Such an algorithm is used successfully by the MAGIC collaboration to lower their energy threshold [Aliu *et al.*, 2009], and may be useful also for event reconstruction at the new H.E.S.S. II telescope, considering its focus on low energies. The VERITAS collaboration uses the peak times to dynamically adjust their integration window for the determination of the pixel amplitude, thus decreasing the influence of noise by background

light [Holder, 2005]. Two other features can be seen in figure 3.9: First, there are a lot of pixels that have their peak in the last bin of the read-out window, which may indicate that their actual peak comes after the end of the read-out window and a part of the signal is lost. This is examined further in section 3.6. Second, it is clearly visible that a *time gradient* is present along the major axis of the shower ellipse. It turns out that this time gradient is a useful parameter for the shower reconstruction, as will be lined out in the following subsection.

#### 3.3.1 Using the time gradient as distance estimator

The first experimental study of the time gradient in Cherenkov images was done using the HEGRA system [Heß *et al.*, 1999], and it was found that it is an almost linear function of the core distance for distances above about 100m, showing a potential for the reconstruction of the shower core. Similarly, it is also a function of the source distance in the camera and can be used in the direction reconstruction. The MAGIC collaboration achieved a significant improvement in the single telescope analysis using the time gradient for source distance and core distance estimation [Aliu *et al.*, 2009], which may be interesting also for the H.E.S.S. II telescope, which will effectively operate in single-telescope mode in the energy range from 20 GeV to 100 GeV.

For a stereoscopic system, the benefit for the core and direction reconstruction is not a priori clear, since the use of stereo imaging already gives a good estimate on the core and source distance. It has been shown however that substituting the standard distance estimator in algorithm 3 with a distance estimator based on the time gradient can improve the performance of a stereo system especially at large core distances, where the stereo angles are small and the distance is poorly defined [Stamatescu *et al.*, 2011]. As such, this concept seems especially valuable for the reconstruction of events towards the high energy end, where the Cherenkov light levels are so high that even showers with large core distances produce usable images in the telescopes. In the TenTen study described in Rowell *et al.* [2008] this is used to increase the telescope spacing to 500m and to achieve an effective area of 1 km<sup>2</sup> above an energy of 30 TeV with a 5 telescope system.

However, events with core positions far away from the telescope can only be used if the field of view of the camera is large enough, since events with large core distances appear far away from the camera centre. In the TenTen study, a camera with a field of view of ten degree diameter is assumed. In H.E.S.S., however, the field of view is only five degrees (which is already the largest field of view of all current instruments), and at high energies the effective area is severely limited by the camera size. As mentioned in the previous section, images with a nominal distance above 2° are not used in the standard analysis, as those images are usually cut off by the camera edge. In such a truncated image, the Hillas parameters, especially the image centre of gravity and the orientation of the ellipse, are often distorted, thus producing wrong core and source positions (and subsequently problems with the energy reconstruction and the gamma hadron separation). Figure 3.10 shows a simulated event with two images, both of which have a nominal distance greater than 2° and are cut off at the camera edge. The orientation of the image from CT 4 is misreconstructed due to the missing part, resulting in a wrong reconstruction of the direction and the core position<sup>2</sup>.

On the other hand, it has been shown by Stamatescu [2010] that the distance estimation using the time gradient is not severely deteriorated if the major axis is misreconstructed up to 30°. It therefore seems that the time gradient reconstruction can also help to recuperate events that are cut off by the limited field of view of the H.E.S.S. camera, thereby allowing to relax the nominal distance cut and include more events with large core distances.

Thus, the benefit for the H.E.S.S. sensitivity would be twofold: The improved core position and direction accuracy for events with large core distances would lead to a better angular resolution and thus to a lower background in the source region, and taking into account additional events with truncated images would increase its effective area and thereby the event statistics at the high energy end. To test this, a variant of the

<sup>2</sup>The abbreviation CT for Cherenkov telescope is used from here on to specify the four H.E.S.S. telescopes.

### 3 Sampling mode event reconstruction for the H.E.S.S. experiment

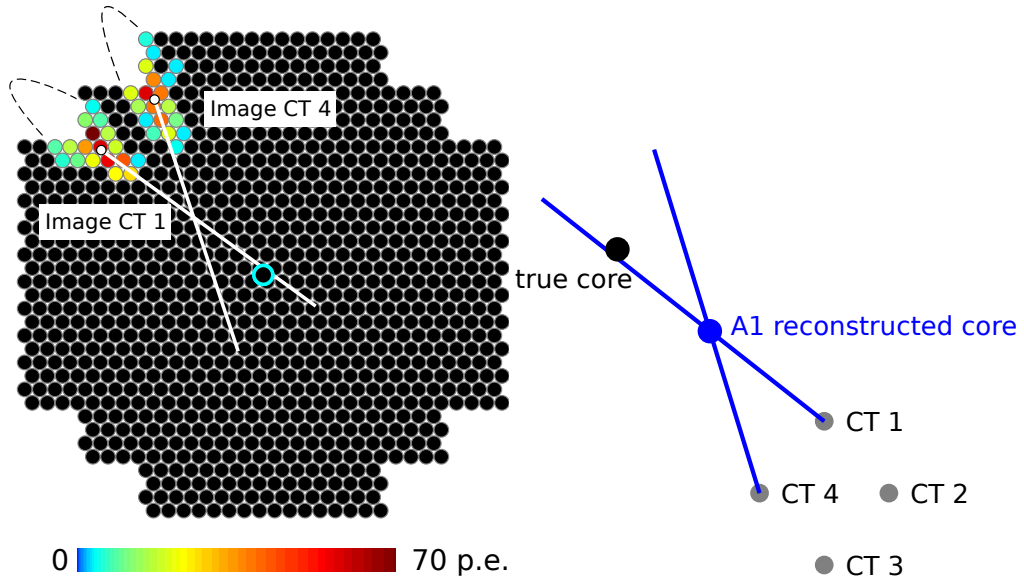


Figure 3.10: Core position and direction reconstruction of a simulated event with two triggered telescopes, using algorithm 1. *Left*: Both images are cut off by the camera edge, the dashed lines indicate the estimated continuation of the ellipses. The orientation of the image from CT 4 is significantly misreconstructed due to the missing part of the image. The direction reconstructed by the intersection of the two major axes (white lines) is about one degree away from the true direction, which is at the camera centre (cyan circle) in this event. *Right*: While the major axis of image 1 points correctly towards the true core position (black point), the wrong reconstructed orientation of image 4 leads to a wrong reconstructed core position (blue point).

timing stereoscopy described in Stamatescu *et al.* [2011] has been developed and will be presented in the following.

#### 3.3.2 Implementation of the time gradient analysis

The time gradient of the individual images is calculated using the method suggested by Stamatescu [2010]: The position of a pixel  $i$  is projected onto the Hillas axis, giving the projected angular distance of a pixel  $d_i$  (see figure 3.11 for definitions):

$$d_i = \begin{pmatrix} \cos \alpha \\ \sin \alpha \end{pmatrix} \cdot \begin{pmatrix} x_i - x_{cog} \\ y_i - y_{cog} \end{pmatrix} \quad (3.9)$$

The pixel peak times<sup>3</sup> are then plotted against the angular distance of the pixel, and a linear fit is applied to the data (see figure 3.12). A linear fit is found empirically to be the most reliable and robust description of the time gradient data [Stamatescu, 2010]. No weighting is applied in the fit here, assuming that the resolution of the peak times is rather uniform over all pixels that survive image cleaning. It should be noted here that the pointing of the major axis is not well defined by the Hillas formalism (i.e. it is not clear which end of the Hillas axis points towards the source position and which points away), and a wrong pointing would lead to a wrong sign of the time gradient. This pointing degeneracy is broken by reconstructing a preliminary source position using algorithm 1 and adjusting the orientation of the Hillas axis accordingly. If the source position is heavily misreconstructed by algorithm 1, the pointing degeneracy may be broken incorrectly, leading to a wrong sign of the time gradient.

<sup>3</sup>For simplicity, the pixel peak times are defined here as the bin with the highest amplitude. No fit or interpolation is used.

### 3.3 Event reconstruction using sampling mode information

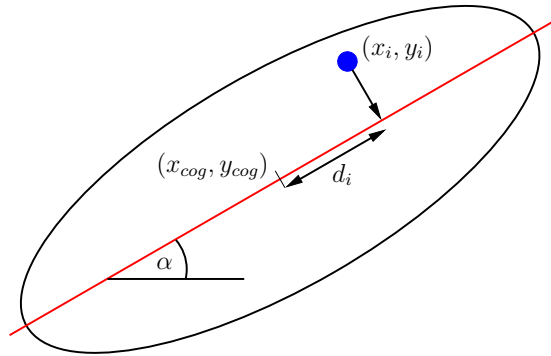


Figure 3.11: Definitions for the calculation of the projected angular distance  $d_i$  of a pixel at the position  $(x_i, y_i)$  with equation 3.9. The centre of gravity of the image is denoted with  $(x_{cog}, y_{cog})$  and the angle of the major axis is called  $\alpha$ .

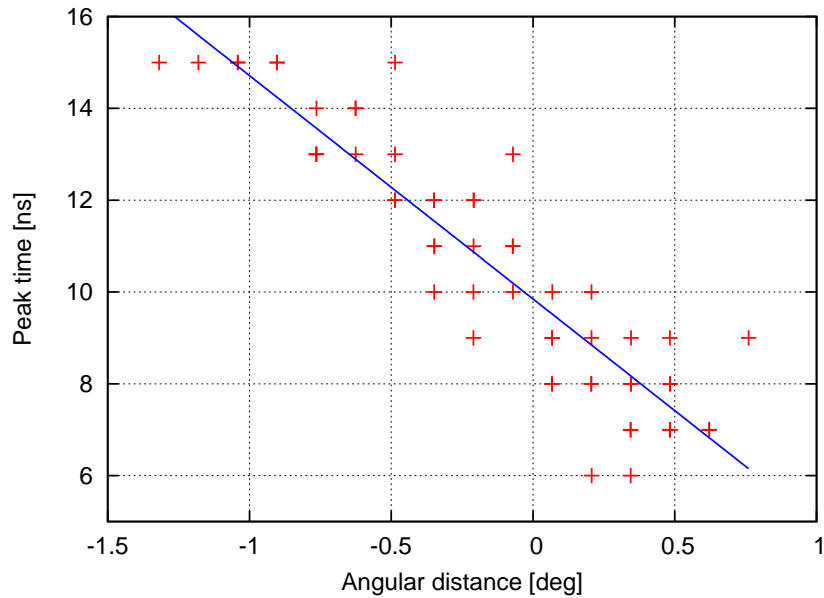


Figure 3.12: Pixel peak times of the image shown in figure 3.9, projected onto the major axis, after image cleaning. The time gradient is given by the slope of a linear fit to the data.

### 3 Sampling mode event reconstruction for the H.E.S.S. experiment

Lookup tables are used to predict the distance from the telescope to the shower core in the shower frame. The tables are generated for specific zenith angles using the simulated events described in the following section. Figure 3.13 shows the time gradient versus the core distance for a data sample of simulated air showers with zenith angle of  $46.5^\circ$ . The distance relation for the lookup table is obtained by interpolating the median values of the time gradient in 50m bins (shown as solid line). As expected, the time gradient provides an accurate prediction of the core distance for distances greater than about 50m. Towards very large core distances the accuracy of the time gradient gets slightly worse as more and more images are weak and poorly parameterised in this regime, but generally the accuracy of the distance prediction is rather independent of the distance. Some “mirrored” data points are also visible, resulting from images for which the pointing degeneracy was broken incorrectly and the wrong sign was assigned to the time gradient.

Figure 3.14 shows a histogram of the distance prediction error for the same dataset, which can be described well by a normal distribution. The width of the distribution, i.e. the resolution of the distance prediction, is  $\sigma = 17.9\text{m}$  for the simulated events in the energy range between 10TeV and 100TeV. For energies between 1 TeV and 10TeV, the resolution is about 37 m (distribution not shown).

#### 3.3.3 New core position and direction reconstruction

In Stamatescu *et al.* [2011] the direction is reconstructed using the time gradient as a source distance estimator in the camera frame. This is not promising for the present case, as the truncated images will have a wrong centre of gravity and even a correct source distance estimation would lead to a wrong source position. Instead, the core distance estimate from the time gradient is used to improve the core position reconstruction. While a reconstruction following algorithm 3 would be the ideal way to do this, it has been decided to use a simpler method in this first study: For each telescope image, a core position is estimated from the direction of the Hillas axis and the distance estimation from the time gradient. The final core position is derived by averaging over these core positions, using the image size as weighting parameter (see figure 3.15, right).

The better core position is then used to improve the direction reconstruction. The potentially misaligned Hillas axes in the images are corrected by using the connection lines from the newly calculated core position to the telescopes. The new Hillas axes are then used to calculate the source position using the conventional algorithm 1 (see figure 3.15, left).

The technical implementation of this new algorithm is discussed in the following section. It is then applied to simulated (section 3.5) and real (section 3.7) events.

## 3.4 Software framework

In this section, the software used to test the new analysis is introduced. Generally, it consists of two layers (see also figure 3.16): In a first step, the data is generated either by Monte Carlo simulations or recorded by the data acquisition system of the H.E.S.S. experiment. The data is stored in a complex ROOT<sup>4</sup> file that contains all necessary information on run, event and pixel levels. The simulation software and the simulated dataset are described in subsection 3.4.1.

From here on, the processing of simulated and real data is (nearly) identical. Usually, these low level data files are converted into higher level data right after data taking at a central point, and only these higher level files – called data summary tapes or DSTs – are used for further analysis. Different software frameworks exist in the H.E.S.S. collaboration for the analysis of the DST files. This procedure is described briefly in subsection 3.4.2.

It turns out, however, that the current version of the software cannot generate DST files from sampling mode data. Since modifications to this software seemed difficult to make it was decided to bypass the DST generation and to develop a new software that can process the raw data directly (see section 3.4.3). This

---

<sup>4</sup><http://root.cern.ch>

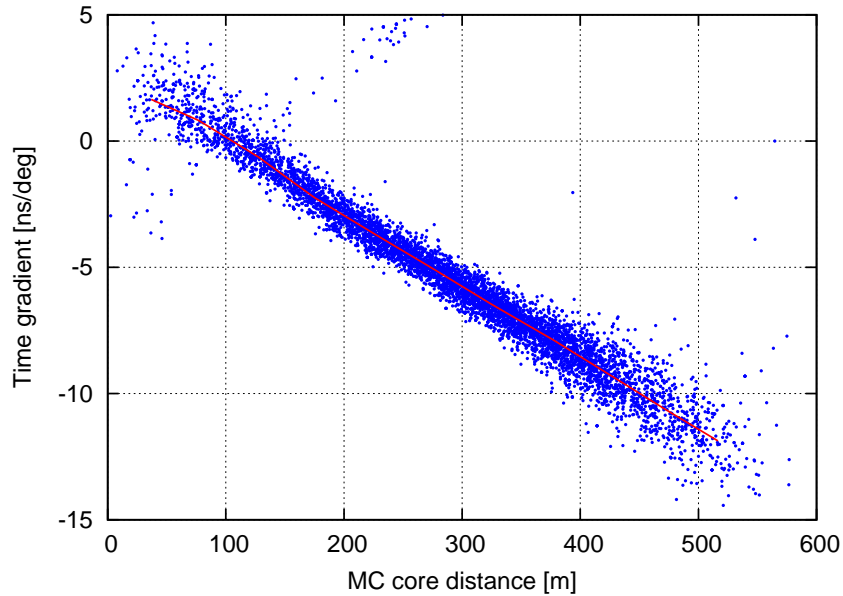


Figure 3.13: The time gradient as function of the distance between telescope and core position. The data points are from simulated gamma-ray events between 10TeV and 100TeV at a zenith angle of  $\theta = 46.5^\circ$  (chosen to match the observations presented in section 3.6). The core distance is given in the shower frame, i.e. by a factor of  $\cos(\theta)$  smaller than on the ground. Only events that are successfully reconstructed by algorithm 1 (needed to break the pointing degeneracy) and telescope images with a nominal distance below  $2.3^\circ$  are used. The correlation used as distance estimator in the reconstruction is shown as red line.

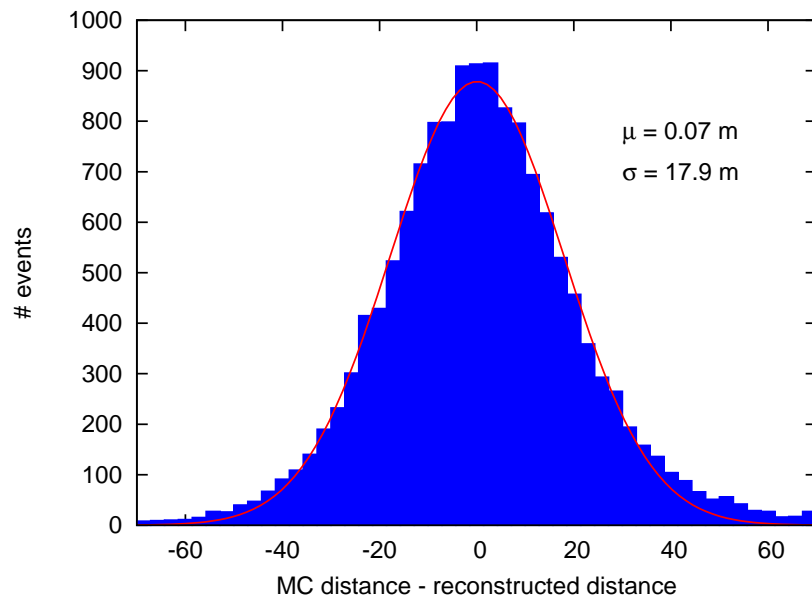


Figure 3.14: Distribution of the distance prediction error using the time gradient with the calibration curve shown in figure 3.13, for events between 10TeV and 100TeV. The solid red line shows the best-fit of a normal distribution to the values.

### 3 Sampling mode event reconstruction for the H.E.S.S. experiment

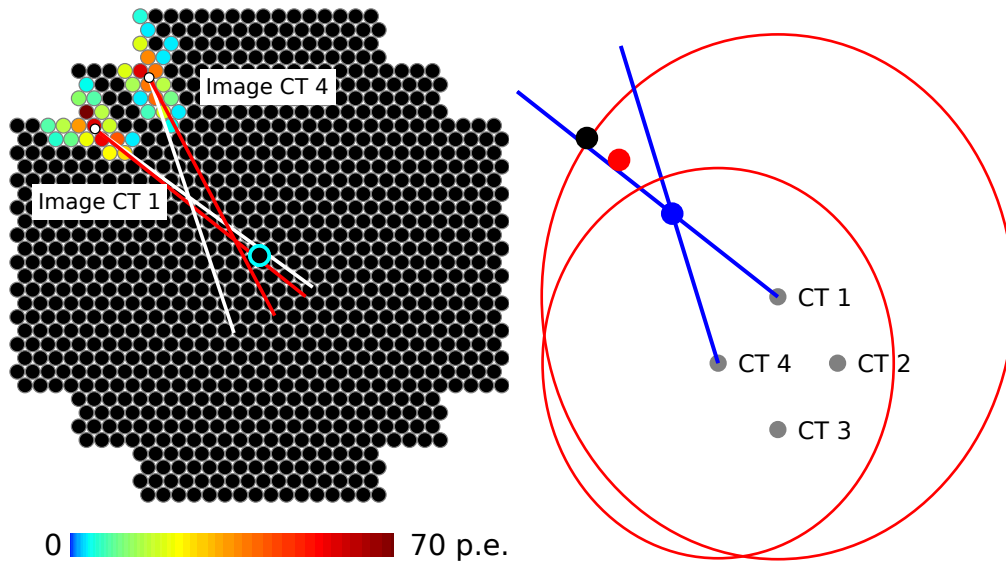


Figure 3.15: Core position and direction reconstruction of the same event as in figure 3.10, using the time gradient as core distance estimator. *Right*: The time gradients from the images give a core distance estimation, indicated by the red circles. Each telescope predicts the core position at the intersections of its distance circle with the corresponding Hillas axis. The final reconstructed core position (red point) is obtained by the (weighted) average of these points. *Left*: The new core position is used to improve the direction of the Hillas axes (red), resulting in an improved direction reconstruction (at the intersection of the red lines).

new software framework provides a full and independent analysis chain from raw data to high level results (e.g. skymaps and energy spectra) and is used to derive all results presented in the following sections. The possible convergence of the new software with the standard framework is discussed briefly in the outlook (section 3.8).

#### 3.4.1 Event simulation

**Simulation software** Air shower events are simulated using CORSIKA v6.735 (see also section 2.4.2), and the resulting data are processed with `sim_telarray` [Bernlöhr, 2008]. This software models the H.E.S.S. telescope array in great detail and generates the expected output of each camera pixel. The sampling mode is fully implemented in `sim_telarray` and can be activated by a command line option.

The output of `sim_telarray` is converted from its native `eventio` format to the standard H.E.S.S. raw data format with the `eventio` tool that is part of the standard H.E.S.S. software package<sup>5</sup>. This tool is not readily able to process sampling mode data and needs some small modifications, which are described in appendix A. The resulting ROOT file can then be processed by the analysis software.

**Simulated dataset** For the evaluation of the new sampling mode reconstruction, a sample of about 4,000 gamma-ray events with energies between 1 TeV and 100 TeV has been simulated. A constant zenith angle of  $46.5^\circ$  is used in order to match the observations of the Crab Nebula presented in sections 3.6 and 3.7. This dataset, called the standard dataset in the following, is used for all simulation results presented in section 3.5. For further tests of the reconstruction algorithms, additional datasets with lower energies, other zenith angles and other primary particles have been simulated. In all cases, a  $\frac{dN}{dE} \propto E^{-1}$  spectrum is used to obtain constant event numbers in logarithmic bins.

<sup>5</sup>Used here is hap-10-06 and ROOT version 5.18.

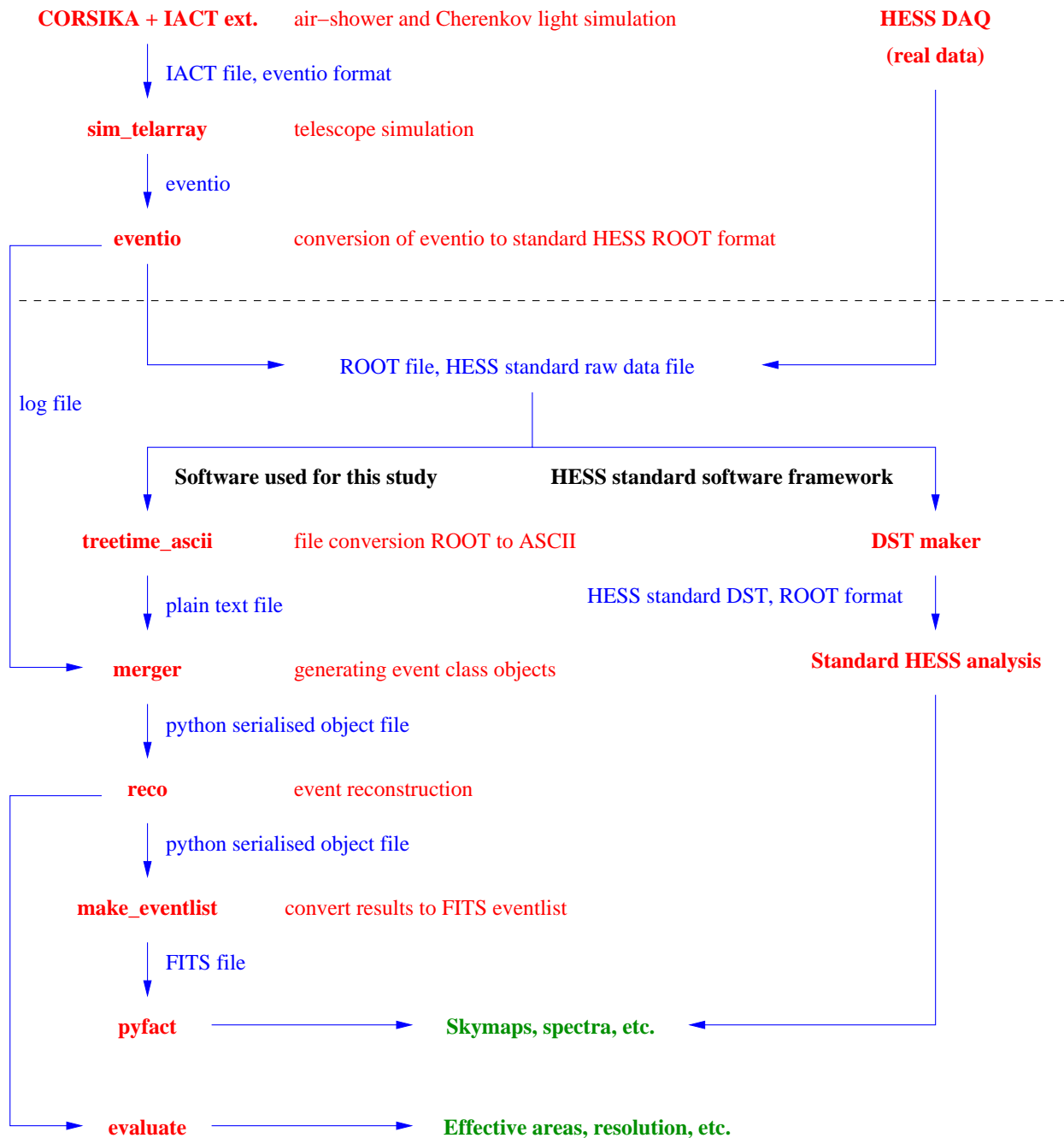


Figure 3.16: Framework for the H.E.S.S. data analysis. The upper part shows the generation of events by simulation (left) or by the real experiment (right). In both cases, a ROOT file in the H.E.S.S. raw data format is generated. The lower part of the chart shows the actual analysis of the data. Usually, the raw data file is pre-processed by a DST maker, and only the higher level data from the DST is used by the actual analysis (right). In this study, the DST maker is bypassed and the analysis is done with newly developed tools (left). The high level analysis is done using the pyfact package [Raue, 2011].

### 3 Sampling mode event reconstruction for the H.E.S.S. experiment

Each simulated event is used ten times by the detector simulation with randomised core positions, which increases the standard dataset to about 40,000 events. The core positions are up to 1000m away from the centre of the array, resulting in a simulated area of 3.14km<sup>2</sup>. This simulated area is sufficient, as even at the highest simulated energies more than 99% of the triggering events have core distances below 1000m. In total, about 12,500 events cause a trigger and can be used for further analysis.

The direction of the telescopes is chosen identical to the direction of the events, which places the direction of origin of the events in the camera centre. Simulations with offsets up to 1° (as often used in real observations) have been used for a cross-check and have produced similar results.

**Real data** In case of real data, no processing is necessary, and the raw data files can be used directly. It should be noted that data from a single run may be distributed over several files of the same structure to avoid overly large file sizes.

#### 3.4.2 Standard H.E.S.S. software

The standard H.E.S.S. analysis is implemented using ROOT and C++. All measured and simulated data is stored in ROOT files in form of data trees. The software provides a set of classes, e.g. a telescope class and a pixel class, that are used to organise and analyse the data. Several different branches of high level analysis are developed and maintained in the H.E.S.S. collaboration in order to cross check results, see e.g. Lemoine-Goumard *et al.* [2006], de Naurois and Rolland [2009] or Ohm *et al.* [2009]. For this work, only a few basic functions of the standard H.E.S.S. software are used to extract the data from the raw data file and convert it to a plain text file format (`treetime_ascii`).

Using the standard DST maker in its currently available form for sampling mode data is not possible for two reasons: First, the use of the sampling mode causes a change in the fundamental data structure. Instead of a single integer number per pixel containing the integrated intensity, each pixel object now contains an array of 16 entries representing the PMT signal. To obtain the total pixel intensity, which is needed for the basic image parameters, these 16 values need to be summed up, which is not currently implemented. Instead, the DST maker simply takes the first of the 16 bins as total intensity value, which results in more or less "empty" images, as usually the signals do not start before the second or third bin. Second, the standard DST maker contains no functions to read in and store the time information in the image, which would therefore be lost even if the correct pixel intensities were calculated.

For these two reasons, it was not possible to use the standard H.E.S.S. DSTs for the sampling mode analysis, and the new analysis software uses the raw data as input.

#### 3.4.3 New sampling mode analysis

Because of the problems lined out in the previous section, it was decided to test the potential of the sampling mode analysis using a small and independent framework written specifically for this task. While such an approach cannot reproduce all features of the standard software, it can be optimised for the task at hand, namely the interpretation of the additional time information obtained by the use of the sampling mode. If the tests are successful, the new approach can afterwards be incorporated into the standard software framework.

As the DST files produced with the standard software do not contain the necessary timing information, the new software reads in the raw camera data directly (using the ROOT script `treetime_ascii`) and skips the standard calibration procedure. The signal pedestal is estimated for each pixel using its average value during the first 1,000 events of the run, and subtracted from the signal. Broken pixels, which contain a constant signal level in all 16 time bins, are marked and excluded in the following analysis. The pixel intensities are calculated with estimated ADC count to photoelectron conversion factors<sup>6</sup>, as no dedicated

---

<sup>6</sup>Low gain channel: 1 ADC count  $\hat{=}$  0.17 p.e; high gain channel: 1 ADC count  $\hat{=}$  0.013 p.e

### 3.5 Simulated performance of the time gradient reconstruction

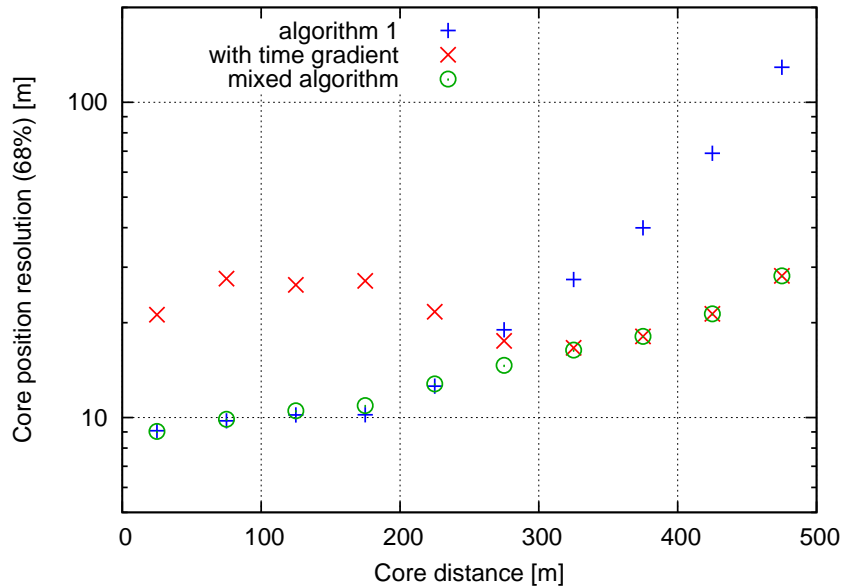


Figure 3.17: Resolution of the core position against the (simulated) core distance for the three discussed algorithms. A nominal distance cut of  $2.0^\circ$  is applied in the reconstruction. Both the distance and the distance error are given in the shower frame.

calibration runs in sampling mode are available. While this produces reasonably looking telescope images, it adds considerable inaccuracies to the pixel amplitudes which may affect all aspects of the reconstruction, and should be improved in a future development.

The corrected pixel signals are passed on to the new event reconstruction software, which was written completely in python and which makes no use of any standard H.E.S.S. software functions. It features methods for standard image cleaning, image parametrisation and Hillas analysis for core position and direction reconstruction (for more details on these methods, see section 3.2). Additionally it incorporates the improved reconstruction that makes use of the sampling mode data as described in section 3.3. Furthermore, it contains a basic energy reconstruction and gamma hadron separation following the scheme outlined in section 3.2.3. For technical details on this event reconstruction software, see appendix A.

The results of the reconstruction are interpreted using several evaluation scripts that compare the reconstructed to the simulated event parameters, which can be used to estimate the performance of the different reconstruction algorithms. For the high level analysis of real data, especially the generation of skymaps and energy spectra, the pyfact package [Raue, 2011] is used. It provides a stand-alone framework that reads in event level data in FITS format and performs all necessary calculations (camera acceptance correction, background subtraction, significance calculation etc.).

### 3.5 Simulated performance of the time gradient reconstruction

The performance of the new sampling mode algorithm is tested using the simulated dataset introduced in section 3.4.1. The results for a standard nominal distance cut at  $2.0^\circ$  and a loosened cut at  $2.3^\circ$  are presented in the following subsections.

#### 3.5.1 Standard nominal distance cut

Figure 3.17 shows the resolution of the core position reconstruction as a function of the core distance. The resolution is defined here – and in the following – as the value at which 68% of the events are contained, which is equivalent to one standard deviation if the distribution is Gaussian. It can be seen that algorithm 1 works well up to about 200m, but becomes rapidly worse at higher core distances. This is the expected behaviour, since at large core distances the stereo angle between the different Hillas axes gets small and the intersections are poorly defined. The time gradient algorithm, on the other hand, does not suffer from this limitation and its accuracy is better than about 30m up to high core distances. The only reason it does get worse at larger core distances is that images from far away events are weaker and the time gradient is defined with less accuracy. At small core distances, however, the time gradient algorithm does not achieve the resolution of algorithm 1. Therefore, a *mixed algorithm* is used, which is a modified version of the time gradient algorithm: For every telescope with core distance prediction from the time gradient of more than 200m, this distance estimate is used like in the normal time gradient algorithm, while for smaller core distances the distance to the previously calculated algorithm 1 core position is used as distance estimate. It can be seen from figure 3.17 that this mixed algorithm can indeed combine the strengths of both other algorithms and achieves an overall accuracy superior to the others.

Figures 3.18 and 3.19 show the core resolution and the angular resolution as a function of energy. The shape of the respective core position and angular resolution distributions are very similar in all cases. All algorithms produce better results at higher energies, where the images contain more photoelectrons and the Hillas parameters as well as the time gradient are better defined. Except for the lowest energy bin, the time gradient algorithm produces better results than algorithm 1. Interestingly, the improvement is largest in the range up to about 15TeV. At even higher energies, the accuracy of the time gradient algorithm remains roughly constant, while the accuracy of algorithm 1 keeps improving, achieving the same resolution at the three highest energy bins. This is probably due to the nominal distance cut at  $2.0^\circ$ , which implicitly introduces a core distance cut, discarding all events further away than about 600m at this zenith angle. In turn, this leads to an improvement of the average image quality with energy, from which algorithm 1 seems to profit more than the time gradient analysis<sup>7</sup>.

The mixed algorithm is better than the other two algorithms at all energies, but again the gain is biggest up to 15TeV. Above, the mixed algorithm is only slightly better than the other two. Compared to algorithm 1, the mixed algorithm can improve the direction reconstruction by at least a factor of 1.5 at certain energies. If the theta cut is adjusted accordingly (see section 3.2.4), this can lead to an improvement of the same factor in the sensitivity of the instrument.

#### 3.5.2 Extended nominal distance cut

The second expected benefit of the time gradient, its robustness against truncated images, is tested in the following by relaxing the nominal distance cut from  $2.0^\circ$  to  $2.3^\circ$ . At a zenith angle of  $46.5^\circ$ , this leads to an increase of the effective area of up to a factor of two at higher energies (see figure 3.20). While the trigger area increases roughly linearly with energy, as more and more distant events produce enough light to trigger the system, the nominal distance cut limits the effective area as it effectively introduces a core distance cut. At the highest energies, it even leads to a slight decrease of the effective area, as the nominal distance of images also increases with the depth of the shower maximum, and thus with energy, as illustrated in figures 3.5 and 3.6 in section 3.2.2. The increasing difference between trigger area and area after nominal distance cut shows that the instrument itself has much greater potential at the highest energies and is limited only by the field of view of the camera. Relaxing the nominal distance cut can help to exploit this potential to some

<sup>7</sup>Considering that at the highest energies the results of the mixed algorithm and algorithm 1 are partly independent, one might expect an improvement in the core position resolution by averaging over the two core positions. However, tests have shown no significant change in the reconstruction accuracy.

### 3.5 Simulated performance of the time gradient reconstruction

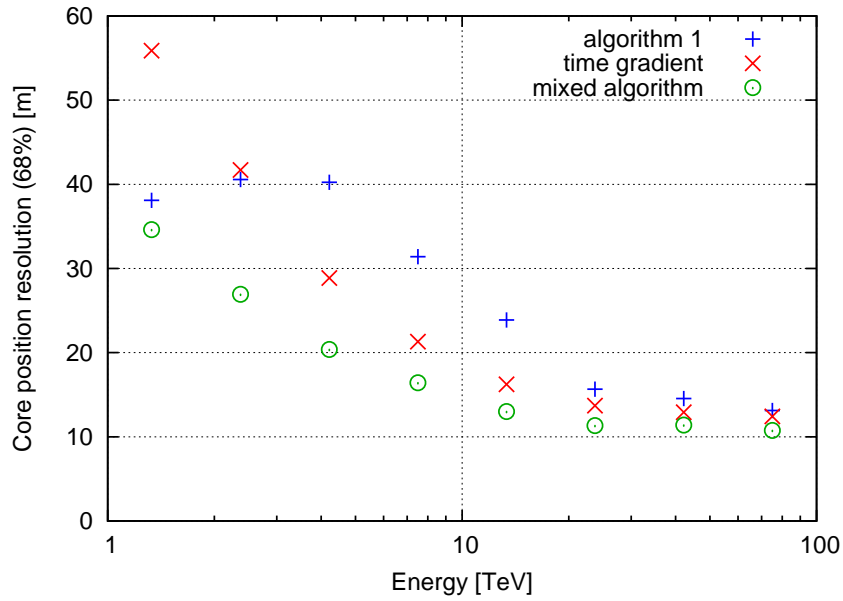


Figure 3.18: Resolution of the core position against the (simulated) energy for the three used algorithms, in shower frame. A nominal distance cut of  $2.0^\circ$  is applied in the reconstruction.

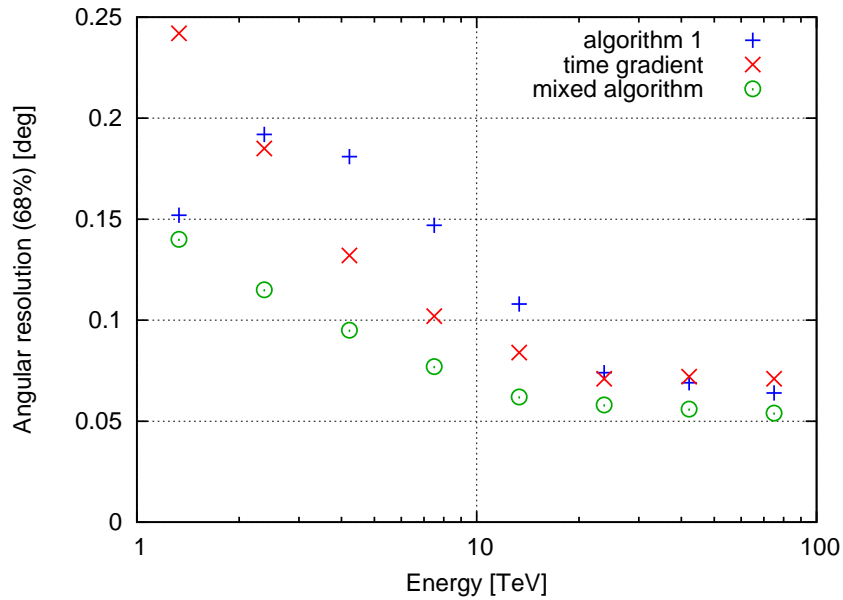


Figure 3.19: Angular resolution against the (simulated) energy for the three used algorithms. A nominal distance cut of  $2.0^\circ$  is applied in the reconstruction.

### 3 Sampling mode event reconstruction for the H.E.S.S. experiment

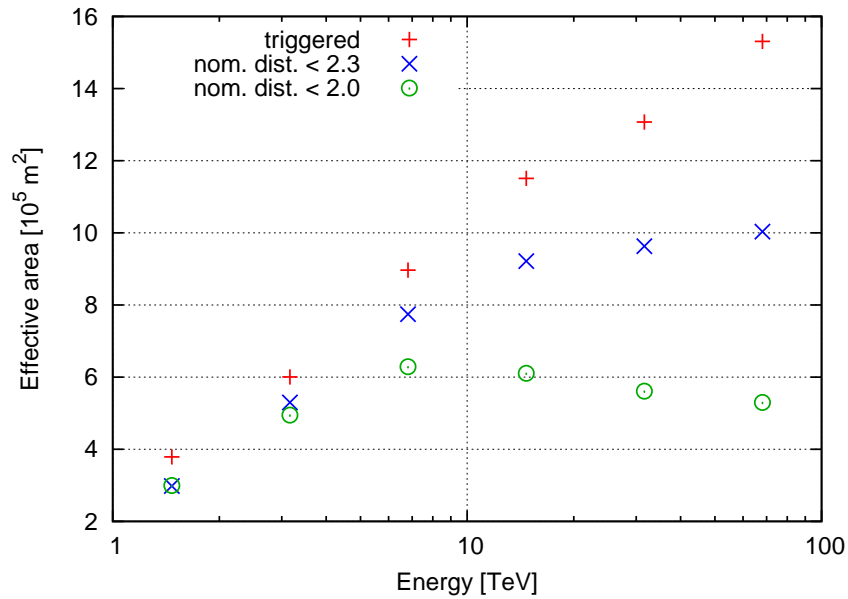


Figure 3.20: Effective areas of the H.E.S.S. experiment as obtained from the described simulations at  $46.5^\circ$ . Shown are the trigger area (all events that have triggered at least two telescopes), and the areas after two different nominal distance cuts at  $2.0^\circ$  and  $2.3^\circ$ .

extent, albeit by taking into account many truncated and therefore poorly parametrised images.

Figures 3.21 and 3.22 show the core position and angular resolution for the different algorithms using the new nominal distance cut. As expected, the inclusion of many truncated images generally deteriorates the accuracy of the reconstruction. This becomes particularly evident at higher energies, where events with a large core distance and thus a large nominal distance make up a large fraction of all events, while at 1 TeV the resolution of the reconstruction is almost unchanged. The impact of the truncated images is strongest on algorithm 1, whose results deteriorate with energy. As expected, the time gradient algorithm suffers much less from the truncated images, and shows an improvement in accuracy with energy. Nevertheless, both its core position and angular resolution are up to a factor of two worse than for the standard nominal distance cut at the highest energies. Again, the mixed algorithm produces the best results, but beyond 10 TeV the improvement against the pure time gradient algorithm is marginal since algorithm 1 cannot contribute considerably to improve the resolution in this regime.

As such, it seems that the increase of the nominal distance cut is not beneficial in the studied case, since the gain in sensitivity by the increase in effective area is cancelled out by a worse angular resolution, which must be accounted for by increasing the  $\theta$ -cut. Only if the sensitivity is not limited by the background but rather by statistics, as it may be the case at the highest energies (depending on the gamma-ray flux, the spectrum and the power of the gamma hadron separation), an increase of the  $\theta$ -cut will have no negative effect while the larger effective area will lead to an overall increase in sensitivity.

#### 3.5.3 Energy reconstruction

Although the energy reconstruction is not a primary topic in this study, it is needed to analyse the energy dependence of the reconstruction accuracy in the observational data. Therefore, the new analysis framework (see section 3.4.3) also contains an energy reconstruction algorithm which follows the concept outlined in section 3.2.3: From the Monte Carlo dataset energy lookup tables with dependencies on the image size and the core distance are generated, which are subsequently used for the energy reconstruction. Only events

### 3.5 Simulated performance of the time gradient reconstruction

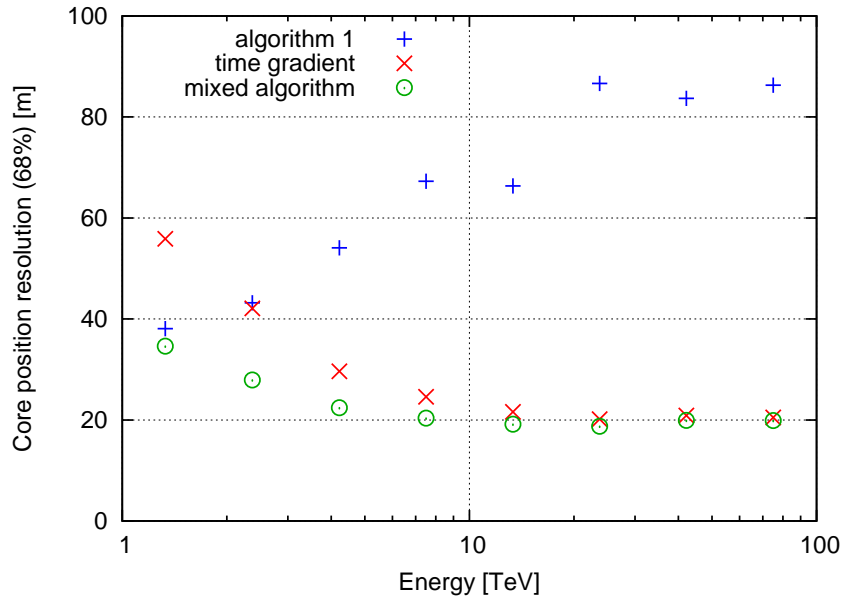


Figure 3.21: Resolution of the core position against the (simulated) energy for the three used algorithms, for the increased nominal distance cut of  $2.3^\circ$ , in shower frame.

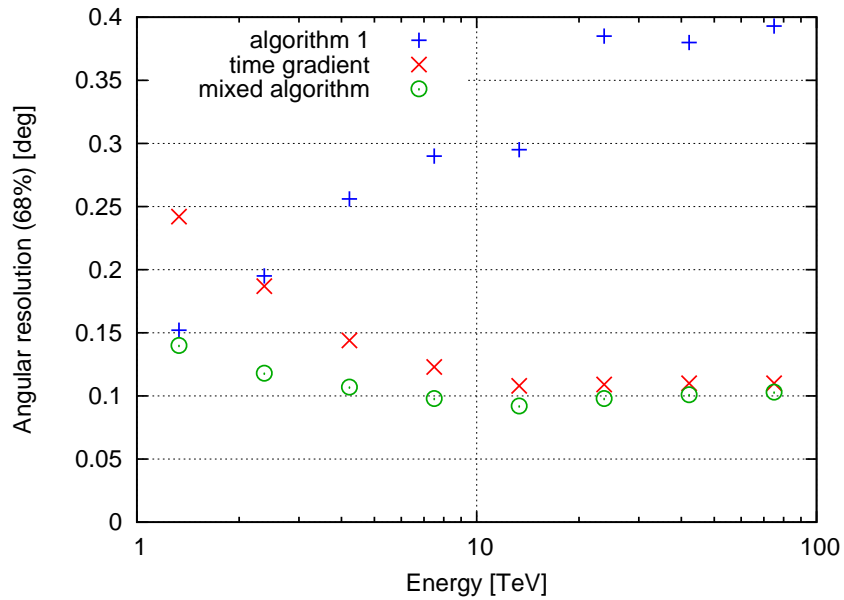


Figure 3.22: Angular resolution against the (simulated) energy for the three used algorithms, for the increased nominal distance cut of  $2.3^\circ$ .

### 3 Sampling mode event reconstruction for the H.E.S.S. experiment

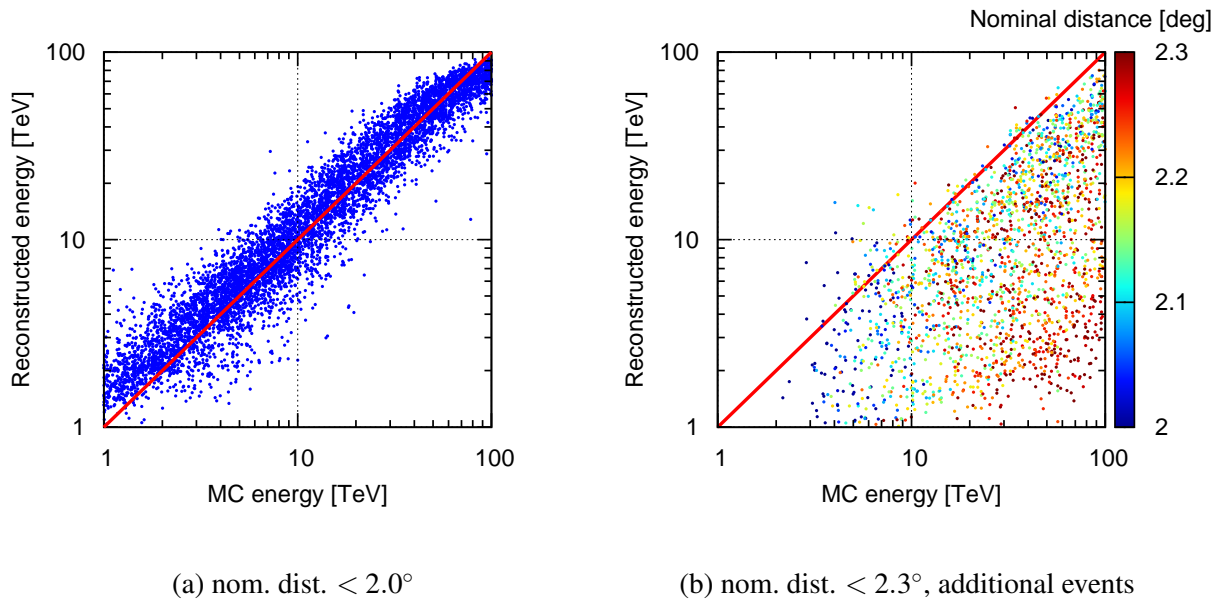


Figure 3.23: Reconstructed energy versus simulated energy for events surviving the standard nominal distance cut (left) and events that are included additionally by the extended nominal distance cut (right). For the second case, the average nominal distance of all images with a nominal distance greater than 2.0° is given in colour code.

which survive the nominal distance cut of 2.0° are used. To take into account a possible systematic bias in the core distance reconstruction, the lookup tables are generated using the reconstructed core position (using algorithm 1).

The energy reconstruction algorithm predicts an estimated energy of the event from every telescope image. The estimates from the different images are averaged using the image size as weighting parameter. Figure 3.23a shows the reconstructed energies against the true energies for all simulated events. In general, the accuracy of the reconstruction is rather good, although systematic deviations are visible towards both ends of the simulated energy range. At the lower end, the energy is usually overestimated, which can be explained as a selection effect: At these energies, only unusually bright events<sup>8</sup> trigger the telescopes and pass the image size cut (see also section 5.4.4 for the discussion of a similar effect in the H<sub>i</sub>SCORE event reconstruction). At high energies the deviations are probably due to the abrupt end of the simulated energies. This offset is however of no concern for the current study, as the relevant energy range for the analysis of the observational data is between 1 and a few 10 TeV. Over the whole energy range, the energy resolution (defined as the 68% containment region of  $(E_{MC} - E_{reco})/E_{MC}$ ) is about 30%.

Serious problems arise, however, if events with a nominal distance of greater than 2° are included. Figure 3.23b shows the reconstructed energies of all events that are included additionally by relaxing the nominal distance cut from 2° to 2.3°. For these events, the energy is systematically underestimated, as their images are usually cut off by the camera edge and the measured image size is no longer proportional to the energy. From the colour code it can be seen that the bias increases with the average nominal distance of the images used for the reconstruction.

To correct for this, the amount of light lost at the camera edge would need to be estimated. As long as the brightest image pixel is not directly at the edge, it should be possible to accomplish this by fitting an expected image shape to the recorded pixel intensities and derive the “true” size of the image from the fit

<sup>8</sup>Events are “unusually bright” if the air shower develops late, i.e. if the shower maximum appears at low altitudes. As the height of maximum depends strongly on the position of the first interaction, it is distributed randomly with a large spread.

parameters. Another approach would be to generate fake pixels beyond the camera edge by mirroring the pixel intensities on the brightest pixel. Such improvements to the energy reconstruction are however not a topic in this thesis and are left for future studies.

## 3.6 Sampling mode data taken with the H.E.S.S. experiment

To test the analysis presented in the previous section, sampling mode data was taken with H.E.S.S. in October 2009. The observations were directed towards the Crab Nebula, a prominent bright gamma-ray source. In the observation proposal [Tluczykont *et al.*, 2009a], 30 hours of total observation time was requested to gather enough statistics at the highest energies to test the impact of the sampling mode reconstruction in this regime. Due to strong competition of other proposals it was decided by the observation committee to limit the observation time to 2 hours for a feasibility study for this observation period.

In this section the recorded data will be discussed, with a special emphasis on problems that may be introduced by switching the system to sampling mode. The analysis of the data, and the results, are presented in section 3.7.

### 3.6.1 Run summary

The observations in sampling mode consist of eleven runs, of which the first two are truncated due to hardware problems and discarded in the following analysis. Each of the remaining nine runs contains about 10 minutes of data (see table 3.1). According to the shift crew, only the first three runs are affected by occasional clouds, while the weather was clear afterwards. During the second night of sampling mode observations, one run (runnumber 054404) was taken in standard mode for comparison. The total exposure of the nine good sampling mode runs is 5472 seconds (91.2 minutes).

### 3.6.2 Data rate

Compared to the usual trigger rate of more than 100Hz, the rate is suspiciously low in the sampling mode runs (see table 3.1). Since the standard mode run 054404, which was recorded directly before one of the sampling mode runs, reaches constant rate of about 120Hz, it seems unlikely that bad weather or other external circumstances are responsible for the lower rate. Also, the event rates are constant both within the sampling mode runs and the standard mode run, and the shift crew noted clear sky conditions for most of the runs.

Instead, the lower rate must be connected to the change of the acquisition mode. When switching the telescope system from standard to sampling mode, the data rate is increased by a factor of almost 16. Since problems with the readout due to this increased data rate were expected, the pixel trigger threshold was increased from 4 to 7 photoelectrons. Due to the energy spectrum of cosmic rays<sup>9</sup>, this is expected to reduce the event rate by about  $(4/7)^{-1.7} \approx 2.6$ .

Despite this precaution, the data rate turned out to be too high to be properly handled by the system. The histograms of the time intervals between events (figure 3.24) show a clear signature of the increased system dead time in sampling mode: In the sampling mode run, no events occur within less than 15ms of each other, while in standard mode the cut-off appears only at below 1ms. For the sampling mode this implies a maximum event rate of 67Hz. The amount of lost events is expressed by the fractional dead time, which reaches about 35% for the sampling mode runs, while being below 5% for the standard mode run.

Together, these two effects – the higher pixel threshold and the increased dead time – offer a reasonable explanation for the low event rate. Considering the fractional dead time, the total live time of the experiment during the sampling mode observations amounts to 3557 seconds (59.3 minutes).

<sup>9</sup>Integral energy spectrum:  $N(E > E_0) \propto E_0^{-1.7}$  (in the energy range relevant here)

### 3 Sampling mode event reconstruction for the H.E.S.S. experiment

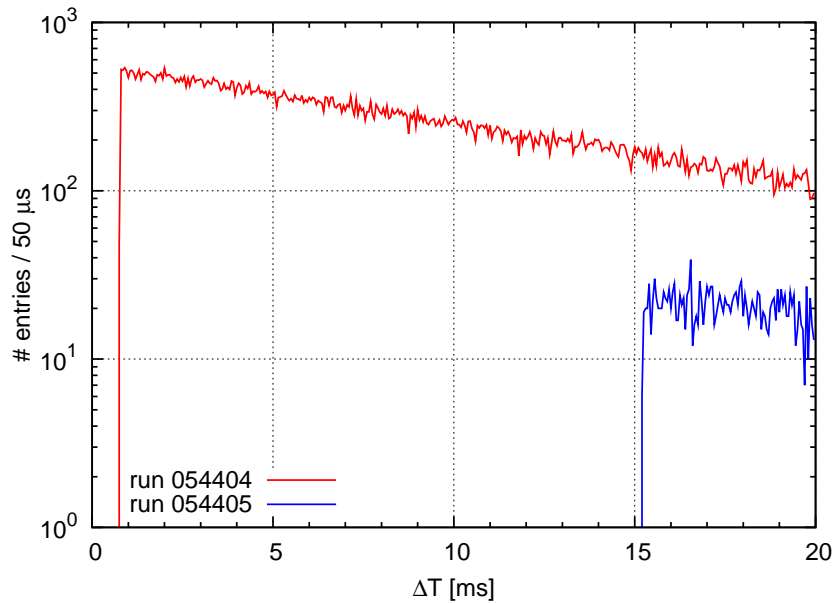


Figure 3.24: Histogram of time differences between events in CT 1 for a normal run (run 054404) and a sampling mode run (054405).

#### 3.6.3 Telescope performance

Table 3.2 shows the performance of the telescope system during the nine sampling mode runs that are used in the analysis. The trigger fraction is between 70% and 80% for all four telescopes, which is well within normal parameters. However, triggered telescopes show empty images in many instances, and the fraction of events with images is only about 50% for CT 1 and CT 2, and only about 25% for CT 3. Telescope 4 did not deliver any images for about half of the total observation time (runs 054369 to 054373), while it achieved the same performance as CT 1 and 2 in the remaining runs.

In the standard mode run 054404, all telescopes function normally and produce images in almost all triggered events. The problems observed here are therefore presumed to be connected to the change of the acquisition mode rather than an actual hardware malfunction. Although the specific nature of the problem is not known, it appears as if the increased amount of data produced in sampling mode could not be handled properly by the data acquisition chain. In consequence, some of the data is lost at some stage. It remains unclear, however, why the four telescopes have been affected in different ways. Before further sampling mode data is taken, these problems should be addressed by in-depth hardware testing on site by experts for the respective subsystems (camera, data acquisition, computer cluster).

Given these circumstances, the results presented in section 3.7 do not reflect the full potential of the sampling mode, as a lot of the data was taken – effectively – with only two or three telescopes.

#### 3.6.4 Position of the peak time

The position of the signal in the readout window must be carefully calibrated in order to lose as little signal intensity as possible. As shown in figure 3.13, the peak times within a single image can be shifted against each other by up to 10ns/deg for distant events. With a readout window size of 16ns this may easily lead to truncated signals, especially at high energies where even distant showers can produce large images.

Figure 3.25 shows two signals from the telescope image shown in figure 3.9 with their high and low gain channels. In figure 3.25a the signal from the brightest pixel is shown, which is well contained in the

### 3.6 Sampling mode data taken with the H.E.S.S. experiment

Runnumber	Date	Start time	# Events	Duration [s]	Rate [Hz]
054366	28/10/2009	00:50:58	4699	309	15
054367	28/10/2009	00:58:30	3751	308	12
054368	28/10/2009	01:06:13	17149	609	28
054369	28/10/2009	01:28:28	14075	608	23
054370	28/10/2009	01:40:46	20746	608	34
054371	28/10/2009	01:53:01	17128	607	28
054372	28/10/2009	02:05:22	21218	608	35
054373	28/10/2009	02:18:33	23140	608	38
054374	28/10/2009	02:30:57	21970	609	36
054405	30/10/2009	02:34:44	28967	607	48
054411	31/10/2009	02:15:13	28936	608	48
054404	30/10/2009	02:03:21	198526	1688	118

Table 3.1: Run summary for the sampling mode observations of the Crab Nebula in October 2009. Run 054404 has been taken in standard mode for comparison. The mean zenith angle of all runs is between  $45^\circ$  and  $48^\circ$ .

Run	Trigger fraction				With image			
	CT 1	CT 2	CT 3	CT 4	CT 1	CT 2	CT 3	CT 4
054368	0.70	0.70	0.73	0.78	0.53	0.53	0.26	0.58
054369	0.69	0.69	0.71	0.77	0.53	0.53	0.26	0.00
054370	0.71	0.71	0.73	0.77	0.51	0.51	0.24	0.00
054371	0.68	0.70	0.73	0.77	0.52	0.53	0.26	0.00
054372	0.70	0.71	0.73	0.78	0.51	0.51	0.24	0.00
054373	0.71	0.71	0.74	0.78	0.50	0.50	0.24	0.00
054374	0.70	0.71	0.74	0.78	0.50	0.50	0.24	0.48
054405	0.72	0.71	0.73	0.80	0.47	0.46	0.22	0.50
054411	0.70	0.71	0.73	0.79	0.46	0.46	0.22	0.50
054404	0.70	0.69	0.72	0.79	0.69	0.69	0.72	0.78

Table 3.2: The table shows the performance of the individual telescopes during the runs, expressed by the fraction of events in which this telescope has triggered, and the fraction of events in which this telescope has a non-zero image size.

### 3 Sampling mode event reconstruction for the H.E.S.S. experiment

recording window. Between the two gain channels a small time shift is visible – this is addressed in more detail below. Figure 3.25b shows the signal from one of the late pixels towards the upper end of the image. It is clearly visible that a large fraction of the signal is cut off at the end, and since the signal has not even reached its peak, the peak time is also misreconstructed.

To judge the seriousness of this problem, a histogram of peak times in the high gain channel is shown in figure 3.26a (using run 054405). Only pixels that pass the image cleaning process are used in the histogram. While the peak never appears in one of the first time bins, it quite often appears in one of the last bins. Conspicuously many pixels reach their highest intensity in the very last time bin, which indicates that a fair fraction of signals would actually only reach their peak *after* the end of the readout window. The problem also appears in the low gain channel (not shown), however less pronounced as the late pixels in the image tail usually have low intensity and are therefore processed using their high gain channel.

To estimate how much signal intensity is lost due to this effect, the average signal of all image pixels in this run is shown in figure 3.26b. For the low gain channel, nearly no light is lost after the readout window. In the high gain channel, however, the last time bin still contains a significant amount of intensity. If the signal is fitted with a normal distribution (which not a very good fit, but should suffice here), the intensity after the end of the readout window is found to be about 10% of the total intensity.

Generally, a loss of 10% of the light should not be a problem. Extending or shifting the readout window could slightly increase the amount of Cherenkov light measured, which might benefit pixels close to the threshold, but the effect would not be substantial. The loss of intensity might be problem if it depended on certain parameters, e.g. the energy or the core distance, as this could introduce a bias in the reconstruction. However, in a study by Balzer [2010] no such dependencies were found.

#### 3.6.5 Time offsets between channels

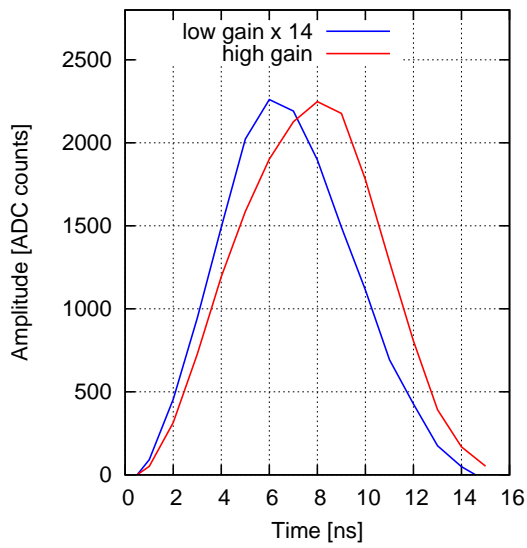
In the example in figure 3.25 a small time shift between the two gain channels is visible. To examine this further, the time differences between the channels are calculated for all events in run 054405. The selected pixels have intensities high enough to produce a reliable signal in the low gain channel, yet small enough to avoid saturation effects in the high gain channel. The resulting histogram is shown in figure 3.27. It shows that the example of figure 3.25 is indeed typical: For most events, the peak in the high gain channel comes 1 ns after the low gain channel peak. Overall, a rather large spread of offsets exists between the channels, which could in principle lead to distortions in the calculation of the time gradient. However, since only the brightest pixels near the image centre are processed using the low gain channel, the effect on the time gradient should be small.

#### 3.6.6 Pedestal gradient

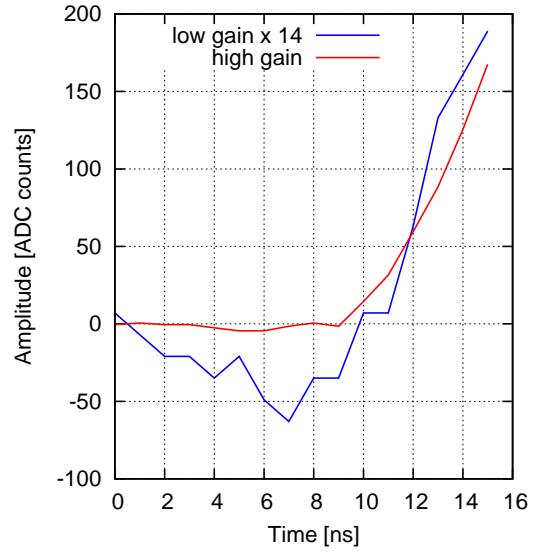
In order to use the signals in the analysis, their pedestals must be subtracted. In standard mode, the pedestal is usually calculated individually for each pixel by averaging the pixel amplitude over all events in which the particular pixel is not part of the image. In principle, the procedure is similar in sampling mode. However, the pedestal can be different for the 16 time bins, and it may be necessary to calculate the pedestal separately for each bin.

To check this, the average pedestal per time bin has been calculated from the first 1,000 events of run 054405 (figure 3.28). Both high and low gain channels behave very similar: The pedestal increases from the first to the second bin and then decreases linearly over the readout window. To check whether all pixels follow this general trend, a histogram of the average pedestal slope of each pixel and event has been generated (not shown). It confirms that all pixels exhibit a falling pedestal with average slopes between -0.1 and -0.4 ADC counts per nanosecond. As an ADC count corresponds to only 0.013 (high gain channel) or 0.17 (low gain channel) photoelectrons, it was decided to ignore this pedestal gradient in the current version of the software, and to assume a constant pedestal value for each pixel. To improve the accuracy of the pixel

3.6 Sampling mode data taken with the H.E.S.S. experiment

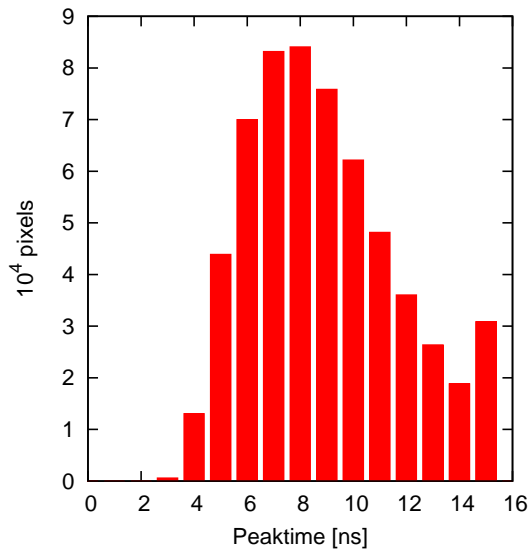


(a) Central pixel

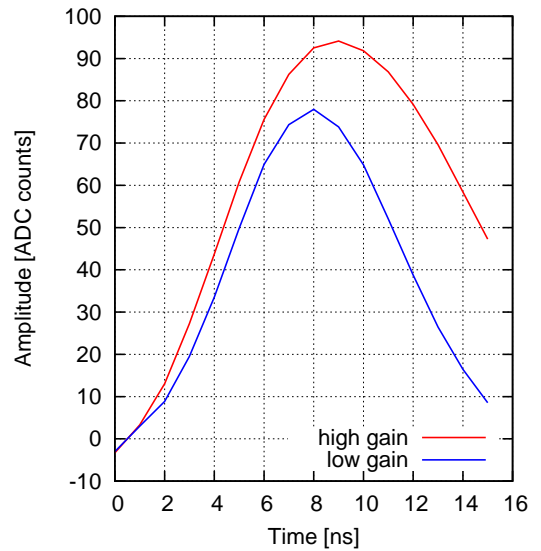


(b) Late pixel

Figure 3.25: Recorded PMT signals from the sampling mode observations. The signals are taken from the image shown in figure 3.9.



(a) Histogram of high gain channel peak times.



(b) Average signal

Figure 3.26: Histogram of pixel peak times (high gain channel), and average high and low gain signals.

### 3 Sampling mode event reconstruction for the H.E.S.S. experiment

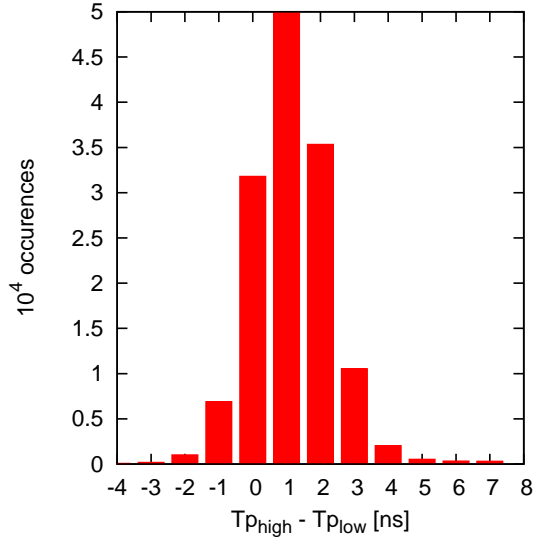


Figure 3.27: Histogram of the shifts between the peaks of the high and low gain channel.

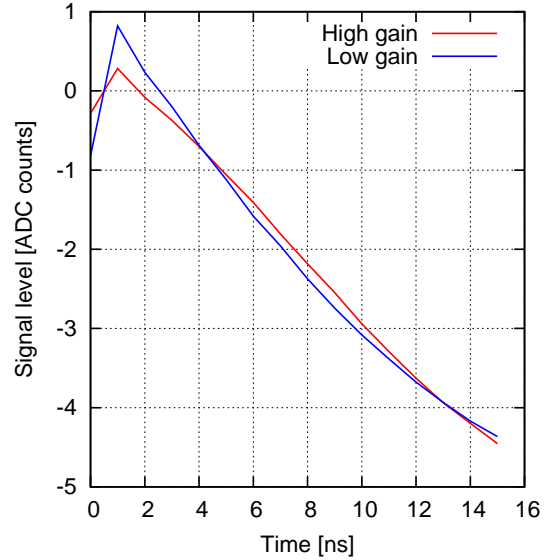


Figure 3.28: Average pedestal of high and low gain channel, calculated from signals of non-image pixels.

amplitude calculation, a future version of the software may include separate pedestal values for each time bin.

## 3.7 Analysis and results of sampling mode data

In this section, the results of the analysis of the sampling mode runs are presented. The target of the observations, the Crab Nebula, is introduced briefly in subsection 3.7.1. The following subsections present a standard analysis of the source (using algorithm 1) and an analysis using the mixed sampling mode algorithm with nominal distance cuts at  $2.0^\circ$  and  $2.3^\circ$ . All results are derived using the analysis software introduced in section 3.4.3.

### 3.7.1 The Crab Nebula

The Crab Nebula, also known as M 1, NGC 1952 and Taurus A, is the remnant of a supernova which has been observed by astronomers in 1054. In its centre, it contains the pulsar that has been formed during the supernova. Both the Nebula and the pulsar itself have been studied extensively with many experiments in different wavebands from radio to gamma-ray energies (see e.g. Hester [2008] for a review). It is located at a right ascension of  $5^h 34^m 31^s$  and a declination of  $+22^\circ 00' 52''$  (in J2000 equatorial coordinates, see Lobanov *et al.* [2011] for the latest precision measurement on the position of the pulsar). Its distance is estimated to about 2 kpc [Trimble, 1973].

The Crab Nebula was the first source to be detected in VHE gamma-rays [Weekes *et al.*, 1989] and has been observed by many other VHE gamma-ray observatories since then, including H.E.S.S. The integral gamma-ray flux above 1 TeV has been measured by H.E.S.S. to be  $(2.26 \pm 0.08_{stat}) \times 10^{-11} \text{ cm}^{-2} \text{ s}^{-1}$ . The energy spectrum follows a power law with index of  $-2.39 \pm 0.03_{stat}$  with an exponential cut-off at  $E_c = (14.3 \pm 2.1_{stat}) \text{ TeV}$  [Aharonian *et al.*, 2006c]. Since it offers a reliable and bright source of gamma-rays, it is often used to test the performance of new experiments or analysis software, and was consequently also

chosen to test the sampling mode analysis presented here.

It is commonly assumed that the energy for the VHE gamma-ray emission originates from the pulsar in form of highly energetic electrons and positrons [Kennel and Coroniti, 1984; Hillas *et al.*, 1998; Meyer *et al.*, 2010]. These leptons transfer their energy via inverse Compton scattering to photons present in the vicinity, mostly synchrotron photons emitted by the same lepton population during their propagation through the magnetic field of the pulsar (Synchrotron self-Compton process). In VHE gamma-rays, the Crab Nebula is seen as point source (see e.g. Aharonian *et al.* [2000]), consistent with expectations [Atoyan and Aharonian, 1996].

Despite the large number of detailed measurements that are available of the Crab Nebula, some open questions remain that motivate further gamma-ray observations not only for tests and calibration, but also from a scientific point of view. Especially, contradictory measurements of the shape of the spectrum at multi-TeV energies have been reported (e.g. no cut-off has been reported by the HEGRA collaboration [Aharonian *et al.*, 2004]). Also, variations in the gamma-ray flux have been found recently by the AGILE and FERMI satellite experiments in the HE band, contradicting the so-far common notion of a steady source [Tavani *et al.*, 2011; Striani *et al.*, 2011; Abdo *et al.*, 2011b]. In fact, it has been suggested that the underlying processes causing these variations may also cause variations of the flux at multi-TeV energies, which may even explain some of the discrepancies between the HEGRA and H.E.S.S. results [Bednarek and Idec, 2011].

It seems also possible that wisps seen in optical and X-ray images of the object [Hester *et al.*, 2002] may cause variations in the TeV gamma-ray flux. These wave-like patterns originate from the pulsar, move outwards and dissolve on the time scale of months. Gallant and Arons [1994] have proposed a model which can explain the observed features as a relativistic wind of ions and plasma of electrons and positrons, which eventually cause a short and localised increase in the synchrotron emission, seen as wisp. As the same lepton population is also responsible for the gamma-ray emission, the appearance of a wisp might be accompanied by an increase in gamma-ray flux [Horns and Aharonian, 2004]. At energies beyond 60 TeV the cooling time of the electrons is on the same time scale as the lifetime of a wisp, which may lead to a signature in gamma-rays with energies beyond 10 TeV simultaneous to the wisp emission [Tluczykont *et al.*, 2009a]. So far, such a connection could however not be observed due to a lack of gamma-ray event statistics in the relevant energy range.

Further observations of the Crab Nebula, especially at multi-TeV energies, can help to resolve the outlined questions and to understand the underlying emission processes better. The data presented here does however not provide enough statistics for studies of the spectrum at multi-TeV energies. Nevertheless, the new sampling mode event reconstruction can help to increase the event numbers at the highest energies, if it reaches its full performance, and can therefore also help to address the open questions concerning the Crab Nebula (and other sources) in the long term.

### 3.7.2 Standard analysis

Figure 3.29 shows the event and excess events skymaps of the observed region. For the excess skymap, the background of cosmic ray events is subtracted using the ring background method as described in Aharonian *et al.* [2006c]. The inner and outer ring radii used here are  $0.3^\circ$  and  $0.7^\circ$ , respectively. A clear excess of about 100 photons can be seen near the nominal source position of the Crab Nebula. The source position is fitted on the excess skymap with a two-dimensional, radially symmetric Gaussian function:

$$G(x, y) = A \exp \left( - \left( \frac{(x - x_0)^2}{2\sigma^2} + \frac{(y - y_0)^2}{2\sigma^2} \right) \right) \quad (3.10)$$

The peak of the emission is found at a right ascension of  $83.59^\circ$  and a declination of  $21.94^\circ$  (J2000 equatorial coordinates), about  $0.1^\circ$  away from the nominal position (black cross). This offset is probably caused by ignoring the standard H.E.S.S. pointing correction [Gillessen, 2004] in the analysis, which is

### 3 Sampling mode event reconstruction for the H.E.S.S. experiment

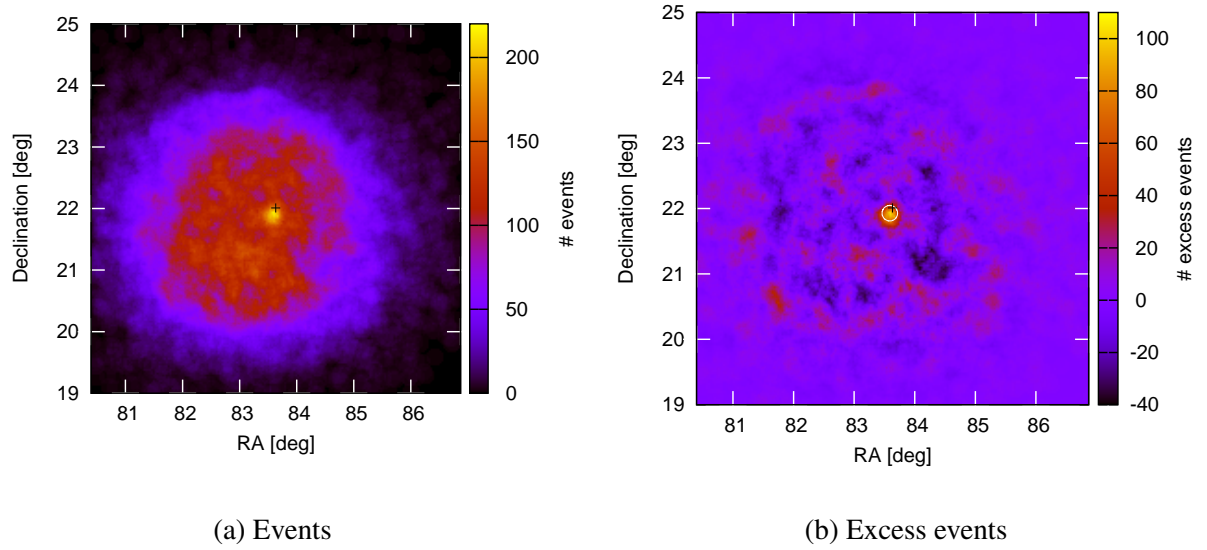


Figure 3.29: Skymaps of the observed region. The arrival directions are reconstructed using algorithm 1 and standard nominal distance cut. The skymaps are generated with an oversampling radius of  $0.125^\circ$ , i.e. each point on the map shows events that fall within this radius around the point. The right skymap shows the count of excess events, calculated using the ring background method. The nominal position of the Crab Nebula is indicated by the black cross in both skymaps. The white circle in the excess skymap shows the  $1\sigma$  radius of the Gaussian fit to the excess.

needed to account for the deformation of the telescope structure at larger zenith angles<sup>10</sup>. As the observations used here are taken at zenith angles between  $45^\circ$  and  $48^\circ$ , this deformation causes a non-negligible error in the telescope pointing. However, since the focus of this study is not primarily on the astrophysical nature of the source, but on the performance of the new reconstruction method, the offset is not relevant here. For the subsequent analysis, the reconstructed source position is used.

The  $1\sigma$  radius of the Gaussian fit is  $0.127^\circ$  (indicated by the white circle in the excess skymap), similar to the 68% containment radius found with the standard analysis,  $0.12^\circ$  [Aharonian *et al.*, 2006c]. The extension of the excess is a combination of the actual extension of the VHE gamma-ray emission and the point spread function (PSF) of the observation. If both components are approximated by normal distributions with widths of  $\sigma_{source}$  and  $\sigma_{PSF}$ , the observed extension is:

$$\sigma^2 = \sigma_{source}^2 + \sigma_{PSF}^2 \quad (3.11)$$

As the actual extension of the VHE emission from the Crab Nebula is much smaller than the PSF [Atoyan and Aharonian, 1996; Aharonian *et al.*, 2000],  $\sigma$  can be used as measure for the angular resolution of the instrument and the analysis. In the following, the source region is defined as a circle with radius  $0.15^\circ$  around the fitted source position to include as many photonic events as possible while keeping the background at a manageable level. The resulting  $\alpha$ -factor, i.e. the ratio of the source region size to the background region size, is

$$\alpha = \frac{\Omega_{src}}{\Omega_{bg}} = 0.104. \quad (3.12)$$

For these parameters,  $229 \pm 15$  events are found in the source region (ON events), compared to  $138.8 \pm 3.8$  for a background region of the same size (OFF events). The excess amounts to  $90.2 \pm 19.2$  events, which

<sup>10</sup>With the correction, the systematic error of the telescope pointing is reduced to about 20 arcseconds per axis. With the more recent precision pointing [Acero *et al.*, 2010b] this can be reduced to 6 arcseconds.

	algorithm 1	Mixed algorithm	
$N_{on}$	$229 \pm 15$	$205 \pm 14$	
$N_{off}$	$1335 \pm 37$	$1324 \pm 36$	
$N_{off} \times \alpha$	$138.8 \pm 3.8$	$137.6 \pm 3.8$	all energies
Excess	$90.2 \pm 19.2$	$67.4 \pm 18.5$	
Significance	$6.59 \sigma$	$5.06 \sigma$	
$N_{on}$	$66 \pm 8$	$76 \pm 9$	
$N_{off}$	$410 \pm 20$	$431 \pm 21$	
$N_{off} \times \alpha$	$42.6 \pm 2.1$	$44.9 \pm 2.2$	$E > 3 \text{ TeV}$
Excess	$23.4 \pm 10.4$	$31.2 \pm 11.0$	
Significance	$3.13 \sigma$	$3.98 \sigma$	

Table 3.3: Event statistics for algorithm 1 and the mixed algorithm using sampling mode. The upper part contains all events above the energy threshold of these observations at about 0.8 TeV, the lower part events above 3 TeV. The  $\alpha$ -factor is about 0.104 for all cases.

gives a significance of the source detection of  $6.59 \sigma$  (following eq. 17 of Li and Ma [1983]). The results are summarised in table 3.3 and are used in the following as reference for the new time gradient analysis.

### 3.7.3 Sampling mode analysis with standard nominal distance cut

From the simulation results in section 3.5.1 a substantial improvement of the core position and direction reconstruction is expected from the use of the *mixed algorithm* for events with energies above a few TeV. While the improvement of the core position reconstruction cannot be checked easily in the observational data, the improvement of the direction reconstruction should manifest itself as a reduced extension of the source region.

For the whole dataset, no improvement is seen by the use of the mixed algorithm (see table 3.3, top right). Instead, the number of events in the source region is substantially reduced, while the background level is unchanged. The excess is reduced to  $67.4 \pm 18.5$ , the significance of the source detection to  $5.06 \sigma$ .

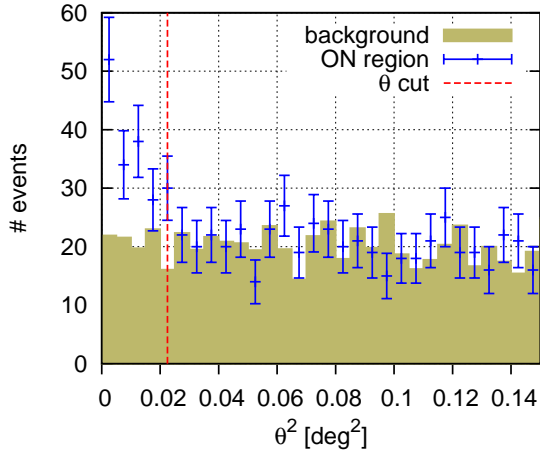
The case is different, however, if only events above 3 TeV are considered. In this case, the use of the mixed algorithm increases the number of excess events in the source region from  $23.4 \pm 10.4$  to  $31.2 \pm 11.0$  (see table 3.3, bottom). Although the low event statistics limit the significance of this result, it seems that the use of the additional sampling mode information has indeed improved the event statistics at higher energies.

To examine more closely the change of the angular resolution, the  $\theta^2$  distribution, i.e. the radial distribution of events around the test position, is shown in figure 3.30 for the different cases (see also section 3.2.4 for the definition of  $\theta$ ). In all cases the events around the source position show an excess at small  $\theta$ , while the background regions show flat distributions.

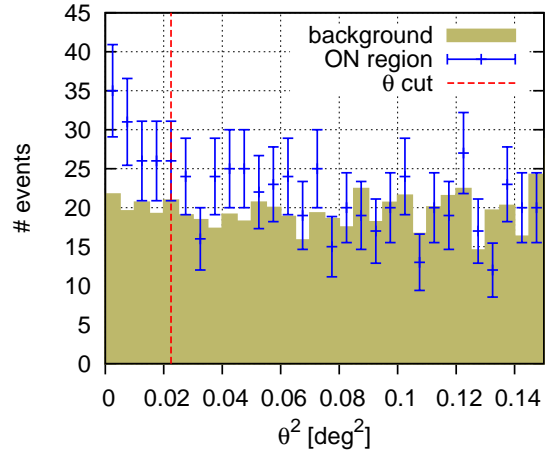
At energies below 3 TeV, the standard algorithm reconstructs almost the total excess at angles below the  $\theta^2$  cut of  $(0.15^\circ)^2$ . At larger angles, the signal and the background region show the same event numbers. As already indicated by the event numbers, the mixed algorithm performs considerably worse at these energies, and the excess is spread out up to about  $0.25^\circ$ . Simulations of gamma-ray events with energies below 1 TeV (not in the standard dataset) also show a deterioration of the angular resolution when using the mixed algorithm, however not to the same extent.

Figure 3.31 shows an example of an event in which the mixed algorithm produces a significantly worse result than algorithm 1. The time gradient from CT 3 estimates the core distance to about 210m, while no time gradient information from CT 4 is used as its time gradient predicts a distance below 200m. Since the core position (with either algorithm) is rather close to CT 4, the image axis of CT 4 is adjusted strongly (right). The adjusted axis leads to a new reconstructed direction (left), which is about  $1^\circ$  away from the

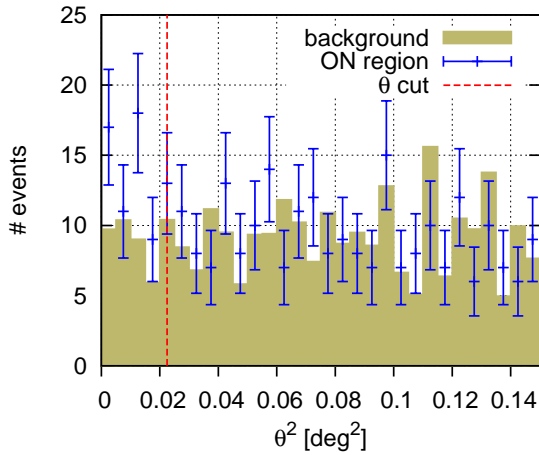
### 3 Sampling mode event reconstruction for the H.E.S.S. experiment



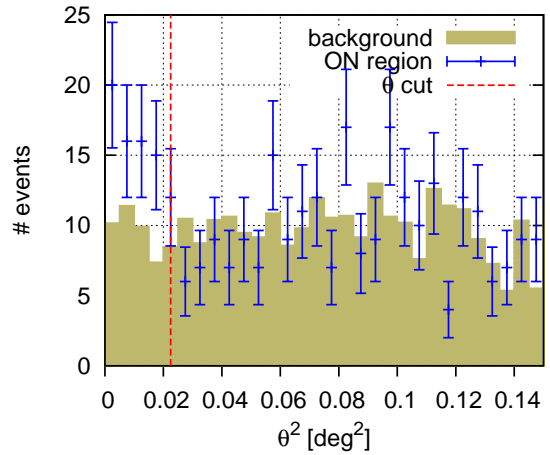
(a) Using algorithm 1,  $E < 3$  TeV



(b) Using mixed algorithm,  $E < 3$  TeV



(c) Using algorithm 1,  $E > 3$  TeV



(d) Using mixed algorithm,  $E > 3$  TeV

Figure 3.30: Radial count number distributions around a given test position (“ $\theta^2$  - plot“). The ON-region corresponds to the area around the best-fit position of the source. The upper panels show events with reconstructed energies below 3 TeV, the lower ones with energies above 3 TeV. The left column shows the result of the standard reconstruction (algorithm 1), the right one the results from the new sampling mode reconstruction (mixed algorithm). The vertical dashed line indicates the region which is used to derive the numbers in table 3.3.

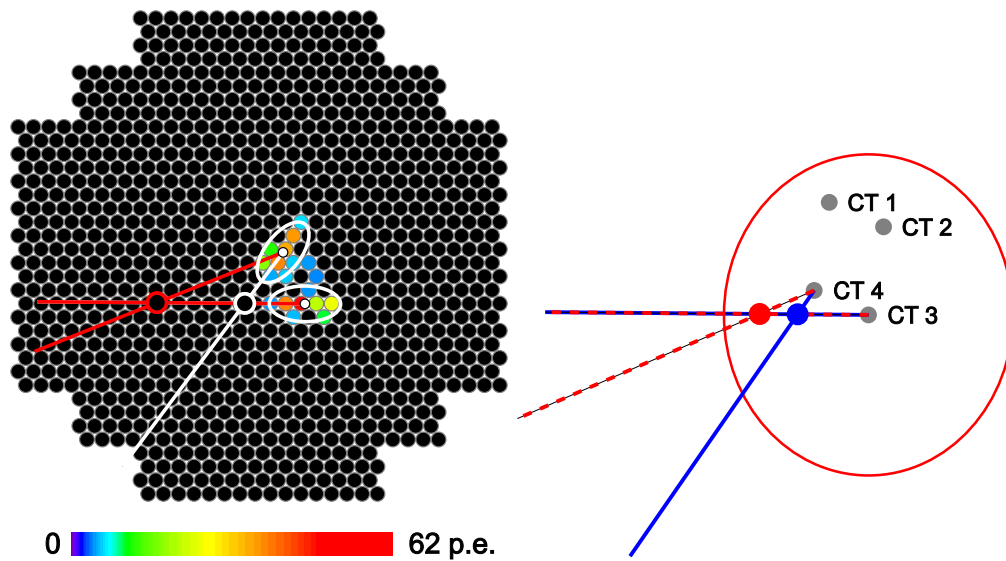


Figure 3.31: Example of an event with failed mixed algorithm reconstruction. *Right:* The time gradient prediction from CT 3 (red circle) is used to obtain a new core position (red point). The image axis of CT 4 is adjusted to the new core position (red dashed line). *Left:* The new axis of CT 4 shifts the reconstructed direction from the white circle to the red circle.

nominal source position. The previous direction by algorithm 1, on the other hand, is only  $0.09^\circ$  away from the source. While there is no way to know whether this actual event is really originating from the source direction, the example illustrates the limitation of the mixed algorithm: In some cases, when the time gradient is poorly defined and the core distance is small, it may reconstruct the direction significantly worse than algorithm 1. At low energies, where most events have small core distances and where the time gradient is defined, on average, with less accuracy, these events dominate and deteriorate the overall angular resolution. It is therefore recommendable not to use the mixed algorithm in its current form at lower energies.

At energies above 3 TeV, the mixed algorithm leads to a better concentration of events around the source position (see lower panels in figure 3.30), which explains the increased event numbers shown in table 3.3. This can also be illustrated by the significance of the source detection as function of the source region radius (figure 3.32). The mixed algorithm achieves its largest significance – close to  $4\sigma$  – around the nominal  $\theta^2$  cut of  $(0.15^\circ)^2$ . Algorithm 1, on the other hand, produces a flatter significance distribution, which reaches a plateau of a  $3\sigma$  significance between  $\theta = 0.13^\circ$  and  $\theta = 0.18^\circ$ .

In conclusion, the results from the analysis show – subject to large uncertainties caused by small event numbers – that using the sampling mode data with the introduced mixed algorithm can improve the angular resolution, and thus the significance of the source detection, at energies above about 3 TeV. This is consistent with the results from the simulations which indicated the largest improvement in angular resolution at low TeV energies. At lower energies, the standard algorithm 1 produces better results.

### 3.7.4 Sampling mode analysis with extended nominal distance cut

From the simulations presented in section 3.5.2 it is expected that the additional inclusion of telescope images with a nominal distance between  $2.0^\circ$  and  $2.3^\circ$  will significantly increase the number of events at energies above about 7 TeV (see also figure 3.20). At the same time, however, the angular resolution is expected to deteriorate by about a factor of 1.5 to 2, cancelling the positive effect of the new cut value. Only in the (almost) background free regime at the highest energies, the extended nominal distance cut can

### 3 Sampling mode event reconstruction for the H.E.S.S. experiment

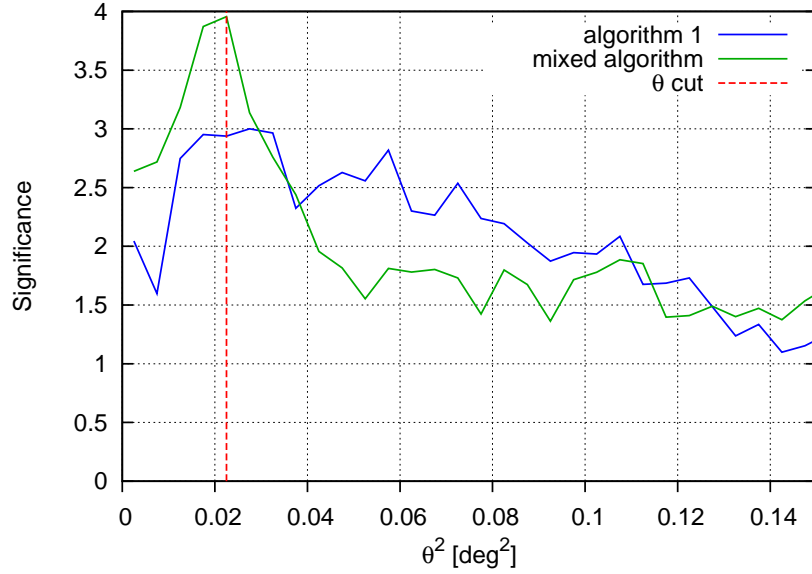


Figure 3.32: Significance of the source detection versus the selected source region radius for events above 3 TeV.

improve the analysis by the inclusion of more gamma events. However, the currently available amount of data is not sufficient for an investigation of the background free energy regime.

Nevertheless, the data can be used to test the expectation concerning the increase of event numbers in general. For this, the number of OFF-events, i.e. the number of events in the ring-shaped background region, is compared for the two values of the nominal distance cut. Figure 3.33 shows the ratio of events obtained with the new cut to the events obtained with the standard cut:

$$R = \frac{N(\text{nom. dist. cut} = 2.3)}{N(\text{nom. dist. cut} = 2.0)} \quad (3.13)$$

For comparison, the plot also shows the ratio of effective areas with the standard and the extended nominal distance cut<sup>11</sup>.

It can be seen that the new nominal distance cut leads indeed to an increase of event numbers, however not to the extent expected from the increase in effective area. The reason for this is the systematic underestimation of the energy of the additional events discussed in section 3.5.3. As a result, the event number of each energy bin is only increased by events with a higher (true) energy. Due to the steep energy spectrum of cosmic rays, considerably fewer events are added to the respective bin than expected from the increase in effective area. In conclusion this means that the increase of the nominal distance cut to 2.3° is only reasonable if the energy reconstruction for the additional events can be improved substantially.

For completeness, the excess event numbers have been calculated for the reconstruction with the larger nominal distance cut. As expected, the problems with the energy reconstruction and the deterioration of the angular resolution result in fewer excess events compared to the reconstruction with the standard nominal distance cut. The mixed algorithm is slightly superior to algorithm 1 in this case, too, as it shows an excess of  $25.10 \pm 11.00$  events, compared to only  $21.45 \pm 10.61$  events obtained with algorithm 1 ( $E > 3$  TeV). The significances are 3.18 and 2.81, respectively, considerably lower than with the standard nominal distance cut.

<sup>11</sup>Used here are effective areas for proton primaries with a camera offset of 0.5° (not from the standard dataset), to match the acceptance to the actual OFF events. The increase in effective area is slightly smaller here than for the gamma-ray dataset, but qualitatively similar.

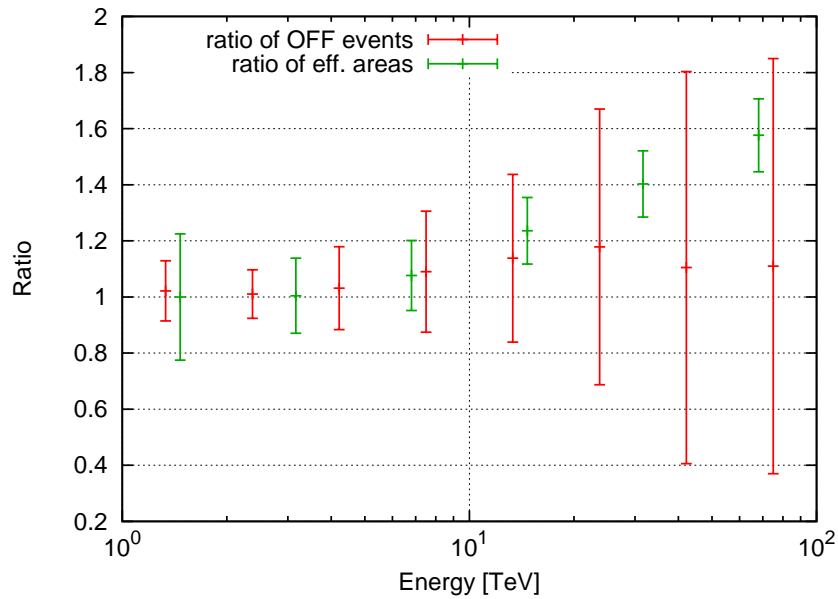


Figure 3.33: Spectrum of the ratio  $R$  of OFF-events for the two nominal distance cuts (see equation 3.13), compared with the increase of effective area (proton primaries, camera offset  $0.5^\circ$ ) expected from the simulations. The errorbars on  $R$  are obtained from the statistical uncertainties on the OFF-event numbers for both cases. However, since these numbers are strongly correlated, the actual errorbars should be much smaller.

### 3.8 Summary and Outlook

In this chapter the use of the sampling mode for the H.E.S.S. experiment has been investigated. The full pixel signal information available in sampling mode has been used to calculate the Cherenkov image time gradient along the Hillas axis, which turns out to be a useful predictor for the distance to the shower core position. Simulations and a newly developed event reconstruction algorithm have been used to evaluate the potential benefit of this additional information for the sensitivity of the experiment to gamma-ray sources. The results indicate that the greatest benefit is achieved at energies between about 3 TeV and 20 TeV. In this regime, using the sampling mode data can improve the accuracy of the core position and direction reconstruction by up to a factor of two compared to a standard algorithm 1 reconstruction.

In order to also improve the sensitivity at even higher energies where the main challenge is posed by the low event numbers, it was tried to relax the nominal distance cut and include events with truncated telescope images. The simulated effective areas indicate that this approach can indeed result in an increase of a factor of 1.5 in gamma-ray event numbers at energies above about 20 TeV. However, this comes at the price of a significantly deteriorated accuracy of the event reconstruction. Even with the sampling mode reconstruction, which is far superior to the standard reconstruction in handling truncated images, the angular resolution is deteriorated by about a factor of two in the relevant energy regime. Therefore, this approach seems only be promising for cases in which the background is no longer the limiting factor for the gamma observations, as it may be the case at multi-TeV energies depending on the gamma-ray flux and spectrum and the power of the gamma hadron separation. On the other hand, problems with the energy reconstruction impede the use of truncated images severely, and a better energy reconstruction algorithm is needed if these events are to be used.

With dedicated observations in late October 2009 it has been shown that the H.E.S.S. telescopes are able to record sampling mode data, which could subsequently be used successfully for a significant detection of the gamma-ray emission from the Crab Nebula. With this it was shown for the first time that a stereoscopic

### 3 Sampling mode event reconstruction for the H.E.S.S. experiment

event reconstruction using the time information of images is possible with data from the H.E.S.S. experiment. However, the increased data rate produced in sampling mode caused several problems with the data acquisition system that will need to be addressed prior to future sampling mode observations. Especially, the fractional dead time of the experiment has increased from about 5% to 35%, leading to the loss of a large number of events and thereby partially cancelling the benefits of the new event reconstruction.

The data gathered was used to examine the angular spread of the gamma-ray events at energies above 3 TeV. Although the event numbers are low and uncertainties large, the results seem to indicate that the benefit of the sampling mode reconstruction can be confirmed with real data when using the standard nominal distance cut. With an extended nominal distance cut, the results are worse than in the standard case, which agrees with the simulations.

At energies below 3 TeV, the time gradient analysis shows a worse performance than the standard algorithm 1, which means that it – in its current implementation – should not be used in that energy regime.

The algorithm used here for the core position and direction reconstruction is only a simple example of the many possibilities for sampling mode event reconstruction. Stamatescu *et al.* [2011] have shown that even algorithm 3, the best currently known algorithm for the direction reconstruction, can be improved by incorporating the time gradient as distance estimator. Also, the software used here for the analysis cannot compete with the standard H.E.S.S. software in terms of gamma hadron separation, energy reconstruction, pointing accuracy and other important aspects. If the use of the sampling mode analysis in H.E.S.S. should be pursued further, it would therefore be recommendable to implement the time gradient analysis in the standard software framework and to use it as distance estimator in the usual algorithm 3 reconstruction. As a first step, the DST maker would need to be expanded to calculate the correct pixel intensities for sampling mode data and to relay the pixel timing information to the DST level. Ideally, both hardware and software should be able to record data in sampling mode by default in order to make this additional information available for all observations.

With the upcoming inauguration of the large H.E.S.S. II telescope, which will essentially operate in single telescope mode at low energies, the time gradient analysis may become even more important. With no stereoscopic images are available, it may be the only reliable parameter to determine the core and source distance. Under similar circumstances, the time gradient proved a valuable addition to the standard reconstruction for the MAGIC experiment [Aliu *et al.*, 2009].

In conclusion it seems that modifications to the data analysis may indeed help to improve the performance of current instruments towards the ultra high energy regime. Ultimately, however, new instruments are needed for a detailed study of gamma-ray sources above a few 10 TeV. The following chapters of this thesis will introduce the concept of the H<sub>2</sub>SCORE detector, which can achieve an unprecedented sensitivity to gamma-ray sources in the ultra high energy regime.

## 4 The H<sub>i</sub>SCORE experiment

The aim of the H<sub>i</sub>SCORE project is to develop a gamma-ray detector with a very good sensitivity in the ultra high energy band (UHE, energies above 30 TeV, see also section 2.3.2) to open up this new window in high energy astronomy. Due to the very low photon flux in this energy regime a large effective area is needed, and the H<sub>i</sub>SCORE detector is designed with the goal to achieve an effective area of 10 km<sup>2</sup> up to 100 km<sup>2</sup>. On the other hand, each air shower event in this regime produces relatively strong Cherenkov light, so that the light sensitive area can be smaller than for detectors in the VHE regime. As a consequence, an array of wide-angle, non-imaging air Cherenkov detectors is proposed as the most suitable system.

A design study has been carried out to assess the possible performance of the detector, and the construction of a prototype detector station has started. Section 4.1 summarises the key scientific goals of the project and introduces the detector concept. Section 4.2 explains in some detail the mechanical, optical and electronic design of the individual stations. One critical point for a good performance of the detector is the time synchronisation between the individual stations — some ideas and possible concepts for this are outlined in section 4.3. A summary and outlook of the hardware development will be given in section 4.4. A detailed simulation of the detector, including an event reconstruction algorithm, and a calculation of the expected sensitivity will be presented in chapter 5.

### 4.1 Scientific goals and detector concept

**Goals** The primary goal of the H<sub>i</sub>SCORE detector project is the discovery and study of gamma-ray sources in the UHE regime. For this, a point source sensitivity at and below the level of current VHE gamma-ray observatories is needed. It will be shown in chapter 5 that the proposed detector concept is indeed capable of achieving this goal. As outlined in section 2.3.2, one of the most prominent open questions of high energy astrophysics, the origin of cosmic rays, may be solved by UHE gamma-ray observations. This leads to the acronym of H<sub>i</sub>SCORE: **H**undred **S**quare kilometre **C**osmic ray **O**Rigin **E**xplorer.

Due to the operating principle of the detector, it will also be sensitive to cosmic rays with energies between 100 TeV and 1 EeV. It can contribute to the existing picture of cosmic rays (see section 2.1) with new measurements of the spectrum, the anisotropy and the composition in this energy regime, which covers the very interesting region around the knee.

Additionally, some particle physics questions can be addressed indirectly using the cosmic ray and gamma-ray measurements. For example, the existence of hidden sector particles or axion-like particles can be probed as they would change the expected absorption of gamma photons in the UHE regime [Mirizzi and Montanino, 2009]. These and other scientific goals of the H<sub>i</sub>SCORE project are discussed in more detail in Tluczykont *et al.* [2011].

**Detector concept** H<sub>i</sub>SCORE will be a large area, wide-angle air Cherenkov detector. It will sample the Cherenkov light generated by extensive air showers induced by high energy gamma photons and cosmic rays. An illustration of the detection principle is shown in figure 4.1. Each detector station will contain four 20 cm (8 inch) photomultiplier tubes (PMTs) aligned towards zenith, equipped with Winston cone light concentrators to increase the light sensitive area to a total of 0.5 m<sup>2</sup> per station (see figure 4.2). The signals from the PMTs will be summed up, digitised by a fast readout system, and sent to a central computer cluster for further processing. If possible, the detector stations should work completely self-contained to avoid

#### 4 The $H_i$ SCORE experiment

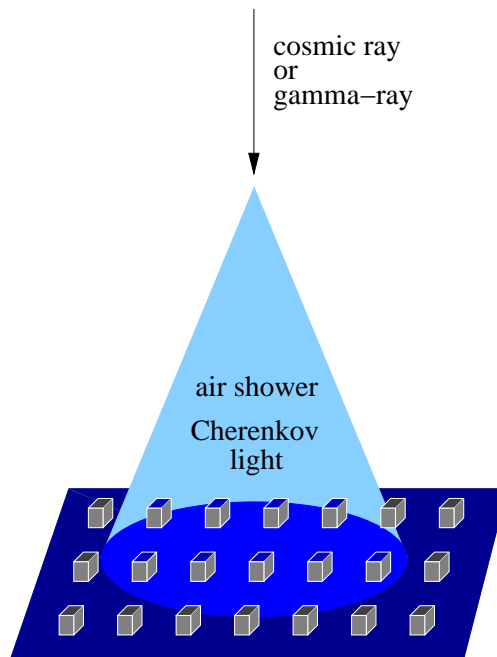


Figure 4.1: Illustration of the  $H_i$ SCORE detector: High energy particles interact with the atmosphere and create an air shower. The resulting Cherenkov light is measured by the detector array.

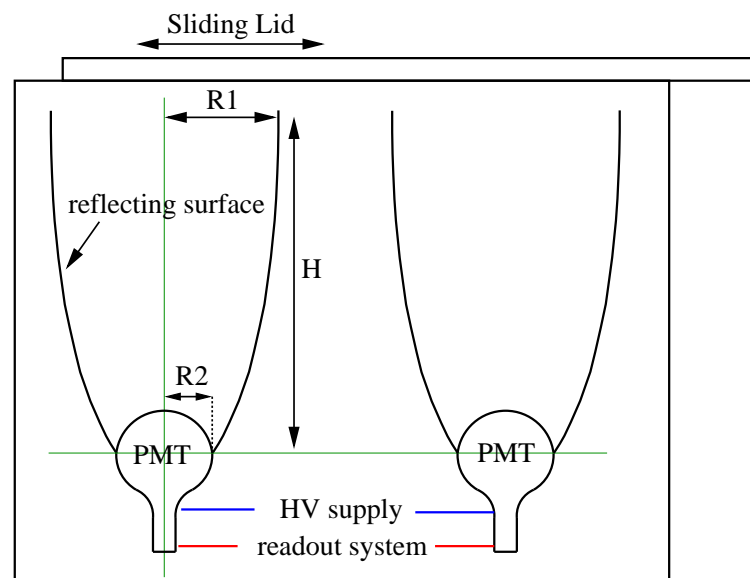


Figure 4.2: Illustration of the detector station. The dimensions are  $R_2 = 10$  cm (fixed by the size of the PMT),  $R_1 = 20$  cm and  $H = 52$  cm. The actual station will contain four channels instead of the depicted two.

expensive cabling, i.e. transmit and receive all data over a wireless network connection and generate their supply power independently, e.g. from solar cells.

The actual layout of the detector array is not yet fixed, but it is likely that it will be implemented as a non-regular grid with denser areas for a low energy threshold and areas with larger spacing to achieve the needed effective area. This can be accomplished either by several clusters of denser spacing scattered throughout the detector area or a denser core with a less dense area around (graded array). In general it will be tried to locate the stations as far apart from each other as possible, to enable a cost-effective instrumentation of a very large area. In order to minimise problems with only partially contained events, the array will have a circular shape. However, for simplicity the current simulations assume a regular grid with an inter-station distance of 150m, and with a square perimeter (see chapter 5).

## 4.2 Development of a detector station prototype

As part of the presented design study for the H<sub>i</sub>SCORE detector, two prototype detector stations have been developed and tested: The first station contains only one channel and was used to test the details of the Winston cone construction, the lid control and the weather resistance. With the experience gathered from this station, a second prototype with two channels was designed and constructed. In the following, the envisaged design of the final detector station will be described on basis of this second prototype. In subsection 4.2.1 the mechanical set-up is described. A special part of this, the Winston Cone, is considered in more detail in subsection 4.2.2. The electronic set-up of the station, including slow-control, high-voltage generation and signal processing, is outlined in subsection 4.2.3.

### 4.2.1 Mechanical set-up

The key design goals of the detector station are an inexpensive construction, high durability in harsh environments and reliability of the moving parts. The casing needs to protect the PMTs, Winston Cones and electronics from rain, snow and dust, maintain a tolerable temperature for all sensitive parts, and keep out the light during the day to protect the PMTs. Aluminium was chosen to be the best construction material in terms of durability, weight and workability. The main structure of the box is made entirely of standard angle profiles of 30 mm × 30 mm × 3 mm in order to reduce costs. The station is closed on all four sides by 1 mm sheet aluminium, on the bottom by a 3 mm plate. The top is sealed with a plexiglass lid and an additional, movable aluminium lid which will be opened during operation. The second prototype station has a base area of 500 mm × 1000 mm and a height of about 900 mm.

The main purposes of the plexiglass lid are to keep off dust and to maintain the desired temperature inside of the box during operation. Plexiglas GS 2458 at 3 mm was chosen as material for this, as it has a high transmittance at short wavelengths, which is important for the measurement of Cherenkov light. The transmission given in the datasheet [Evonik Industries, 2000] was cross-checked with a Lambda 800 UV/VIS spectrometer by Perkin Elmer, with consistent results. Figure 4.3 shows the transmission spectra from the datasheet and the measurement in relation to the Cherenkov light spectrum expected at the detector (after atmospheric absorption). The cut-off occurs at sufficiently short wavelengths in order to keep most of the Cherenkov light. The effective transmission between  $\lambda_1 = 250$  nm and  $\lambda_2 = 700$  nm is

$$T_{eff} = \frac{\int_{\lambda_1}^{\lambda_2} d\lambda T(\lambda) I(\lambda)}{\int_{\lambda_1}^{\lambda_2} d\lambda I(\lambda)} \approx 86\% \quad (4.1)$$

using the transmission  $T(\lambda)$  and Cherenkov spectrum  $I(\lambda)$ .

For the movable aluminium lid, a horizontal opening mechanism was decided to be the most reliable, especially in the view of potential snow cover. The lid itself is made from 3 mm aluminium and mounted using a pair of standard drawer slides in the first prototype. In the second prototype the drawer slides were

#### 4 The $H_i$ SCORE experiment

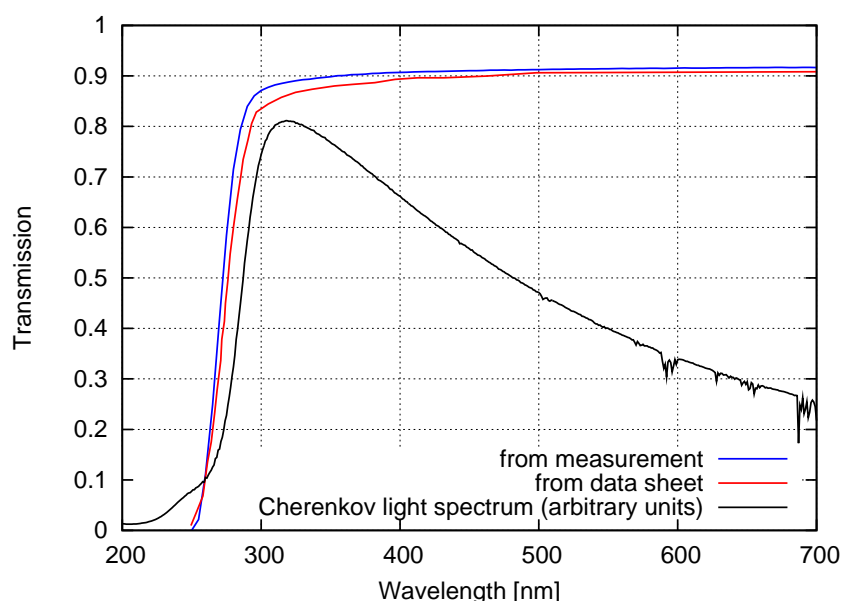


Figure 4.3: Transmission spectrum of Plexiglas GS 2458 from datasheet [Evonik Industries, 2000] and from own measurement. For reference, a typical Cherenkov light spectrum after atmospheric absorption is shown as well.

replaced by a custom-made sliding mechanism resting on a series of small plastic wheels for better durability and easier motion. Brushes and rubber lips are used to seal the box against stray light (which may damage the PMTs even when they are switched off) and water. The lid is opened by a drive motor via a rope system, and closed by the pull of two weights. Currently, it is kept open by the friction of the motor gear, and the motor needs to unwind the rope in order to close the lid. However, it is also possible to upgrade to a power failsafe system by using a stepper motor which only holds the lid open as long as it is supplied with power. Such an inherently safe system will be important for a large array in order to reliably protect the PMTs from sunlight, as it may not be possible to close the lid of a remote station manually in time in case of a malfunction. Care must be taken, however, to avoid problems with the PMT operation due to the magnetic field generated by the stepper motor. To that end, it may be necessary to install additional electromagnetic shielding around the motor and / or the PMT. A shielding of the PMT may be necessary in any case to avoid problems with the geomagnetic field<sup>1</sup>.

In order to control the lid remotely, sensors for the lid position are needed. Currently, two reed contacts are used at either end to signal if the lid is fully closed or opened. For safety, a second independent system to monitor the lid position would be desirable for the final set-up. One possibility would be a multi-turn potentiometer that is turned by the motion of the lid — such a system could also give information about the exact position of the lid between its final states, and might be useful to diagnose problems remotely. Another option might be monitoring the current drawn by the motor. In any case, care must be taken to make sure that the motor is switched off in time even in the case of problems.

In order to prevent ice coverage of the plexiglass lid and Winston cone surfaces, the box is warmed by a heating wire. This is especially important for the first tests, which will take place at the TUNKA site in Siberia (see also section 6.2.2). At other sites, no heating may be necessary, especially since some electronic

<sup>1</sup>The efficiency of the PMTs that will be used (at least) for the first stage of the project (ET 9352 KB, see section 4.2.3) decreases by about 50% in a magnetic field of  $0.4 \times 10^{-4}$  T (see datasheet in appendix E). This is about one order of magnitude above the strength of the geomagnetic field [NOAA, 2005].

## 4.2 Development of a detector station prototype



Figure 4.4: The second prototype for a H<sub>i</sub>SCORE detector station. The left picture shows the station from outside, including the lid mounting. The right picture shows the inside of the station with the two Winston cones (the right cone is temporarily shielded with black paper for tests) and the PMTs.

components dissipate a non-negligible amount of heat.

The second prototype of the H<sub>i</sub>SCORE station is shown in figure 4.4. On the left side, the box is shown from outside, illustrating the lid mounting system. The right hand picture shows the station interior, which already contains the Winston cones and PMTs. The slow control board (white box) is already connected for tests, but not yet installed permanently.

### 4.2.2 The Winston cone light concentrator

**Mathematical description** One of the key parts of the mechanical set-up is the Winston cone light concentrator. It has two principle functions: To increase the light sensitive area of the PMT and to restrict the field of view in order to reduce the noise by night sky brightness. The Winston cone shape is optimised to collect as much light as possible at angles below the cut-off angle  $\Theta$  and to exhibit a steep cut-off in the angular transmission [Winston, 1970]. The cut-off angle depends on the desired increase of the light sensitive area, i.e. on the ratio of the upper and lower opening  $R_1$  and  $R_2$  (see figure 4.2):

$$\sin \Theta = \frac{R_2}{R_1} \quad (4.2)$$

When using a ratio of diameters of two, i.e. an increase of the light sensitive area by a factor of four, the critical angle is  $\Theta = 30^\circ$ . The values for the radii are then  $R_2 = 10\text{cm}$  (fixed by the PMT diameter) and  $R_1 = 20\text{cm}$ . The height of the cone is given by

$$H = \frac{R_1 + R_2}{\tan \Theta} \quad (4.3)$$

which results to  $H = 52\text{cm}$  in the described case.

The Winston cone curvature can be described in cylindrical coordinates by giving its radius  $\rho$  at the height  $z$  [Jordan and Krennrich, 2004]:

$$\rho(z) = \frac{-a_1 + \sqrt{a_1^2 - 4a_2a_0}}{2a_2} - R_2 \quad (4.4)$$

#### 4 The $H_i$ SCORE experiment

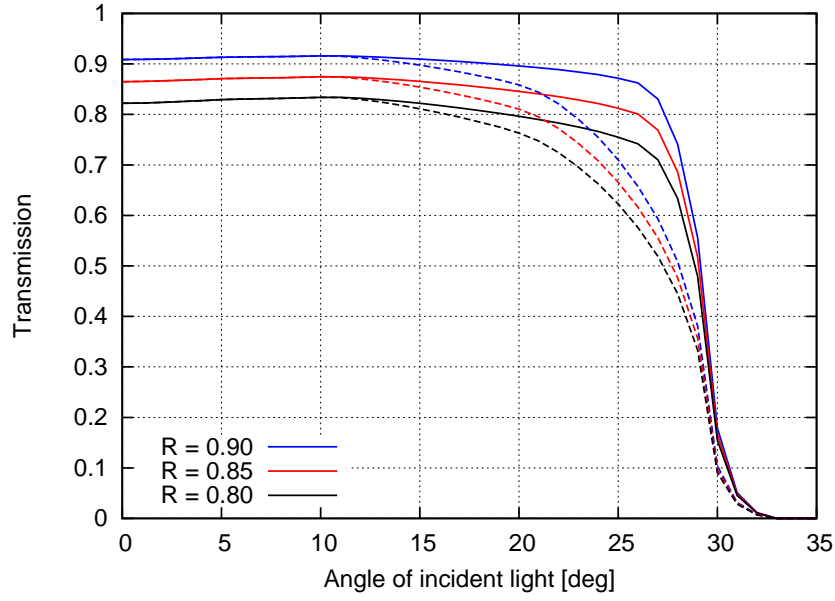


Figure 4.5: Transmission of the Winston cone depending on the angle of the incident light for different reflectivities  $R$  of the inner cone surface. Solid lines: All light at the bottom is counted; dashed lines: light with an angle greater than  $70^\circ$  (with respect to zenith) at the bottom is not counted, showing the effect of the angular acceptance of the PMT.

with

$$\begin{aligned}
 a_2 &= \cos^2(\Theta) \\
 a_1 &= 2z \sin(\Theta) \cos(\Theta) + 4f \sin(\Theta) \\
 a_0 &= z^2 \sin^2(\Theta) - 4f(z \cos(\Theta) + f) \\
 f &= R_2 \cdot (1 + \sin(\Theta))
 \end{aligned}$$

**Ray tracing simulation** A ray tracing algorithm is used to characterise the Winston cones. For each angle of incident light,  $10^5$  parallel light rays are scattered uniformly across the upper opening and propagated through the cone. The intensity of a light ray is reduced at each reflection on the inner cone surface, with the reflectivity set at a constant value, independent of wavelength and angle<sup>2</sup>. The normalised intensity of the light rays at the bottom of the cone is recorded and used to obtain the angular acceptance of the cone and the spatial and angular distribution of the light at the bottom, i.e. at the PMT. All results shown here are for ideal Winston cones and a flat surface at the lower end of the cone (rather than a spherical PMT surface).

Figure 4.5 shows the angular acceptance of the Winston cone for different values of the reflectivity of the inner cone surface. For Cherenkov light, a reflectivity between 80% and 90% seems to be realistic (see below). For the solid lines, the PMT is assumed to have no variation in its angular acceptance, so that all light up to  $90^\circ$  is detected with the same efficiency. In that case, a rather sharp cut-off appears around  $27^\circ$  to  $29^\circ$ , consistent with the expectation from equation 4.2. Up to  $25^\circ$  the acceptance changes less than 10%.

<sup>2</sup>The wavelength can be safely ignored as the used reflectivity is an effective value calculated using a typical Cherenkov light spectrum (see “mechanical construction” below). Ignoring the angle, on the other hand, may introduce a slight error as the angles in the individual reflections are not distributed uniformly. In this sense, the obtained values are conservative, since the reflectivity for perpendicular light is used, which is smaller than the one for larger angles. However, given the already large value of the reflectivity, the overall transmission is not expected to be affected strongly by this effect.

#### 4.2 Development of a detector station prototype

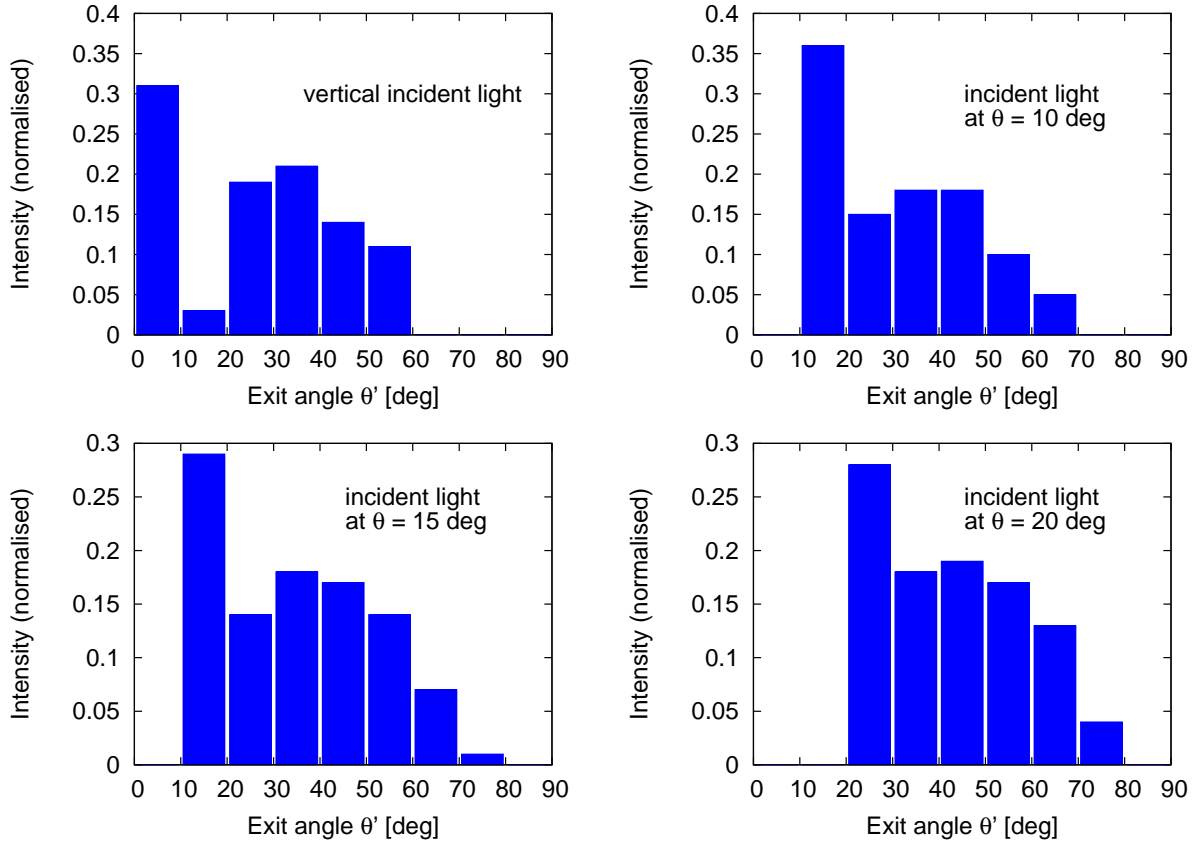


Figure 4.6: Angular distribution of light at the bottom of the Winston cone for various incident angles.

The dashed lines show the acceptance for the case that the PMT can detect light only up to  $70^\circ$ , as a rather extreme scenario for a non-uniform PMT acceptance. While the instrument acceptance remains similar up to about  $15^\circ$ , it decreases faster and has a less pronounced cut-off. At  $25^\circ$ , about 20% less light is detected compared to the first case. As soon as the angular acceptance of the PMT is known, it can be incorporated into the ray tracing algorithm in order to obtain a more realistic angular acceptance of the detector system.

The effective solid angle of the Winston cone can be calculated from the angular acceptance  $\varepsilon(\theta)$  by

$$\Omega = 2\pi \int \varepsilon(\theta) \cos(\theta) \sin(\theta) d\theta \quad (4.5)$$

In this equation the additional cosine function (as compared to the usual solid angle calculation) is needed to take into account the reduced effective area of the upper cone opening for light at an incident angle  $\theta$ . Using the angular acceptance for a reflectivity of 80% and a uniform PMT acceptance, the effective solid angle becomes

$$\Omega = 0.59 \text{ sr} \quad (4.6)$$

It should be emphasised that this  $\Omega$  is not identical to the solid angle of the H<sub>i</sub>SCORE detector for air shower events, which depends on the angular cut-off defined in the event reconstruction and analysis. It turns out, however, that by coincidence the solid angle for air shower observations is also 0.59 sr for the standard zenith angle cut on  $25^\circ$  (see also section 5.4).

To characterise the properties of the cone further, the angle and position of the light at the lower end are recorded. Figure 4.6 shows the angular distribution of the light at the bottom of the cone (given by the angle between the arriving light ray and zenith,  $\theta'$ ) for various incident angles  $\theta$ . Due to the shape of the

#### 4 The $H_i$ SCORE experiment

Winston cone, the angle of light rays increases at each reflection. Therefore, no light is detected with angles smaller than the incident angle. The average angle of light rays is larger after the passage through the cone, which agrees to Liouville's theorem that demands the conservation of phase space: The smaller the *area* onto which the rays are concentrated, the larger the *angular* phase space must become.

At all incident angles, a substantial fraction of the light passes through the cone without reflection and change of angle. Almost all light reaches the lower end of the cone at angles below  $70^\circ$  up to incident angles of  $20^\circ$ , which is consistent with figure 4.5.

Figure 4.7 shows the distribution of light at the bottom of the Winston cone for the same four incident angles. The light is usually concentrated on one half of the PMT, and the highest light concentration is generally within the inner 7 cm. This is important as measurements show that the acceptance of the PMTs foreseen for the experiment (see also section 4.2.3) is decreasing significantly towards the edge of the photocathode [Nachtigall, 2011; Einhaus, 2012].

Since the signal duration will be an important parameter in the event reconstruction, the time spread induced by different light path lengths in the Winston cone needs to be known. The simulations show that for vertical incident light the path length varies between 52 and 55 cm, and for light at  $30^\circ$ , the most extreme case, between 60 and 80 cm. Hence even in the worst case the light paths differ by no more than 20 cm, which increases the signal duration by less than 1 ns in one Winston cone. An additional effect comes from adding up the signals of the four Winston cones, whose most distant parts will be about 1 m from each other. At  $30^\circ$ , the difference in arrival times can be up to 2 ns, which results in a total extension of 3 ns in the worst case. This is included in the simulations.

**Mechanical construction** The Winston cone for the prototype station is constructed from ten blades of 0.5 mm aluminium mounted like a barrel (see figure 4.4). A special coating, commercially available as ALANOD<sup>3</sup> 4300UP, is used to ensure a high reflectivity especially at short wavelengths and a high durability (see also datasheet in appendix E). The wavelength dependent reflectivity has been measured with the Lambda 800 UV/VIS spectrometer. Since this device is designed only for transmission measurements, a set-up of four small mirrors of the material has been used to construct a light path between the light source and the detector of the spectrometer (see figure 4.8). The reflectivity of the material  $R$  is estimated from the transmission  $T$  by  $R = \sqrt[4]{T}$ . It should be noted that this measurement gives only the transmission at  $45^\circ$ , which should be slightly higher than the reflectivity for perpendicular light. On the other hand, the measured reflectivity may be lower than the actual one as some of the reflected light (especially the diffuse component) may not be registered by the relatively small detector in the spectrometer. Nevertheless, the results are in reasonable agreement with the data given by the manufacturer (see figure 4.9). The cut-off occurs at sufficiently short wavelengths in order to keep most of the Cherenkov light signal. The effective reflectivity over the whole wavelength range of the shown Cherenkov spectrum is 83% for the measured reflectivities and 81% reflectivity for the spectrum from the datasheet. For the simulations a value of 80% is used as a conservative estimate. With this reflectivity, the Winston cone transmits between 75% and 83% of the light, depending on the incident angle (see also figure 4.5).

The shape of an ideal Winston cone is reasonably well approximated by the ten aluminium blades. Nevertheless, the exact properties of the cone, especially the light distribution at the lower end, may differ slightly. The impact on the overall reflectivity and the angular distribution, however, is expected to be small: In the simulation most light rays are reflected only once before arriving at the lower end, which should not change substantially by the non-ideal approximation, resulting in the same value for the transmission. Also, other experiments have good experience with segmented Winston cones, e.g. hexagonal cones are used successfully in the camera of the H.E.S.S. telescopes [Bernlöhr *et al.*, 2003].

---

<sup>3</sup>ALANOD Aluminium-Veredlung GmbH & Co. KG, Egerstrasse 12, 58256 Ennepetal, [www.alanod.de](http://www.alanod.de)

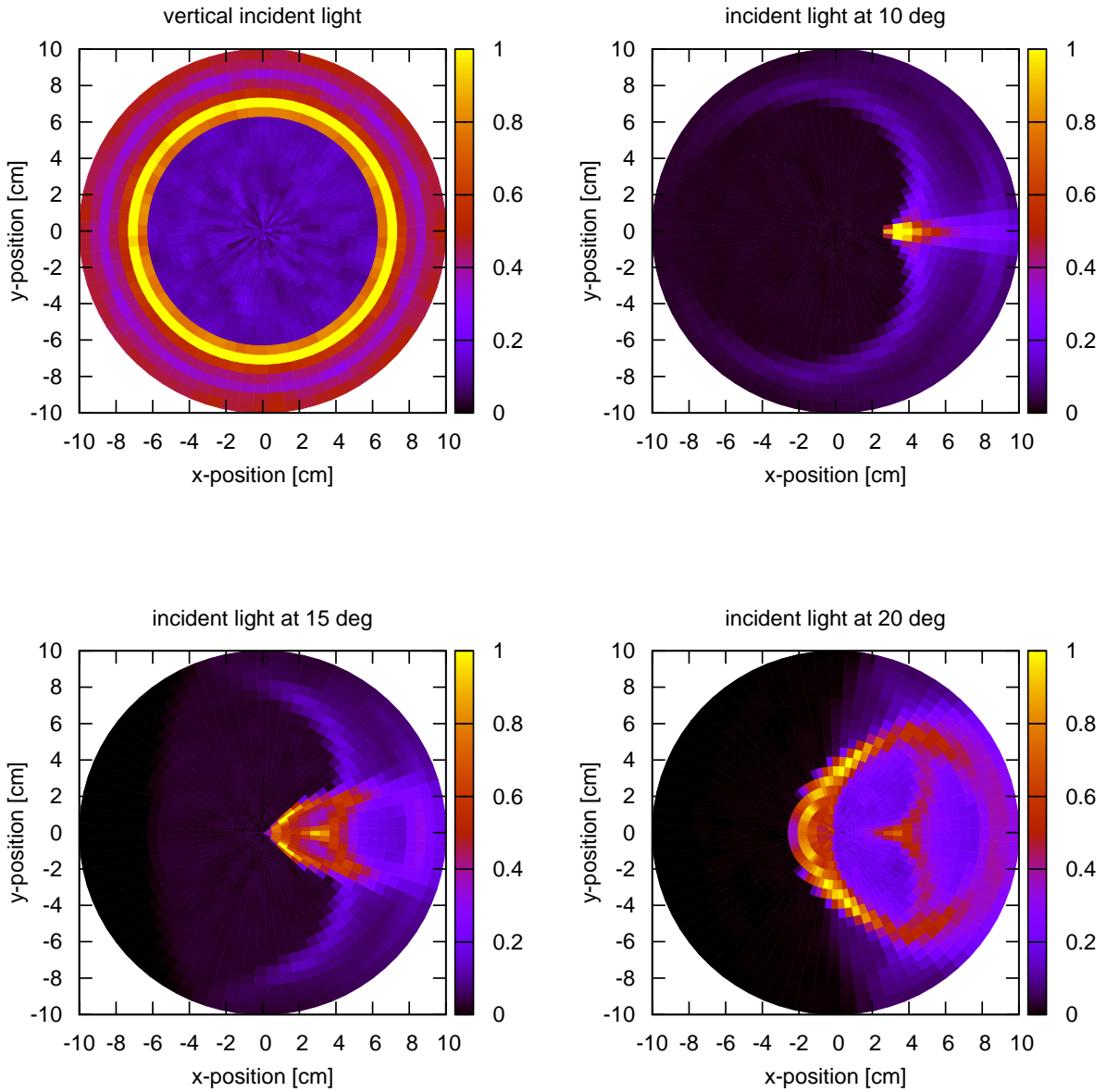


Figure 4.7: Intensity distribution of light at the bottom of the Winston cone for various incident angles. For angles  $> 0$ , the light arrives from the left side. The intensity is given by a relative colour scale.

#### 4 The $H_i$ SCORE experiment

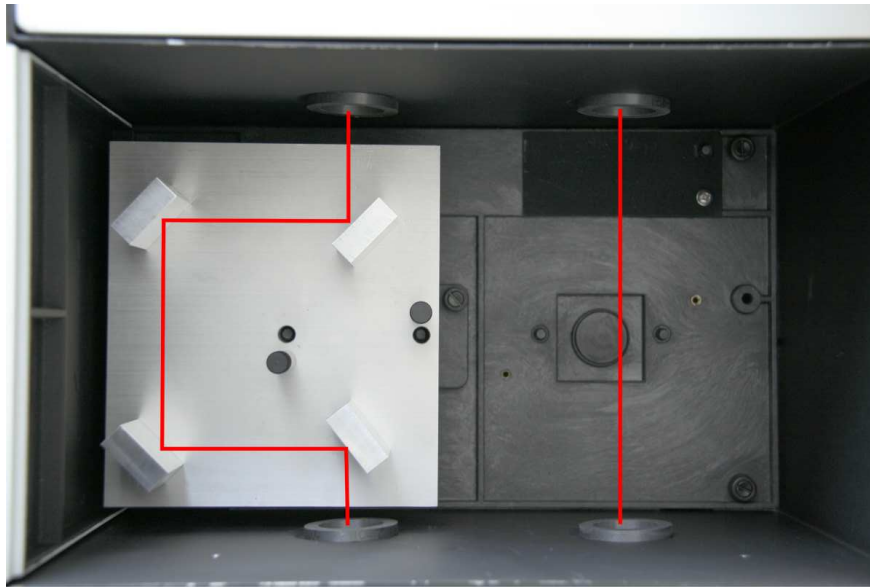


Figure 4.8: Reflectivity measurement of the ALANOD 4300UP aluminium used for the inner surface of the Winston cones. Since the spectrometer is designed for transmission measurements, a set-up with four small mirrors was used. The light paths of the reference beam (right) and the measurement (left) are indicated by red lines. The light source of the spectrometer is on the top, the detector on the bottom. The results of the measurement are shown in figure 4.9 (Picture by Joachim Ebert).

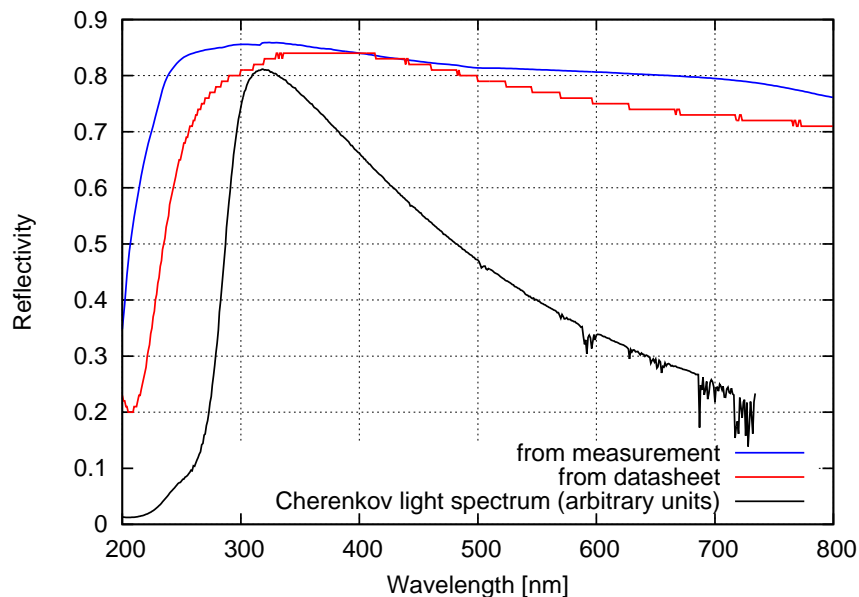


Figure 4.9: Reflectivity spectrum of Alanod 4300 UP from datasheet [ALANOD customer service, 2009] and from own measurement. For reference, a typical Cherenkov light spectrum after atmospheric absorption is shown as well.

Manufacturer	Model	Diameter [cm]	Dynodes	Gain	PMTs needed
Hamamatsu	R5912	20.2	10	$10^7$	4
Hamamatsu	R7081	25.3	10	$10^7$	2-3
Hamamatsu	R8055	33.2	11	$5 \times 10^7$	1-2
Hamamatsu	R3600	50.8	10	$10^7$	1
Electron Tubes	ET9352KB	20.6	6	$10^4$	4

Table 4.1: Possible photomultiplier candidates for the  $H_i$ SCORE detector. The column *PMTs needed* gives the number of PMTs needed to cover an area of  $0.125\text{ m}^2$ , which results in a total light sensitive area of  $0.5\text{ m}^2$  if Winston cones with a 2:1 diameter ratio are used.

### 4.2.3 Electronic set-up

**Photomultipliers** The key component of the detector station are the photomultiplier tubes. In order to achieve a sufficient light sensitive area with only a few channels, large spherical PMTs are needed. Several possible candidates have been identified, their properties are summarised in table 4.1.

While Hamamatsu offers a range of different interesting models, all of them have a gain of at least  $10^7$ . This may be problematic, since it is expected that the night sky brightness will induce a flux of up to 29 photoelectrons per nanosecond at the PMT cathode (see section 6.4.4). With a gain of  $10^7$ , this results in  $2.9 \times 10^{17}$  p.e. per second at the anode, equivalent to a current of 46 mA, which exceeds the maximum anode current given by the manufacturer of 0.1 mA by more than two orders of magnitude. Nevertheless, it may be possible to use the Hamamatsu PMTs, if they are operated at a significantly lower voltage (and therefore gain), or if only the first six or seven dynodes are used. Additionally, discussions about the possibility for the development of a six-stage, low gain PMT are underway with representatives of Hamamatsu.

On the other hand, the ET9352KB by Electron Tubes was developed originally for the AIROBICC experiment and seems to be ideally suited for the needs of the  $H_i$ SCORE experiment, therefore it was used for the prototype development and the simulations. The datasheet of this PMT can be found in appendix E, and a study of the characteristics of these PMTs with a focus on their applicability in  $H_i$ SCORE was done by Nachtigall [2011].

**High voltage supply** Figure 4.10 shows the basic layout of the signal and trigger chain in the detector station. The custom-made high voltage supply board PHQ9352 by ISEG is used to power the PMTs (see datasheet in appendix E). The high voltage is generated locally from a 12 V supply and can be adjusted via a 0-5 V control voltage. The actual high voltage and the total current through the PMT are mapped to 0-5 V monitor outputs. The supply board is controlled with an Arduino micro-controller and a small Guru PlugPC, that is also used for other slow control tasks in the detector station (see below).

**Signal amplification and dynamic range** The PHQ9352 provides connections to the PMT anode and the last but one dynode, thus offering the possibility to read out the signals at two different gains, making it easier to cover a large dynamic range. The difference between the two signals can also be used to calculate the gain of the PMT [Nachtigall, 2011], which allows a simple automatic monitoring and adjustment of the PMT gains. The high and low gain signals of all four PMTs in a station are added up separately and digitised by two channels of the DRS 4 readout board.

It is currently foreseen to set the trigger threshold to a signal strength of around 180 photoelectrons (see section 5.2). At a gain of  $10^4$ , this produces a charge of

$$C = 2.9 \times 10^{-13} \text{ C} \quad (4.7)$$

#### 4 The $H_i$ SCORE experiment

This charge is drained by a standard  $50\Omega$  termination resistor in the preamplifier circuit. Assuming a pulse duration of about 10ns, it produces a current of about  $2.9 \times 10^{-5}$  A, which in turn leads to a voltage of about 1.4mV. To produce a usable signal in the readout board, a preamplification by about a factor of 10 is needed in the high gain channel. As the maximum voltage that can be measured by the DRS 4 board is 1 V, the maximum signal strength that can be processed by the high gain channel amounts to about 12,000 photoelectrons (giving an effective dynamic range of about 70).

To ensure a sufficient overlap between the channels, the low gain channel should be adjusted to be about 50 times weaker than the high gain channel. This can be accomplished in two ways: First, the output from the PMT anode could be attenuated, e.g. by a simple voltage divider, by about a factor of five. Using a potentiometer in the voltage divider would make it possible to fine-tune the signal to the needed level. Second, the dynode output of the PMT base may be used without amplification or attenuation. Assuming a PMT gain of  $10^4$  and a constant amplification factor at each PMT stage, the signal should be about seven times weaker at the dynode than at the anode, roughly at the required level for the low gain channel.

At higher energies, the central detector station records about 1000 p.e./100TeV, which means that all signals can be sampled using the high gain channel up to energies of about 1PeV. With the use of the low gain channel, energies up to about 50PeV can be measured without exceeding the dynamic range of the readout system. For the rare case of a higher energy event (see also section 5.6.3 for the expected event rates), the event reconstruction may still be possible to some extent, as all needed quantities may be extracted from detector stations further away from the shower core. Additionally, a third gain channel may be used for recording the signals from very high energy events (not foreseen in the current design).

**Signal readout and digitisation** The DRS 4 evaluation board<sup>4</sup> offers an easy-to-use interface between the analogue signals and a computer. It features four inputs that can record signals with an analogue bandwidth of 700MHz and a sampling frequency of up to 5GHz. The signals are transferred to the computer via a USB2.0 interface and can be saved and processed using the C++ API library provided along with the board. Currently it is foreseen to use two channels for signal recording (high and low gain of summed signals) and to operate the DRS board at 1GHz. The other two channels may be used for time synchronisation (see section 4.3) or, if the time synchronisation uses only one channel, for an additional third gain channel to increase the dynamic range.

The DRS 4 board is controlled using a Guru PlugPC with Debian Linux. The PlugPC offers two USB connectors, ethernet and wireless network connections. The signals are stored temporarily on the internal memory and sent to a central computer cluster over a wireless link. The software for this is under development, some first tests are described in Eichler [2011]. The maximum data rate achieved so far is 80Hz, however an increase in this seems possible with the newest version of the DRS firmware and API [Ritt, 2011]. A reduction of the data volume, and therefore an increase in possible event rate, could also be achieved by selecting a region of interest around the trigger. In standard mode the DRS 4 board transfers the content of all 1024 data cells of a channel, which corresponds to 1  $\mu$ s, almost eight times longer than the longest signals expected from Cherenkov flashes (see section 5.4.1).

**Trigger scheme** The local station trigger is generated using a clipped sum system, similar to the sum trigger used for low threshold observations with the MAGIC Cherenkov telescope system [Aliu *et al.*, 2008]: The signals of the four channels are clipped at a certain level before being added up. The sum signal generates a trigger if it is found to be above the trigger threshold by the comparator for a certain duration, typically less than 10ns (in the simulations, 7ns are assumed). The clipping level must be at least one fourth of the threshold level and should be no greater than one third, ensuring that all channels contain at least some signal. The trigger is supplied to the DRS 4 board in TTL standard.

---

<sup>4</sup>Domino ring sampler, developed by the Paul Scherrer Institute, see <http://drs.web.psi.ch/>

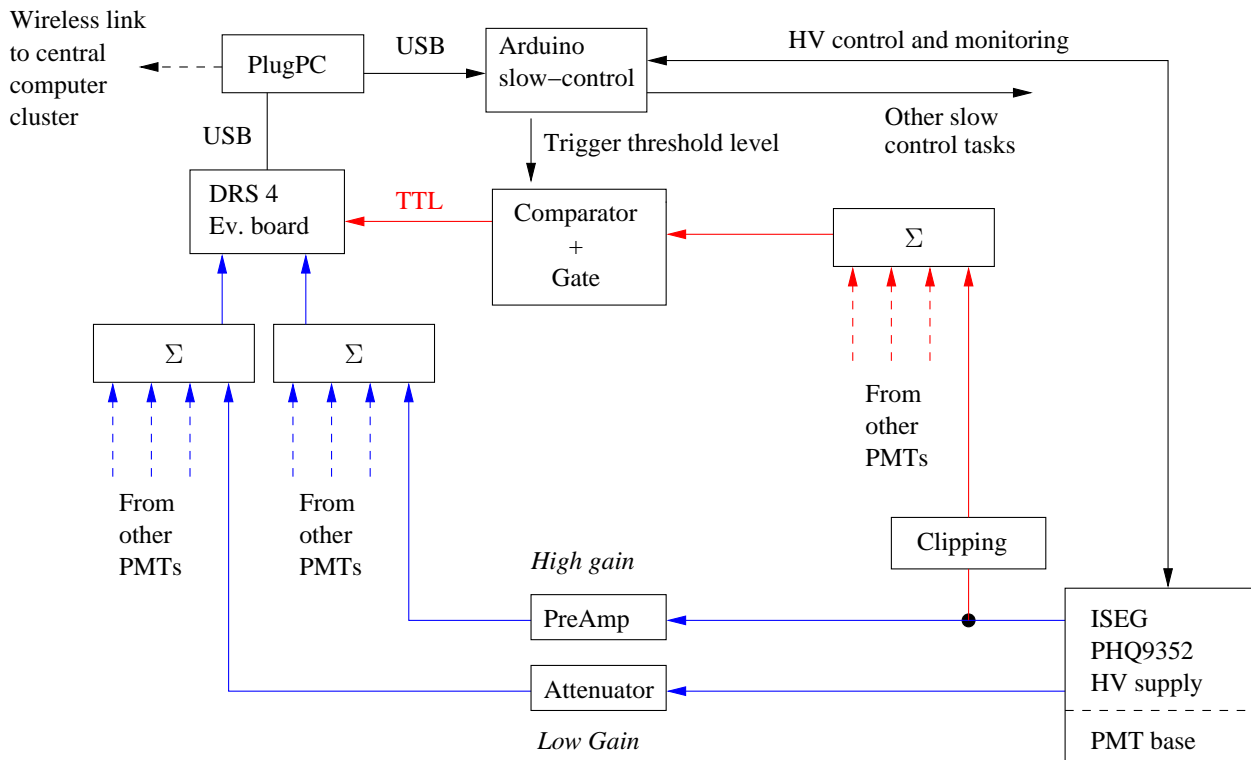


Figure 4.10: Schematic of the signal (blue) and trigger (red) chains.

A clipped sum trigger is better suited for the detection of small signals in noise than a simple coincidence of the four channels or a standard sum trigger. Small signals that appear in all four channels are reliably detected, while large fluctuations or afterpulses in individual channels are discarded. Figure 4.11 illustrates the working principle of the three trigger systems (only two inputs are shown for simplicity), and reveals the particular strength of the clipped sum system: It can correctly identify a weak signal where one channel is slightly below the trigger threshold (middle column, red) while at the same time it rejects a false event that produces a large signal only in one channel (right column, green). It is therefore the best choice for the  $H_i$ SCORE detector that will need to have a low light threshold in order to keep the energy threshold low, while at the same time it is especially vulnerable to many false triggers due to the high light flux from night sky brightness. The false trigger rates due to night sky brightness have been simulated for the three possible trigger systems, and as expected the clipped sum trigger suffers significantly less from false triggers than a standard sum trigger system (see section 5.2).

Care must be taken to use only fast components with a bandwidth of at least in the order of 1 GHz in the whole set-up, in order to keep the impact on the time structure of the signals as small as possible. The electronic set-up of the signal and trigger chains is described in more detail in Kunnas [2012].

**Slow control** Apart from the signal electronics the detector station also contains a slow-control system that is used to remotely control the station lid, measure environmental parameters like the light level outside and the temperature inside of the casing, to control the heating, to set and control the high voltage at the PMTs, set the trigger level and other similar tasks. An Arduino micro-controller board<sup>5</sup> is used for the interface between the slow control software (on the PlugPC) and the electronic and mechanical components. The Arduino board features 54 digital input/output ports, of which 14 can be used as analogue outputs via

<sup>5</sup>Arduino Mega, using the ATmega2560 micro-controller, see <http://www.arduino.cc/>

#### 4 The $H_i$ SCORE experiment

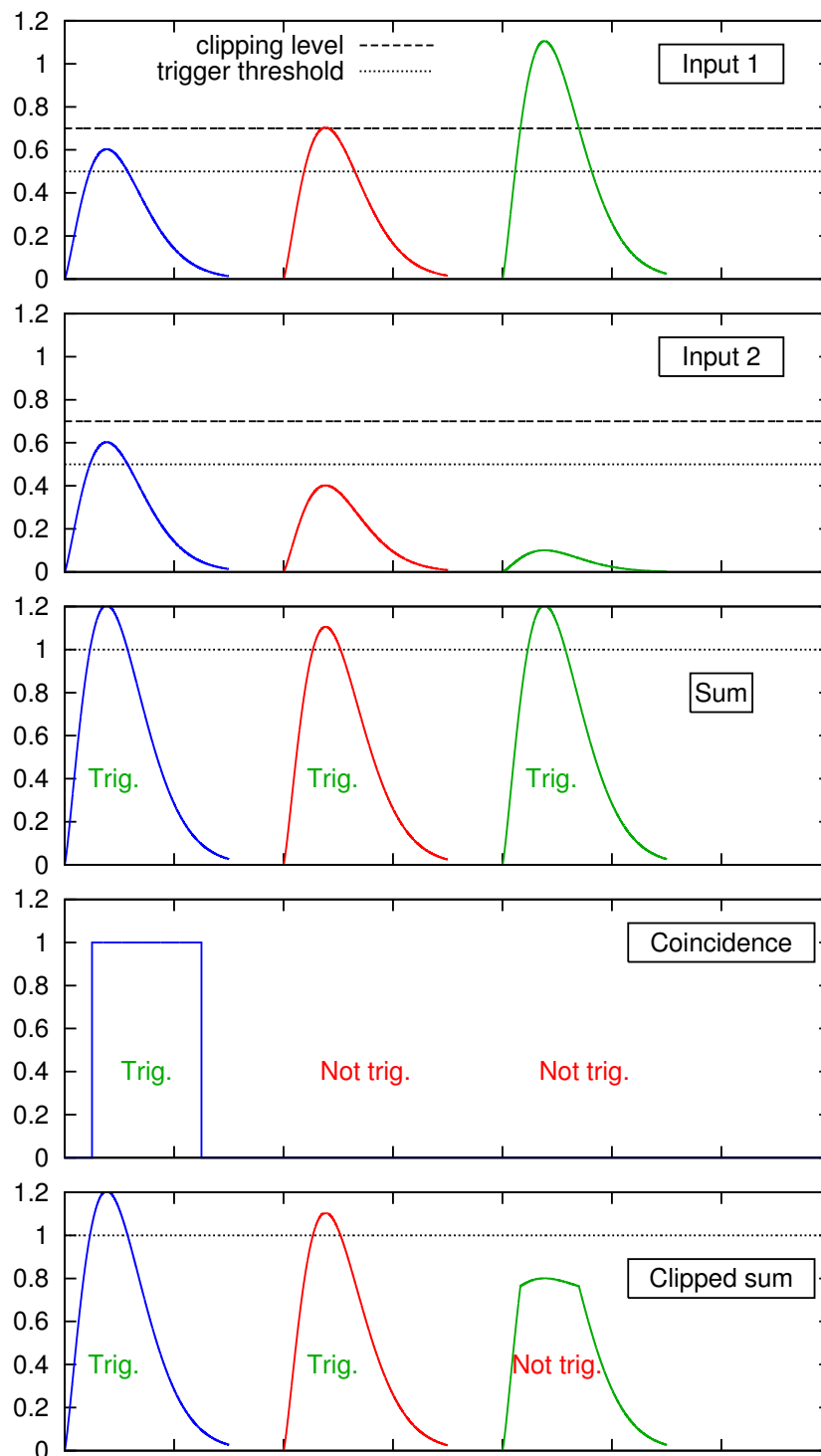


Figure 4.11: Illustration of a standard sum trigger, a coincidence trigger and a clipped sum trigger for two inputs and three different example situations (columns): In the first one (blue), there are two identical signals at 10% above the trigger threshold. All three systems trigger correctly. In the second one (red), one signal is slightly below the trigger threshold, the other above. Both sum triggers identify this event correctly, but not the coincidence trigger. In the third one (green), there is a large spike in one channel, but nearly nothing in the other, which is a sign of a false signal. Both the coincidence and the clipped sum trigger reject this event, while the standard sum trigger accepts it erroneously.

pulse-width modulation, and 16 analogue inputs. It can be programmed via a specifically designed, C-like language and can communicate with the PlugPC over a serial interface. On the PlugPC a python script receives and decodes commands from the central computer cluster and relays them to the Arduino, which returns sensor readings on the same way. The slow control uses the same wireless link used for the data transfer, but since the data volume and rate for the slow control is low, no significant impact on the data rate is expected. On the computer in the control room a graphical user interface based on python scripts is used to display information about the stations and send commands. The software development for the slow-control is described in Eichler [2011].

**Power supply** It is foreseen to use a common 12V supply system for all components in the detector station. For components that need a lower voltage (e.g. 5V like the PlugPC) or a negative voltage like some of the ICs in the trigger chain, switched voltage regulators are used. The power consumption is dominated by the Guru PlugPC (about 15W) and the heating, if necessary (which depends on the operating site). For the first test stage a 12V supply generated from grid power will be used, but an independent power supply using solar panels and batteries is envisaged to eliminate the need for any cables between the stations.

### 4.3 Ideas for time synchronisation

For an accurate event reconstruction a precise time synchronisation of the detector stations is needed. The relative time delay between the signals is used to reconstruct the direction of the particle and can also help in the particle identification. A good time resolution is therefore vital for the use of H<sub>i</sub>SCORE as gamma-ray observatory. Simulations show that a direction resolution of better than 0.1° can be achieved if the relative delay of signals is known with an accuracy of 1ns (see section 5.4.3). The time jitter of the PMT itself introduces an unavoidable uncertainty, which is however well below 1ns for the ET 9352KB PMT [Nachtigall, 2011]. Since it is impossible to transmit the signals over a standard wireless connection without losing its time information, a time stamp has to be generated at the detector station and transmitted along with the digitised signals. A similar technique is also used for other large area detector arrays, like the Pierre Auger Observatory, where the surface detectors generate a time stamp from a GPS module. With this technique, a time resolution of about 10ns is achieved, which allows for the good direction reconstruction needed for the search for anisotropies of ultra high energy cosmic rays [Pryke and Lloyd-Evans, 1995].

For H<sub>i</sub>SCORE, however, a time resolution of 10ns is not sufficient. Some dedicated timing GPS modules are capable of producing a time stamp with a better accuracy, like the M12M Timing GPS module<sup>6</sup> which is claimed to achieve an accuracy of 2ns (see datasheet in appendix E). While this would be nearly sufficient for H<sub>i</sub>SCORE, and a first stage of the experiment may be using only this, finally an even better time stamp is needed to achieve the desired accuracy in the direction reconstruction.

The proposed method for this is inspired by the VLBI (very long baseline interferometry) technique used in radio astronomy (see e.g. Middelberg and Bach [2008]). While the phase information of measured signals can be used directly in radio astronomy, an artificial radio signal must be produced for the synchronisation in H<sub>i</sub>SCORE. For the following argument we will assume that a 10MHz sine signal is generated and transmitted from a central point in or near the detector array. The signal is received and amplified by each station and recorded directly by a free channel of the DRS 4 chip in the case of an event trigger (see figure 4.12). Since the different channels of the DRS 4 chip are very well synchronised to each other ( $\sigma < 0.2\text{ns}$ , see Bükér [2012]), the recorded sine wave can be used to define the relative time offset of the PMT signal after the signals have been transmitted to the central computer cluster. A similar set-up has been tested successfully by Schröder *et al.* [2010] to monitor the time synchronisation between LOPES detector stations, which are used to measure radio signals generated by extensive air showers, with an accuracy of 1ns.

<sup>6</sup>by i-lotus, see [http://www.ilotus.com.sg/m12m\\_timing\\_oncore](http://www.ilotus.com.sg/m12m_timing_oncore)

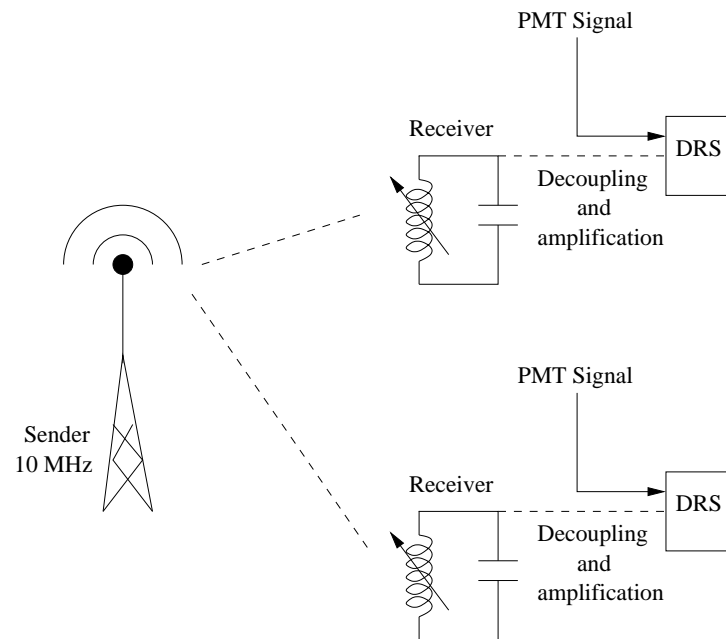


Figure 4.12: Illustration of the time synchronisation using radio signals. A radio signal is generated at a central point in the array. The signal is received and amplified at each station. The DRS 4 board records the signal in the case of an event trigger.

Essentially, the time synchronisation scheme envisaged for  $H_i$ SCORE consists of two steps: First, a GPS clock is used for a “coarse” time stamp (with an accuracy of around 10 ns). In the second step, the phase of the recorded sine waves is used to align the signals to better than 1 ns.

The process is illustrated in figure 4.13 for two stations which have seen the Cherenkov light at exactly the same time, but whose signals are misaligned by 10 ns to each other when using only the GPS time stamps. For simplicity, the distances of the two stations to the sender are assumed to be equal<sup>7</sup>. Therefore, the two sine waves are expected to be in phase, no matter what the actual delay between the Cherenkov signals is. For a 10 MHz signal and a readout window of 1  $\mu$ s the phase can be determined with great accuracy, and the sine waves – and thereby also the Cherenkov light signals – can be aligned to each other with a precision of well below 1 ns.

The requirement on the GPS accuracy can be relaxed further, if the radio signal contains several sine waves with similar frequencies. In this case the primary, coarse time information could be derived by the phase shift between the sine waves.

The development of the two-stage time synchronisation system outlined here is a high priority in the  $H_i$ SCORE project. First results will be presented in Bükér [2012].

#### 4.4 Concluding remarks and outlook

The principal design of the  $H_i$ SCORE detector stations has been presented in this chapter. Almost all aspects of the hardware development are to be seen as preparatory work to develop a station design that can be fabricated efficiently in large numbers for the full scale array. Concerning the mechanical design, long term tests of the materials, especially the Winston cone surfaces and the plexiglass window, in realistic operating

<sup>7</sup>If this is not the case, the phase shift induced by the difference of the distances must be corrected for before further processing. Since the positions of the stations have to be known with high accuracy anyway, this means no substantial complication.

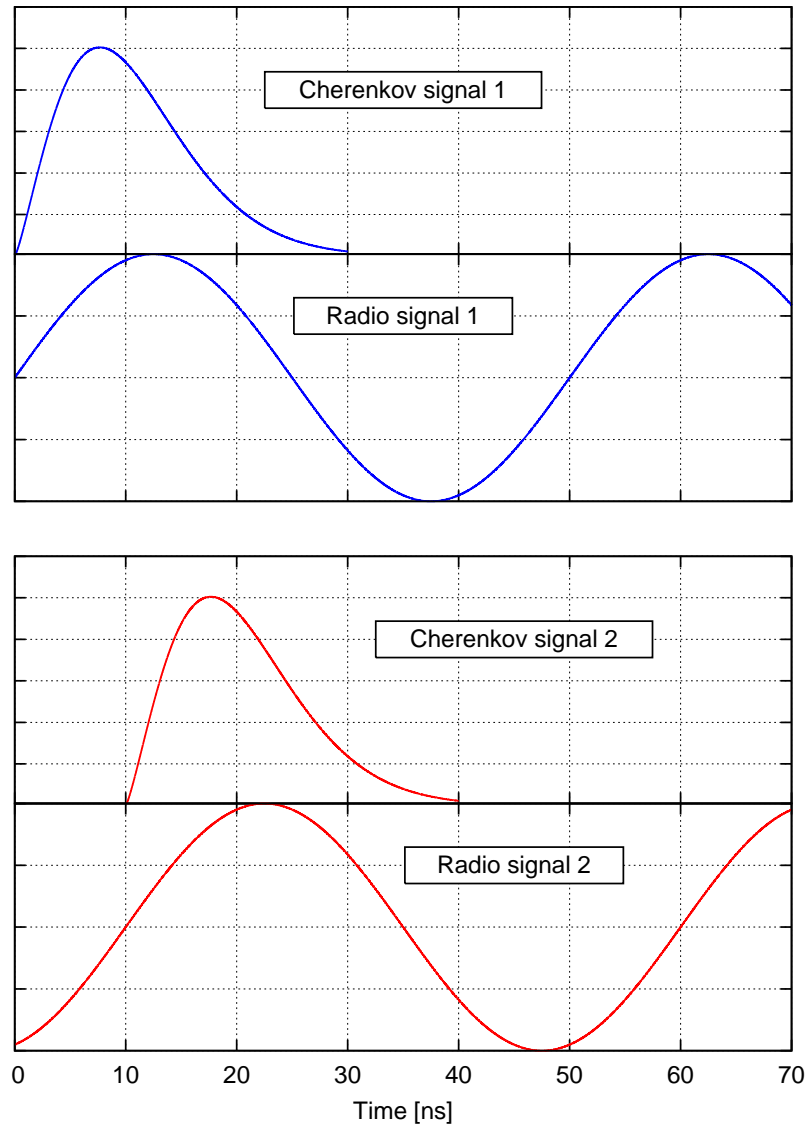


Figure 4.13: Example of the alignment of two signals from different stations. Each station records the Cherenkov light signal and the radio signal simultaneously (on two different DRS 4 channels). The signals are assumed to be recorded exactly at the same time, but misplaced by the GPS time stamp by 10ns. This misalignment can be seen in the phase difference of the sine waves. If the phase shift is compensated by shifting signal 2 (bottom) back ten nanoseconds, the Cherenkov signals are exactly synchronous.

#### 4 *The H<sub>i</sub>SCORE experiment*

conditions are important to judge the rate of degradation of reflectivity and transmission, respectively. Another important aspect is the optimisation of the support structure and the Winston cone towards a design that can be produced in large numbers in reasonable time, at low cost and high reproducibility.

The electronic system must be developed further to achieve a stable operation with the slow control and the data readout. The different parts of the electronics, i.e. the slow control and the trigger and readout electronics, should be joined into one integrated station control system. The most important, and probably most challenging part of the on-going work is the development of a time synchronisation system following the concept outlined in section 4.3. Along that line, a medium-term goal should be the use of an application specific FPGA (Field Programmable Gate Array) that merges the DRS 4 signal readout and the time synchronisation into a single unit. The slow control and the data communication may be incorporated as well, making the use of the Arduino micro-controller and the Guru PlugPC obsolete. Such a system should be more efficient than the current test set-up with discrete components both in terms of energy consumption (important for a self-contained station design) and cost.

Finally, the whole system must be tested for its durability in heavy weather, such as strong rain, snowfall and extremely high and low temperatures, and the design may need to be adjusted according to the test results before mass-production of detector stations can commence.

The current prototype can be used for the first tests which can provide valuable insights to potential problems in the design. It can also be used to gain experience with the system response to Cherenkov light signals, e.g. the handling of the data rate, the gain calibration and stabilisation or the time response of the PMTs and the electronics. In the short term, tests of the detector station at the site of the TUNKA experiment (see also section 6.2.2) are foreseen, where valuable experience can be gathered from the comparison with the data measured by the TUNKA detector.

## 5 H<sub>i</sub>SCORE simulations and event reconstruction

In this chapter, the simulation of the H<sub>i</sub>SCORE detector and its results will be presented. Section 5.1 gives an overview of the simulation software, the data flow, and the simulated datasets. In section 5.2 the effect of night sky brightness (NSB) on the detector is discussed. The simulation presented there takes the NSB levels measured during the site evaluation campaign at Fowler’s Gap in Australia (see section 6.4) as input and generates samples of typical noise fluctuations. These are used in the detector simulation to include the effect of NSB on the measured signals, and to determine a suitable trigger threshold. Section 5.3 describes the detector simulation `sim_score` that reads in the air shower simulation results and calculates the detector response to a given event, including the trigger calculation, signal shaping and acceptances of the various components.

In section 5.4 one of the key components of this work, the development of an event reconstruction algorithm for the H<sub>i</sub>SCORE detector, is described. The large inter-station spacing compared to similar projects, e.g. AIROBICC [Karle *et al.*, 1995], poses a significant challenge for the event reconstruction, especially at low energies where events trigger only very few detector stations and produce signals only slightly above the noise from NSB. In this section, the individual steps for the reconstruction of the various parameters (core position, primary particle direction, energy etc.) are described, while a more technical description of the event reconstruction software is postponed to appendix A. This section also presents the results of the event reconstruction in terms of the reconstruction accuracy of key parameters. In section 5.5 possibilities for a gamma hadron separation, that make use of the previously reconstructed values, are described.

In section 5.6, the results from this framework are used to estimate the sensitivity of the H<sub>i</sub>SCORE detector to gamma-ray sources. In section 5.7 different alternatives to the standard detector layout (described in section 5.1) are discussed, such as a different inter-station spacing or the set-up of the detector at a higher altitude.

### 5.1 Overview

Figure 5.1 gives an overview of the software framework developed and used for the H<sub>i</sub>SCORE simulations presented in this chapter.

The CORSIKA package [Heck *et al.*, 1998] is used to generate air shower events, its IACT extension [Bernlöhner, 2008] to derive the Cherenkov light flashes seen at the predefined detector positions. The event parameters, such as primary particle type, energy and direction, are given by an “inputcard“, a plain text file with a list of keywords described in the CORSIKA documentation. The resulting Cherenkov light data is stored in a binary file (IACT eventio format<sup>1</sup>), while additional data about the shower development can be found in the CORSIKA screen output, which is logged, and various plain text files.

The Cherenkov light data is used as input for the detector simulation `sim_score`, which calculates the detector response to the Cherenkov light. This includes the geometric acceptance of the detector, especially the Winston cone light concentrators (see section 4.2.2), the wavelength dependent acceptance of the PMTs, the discrete 1 ns sampling of the readout electronics, and the simulation of station and array triggers. Random noise induced by night sky brightness is added from a pre-generated noise file (as described in section 5.2). The resulting station signals are stored in a plain text format. All simulated events, also those that have not triggered any detector station, are retained throughout the whole process.

---

<sup>1</sup>Details about this format can be found in the CORSIKA documentation, especially the documentation of the “bernloehr“ module.

## 5 $H_i$ SCORE simulations and event reconstruction

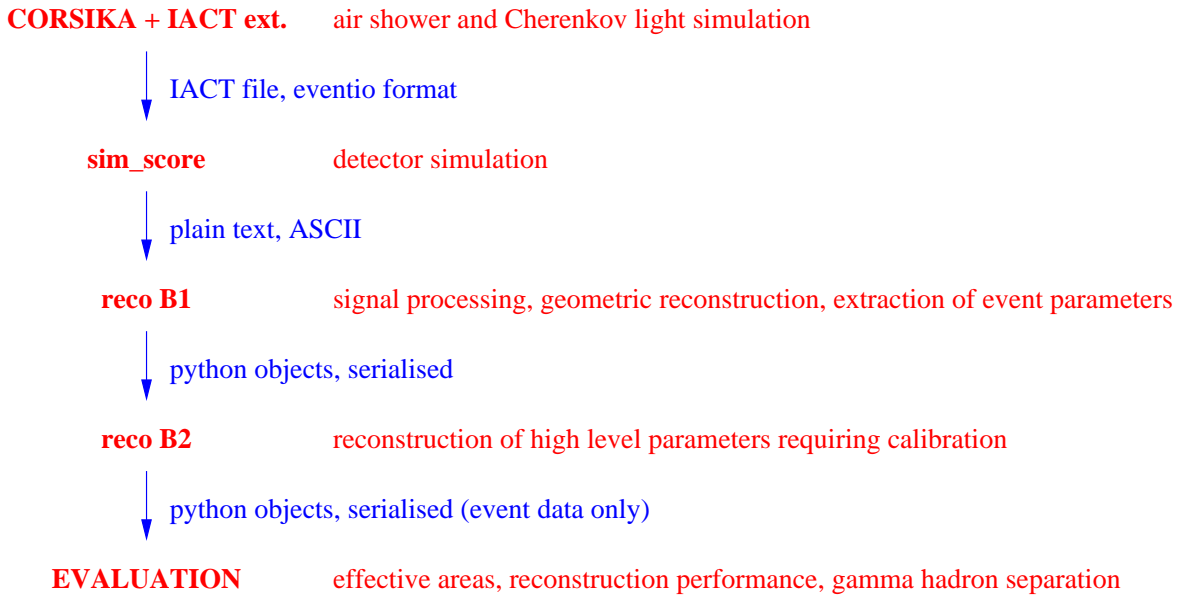


Figure 5.1: Framework for the  $H_i$ SCORE simulations. Software levels are shown in red, file formats for transfer of data between the levels in blue.

The event reconstruction starts with level B1, on which the detector signals are read in and transferred to a custom python event class, which is used for all further processing<sup>2</sup>. On level B1, the geometric properties of the event are reconstructed, such as the shower core or the direction, and fit parameters that describe the intensity and time distribution of the detector signals are generated. The results are stored in the event class objects, which are saved using the python serialising function<sup>3</sup>. At this point, the detector signals are discarded to reduce memory usage and processing time of subsequent steps.

On level B2, high level event data that requires calibration is reconstructed, such as the shower depth and the primary particle energy. This has been separated from the first step in order to allow a quick reprocessing of the data after a change of calibration. In practice, levels B1 and B2 are usually run together. After this processing, the data is stored again in the event class, however all individual detector data is discarded to further reduce the data volume, i.e. only event level data is retained. At this stage, the average memory needed per event is 3 kilobytes.

The originally simulated event parameters, also called Monte Carlo (MC) values, are read in from the CORSIKA inputcard and output files and stored together with the reconstructed values in the event object<sup>4</sup>. On the evaluation level, these are compared to the reconstructed values and the average deviations are calculated (usually as a 68% containment region). From this, the accuracy of the core position, direction, energy and shower depth reconstruction can be estimated. Usually, these values are only calculated for a subset of events that pass certain acceptance criteria, such as a maximum (reconstructed) zenith angle or a core position inside of the detector array. Additionally, the effective areas after various cuts are calculated on this level. All values are given as function of primary (MC) energy, as this parameter has the strongest influence on the signal strength and the number of triggered stations and thus on the reconstruction accuracy. To evaluate the behaviour of the detector in detail, some results are also calculated as function of other MC

<sup>2</sup>Originally, there was also a level A, that was used merely for data reduction and processing purposes. It has later been merged into level B1, yet the nomenclature remained

<sup>3</sup>A serialising function generates representations of all objects (built-in and custom) which can be saved in a plain text or binary file.

<sup>4</sup>For simplicity, this happens already on the B1 level, even though these values are not used until the evaluation level except for control screen printouts.

variables, e.g. the zenith angle. All results are stored as plain text files that can be used for plotting or evaluation in further calculations (e.g. the sensitivity calculation presented in section 5.6.4).

The main dataset used for testing and optimising the event reconstruction algorithm uses a detector layout of  $22 \times 22$  stations with a spacing of 150m in a regular grid, covering an area of  $3.15 \text{ km} \times 3.15 \text{ km} = 9.92 \text{ km}^2$ . Each station contains four detector channels consisting of a PMT and a Winston cone each, resulting in a total light sensitive area of  $0.5 \text{ m}^2$  per station. The detector is placed at sea level. From here on, this configuration will be referred to as the H<sub>i</sub>SCORE standard layout.

About 145,000 air shower events with energies between 10TeV and 5PeV have been simulated for this configuration, using a  $\frac{dN}{dE} \propto E^{-1}$  spectrum to obtain constant event numbers in logarithmic bins. The events consist of gamma, proton and helium primaries with about 25,000 events each and nitrogen and iron primaries with about 35,000 events each<sup>5</sup>. The direction is randomly chosen for each event with a maximum zenith angle of 30 degrees. The shower core position lies within a rectangle of  $3.8 \text{ km} \times 3.8 \text{ km} = 14.44 \text{ km}^2$ , i.e. can be up to 325m outside of the instrumented area.

Other, smaller datasets are generated for other layouts, e.g. a different detector spacing or a different altitude. A summary of the findings from comparing the different layouts, with a focus on the energy threshold, is presented in section 5.7.

In order to keep track of the simulations and for fast and efficient testing, a database system with a graphical interface has been developed. It allows the selection of events on different criteria, e.g. the particle type or the energy range, and passes that list on to all scripts of the evaluation level. Additionally, a framework to start many simulations in parallel has been developed, especially the CORSIKA and `sim_score` levels are usually run on the local multi-core computer cluster.

For a typical H<sub>i</sub>SCORE simulation run with events between 100TeV and 1PeV, the average processing times per event are about one to two minutes for CORSIKA, 20 to 30s for `sim_score`, about 1.5s for reco B1 and 40ms for reco B2 (all on a 2GHz processor). On the evaluation level, many thousand events can usually be processed within a few seconds.

A more technical documentation of the software framework including documentation for future users can be found in appendix A.

## 5.2 Night sky brightness simulation

Night sky brightness (NSB), i.e. the residual light of the sky during dark, moonless nights poses a major source of noise for all atmospheric Cherenkov detectors, but especially for wide-angle detectors such as H<sub>i</sub>SCORE, as it is proportional to the solid angle of the observation. A measurement of the NSB levels at one potential detector site is presented in section 6.4, a more detailed description of the origin and characteristics of NSB can be found there.

From these measurements, the noise photon rate in one H<sub>i</sub>SCORE channel is estimated to be between 1.5 and  $3.1 \times 10^{11}$  photons/s, depending on the region of the sky looked at, with the highest NSB levels towards some regions of the Galactic plane. These levels convert to 14 to 29 *photoelectrons* (p.e.) per nanosecond using an average PMT quantum efficiency of 0.0935 p.e./photon (see section 6.4.4). For the simulations, an average level of 21.5 p.e./ns is used.

The aim of the NSB simulation is two-fold: First, to obtain a realistic noise signal that can be used in the detector simulation to predict the deterioration of the reconstruction accuracy due to noise, second to determine a suitable trigger threshold that keeps the false triggers from noise fluctuations at a manageable level.

---

<sup>5</sup>No electrons have been simulated, as their flux is negligible at multi-TeV energies due to their soft spectrum and the spectral cut-off around 1 TeV, see e.g. Egberts and H.E.S.S. Collaboration [2011].

## 5 $H_i$ SCORE simulations and event reconstruction

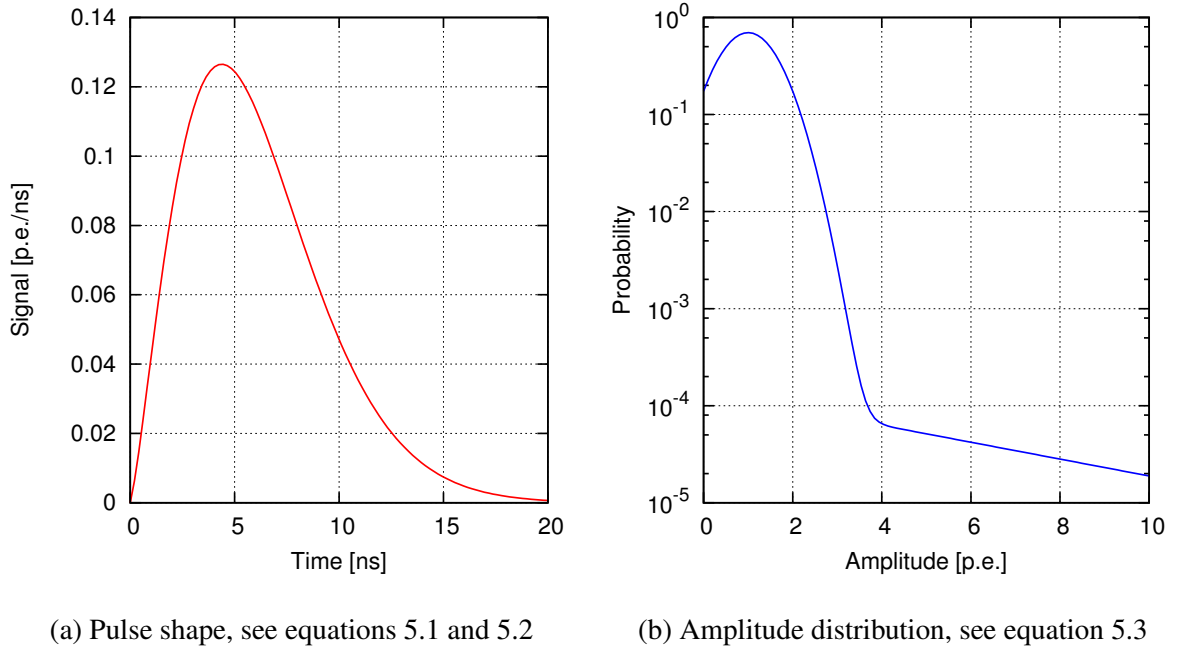


Figure 5.2: PMT single photon response function, characterised by the pulse shape (left) and the amplitude distribution (right).

**Generation of noise signal** The noise signal is generated taking into account the 1 ns quantisation of the readout electronics and the detector response function, which is given by the pulse shape and the amplitude spread of the single-electron response of the PMT. For the pulse shape, the response function from the AIROBICC simulations for the ET9352KB PMTs [Henke, 1994] is used, which describes the signal produced by a single photoelectron as:

$$R(t) = \frac{7}{4} \frac{c b^{\frac{a+1}{c}}}{\Gamma(\frac{a+1}{c})} \times \left(\frac{7}{4}t\right)^a \times \exp\left(-b\left(\frac{7}{4}t\right)^c\right) \quad (5.1)$$

with

$$a = 1.25 \quad b = 0.0414 \quad c = 1.48 \quad (5.2)$$

The time  $t$  is given in nanoseconds, the response  $R$  in p.e. per nanosecond. The peak value of the function is 0.1259 p.e./ns, its width about 7.4 ns. The function is shown in figure 5.2a.

The amplitude spread, i.e. the probability that a single photon causes an amplitude  $A$ , is approximated by a Gaussian function with an exponential tail to include the effect of rare but large afterpulses, following the approach in Bernlöhner [2008] (see also figure 5.2b):

$$P(A) = \frac{1}{1.433} \left( \exp\left(-\frac{1}{2} \left(\frac{A-\mu}{\sigma}\right)^2\right) + 2 \times 10^{-4} \times \exp\left(\frac{-A}{5}\right) \right) \quad (5.3)$$

with  $\mu = 1$  p.e. and  $\sigma = 0.6$  p.e.. The normalisation is calculated numerically by integrating the function from 0 to 40 p.e.

Further influences on the detector response function, e.g. by the analogue electronics between the PMT and the readout board, are not (yet) included in the simulation.

A sample of NSB induced noise of the length  $T$  is simulated by distributing  $21.5 \frac{\text{p.e.}}{\text{ns}} \times T$  photoelectrons uniformly within the time interval  $T$ . Each photoelectron produces a signal according to the amplitude

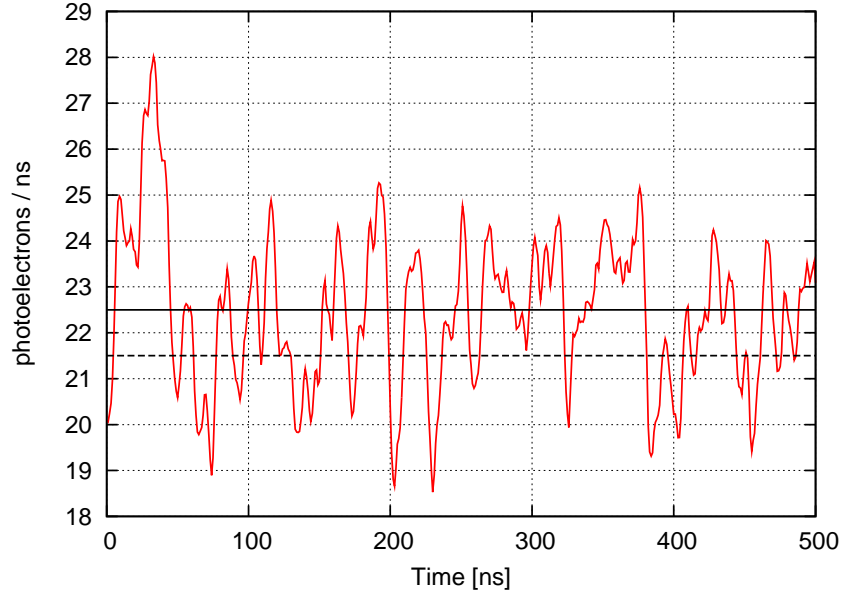


Figure 5.3: Example of generated NSB signal for one channel. The input level is indicated by the dashed black line, the actual average level by the solid line.

spread and pulse shape discussed above. Figure 5.3 shows a short example of such a noise signal. It can be seen that the time scale of the fluctuations is on the same level as the PMT response function. The average level of the noise is slightly increased from the 21.5 p.e./ns used as input to about 22.5 p.e./ns by the amplitude distribution function. For the detector simulation `sim_score` the noise is simulated for four detector channels and for a duration of 0.4 ms (400,000 bins). In the following, only the sum of the four channels is considered, with an average noise level of

$$\langle noise \rangle = 90 \frac{\text{p.e.}}{\text{ns}} \quad (5.4)$$

**False triggers by NSB** The station trigger is activated if the signal is above a certain level  $L_T$  for more than 7 ns. The number of photoelectrons needed to produce a signal that touches the trigger level is given by:

$$Npe_{threshold} = \frac{L_T - \langle noise \rangle}{0.1259} \quad (5.5)$$

The factor of 0.1259 is given by the peak value of the pulse shape function (equation 5.1). To activate the trigger, i.e. to produce a signal above  $L_T$  for more than 7 ns, a higher number of photoelectrons,  $Npe_{trigger}$ , is needed. The signal reaches a width of 7 ns at a level of 0.069, i.e. at about 55.2% of the peak value, from  $R(1.61 \text{ ns})$  to  $R(8.61 \text{ ns})$ . Therefore, the minimum number of photoelectrons needed to trigger a station is given by

$$Npe_{trigger} = \frac{Npe_{threshold}}{0.552} = \frac{L_T - \langle noise \rangle}{0.1259 \times 0.552} \quad (5.6)$$

In reality, the actual number of photoelectrons needed to produce a trigger will be a little higher than  $Npe_{trigger}$ , since not all photons will arrive at exactly the same time. This is however not a problem, as both the NSB and the detector simulations use  $L_T$  for the trigger generation, and  $Npe_{trigger}$  is used only for illustrative purposes. Figure 5.4 visualises the relation of the quantities involved in the trigger calculation.

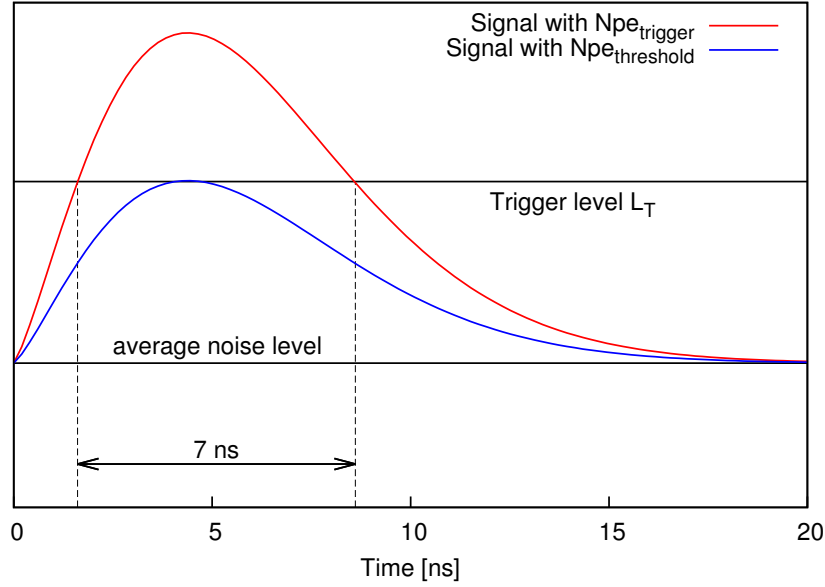


Figure 5.4: Quantities used in the trigger calculation.

If the real comparator used in the experiment is slower than assumed here, the value of 7 ns above  $L_T$  will need to be adjusted in the calculation. In that case, the threshold  $L_T$  can be decreased accordingly to allow the same number of photoelectrons to trigger the detector.

The station trigger rate is estimated by going through a simulated noise signal of 1 s length with a full trigger simulation for three possible trigger configurations (see also section 4.2.3):

1. The coincidence trigger system requires each of the four detector channels to trigger independently (using a trigger threshold of  $L_T/4$ ), within a coincidence window of 10 ns.
2. The sum trigger system adds up all four channels and requires the sum signal to trigger with a threshold of  $L_T$ .
3. The clipped sum trigger clips each signal at  $1.05 \times L_T/4$  before adding up the four signals. The sum of the clipped signals must trigger with a threshold of  $L_T$ .

Figure 5.5 shows the simulated trigger rates for the three cases and for different threshold from  $L_T = 95$  to  $L_T = 104$ . As expected from the argument in section 4.2.3, the sum trigger is most vulnerable to false triggers, while the coincidence trigger rejects most of the noise (but also most of the small signals). The clipped sum trigger was chosen to be the best alternative and has been implemented in `sim_score`, using a threshold of  $L_T = 102.59$  p.e./ns (i.e. 12.59 p.e./ns above the average noise level), corresponding to  $Npe_{threshold} = 100$  or  $Npe_{trigger} = 181$ . With this system, a noise trigger rate of about 330 Hz is expected. While this is more than the current readout system can handle (maximum achieved rate with the DRS 4 board was 80 Hz [Eichler, 2011]), it seems reasonable to expect that such a rate can be handled by the system that will be used in the final set-up<sup>6</sup>. On the other hand, even a small increase of the trigger threshold would decrease the trigger rate significantly, e.g. with a threshold of  $L_T = 104$  p.e./ns the trigger rate would go down to 26 Hz. The impact of such a change on the energy threshold of the  $H_i$ SCORE detector has not yet been examined systematically.

<sup>6</sup>According to the developer, a rate close to 500 Hz should be achievable when using a “decent computer” for readout [Ritt, 2011].

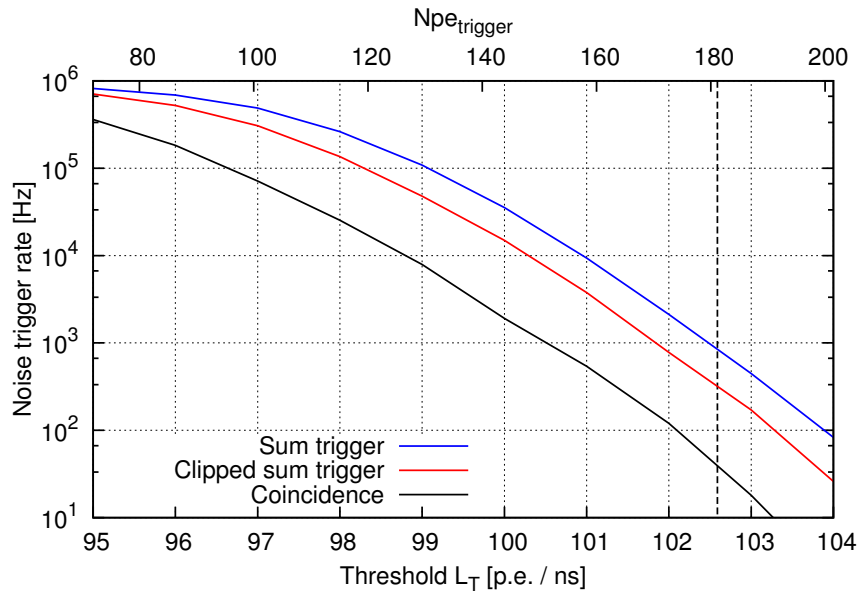


Figure 5.5: Simulated single station trigger rates for the three described trigger configurations. The vertical dashed line denotes the threshold used in `sim_score`.

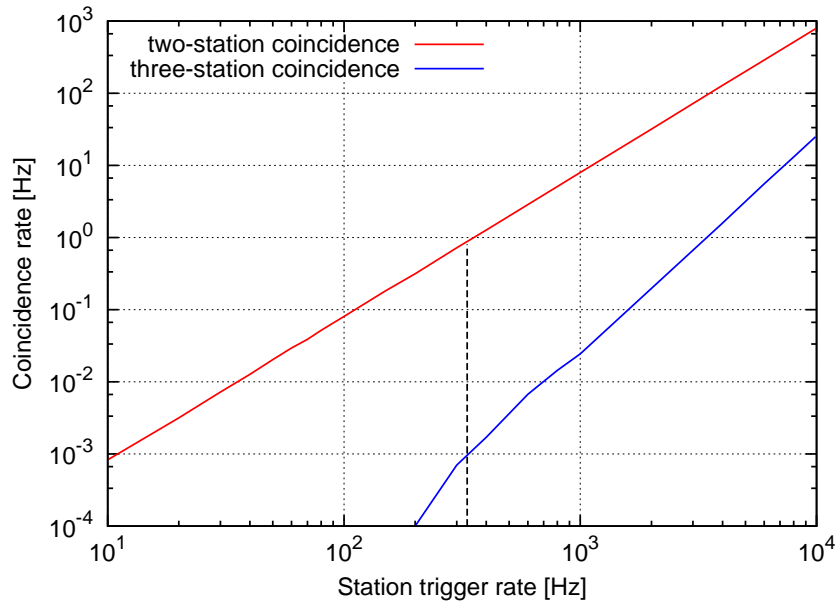


Figure 5.6: Rate of coincident triggers in two or three neighbouring stations. The vertical dashed line denotes the station trigger rate for the trigger threshold used in `sim_score`.

**N-station coincidence trigger** Another possibility to decrease the trigger rate is to implement a two-station, next-neighbour coincidence trigger, which starts the readout only if at least one neighbouring station reports a trigger signal as well. Given the depth of the DRS 4 readout buffer of 1  $\mu\text{s}$  (at 1 GHz sampling frequency) and the station distance of 150 m (corresponding to 500 ns at the speed of light), this would require a very fast communication link between the stations, which in turn would require additional electronics and probably a direct cable connection between the stations. Since at least three stations are needed for the reconstruction of a real event, such a system would not increase the energy threshold for air shower events.

To simulate the effect of such a two-station trigger on the noise trigger rate, random trigger times are assigned to a central and four neighbouring stations according to their station trigger rates, and coincidences within a window of 1  $\mu\text{s}$  are counted. This simulation is also used to estimate the rate of *three*-station triggers caused by NSB noise, which will in any case survive the cut in the reconstruction and will therefore be counted as real signal. Figure 5.6 shows the resulting trigger rates as function of the station trigger rate. It can be seen that the two-station coincidence system achieves a very effective suppression of noise triggers, which would significantly reduce the data rate that needs to be sampled and transmitted from the stations. For the currently used threshold, the rate is reduced from the single station trigger rate of 330 Hz to about 1 Hz. Alternatively, it would also be possible to slightly lower the trigger threshold and thereby the energy threshold of the detector while keeping the false trigger rate at a manageable level. Currently, however, such a system is foreseen neither in the detector simulation nor the hardware development, as the possible benefits are not expected to justify the additional costs in the set-up. This may be re-evaluated once the trigger and readout system, and its limitations (e.g. in data transmission speed), are known better.

The three station NSB trigger rate is two to three orders of magnitudes below the two-station coincidence rate, and amounts to about  $10^{-3}$  Hz for the currently used threshold. These signals will not be distinguishable from air shower events in the reconstruction and will be counted as such<sup>7</sup>. In a detector of the standard layout (484 stations), the total rate of these false events will be about 0.5 Hz. Compared to the trigger rate caused by cosmic rays of about 1 kHz (see section 5.6.3), this noise rate is negligible.

It should be emphasised at this point that all threshold levels and rates calculated here are valid only for an average level of NSB. Towards bright regions of the sky, e.g. the central Galactic region, a higher level of NSB is expected, while other regions have a lower level of NSB (see section 6.4.4). Additionally, bandpass filters may be used in the detector to reduce the NSB level while keeping a large fraction of the Cherenkov light (see section 6.4.6). In practice, the trigger threshold will have to be set to a value that keeps the noise trigger rate at a manageable level, possibly depending on the region of the sky looked at. The energy threshold of the detector system will vary accordingly.

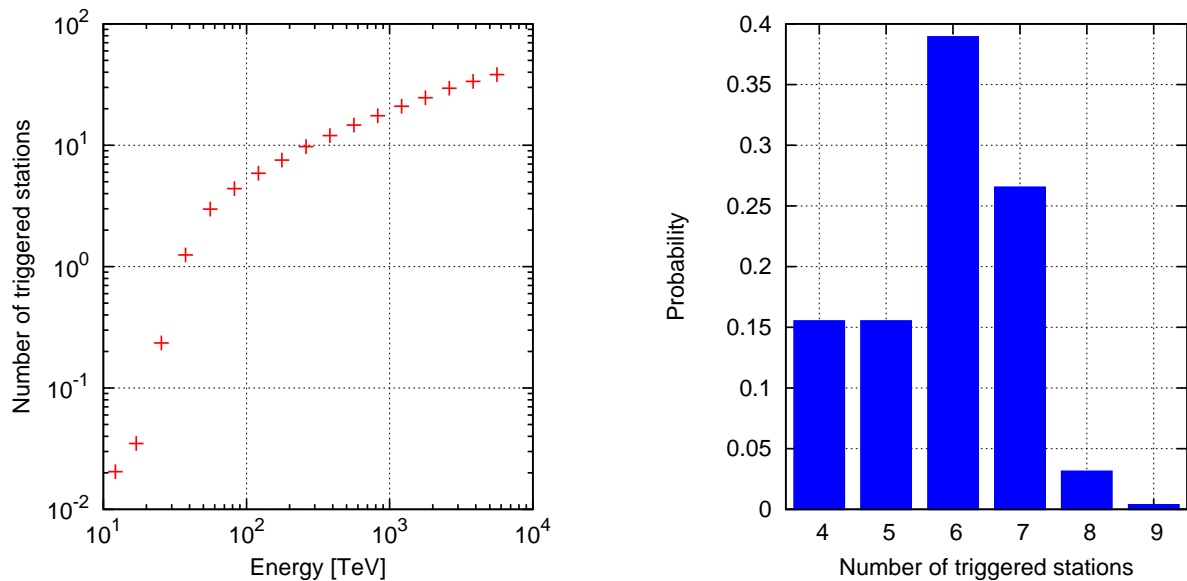
### 5.3 Detector simulation `sim_score`

The detector simulation reads in the Cherenkov photon data generated by CORSIKA and calculates the signals seen in each station, and generates a trigger flag if the trigger conditions are met. The signals are stored in arrays with 4000 bins, each one representing 1 ns, centred around the zero point of the CORSIKA time frame, which is set by the time at which the primary particle would have arrived at the observation level had it passed through the atmosphere without interaction.

The probability of each emitted photon to arrive at the observation level is simulated using wavelength dependent atmospheric transmission tables from MODTRAN [Kneizys *et al.*, 1996]. For each arriving Cherenkov photon, the probability of detection is calculated using the angle-dependent Winston cone transmittance shown in figure 4.5 on page 80 (using 80% reflectivity and a homogeneous PMT acceptance) and the wavelength dependent quantum efficiency of the PMT as given by the manufacturer (see datasheet in

---

<sup>7</sup>Actually, not all these noise signals will be counted as air shower events. As the coincidence window in the trigger simulation is 1  $\mu\text{s}$ , noise events will be reconstructed with angles up to  $60^\circ$  and therefore be discarded by the angular cut at  $25^\circ$ . Therefore, the noise rate will be even lower than calculated here.



(a) Average number of triggered stations versus energy

(b) Distribution of triggered stations for events with energies between 100 and 147 TeV

Figure 5.7: Number of triggered stations as derived from the detector simulation

appendix E). Additionally, a photoelectron collection efficiency of 0.9 is assumed for the PMT.

Each surviving photon is filled into the station's signal array using the PMT response function described in section 5.2. Noise from NSB is added using a random part of the pre-generated noise signal. Other noise sources are not taken into account, as they are believed to be negligible against the very high noise level caused by NSB. The transfer function of the electronic circuits between the PMT and the readout electronics is not yet known and therefore not taken into account, either. Preliminary tests (see also Kunnas [2012]) indicate that the limited bandwidth achievable in the analogue summer and amplifier circuits will alter the signals to some degree; this will be incorporated into the simulation as soon as more systematic data is available.

A simulation of the two trigger levels currently planned for the detector is also included in *sim\_score*. If the analogue clipped sum is above a certain threshold for at least 7 ns (see also section 5.2), a *station trigger* is issued. Only triggered stations and stations with a triggered neighbour station<sup>8</sup> are retained and passed on to the reconstruction software. For triggered stations, a signal of 200 ns duration is recorded, starting 15 ns before the trigger start time. For stations without own trigger, 400 ns are added before and after the readout window of the (triggered) neighbour station, resulting in a readout window of 1  $\mu$ s, to allow for time delays caused by inclined showers. A trigger flag is saved along with the signal data of each station.

The *array trigger* is activated if the event has triggered at least three stations. This is used here only for event rate calculations and does not affect the treatment of the event in the detector simulation. The reconstruction software, however, uses only events with an array trigger.

Figure 5.7a shows the average number of triggered stations versus the simulated energy of the primary particle. Below 50 TeV there are less than three triggered stations on average, however, some of these events

<sup>8</sup>Direct neighbours only, not diagonal. It is not yet decided whether the actual experiment will contain a system to activate next neighbour stations (which would require a fast, direct communication link between the stations). In the simulations these stations are retained to evaluate their benefit to the reconstruction (see also section 5.8).

## 5 *H<sub>i</sub>SCORE simulations and event reconstruction*

still trigger three or more stations and can be used in the event reconstruction. Above about 1 PeV more than 20 stations are triggered on average. Figure 5.7b shows the distribution of triggered stations in the energy bin between 100 TeV and 147 TeV, which has an average of 5.9 and a spread from 4 to 9 triggered stations.

Figure 5.8 shows a simulated gamma-ray event of 509 TeV energy, colour coded for signal intensities and signal peak times (see section 5.4.1 for the exact definition of these parameters). The next-neighbour readout scheme results in an extra ring of signals around the triggered stations. The intensities are high in the stations directly adjacent to the shower core and fall off quickly to larger distances. The station peak times are indicative of the particle direction, the zenith angle of  $23^\circ$  leads to a delay of over  $1 \mu\text{s}$  between stations on the right and on the left. Since all stations record the signal in their own time-frame along with an absolute timestamp (see also section 4.3), this is not a problem. The following section describes the algorithm used to reconstruct the event properties from the shown (and other) signal parameters.

### 5.4 Event reconstruction

The reconstruction is implemented in form of a python event class that contains the event data and reconstruction methods. The data can be categorised into MC data (simulation input values), the results of the detector simulation (mainly the detector signals and trigger flags) and reconstructed values that are filled during the course of the reconstruction procedure. Each event object contains a list of all stations that are read out in this event by `sim_score`. The detector stations are implemented as an own class, containing the detector signal and signal parameters that are filled during the first steps of the reconstruction, such as the signal intensity, peak time and signal duration. As mentioned in section 5.1, the detector signals are discarded after reconstruction level B1, keeping only the signal parameters. The whole detector list is deleted at the end of step reco B2, keeping only event data from this point on.

**Reconstruction level B1** On this level, the signals are evaluated, global distributions of parameter values are fitted and the geometric shower properties are reconstructed. The individual steps are:

1. Pre-processing of detector signals to extract signal parameters
2. Preliminary estimation of the shower core position by centre of gravity of signal intensities
3. Preliminary direction reconstruction by fitting a plane to the arrival time distribution

If only three or four signals are available, the rest of the reconstruction is skipped, and these quantities are the only reconstructed values available for the event.

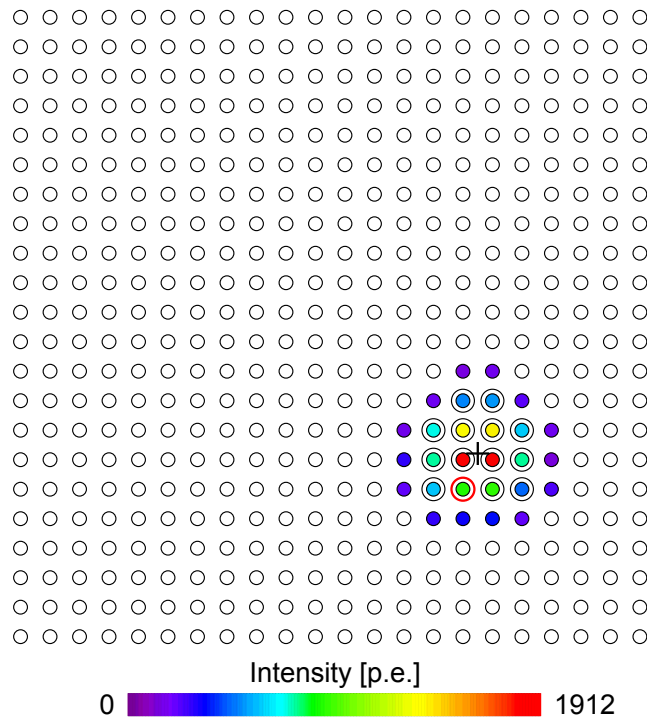
4. Improvement of the core position by fitting the light distribution function (LDF)

If this fit is not successful, e.g. because of contradictory data points, the rest of the reconstruction is skipped.

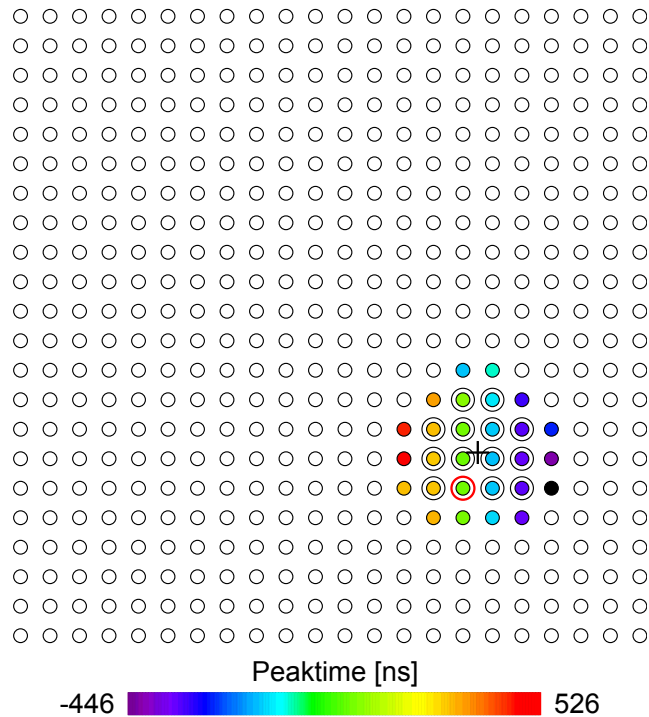
5. Improved direction fit using arrival time model
6. Fit of signal widths

**Reconstruction level B2** The following steps are done on reconstruction level B2:

7. Estimate the particle energy using fit parameters and lookup tables
8. Estimate the atmospheric depth of the shower maximum with various methods



(a) Station intensities



(b) Station peak times

Figure 5.8: Event display ( $H_i$ SCORE standard layout), colour coded for station intensities (top) and station peak times (bottom), of a simulated gamma-ray event with 509 TeV primary energy and a zenith angle of  $23^\circ$ , coming from the right. The MC shower core position is denoted by the black cross. Triggered stations are marked by an extra ring around the station. The signal of the station marked with a red circle is shown in figure 5.9.

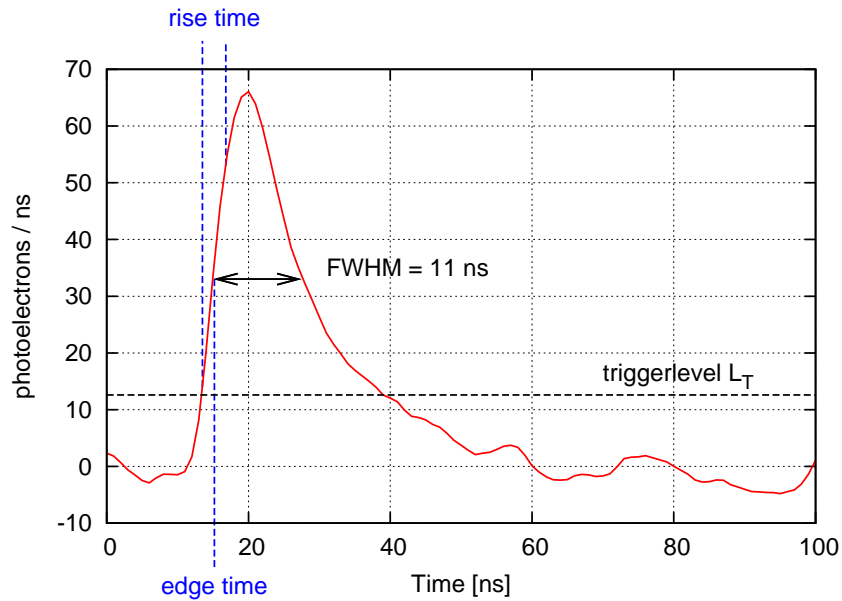


Figure 5.9: Cherenkov light signal of a triggered station of the event shown in figure 5.8 (indicated by the red circle around the station), and the signal parameters *edge time*, *rise time* and *width* (duration of signal given by the FWHM). The average noise level of 90 p.e./ns has been subtracted. The trigger threshold  $L_T$  is shown for reference.

The success of each step (usually as simple binary information) is stored in the event class for later selection cuts. The accuracy of the reconstruction is judged by its resolution, defined as the value at which 68% of the events are contained. Numeric values of the results for reference and further processing can be found in the appendix in table B.1 (page 189).

The goal of the event reconstruction is to estimate the properties of the primary particle, i.e. its direction of origin, its energy and its type (gamma or other, possibly the mass in the case of hadrons), as accurately as possible. It is tested on a subset of gamma-ray events from the standard layout dataset defined in section 5.1. This subset contains events that survive the *acceptance cuts*, which select events with at least three triggered stations, a reconstructed shower core inside the detector array boundaries, and a reconstructed zenith angle below  $25^\circ$ . These cuts are rather strict and limit the dataset to events which are not noticeably affected by edge effects. The potential for relaxing these cuts is discussed briefly in section 5.6.1.

In the following, the individual steps of the reconstruction and their performance are presented in contextual (rather than chronological) order.

#### 5.4.1 Signal pre-processing

In a first step, the Cherenkov light signal is parametrised by the following quantities (“signal parameters”, see also figure 5.9):

- Intensity, standard window, in p.e.: Integrated area below the signal within a readout window from  $-15$  ns to  $25$  ns relative to the trigger time<sup>9</sup>. This time window is chosen to include most of the signal while minimising the influence of noise. Simulations without noise show that no signal is lost before the window, while about five to ten percent is lost after the window. The actual amount of signal

<sup>9</sup>The trigger time is defined as the time at which the trigger switches, i.e. the time at which the signal level has been over the threshold for 7 ns.

intensity lost after the integration window depends strongly on the distance of the station from the shower core, as the signal width increases with core distance (for a detailed discussion on this see section 5.4.5), and increases to about 30% at distances over 300m. Additionally, it depends on the shower depth and the type of primary particle. Therefore, these intensities are used only for core position and energy reconstruction, but not for the shower depth estimation which is needed in the context of gamma hadron separation.

- Intensity, extended window, in p.e.: Integrated area below the signal in a readout window from  $-15$  ns to 130 ns. While this extended time window leads to the inclusion of a lot of noise, it ensures that no late arriving Cherenkov photons are lost. Simulations show that for all tested particles, the whole simulated energy range and detector distances of up to 500m from the core, more than 99.5% of the signal is contained. These intensity values are used for the second LDF fit needed in the depth reconstruction (section 5.4.5).
- Peak time, in ns: Time at which the signal reaches its maximum (no interpolation)
- Edge time, in ns: Time at which the signal reaches 50% of its maximum (linearly interpolated between adjacent time bins)
- Rise time, in ns: Duration in which the signal rises from 20% of its peak value to 80% (interpolated).
- Width, in ns: Duration of the signal, defined as its full width at half maximum, FWHM.

The typical distributions of these parameters in an event and the information that can be derived from these distributions are discussed in the following sections. For the fits to the distributions, the uncertainties to the values must be calculated. For the signal intensity the uncertainty is estimated by

$$\sigma_{int} = \sqrt{(intensity) + p.e.(NSB)} \quad (5.7)$$

where  $p.e.(NSB)$  is the number of photoelectrons expected within the integration window from night sky brightness. The uncertainties on the times and the signal width are estimated using empirical functions of the signal intensity.

#### 5.4.2 Shower core position

The reconstruction starts with a preliminary reconstruction of the shower core position, which is defined as the intersection of the shower axis with the detector level, by a centre of gravity calculation using the signal intensities of all triggered stations (reconstruction step 2). This is a robust method that usually gives a good approximation of the core position even if only a few stations have triggered, and was already used successfully in the AIROBICC event reconstruction [Karle *et al.*, 1995].

If signals from at least five stations are available, an improved core position can be obtained by fitting the expected lateral light density function (LDF) to the recorded signal intensities (rec. step 4), as suggested in Prosin *et al.* [2009]. The LDF is being parametrised as an exponential function near the shower core and a power law at larger distances, with the break between the two at  $c_{LDF} \approx 120$  m, similar to the LDF used in the BLANCA analysis [Fowler *et al.*, 2001]. The free parameters in the fit function are the absolute normalisation  $P$ , the indices of the exponential function  $d$  and the power law  $k$ , and the position of the shower core  $(x, y)$ . If at least six detector signals are available,  $c_{LDF}$  can be a free fit parameter as well, which has been found to slightly improve the core reconstruction.

$$LDF(r) = \begin{cases} P \exp(dr) & \text{for } r < c_{LDF} \\ Qr^k & \text{for } r > c_{LDF} \end{cases} \quad (5.8)$$

## 5 $H_i$ SCORE simulations and event reconstruction

with

$$r = r(x, y) = \sqrt{x^2 + y^2} \quad (5.9)$$

$$Q = \frac{P \exp(d c_{LDF})}{(c_{LDF})^k} \quad (5.10)$$

Typical values are -0.01 to 0 for  $d$ , and -2.6 to -1.8 for  $k$  (for  $r$  in metres). The normalisation  $P$  is roughly proportional to the energy of the primary particle. The use of these parameters for the energy and shower depth reconstruction is discussed in sections 5.4.4 and 5.4.5. Two examples of fitted LDFs, in two-dimensional projection, are shown in figure 5.10.

Figure 5.11 shows the resolution of the shower core position reconstruction for the centre of gravity method and the LDF fit method. The accuracy of the LDF method is superior to the centre of gravity method above energies of 100TeV. Its resolution is about 35m near the threshold and improves to below 5m at higher energies.

After the reconstruction of the shower direction (see next section) the station positions can be transformed into the shower plane (the plane perpendicular to the shower axis), and the core position fit can be repeated using the new coordinates, which yields a slight improvement especially for events with large zenith angles.

While the centre of gravity method can only reconstruct showers within the array, the LDF fit can also be applied to showers that are outside the array, however, it gets inaccurate quickly as the shower core moves away from the array border. At 1 PeV, the resolution deteriorates from 5m for contained events to 15m for showers up to 150m away from the detector the core, and to about 35m for showers between 150m and 300m away from the detector.

A better method for showers with core positions outside of the array is the usage of the *signal width*, which can be used up to far distances from the array as long as enough light is received in the detector to accurately measure the signal widths. This method has successfully been tested by the AIROBICC collaboration [Henke, 1994] and is also used by the TUNKA collaboration [Budnev *et al.*, 2009] to increase the effective area of their detector. This method has however not been pursued here, and only events that are reconstructed to be inside of the array are used for further analysis.

### 5.4.3 Direction of origin

**Direction reconstruction with simple plane fit** The direction of the primary particle is calculated using the delays between the arrival times of the Cherenkov photon signal at different stations (see also figure 5.8b). A preliminary direction (rec. step 3) is obtained by fitting a plane to the arrival time distribution:

$$t(x, y) = \frac{\sin(\theta) \cos(\phi) x + \sin(\theta) \sin(\phi) y}{\cos(\theta) c_{air}} + t_0 \quad (5.11)$$

where  $\theta$  and  $\phi$  are the zenith and azimuth angle of the direction, respectively, and  $c_{air} = c/n$  is the speed of light in air. The constant  $t_0$  is used only to adjust the function to the absolute time frame and yields no information. This method can be used if a minimum of three stations is available, however its accuracy is limited (see below) since it does not take into account the curvature of the Cherenkov light front.

**The arrival time model** If at least four stations are available, the curvature can be taken into account by using the arrival time model developed by Stamatescu *et al.* [2011]. This model has been developed originally for timing stereoscopy with Cherenkov telescopes (as described in section 3.3) and is presented here in an adapted version for an array detector. The goal is to derive an expression that predicts the arrival time of Cherenkov light at a given detector as a function of the shower direction, given by zenith and azimuth angles  $\theta$  and  $\phi$ , and the height of light emission  $z$ :

$$t_{det} = t_{det}(\theta, \phi, z) + t_0 \quad (5.12)$$

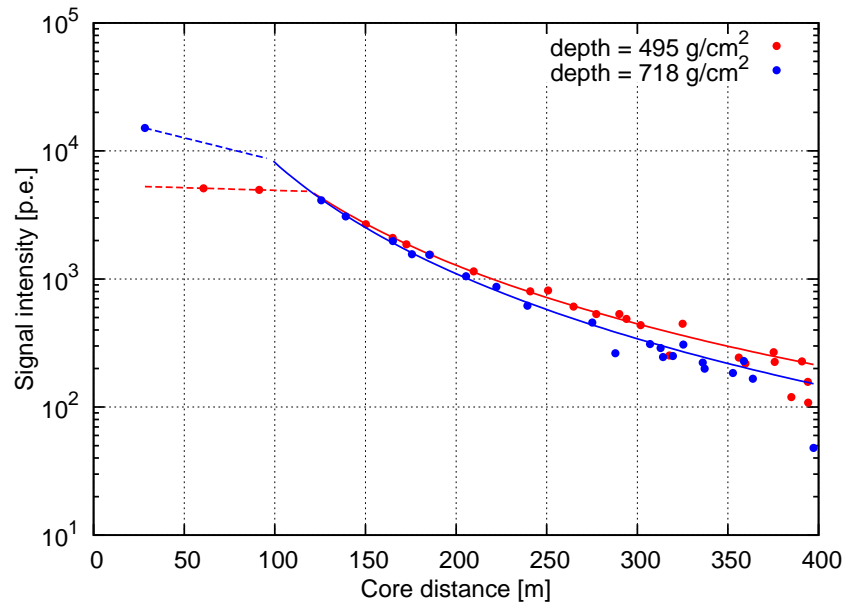


Figure 5.10: The LDF of two 750 TeV gamma-ray events with different shower depths. The distributions are fitted with equation 5.8. The dashed line represents the exponential part of the LDF, the solid line the power law part.

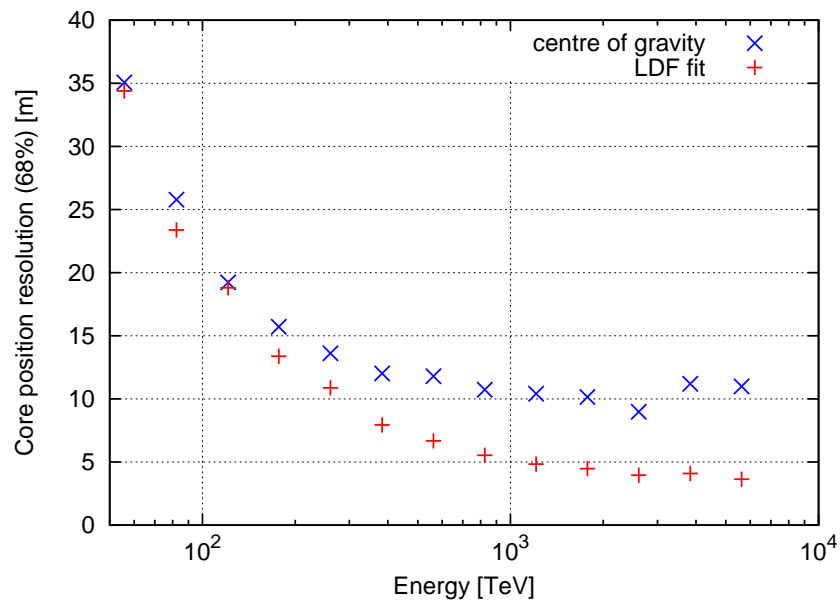


Figure 5.11: Resolution (68% containment) of the shower core position reconstruction with the centre of gravity calculation and with the light distribution function fit method.

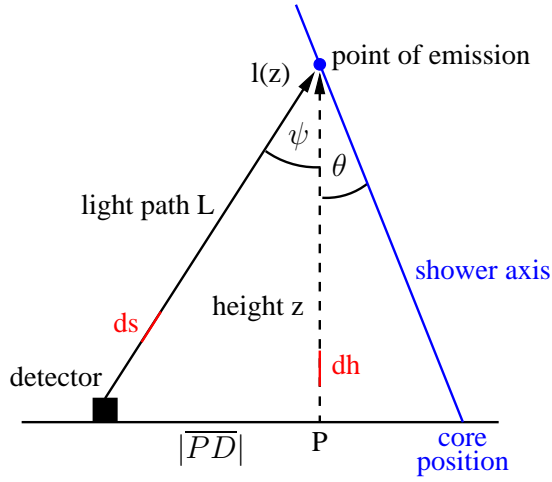


Figure 5.12: Illustration of the calculation of the light path used for the arrival time model.

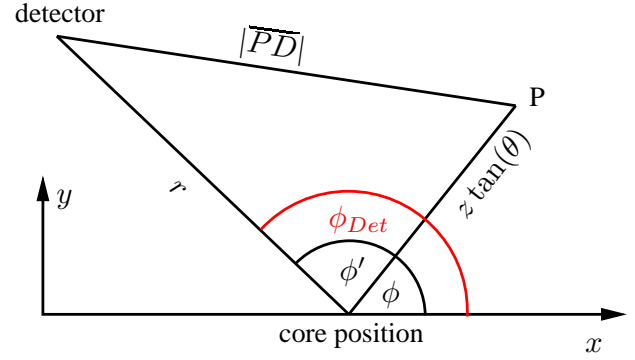


Figure 5.13: Illustration of the calculation of the planar distance between the detector and the projection point  $P$  used for the arrival time model (seen from above).

Assuming that the peak arrival time of Cherenkov photons in the detector corresponds to the light emitted at the shower maximum, a fit of this function (with  $\theta$ ,  $\phi$ ,  $z$  and  $t_0$  as free parameters) to all detector peak times yields an estimation of the shower direction and the height of the shower maximum.

The expected arrival time is calculated by using the length of the light path  $L$  from the detector position on the ground to the position of Cherenkov light emission at the height  $z$ :

$$t_{det}(\Psi, z) = \frac{L(\Psi, z)}{c} + t_0 \quad (5.13)$$

In this,  $\Psi$  is the angle of the light path (see figure 5.12), and  $c$  is the speed of light in vacuum. It will be shown below that  $\Psi$  can be expressed as function of the shower parameters  $\theta$ ,  $\phi$  and  $z$ , giving  $t_{det}$  the desired dependencies.

The light path length  $L$  is given by the integral along the path over the height-dependent refractive index of air  $n(h)$  from 0 (detector position) to  $l(z)$  (point of emission):

$$L(\Psi, z) = \int_0^{l(z)} n(h) ds = \int_0^z n(h) \frac{ds}{dh} dh = \int_0^z \frac{n(h)}{\cos(\Psi)} dh \quad (5.14)$$

As the refractive index of air is – in good approximation – proportional to the air pressure (see e.g. Edlén [1966]),  $n(h)$  can be modelled according to the barometric formula:

$$n(h) = 1 + \eta_0 \exp(-h/h_0) \quad (5.15)$$

with  $h_0 = 8\text{ km}$  and  $\eta_0 = 2.76 \times 10^{-4}$  (where  $n = 1 + \eta_0$  is the refractive index of air at sea level). With this dependence, the light path becomes

$$L(\Psi, z) = \frac{z + \eta_0 h_0 (1 - \exp(-z/h_0))}{\cos(\Psi)} \quad (5.16)$$

To connect the obtained light path length to the shower parameters, the angle  $\Psi$  is expressed in terms of the distance from the point  $P$  to the detector,  $|PD|$ , and the height  $z$ :

$$\cos(\Psi) = \frac{z}{l} = \frac{z}{\sqrt{z^2 + |PD|^2}} \quad (5.17)$$

The point  $P$  is defined as the projection of the point of light emission to the observation level (see figure 5.12). Its position, and thereby the distance  $|\overline{PD}|$ , can be calculated using the known shower core position and the shower parameters  $\theta$ ,  $\phi$  and  $z$ .

In general, the shower core, the projection point  $P$  and the detector will not be positioned along a straight line as implied by figure 5.12. Instead, the value of  $|\overline{PD}|$  must be calculated as distance in the  $x$ - $y$  plane as illustrated in figure 5.13. The vector from the core position to the detector is known from the previous reconstruction of the shower core position and parameterised by its length  $r$  and its angle  $\phi_{Det}$  relative to a fixed coordinate system. The vector from the core position to the point  $P$  is connected to the shower parameters and parametrised by its length ( $z \tan(\theta)$ ) and its angle  $\phi$ , i.e. the azimuth angle of the shower axis. Using these two vectors,  $|\overline{PD}|$  is calculated using the law of cosines:

$$|\overline{PD}| = \sqrt{r^2 + z^2 \tan^2(\theta) - 2rz \tan(\theta) \cos(\phi')} \quad (5.18)$$

The angle between the two vectors needed here is simply given by  $\phi' = \phi_{det} - \phi$ .

Combining equations 5.17 and 5.18, the angle  $\psi$  is found to be

$$\cos(\psi) = \frac{z}{\sqrt{r^2 + \frac{z^2}{\cos^2(\theta)} - 2rz \tan(\theta) \cos(\phi')}} \quad (5.19)$$

Plugging this into equation 5.16, the time function 5.13 becomes

$$t_{det}(\theta, \phi', z) = \frac{1}{c} \sqrt{r^2 + \frac{z^2}{\cos^2(\theta)} - 2rz \tan(\theta) \cos(\phi')} \left( 1 + \frac{\eta_0 h_0 (1 - \exp(-z/h_0))}{z} \right) + t_0 \quad (5.20)$$

As  $\phi'$  depends only on the (known)  $\phi_{det}$  and on  $\phi$ , equation 5.20 can be used to fit the shower direction given by  $(\theta, \phi)$  and the height of emission,  $z$ . For this, at least four data points are necessary, since the absolute time offset  $t_0$  must be fitted as well.

For vertical showers, this function becomes approximately parabolic, while for large zenith angles it approaches a plane. Figure 5.14 shows the arrival times predicted by equation 5.20 for a shower with  $\theta = 2^\circ$  and  $\phi = 45^\circ$ . At this zenith angle, the parabolic form is still visible while on the other hand the delay caused by the inclination of the shower is already dominating the behaviour of the function.

Figure 5.15 shows the predicted arrival time distribution for vertical showers of different typical emission heights between 6km and 8km (corresponding to shower depths between 500 and 390 g/cm<sup>2</sup>). It shows that the height of emission  $z$  has only a small impact on the time distribution. Nevertheless, the time distribution may be used to gain an estimate of the height of maximum Cherenkov light emission (the shower maximum), a method that is discussed further in section 5.4.5.

**Direction reconstruction** For the direction reconstruction (reconstruction step 5), a fit with recursive outliers removal is used: First, equation 5.20 is fitted using all available signals. The data point with the largest deviation from the fit (expressed as multiple of its estimated error  $\sigma$ , see section 5.4.1) is removed from the dataset, and the function is fitted to the new, reduced dataset. This procedure is repeated until all data points are within  $1\sigma$  of the fit. The result of this recursive fit is usually more accurate than a standard fit, since huge spikes in the NSB noise can result in a peak time off by several ten nanoseconds. Such outliers are usually reliably identified and eliminated by the described procedure.

While in general the reconstructed angles are in good agreement with the simulated MC values, a systematic underestimation of the zenith angle can be observed. Figure 5.16 shows the deviation between the reconstructed zenith angle  $\theta_{reco}$  and the MC value  $\theta_{MC}$  for gamma-ray events between 100 TeV and 1 PeV. It increases slightly with zenith angle, from about  $0.07^\circ$  at  $10^\circ$  to about  $0.11^\circ$  at above  $20^\circ$ . The deviation increases strongly at about  $26^\circ$ , suggesting a connection to the Winston cone acceptance that shows a cut-off

5  $H_i$ SCORE simulations and event reconstruction

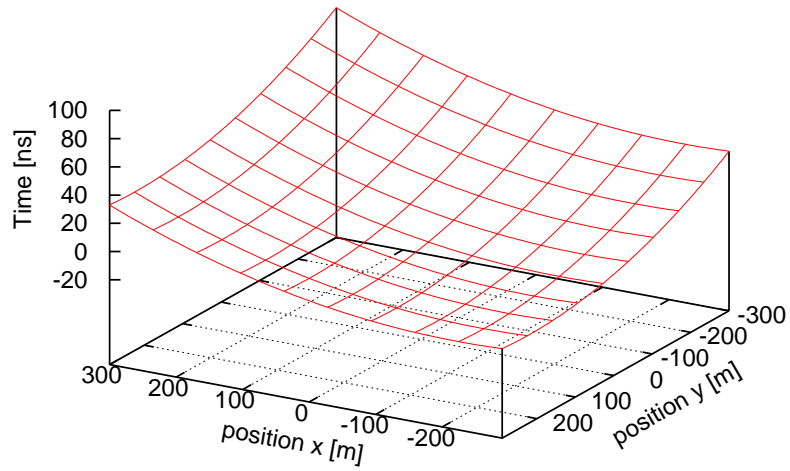


Figure 5.14: The arrival times calculated by equation 5.20 for a shower with  $\theta = 2^\circ$ ,  $\phi = 45^\circ$  and  $z = 8$  km.

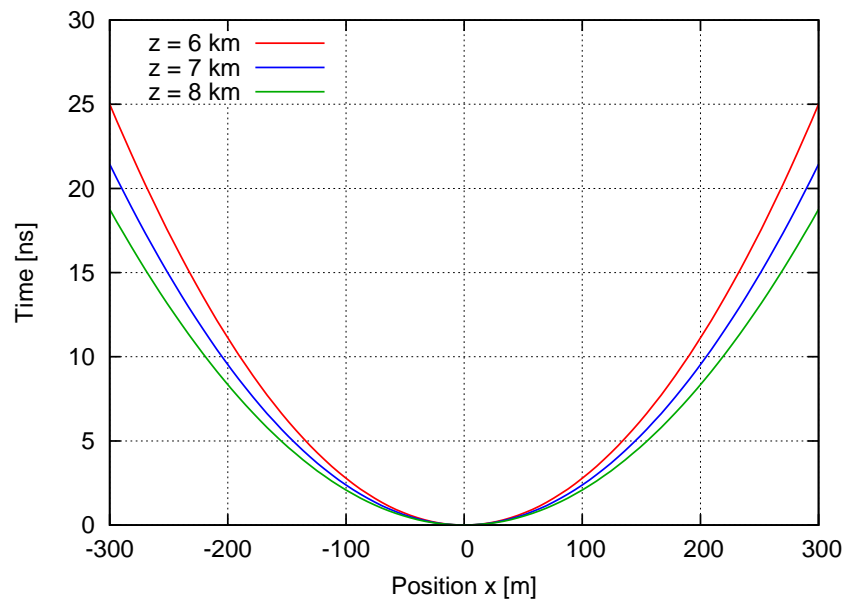


Figure 5.15: Predicted arrival times (according to equation 5.20) for vertical air showers with different heights of the shower maximum  $z$ .

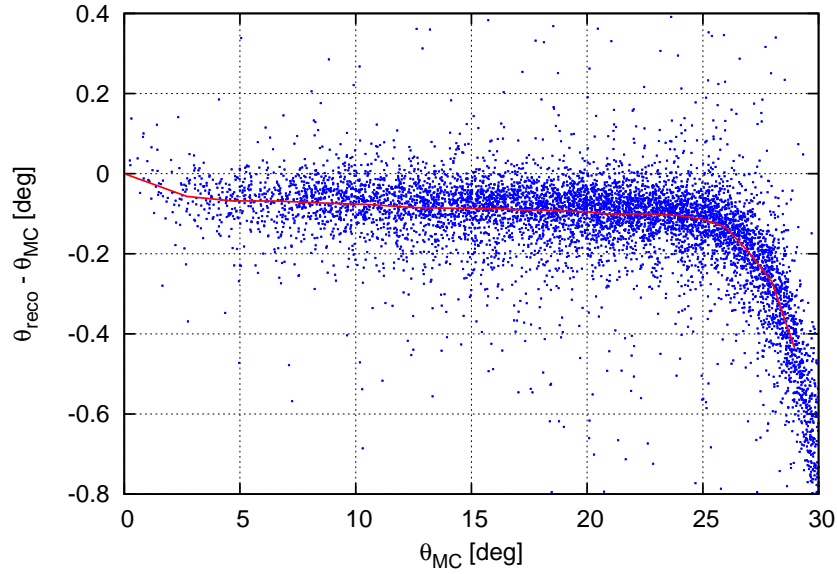


Figure 5.16: The systematic error of the zenith angle,  $\theta_{reco} - \theta_{MC}$ , against the MC zenith angle  $\theta_{MC}$ . The red solid line shows the empiric correction used to eliminate the systematic deviation.

at about this angle (see figure 4.5 on page 80). A possible explanation is that due to this cut-off the detector stations “on the far side” of the shower core (e.g. on the right of the shower core in figure 5.12) have a lower acceptance for light emitted at low altitudes than stations on the other side with the same core distance. Typically, this light will be arriving at the detector station later than light from higher altitudes (see e.g. figure 5.15). Therefore, the angular cut-off leads to a systematic shift of the measured peak arrival times to earlier times at the far side, causing an underestimation of the zenith angle. In the reconstruction, this deviation is corrected for by an empirical function shown as solid line in figure 5.16. After that, the accuracy of the direction reconstruction is found to be roughly constant with zenith angle up to  $25^\circ$ .

The accuracy of the direction reconstruction is evaluated by computing the angular distance between the simulated and reconstructed directions  $\vec{d}_{MC}$  and  $\vec{d}_{reco}$ , given by

$$\text{dist}(\vec{d}_{MC}, \vec{d}_{reco}) = \cos^{-1}(\vec{d}_{MC} \cdot \vec{d}_{reco}) \quad (5.21)$$

with

$$\vec{d}_x = \begin{pmatrix} \sin(\theta_x) \cos(\phi_x) \\ \sin(\theta_x) \sin(\phi_x) \\ \cos(\theta_x) \end{pmatrix} \quad (5.22)$$

Figure 5.17 shows the angular resolution (68% containment region) achieved by fitting the time function (eq. 5.20) to the signal peak times and to the signal edge times, versus the particle energy. In both cases, the angular resolution improves from about  $0.35^\circ$  near the threshold to about  $0.05^\circ$  at PeV energies. While the performance of the two methods is very similar, the fit to the signal edge times yields slightly better results, as this quantity is usually better defined, even in noisy signals. Therefore, the edge time variant is used in the following. Compared to the results of these methods, the simple plane fit (eq. 5.11) results in a significantly worse direction reconstruction with an angular resolution between  $0.4^\circ$  and  $0.6^\circ$ , roughly constant with energy (not shown in the figure).

So far, a perfect synchronisation between the signals has been assumed to optimise the reconstruction for the ideal case. In reality, however, a small jitter between the signal time frames will not be avoidable. The PMT and the DRS 4 readout board have been found to introduce a time jitter of about 0.37 ns [Nachtigall,

5  $H_i$ SCORE simulations and event reconstruction

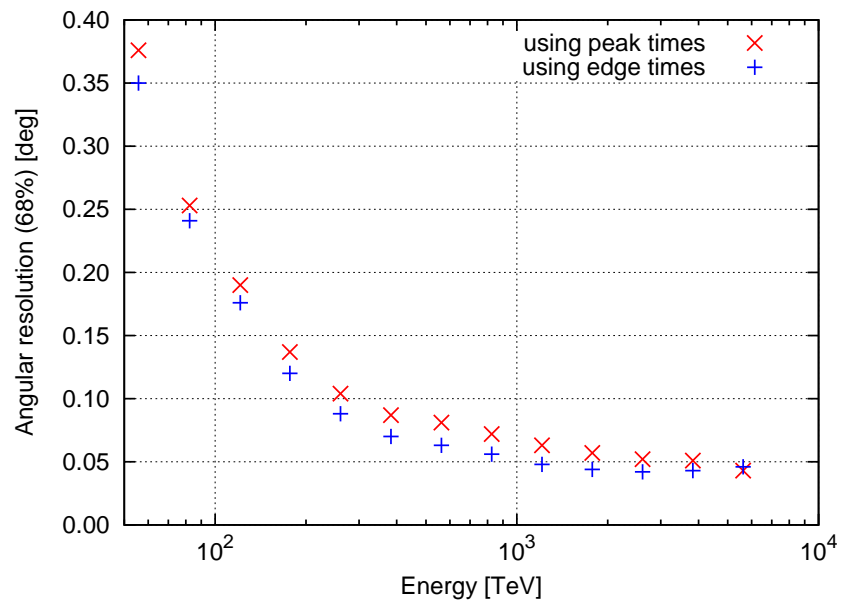


Figure 5.17: Angular resolution (68% containment) achieved by fitting the expected arrival times to the signal peak times and to signal edge times, versus the simulated particle energy.

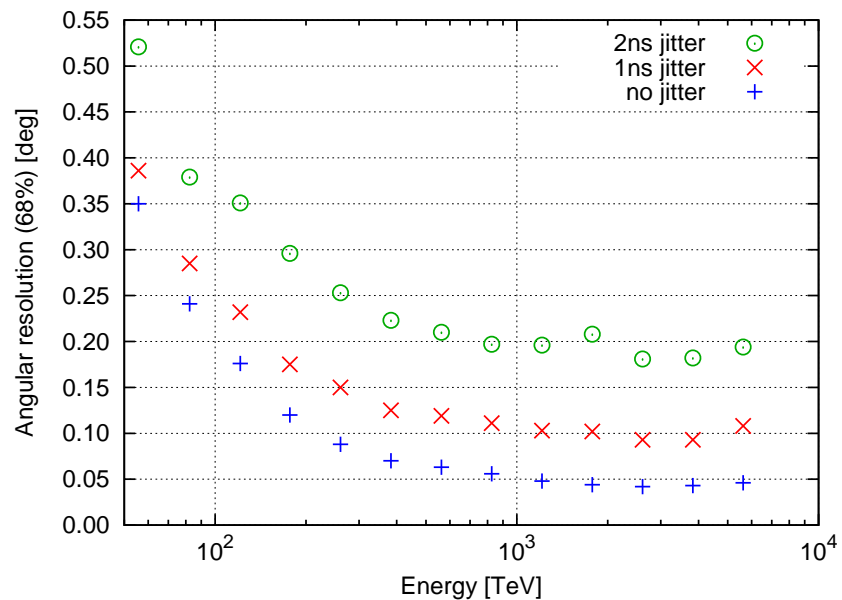


Figure 5.18: Angular resolution (68% containment) of the direction reconstruction using different values for the time jitter between individual signals.

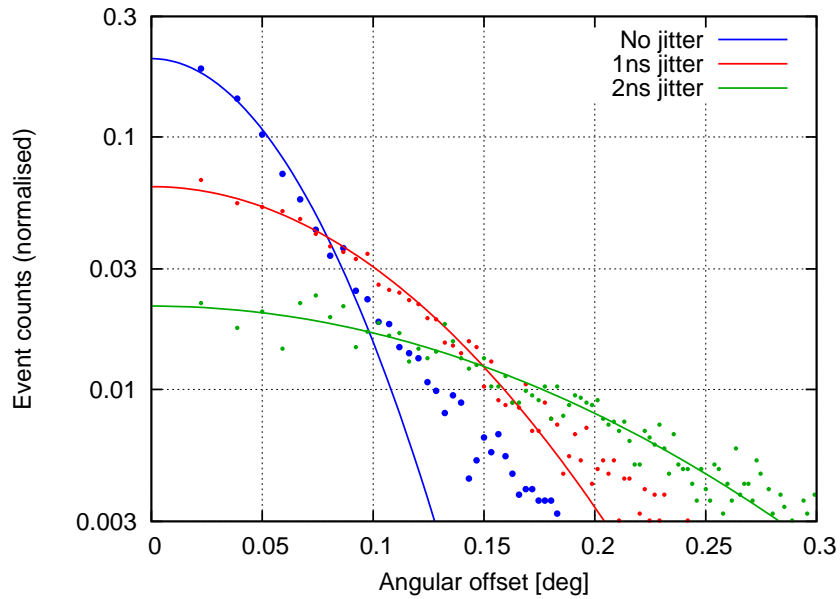


Figure 5.19: Point spread functions of the direction reconstruction (arrival time model, edge times) for different values of the time jitter, for events with energies between 100 TeV and 1 PeV. The size of the bins decreases with  $(1/r)$  to account for the increasing phase space of events with larger angular deviation. The solid lines show normal distributions fitted to the data.

2011], while the accuracy of the time synchronisation is not yet known. It seems however reasonable to assume that its contribution to the overall time jitter should be in the same order of magnitude. The impact of a time jitter on the direction reconstruction is estimated here by shifting each signal  $i$  by a time  $\Delta t_i$ , which is generated randomly according to a normal distribution with a width  $\sigma_{jitter}$ . Figure 5.18 shows the angular resolution for  $\sigma_{jitter} = 1$  ns and  $\sigma_{jitter} = 2$  ns, compared to the ideal case. The deterioration of the angular resolution is roughly constant with energy, about  $0.05^\circ$  for a 1 ns jitter and about  $0.15^\circ$  for a 2 ns jitter. At higher energies, this means a deterioration of a factor two and four, respectively. Therefore, every reasonable effort to keep the time jitter of the electronics and the time stamp generation at a minimum should be taken. Also, if other PMTs than the ET9352KB are considered for use in H<sub>i</sub>SCORE, they should be tested with a special focus on their time jitter. It should be noted that the edge time method is superior to the peak time method also for the case of non-zero time jitter.

Figure 5.19 shows the point spread function achieved by the reconstruction for different values of the time jitter. While the events are well centred around the nominal direction for the case of no time jitter, a non-zero time jitter leads to a much wider spread of the angular distances, as expected from the angular resolution shown in figure 5.18. The simulated point spread function can be approximated by a normal distribution, however a deviation of the data points from the fit is visible at larger angles, most pronounced for the case of no jitter.

#### 5.4.4 Particle energy

**General considerations** In an air shower, the number of relativistic particles is roughly proportional to the energy of the primary particle (see also section 2.4.2). As each relativistic particle emits the same amount of Cherenkov light independently of its energy (see equation 2.11), the total amount of Cherenkov light can be used to estimate the primary particle energy (rec. step 7). In other words, the atmosphere acts like a giant calorimeter for high energy particles that is read out by a Cherenkov light detector.

Due to the large station spacing in the H<sub>i</sub>SCORE experiment, only a small fraction of the total light is

## 5 $H_i$ SCORE simulations and event reconstruction

captured by the detectors (about 0.002%). Therefore, the fitted light distribution function (LDF, see section 5.4.2) has to be used to estimate the amount of generated Cherenkov light. The energy reconstruction is complicated by the fact that the shape of the LDF depends on the height of the shower maximum: The lower a shower maximum occurs in the atmosphere, the steeper the LDF will be, with more light closer to the shower core and less light at larger core distances (see figure 5.10). While this dependence is useful to estimate the shower depth (see section 5.4.5), the goal here is to find a parameter that is largely independent of the shower depth to obtain a robust estimation of the particle energy.

**Energy reconstruction** Generally, the influence of the shower depth on the LDF is weakest at core distances between 200m and 300m, therefore the light intensity in this regime is suited best for the energy reconstruction (in that respect, the examples in figure 5.10 are not quite typical). At smaller core distances the energy of events with a low maximum (i.e. a large shower depth) is usually overestimated, while at core distances well above 300m the situation is reversed. Additionally, the intensities at large distances are smaller and have larger relative errors. The optimal core distance depends on the energy and should therefore ideally be chosen after a preliminary energy estimate, an approach which is however not pursued here. Instead, the value of  $LDF(x = 220\text{m})$  is used, which has been found to work reasonably well over the whole simulated energy range.

Figure 5.20 shows the correlation of this parameter with the simulated energy for different primary particle species, using the standard layout dataset. As expected, there is a good correlation between the recorded light levels and the energy, and the spread of  $LDF(220\text{m})$  for a given energy is rather small. The solid red line shows the calibration curve used in the energy reconstruction. It is obtained by calculating the median values of MC energy and  $LDF(220\text{m})$  in every energy bin (using six bins per decade) and interpolating linearly between these points. The median is preferred to the average value here (and in the following reconstruction steps) since it is more robust against outliers resulting from a bad LDF fit. The plot also shows that for a given energy the light yield is smaller for protons than for gamma-rays, and even smaller for heavier particles such as iron nuclei. This effect is caused by the smaller number of electrons produced in a hadronic air shower compared to a gamma-ray induced air shower of the same energy (see also figure 2.10 in section 2.4.2).

**Systematic bias in the reconstruction** Figure 5.21 shows the relative bias of the reconstructed energy obtained with the previously shown calibration curve, defined as

$$\frac{\Delta E}{E} = \frac{E_{reco} - E_{MC}}{E_{MC}} \quad (5.23)$$

No systematic bias is visible in the energy reconstruction of gamma-rays in the energy range from 50TeV to 5PeV. Below 50TeV the event statistics are low, but the results seem to indicate an overestimation of the energy close to the threshold. It can be explained as a selection effect, since at energies close to or below the threshold (depending on the actual definition of the threshold) only exceptionally bright events pass the trigger conditions. The systematic underestimation of the energy of cosmic ray particles is also clearly visible in this plot. In relative terms, it decreases with energy.

Figure 5.22 shows the median of the relative energy error in each energy bin for all five simulated particle species. The selection effect is clearly visible not only for gammas, but also for protons, helium and nitrogen nuclei close to their respective thresholds. The median energy shift becomes as large as 60% for iron nuclei around 120TeV, which means that the reconstructed energy amounts to only 40% of the actual energy of the particle in this case.

When deriving an all-particle cosmic ray energy spectrum from the measurements of the  $H_i$ SCORE detector, it is important to take this systematic bias into account. Since each particle species has a different bias, a composition of cosmic ray particles has to be assumed to generate the all-particle spectrum. The

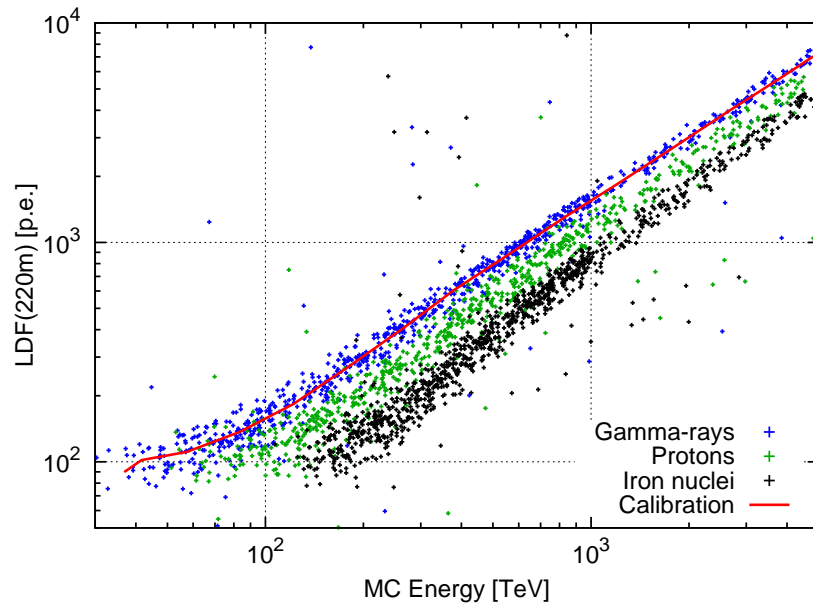


Figure 5.20: Correlation of  $LDF(220m)$  with the simulated energy for air showers induced by gammas, protons and iron nuclei. The solid red line shows the calibration used in the reconstruction. Only every tenth data point is shown for clarity.

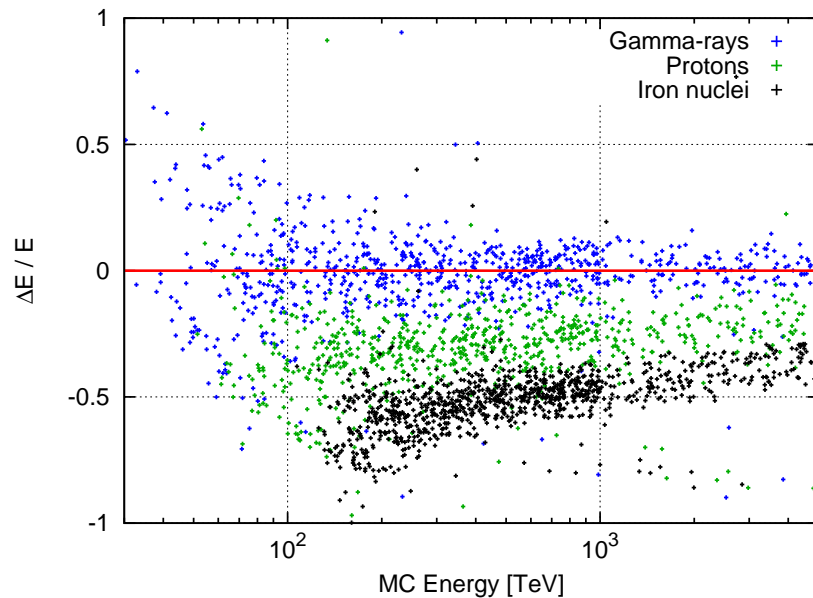


Figure 5.21: Relative error in the energy reconstruction  $\Delta E/E$  (see equation 5.23) versus the simulated energy. Only every tenth data point is shown for clarity.

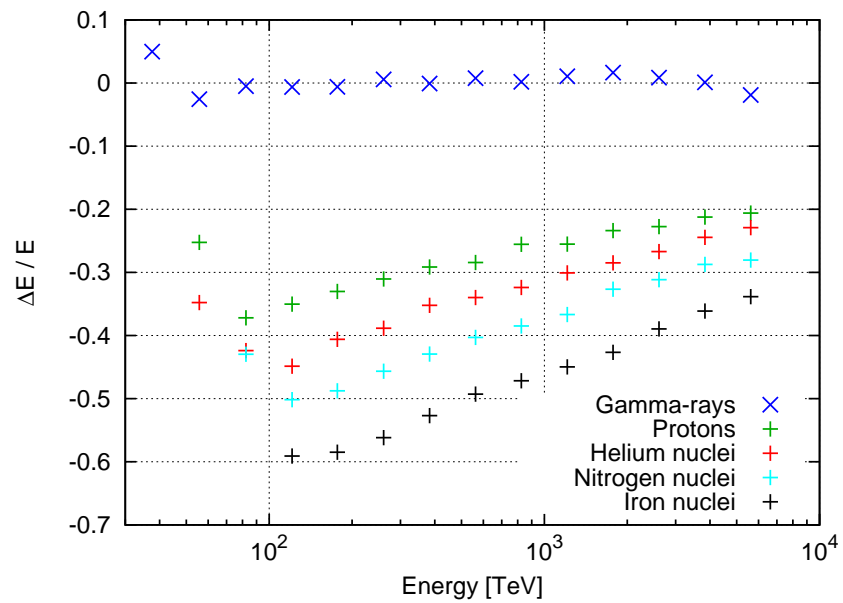


Figure 5.22: The median of the relative energy error versus MC energy for all five simulated particle species. Only data points with at least ten events are shown.

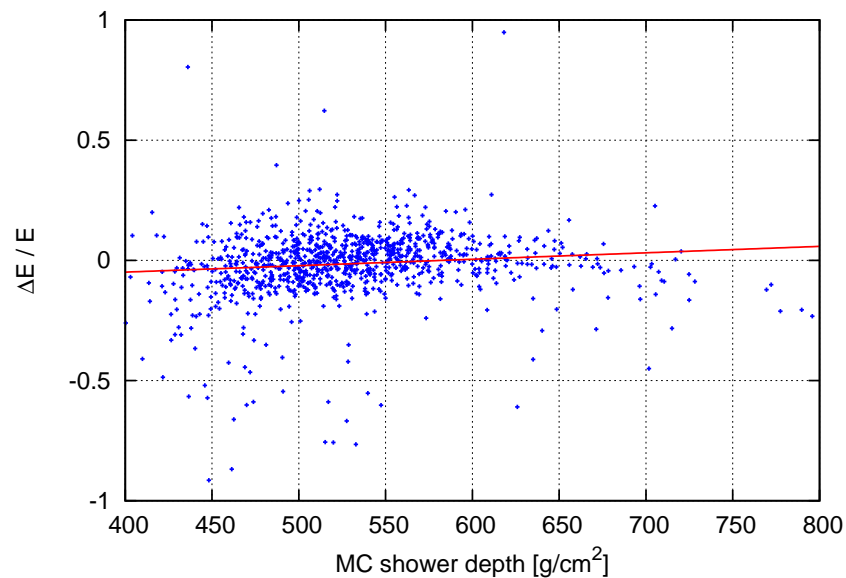


Figure 5.23: Relative error in the energy reconstruction  $\Delta E/E$  for gamma-rays versus the MC shower depth. The solid line shows a linear fit to all data points (slope  $m = 0.00027$ ). Only every second data point is shown for clarity.

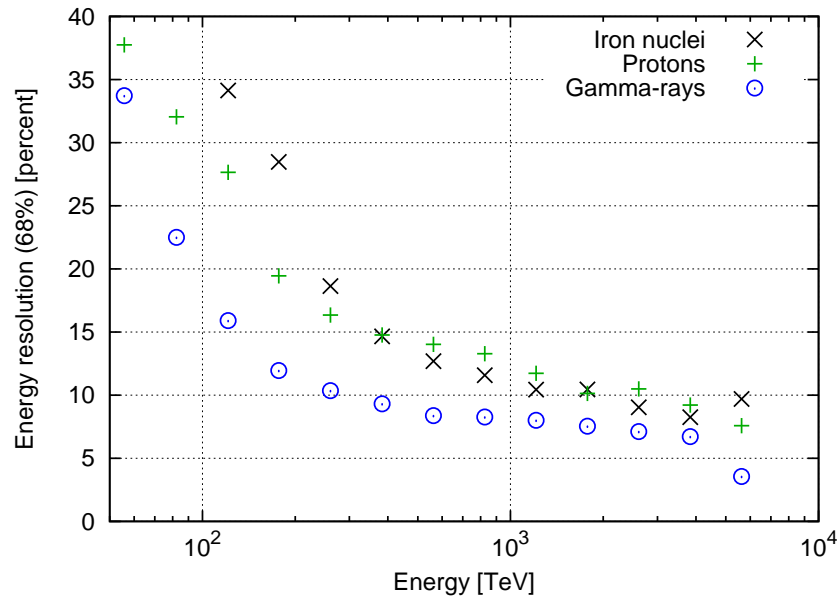


Figure 5.24: Energy resolution (68% containment) for gamma-rays, protons and iron nuclei versus MC energy.

energy bias is also important when calculating the instrument sensitivity to gamma-ray sources, since in the analysis the background for a given gamma-ray energy consists of cosmic rays with a higher energy (see sections 5.5.5 and 5.6.4).

Figure 5.23 shows the relative error in the energy reconstruction for gamma-rays as function of the MC shower depth. It can be seen here that the chosen parameter  $LDF$  (220m) depends indeed only weakly on the shower depth, as stated in the beginning of this section. A linear fit to all data points shows a slope of 0.02 per 100 g/cm<sup>2</sup>. The fit is however dominated by events with small shower depths, and above about 500 g/cm<sup>2</sup> the slope of the energy bias is significantly smaller and finally even becomes negative. It seems reasonable to assume that an event reconstruction that derives both the particle energy and shower depth at the same time, using the full LDF information, might improve the reconstruction accuracy of both parameters. This has however not been tested here.

**Energy resolution** Figure 5.24 shows the relative resolution of the energy reconstruction (68% containment region for  $|\Delta E/E|$ ) for gamma-rays, protons and iron nuclei. The resolutions for helium and nitrogen primaries are similar to the one for protons and therefore not shown. For cosmic rays, the reconstructed energy is corrected using the systematic shift shown in figure 5.22 before calculating the resolution. In reality, this is not possible for individual events, but a general correction using an assumed composition can be applied, and the energy resolution after this correction should be similar to the values shown here. For gamma-rays, the energy resolution is calculated using the standard calibration without corrections. Their energy resolution is about 35% near the threshold and improves to below 10% at higher energies. The energy resolution for gamma-rays is superior to those for cosmic rays at all energies, which is probably due to the smaller amount of light generated by cosmic rays at the same energy and the larger fluctuations in the development of hadronic air showers.

#### 5.4.5 Vertical position of the shower maximum

The vertical position of the shower maximum, i.e. the height at which the number of relativistic particles in the shower and therefore also the emitted Cherenkov light reach their maximum, is an important quantity in

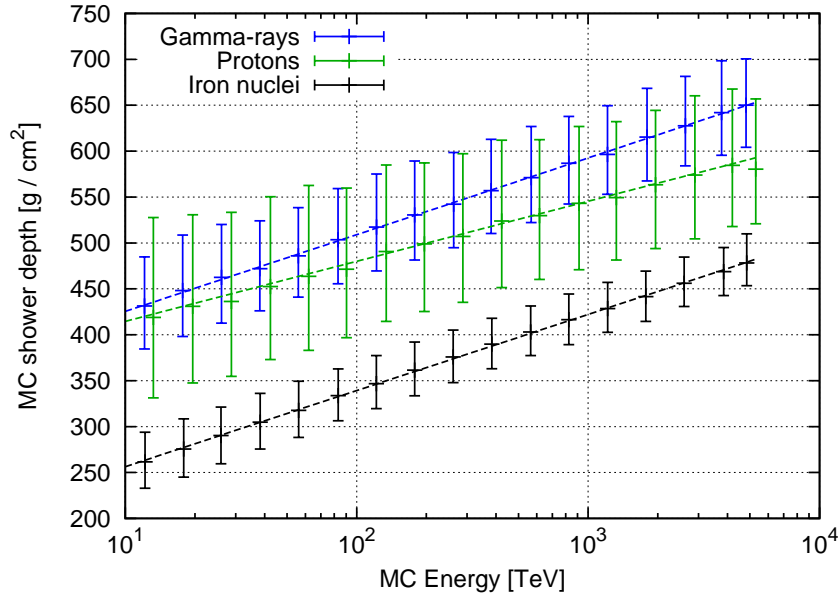


Figure 5.25: Median depth of shower maximum versus energy for showers induced by gamma-rays, protons and iron nuclei, as given by the CORSIKA simulations. The error bars denote a 68% containment region centred on the median. The dotted lines are the best fit to the average values. The data points for protons are shown at 10% above their actual energies for better visibility.

the event reconstruction. While not of immediate interest (as are the direction and the energy of the particle), it is a useful parameter for the separation of gamma-rays from cosmic rays (hadrons), and the estimation of the particle mass in case of a hadron. It may also be used for particle physics, mainly for the determination of cross-sections of nuclei with air, if a sound assumption for the cosmic ray composition can be made.

Different ways of expressing the position of the shower maximum exist in the literature: It can be defined by its height above sea level or above the detector level, or by the airmass above or below it. Here it will always be given as atmospheric depth  $X$ , i.e. the air column the shower has already traversed since it started at the top of the atmosphere, in units of  $\text{g}/\text{cm}^2$ . It is obtained by integrating over the air density  $\rho(z)$  from the height of maximum  $z_0$  to infinity:

$$X = \frac{1}{\cos \theta} \int_{z_0}^{\infty} \rho(z) dz \quad (5.24)$$

The factor of  $1/\cos(\theta)$  is needed to account for the additional air-mass traversed by inclined showers.

Using the standard barometric formula for the air density,  $\rho(z) = \rho_0 \exp(-z/h_0)$ , the depth can be calculated by

$$X = \frac{1}{\cos \theta} \rho_0 h_0 \exp\left(-\frac{z_0}{h_0}\right) \quad (5.25)$$

where  $\rho_0 = 0.001225 \frac{\text{g}}{\text{cm}^3}$  is the density of air at sea level and  $h_0 = 8400 \text{m}$  [US Standard Atmosphere, 1976].

The advantage of this number is its independence of atmospheric conditions, observation level and inclination of the shower. Its disadvantage is that the calibration parameters in the depth reconstruction depend on the detector altitude and must be adjusted if the altitude changes (which will not happen with the real detector, but may be done easily in the simulations to study the impact of the observation level on the detector performance).

Figure 5.25 shows the average shower depth as function of energy for different simulated primary particle species as given by the CORSIKA simulations. As expected from the discussion in section 2.4.2, it

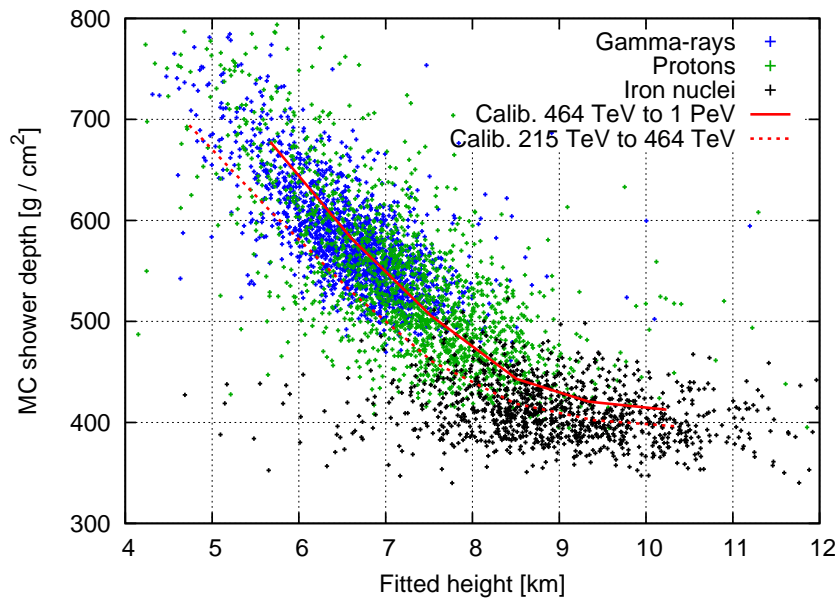


Figure 5.26: Correlation of emission height obtained from the arrival time fit and the MC shower depth for gammas, protons and iron nuclei with simulated energies between 464 TeV and 1 PeV. The solid red line shows the calibration used for the depth reconstruction in this energy range. For comparison, the dotted line shows the calibration curve of the next lower energy bin, from 215 TeV to 464 TeV.

increases logarithmically with energy and decreases with particle mass. The event-to-event fluctuations of the depth are also different for the individual particles, largest for protons and smallest for iron nuclei. These differences can be used to estimate the average mass of measured cosmic rays, thus obtaining insights to their composition, and to separate gammas from cosmic rays. This is discussed further in section 5.5.

In the following, different methods to experimentally measure the shower depth (reconstruction step 8) will be discussed. The methods are compared quantitatively towards the end of the section.

**Timing method** As mentioned in section 5.4.3, the fit to the arrival times also yields an estimate of the height of maximum Cherenkov light emission, i.e. the shower maximum (see also figure 5.15). Figure 5.26 shows the correlation of this height parameter from the arrival time fit with the MC shower depth for three different particle species in the energy range from 464 TeV and 1 PeV. The correlation is clearly visible, and the different particles can be fitted with a single calibration curve. However, it turns out that the correlation is slightly energy dependent: At the same depth, the fitted height is lower for smaller energies. The scale of this shift is indicated in figure 5.26 by the calibration curve for the next lower energy bin. Towards higher energies, the energy dependence becomes weaker. In the depth reconstruction this is handled by using energy-dependent lookup tables. The tables are generated by determining the median depth for different values of the height parameter, using a combination of proton and iron events.

It should be noted that the correlation shown here assumes no time jitter between the detector stations and may deteriorate slightly for a non-ideal synchronisation. It should also be remembered that the height parameter used here is obtained by a fit to the signal *edge* times, not the peak times, and therefore gives the height of the beginning of the shower rather than the maximum. This is the reason why the correlation seen here is not described well by the known relation between the depth  $X$  and the height  $z$  (equation 5.25). The edge time and peak time are however correlated closely enough to justify this procedure.

**LDF method** It has been noted in many theoretical and experimental studies of air shower Cherenkov light detection that the depth of the shower maximum is correlated with the steepness of the lateral light density function (LDF). An early comprehensive overview is given in Patterson and Hillas [1983b], where computer simulations are used to explain the connection between the LDF slope and the shower depth. It was found that light emitted at small shower depths produces a roughly flat intensity distribution up to about 120 m at the observation level, while light emitted closer to the detector is centred closely around the shower core. Depending on the position of the maximum, the one or the other dominates and shapes the integrated LDF seen by the detector. The authors suggest two possible parameters for the shower depth estimation: The slope of the inner region of the LDF (30 – 125 m from the core) or the ratio of the light intensities at 50 and 150 m, i.e.  $LDF(50)/LDF(150)$ . Dawson *et al.* [1989] have used the steepness of the LDF out to 150 m to derive the shower depths in the analysis of data from the Buckland Park detector near Adelaide. The AIROBICC reconstruction also used the slope to determine the shower depth, however only within a range of 20-100 m due to the limited size of the array [Lindner, 1998]. More recently, data from the BLANCA detector in the United States [Fowler *et al.*, 2001] and the Russian TUNKA detector [Budnev *et al.*, 2005] was analysed using the steepness of the LDF to derive conclusions about the composition of cosmic rays at energies near the knee.

For  $H_i$ SCORE, the slope of the inner region is not well defined due to the large station spacing. Therefore, the ratio  $LDF(50)/LDF(220)$  is used for the depth reconstruction. Tests using other ratios, such as  $LDF(50)/LDF(120)$  or  $LDF(50)/LDF(150)$ , show that their performance is nearly the same, which is to be expected since the values of  $LDF(x)$  for  $x > 120$  m are strongly correlated through the LDF fit.

In principle, this step of the reconstruction could make use of the previously fitted LDF that was used for the core position reconstruction and the energy estimation. However, it turns out that the short standard integration window used for the signal intensity calculation (see section 5.4.1) introduces a bias to the slope of the LDF by cutting off the last part of long signals. Since the signal width increases with distance from the shower core (see also next paragraph), the signal intensities are systematically underestimated at far distances, and the slope of the LDF is overestimated. Furthermore, the signal widths depend also on the type of primary particle, which additionally impedes a use of the LDF for a (particle-independent) depth measurement. Therefore, the LDF is fitted again here, using a fixed core position and the signal intensities from the extended time window, which includes more than 99.5% of the total Cherenkov light arriving at the detector station.

Figure 5.27 shows the correlation of  $LDF(50)/LDF(220)$  and the MC shower depth for gammas, protons and iron nuclei in the energy range from 464 TeV and 1 PeV. The distributions for the different particles do not overlap perfectly: For a given shower depth, the slope of the LDF is slightly steeper for protons than for gamma-rays (especially towards smaller depths), and steeper again for iron nuclei. The calibration, indicated by the solid line, is optimised for protons.

The differences are believed to be due to the fact that air showers of cosmic rays, especially those of heavy primaries, develop a longer tail below the shower maximum than air showers induced by gamma-rays. At the same shower depth, cascades of heavy primaries contain more energy (the difference amounts to almost two orders of magnitude in the case of iron nuclei and protons, see figure 5.25), and carry more particles to lower altitudes. The light emitted at low altitudes appears close to the shower core and increases the slope of the LDF. Muons, that are produced in much larger numbers in hadronic air showers, penetrate deeply into the atmosphere (see figure 2.10 on page 28) and also produce Cherenkov light close to the shower core, thereby increasing the slope of the LDF additionally. Apparently these effects overcompensate the larger transversal momenta of particles in hadronic showers, which should lead to a flatter LDF.

A similar effect, although less pronounced, was seen in the simulations for AIROBICC [Haustein, 1996, section 4.2]. The reason for the deviations seen there being smaller may be the high altitude of the AIROBICC detector: It was located at about 2200 m above sea level, corresponding to an atmospheric depth of 800 g/cm<sup>2</sup>. As can be seen from figure 2.10, deeply penetrating muons and hadrons only contribute significantly to the overall number of relativistic particles at shower depths close to 1000 g/cm<sup>2</sup>. In the other

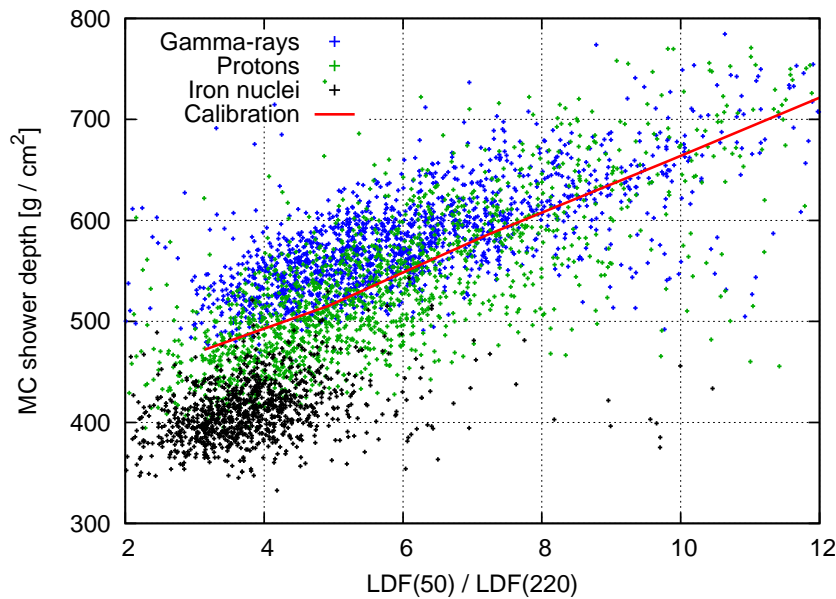


Figure 5.27: Correlation of the ratio  $LDF(50)/LDF(220)$  and the MC shower depth for gammas, protons and iron nuclei with simulated energies between 464 TeV and 1 PeV. The solid red line shows the calibration used for the depth reconstruction.

studies cited above no differences between different particle species were reported. The reason for this may be that most of them looked at higher energies, where the shower depths are larger and no long tail can develop below the maximum in any case. Also, most of them did not include gamma-rays in their simulations, for which the deviation is more obvious. A similar effect is seen in the depth reconstruction via the Cherenkov light signal widths (see next paragraph). The issue of the particle dependent shifts is discussed in more detail below (“Systematic offsets between particles”, page 126).

This depth reconstruction via the LDF exhibits no strong energy dependence. Only at energies near the threshold the LDF is slightly steeper than expected for a given shower depth. To include this effect, the lookup tables used in the LDF depth reconstruction are energy dependent as well. They are filled using only proton simulations, which leads to a systematic bias in the reconstructed depth for other particles.

In conclusion, the steepness of the LDF provides a sensitive measure for the shower depth, however with a significant offset between different particles.

**Width method** Another well-known parameter for the determination of the shower depth is the duration of the Cherenkov light flashes at large core distances ( $\gtrsim 200\text{m}$ ). Early experimental evidence for this dependence was found by comparing the reconstructed shower energy with the signal width at large core distances, assuming a priori that the maximum of showers with greater energy appears on average lower in the atmosphere [Thornton and Clay, 1978]. It was also used by Kalmykov *et al.* [1979] in the interpretation of air shower measurements with the Yakutsk detector. Patterson and Hillas [1983a] used their previously mentioned computer simulation to examine the sensitivity of the signal width to the shower development. They found that the lower the point of maximum emission is in the atmosphere, the larger is the spread of Cherenkov photon arrival times and thus the duration of the recorded pulses. At a given core distance, the signal width (FWHM) is found to increase almost linearly with shower depth. The sensitivity (i.e. the slope of the relationship) increases with core distance, on the other hand the signals are weaker at large core distances and the experimental error on the measured widths increases. This becomes an especially important issue when lower energies are addressed, where the total amount of Cherenkov light is small. In

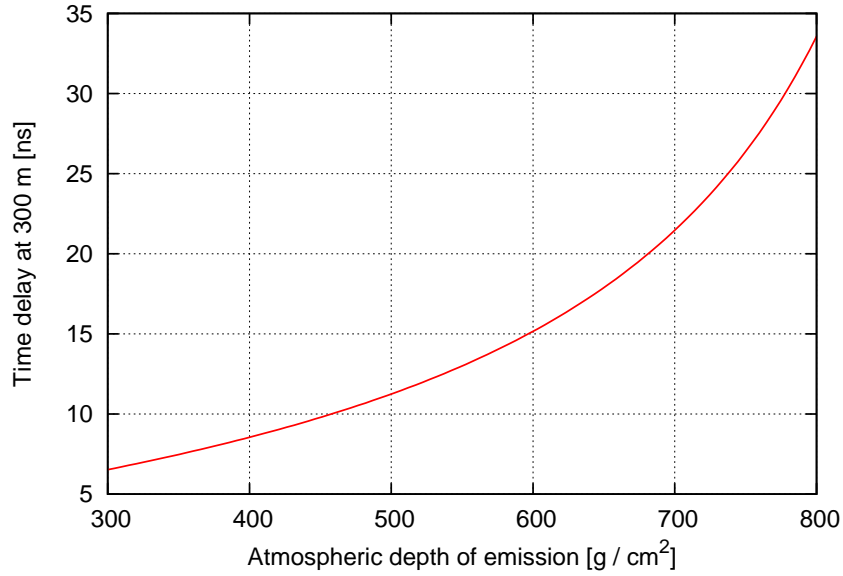


Figure 5.28: Arrival time  $T$  at 300m from the shower core versus the atmospheric depth of emission  $X$ , according to equation 5.20.

the AIROBICC experiment the widths within 200m from the core were used to derive the depth of maximum for events with energies between 500TeV and 5PeV [Haustein *et al.*, 1995]. In the TUNKA analysis, the FWHM at 400m from the core is used [Korostelev *et al.*, 2009].

The reason for the sensitivity of the signal width to the position of the maximum can be explained using the arrival time model presented in section 5.4.3: At a given distance from the shower core, the arrival time is later for light emitted lower in the atmosphere (see figure 5.15). For sufficiently large core distances ( $r \gtrsim 200$ m), the longitudinal development of a shower is mapped onto the arrival times of photons: Light emitted before the shower maximum is registered at early, light emitted after the maximum at late times. If the height  $z$  in equation 5.20 is substituted by the atmospheric depth of the emission  $X$  (using equation 5.25), one finds that the arrival time function  $T(X)$  is not linear, as shown in figure 5.28.

Consider now an air shower cascade that reaches half of its maximum number of particles (and thus of its light emission) at  $X_{start}$  (above the maximum) and decays to half its intensity at  $X_{end}$  (below the maximum). The FWHM of the Cherenkov signal is then, to first approximation, given by  $\Delta T = T(X_{end}) - T(X_{start})$ . For a given particle, the air shower development is usually rather independent of the shower depth, and  $X_{end} - X_{start}$  can be considered constant. However, due to the non-linear shape of  $T(X)$ , the signal width  $\Delta T$  depends on the shower depth: The larger it is, the larger will be  $\Delta T$ .

Since the measurement of the signal width at a specific core distance is not possible for every shower, a function  $W(r)$  must be fitted to the distribution of the signal widths to obtain the width at a certain distance. Different candidates for  $W(r)$  have been suggested, most of them either linear [Thornton and Clay, 1978; Henke, 1994], following a power law [Kalmykov *et al.*, 1977] or an exponential function [Prosin *et al.*, 2009]. It should be noted that the linear relationship was usually found when looking at rather low energies (TeV to PeV) while the other shapes are from studies at higher energies (multi-PeV). For the  $H_i$ SCORE event reconstruction presented here, a linear fit is used.

At energies below a few hundred TeV the use of the signal width as shower depth estimator is rather challenging, as very little light is captured at the large core distances needed for this analysis, and the determination of the signal width is prone to large errors. Therefore, the signals from detectors at similar core distances are added up before calculating the signal width (*signal stacking*). This is made possible

by the expected very good time resolution and direction reconstruction of the H<sub>i</sub>SCORE experiment. The optimal size of the distance bins depends on the energy (at higher energies, the bin size can be reduced as there is more light in every station) and on the core distance (at larger distances, larger bins are needed to include enough signal intensity), but here a constant value of 50m is used. This results in a linear increase of included stations with distance, and leads effectively to a flatter decrease in signal intensity. Additionally, the signal is smoothed by averaging over five adjacent time bins before calculating its FWHM (which is done in reconstruction step 6).

Despite the signal stacking, signals beyond 400m are usually too small for medium energies, and are not used in the fit of  $W(r)$ . Data points at distances below about 150m are excluded as well, as the Cherenkov light flash is considerably shorter than the response function of the instrument in this regime. Here, the measured widths are constant with  $r$  and  $X_{max}$  and merely reflect the instrumental time response.

Figure 5.29 shows an example of two gamma-ray events with the same energy, but different shower depths. The signal widths are shown after stacking, and linear fits are applied to the distributions. As expected, the event with the larger shower depth (i.e. lower height of maximum) generally produces longer signals than the other. The difference in signal widths increases with core distance.

The fitted width at 300m from the core, i.e.  $W(300\text{m})$ , is used here for the depth reconstruction. Its correlation with the MC shower depth is shown in figure 5.30 for the different particle species in the energy range from 464TeV and 1 PeV. The picture is similar to the one found with the LDF method: The width parameter is well correlated to the shower depth, however the calibration is different for the different particles. At the same depth, hadronic showers, especially of heavy primaries, produce a longer Cherenkov signal. To be compatible with the LDF method, the calibration is optimised for protons. No strong energy dependence is found, nevertheless energy dependent lookup tables are used to obtain the optimal correlation.

The deviations seen between different particles here are related to the ones seen when using the LDF for depth reconstruction. As mentioned in that context, cosmic rays, and especially heavy nuclei, produce a longer cascade below the maximum than gamma-rays. The signal width reflects that, as it is significantly longer for iron nuclei than for gamma-rays at the same depth. Generally, protons also produce longer signals than gamma-rays, except for deeply penetrating showers whose bottom part may not be seen by the detector: Due to the angular acceptance of the Winston cones, the last 700 to 800m (corresponding to depths below 920 g/cm<sup>2</sup>) of a vertical shower are not seen at 300m distance from the shower core. For non-vertical events, the cut-off height is even higher for detectors on the far side of the core.

In conclusion, the signal width at 300m from the shower core is a complementary method to measure the shower depth, that is however correlated with the depth obtained by the LDF and shows the same bias between particles.

**Spectrum method** Since the absorption of light in the atmosphere depends on the wavelength and on the height, it is in principle also possible to deduce the height of maximum emission from the measured Cherenkov light spectrum. Figure 5.31 shows the transmission of UV, blue and green light versus the emission height. The UV light is absorbed quickly, and all UV light seen at the observation level must originate from very low altitudes. It can therefore be used to gain information about the latest stages of the shower development, which is discussed in section 5.5.4, but it is not useful to estimate the depth of the shower maximum. Here, only the blue and green channels will be discussed.

When emitted at 6km, about 62% of the blue and 84% of the green light arrives at the ground. For light emitted at 8km, these numbers change to 57% and 82%, which is a slightly different ratio. As the shape of the Cherenkov light spectrum at the emission is always the same (roughly a  $\lambda^{-2}$  dependence in the visible wavelength regime), the ratio between blue and green light seen on the ground should be slightly different for different emission heights.

Figure 5.32 shows the Cherenkov light spectra at the detector (including the detector response function) for gamma-ray showers in different depth ranges. As expected, the showers evolving high up in the atmo-

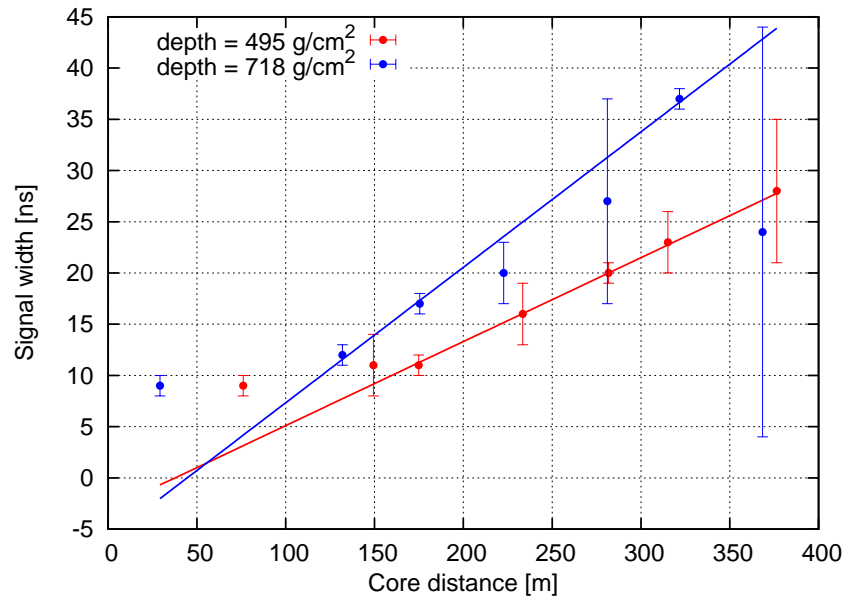


Figure 5.29: The signal width versus core distance for the same two events shown in figure 5.10 (gamma-rays with 750 TeV energy). Signals from similar core distances are added up before calculating the width (signal stacking). The errors are estimated using an empirical function of the signal intensity. The solid lines are linear fits between 150 and 400 m.

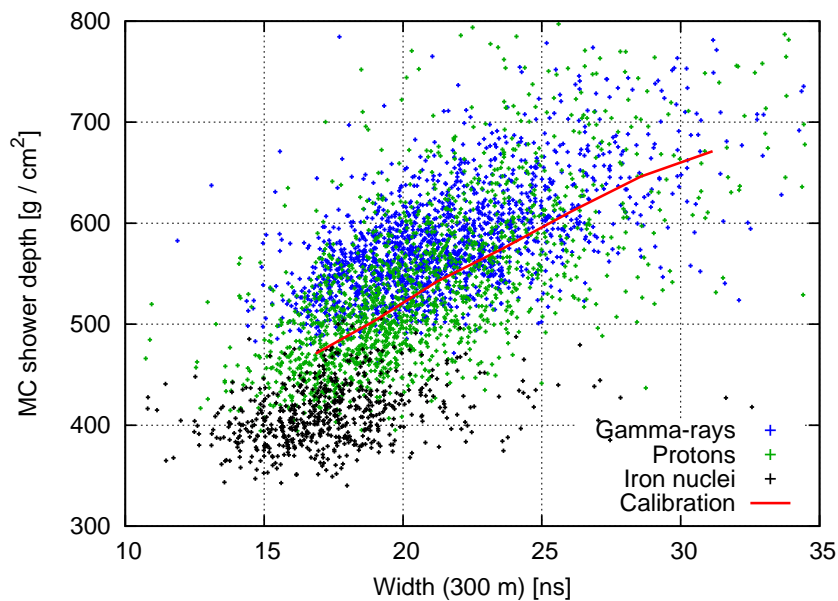


Figure 5.30: Correlation of the signal width at 300m from the shower core with the MC shower depth for gamma-rays, protons and iron nuclei with energies between 464 TeV and 1 PeV. The solid red line shows the calibration to protons in this energy range.

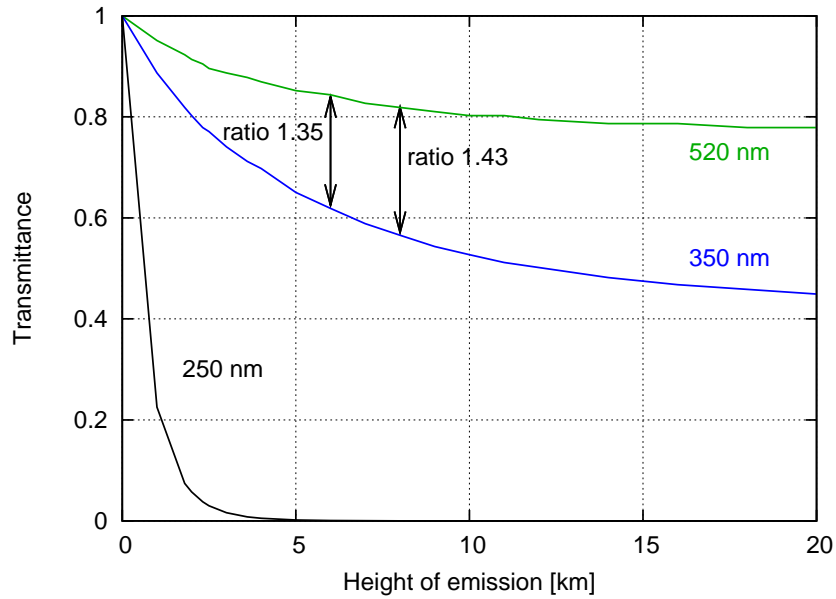


Figure 5.31: Atmospheric transmission used in the simulation for three different wavelengths versus the height of light emission [Kneizys *et al.*, 1996].

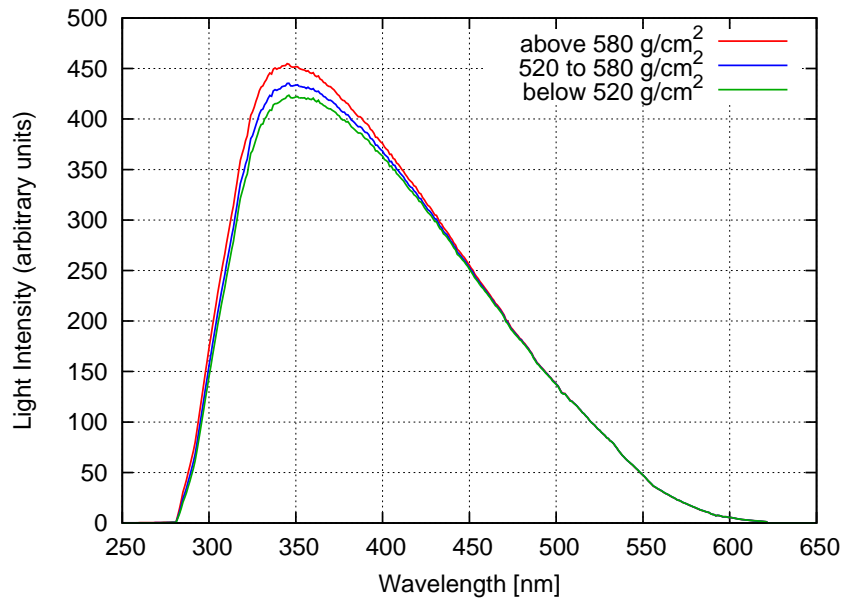


Figure 5.32: Averaged Cherenkov light spectra of 4000 gamma-ray showers between 100 TeV and 1 PeV for different shower depth ranges. The wavelength dependent response function of the detector is included. The spectra are normalised to 100 at a wavelength of 520 nm.

## 5 $H_i$ SCORE simulations and event reconstruction

sphere (small shower depth) show a deficit of blue light compared to showers evolving late. The largest difference is seen around 350nm and amounts to a little more than 5% for the highest and lowest maxima. If the detector response function is not included, the largest difference is seen around 320nm and amounts to about 10% (not shown).

To test whether this difference can be exploited for a measurement of the shower depth, the stations in the detector simulation are altered to include two extra channels, one sensitive to blue light, the other to green light. The acceptances of the two channels are modelled according to standard astronomical Johnson B and V filters with wavelength midpoints at 356 nm and 551 nm (for transmission curves, see e.g. Omega Optical [2010]). Apart from the wavelength filters, the channels are identical to the standard channels, i.e. using the same Winston cone acceptance and the same PMT response function. The signals are stored separately from the standard signal and are processed in the standard way in the event reconstruction. The ratio of their signal intensities is used as shower depth estimator.

Two possible scenarios are tested: In the first one, only the U to V ratio at the central detector station (i.e. the detector nearest to the reconstructed shower core) is used, in the second one the U and V intensities of all stations are added up before calculating the ratio. It turns out that neither method is sensitive enough to be used as a depth estimator. Any possible correlation between the U to V ratio and the MC shower depth is lost under large event to event fluctuations.

Additionally, the spectra were tested for possible differences between different particles, but no difference was found: When using showers with approximately the same shower depth, the spectra of different particles are nearly identical. The use of the UV content of the Cherenkov light for particle identification is discussed in section 5.5.4.

### Comparison of different methods

**Systematic offsets between particles** Except for the spectrum method, all examined methods provide a reasonable measure of the depth of the shower maximum. However, a systematic bias between particles is present, to a certain degree, in all three methods. The LDF and the width method are correlated, as they are both sensitive to the whole length of the particle cascade. Consequently, these two methods show an overestimation of the shower depth for hadronic events, especially if induced by heavy elements, as these produce a longer tail below the maximum. The timing method, on the other hand, is sensitive only to a specific point in the shower development: The maximum, if peak times are used in the arrival time fit, or the point where the light emission reaches half of its maximum, if edge times are used (as done here).

Figure 5.33 shows the energy and particle dependent shifts between the reconstructed and true depths for the three methods. The protons show almost no offset in the LDF and the width method, as the calibration was optimised to them. In the timing method, the calibration also included iron, and at small energies this produces a significant offset for protons (which is, as it must be, counterbalanced by a roughly equally large offset to the other direction for iron nuclei). In all three methods the depth of iron showers is strongly overestimated, as expected, but in the timing method the shift is significantly smaller. The depth of gamma showers is systematically underestimated in the LDF and width method. In the timing method, their shift shows a peculiar behaviour: At energies up to about 800 TeV it is negative, but decreasing, above that energy it increases to positive values and approaches the same level as for iron events.

The values are shown only up to 3 PeV, since above that energy the lookup tables for the reconstruction are affected by the end of the simulated energy range at 5 PeV.

Generally, the shifts are very similar in the LDF and width method, but quite different in the timing method. This can be exploited for a particle separation scheme, as will be discussed in the following section. If the depth itself is of interest, an assumption of the composition of the events must be put into the calculation.

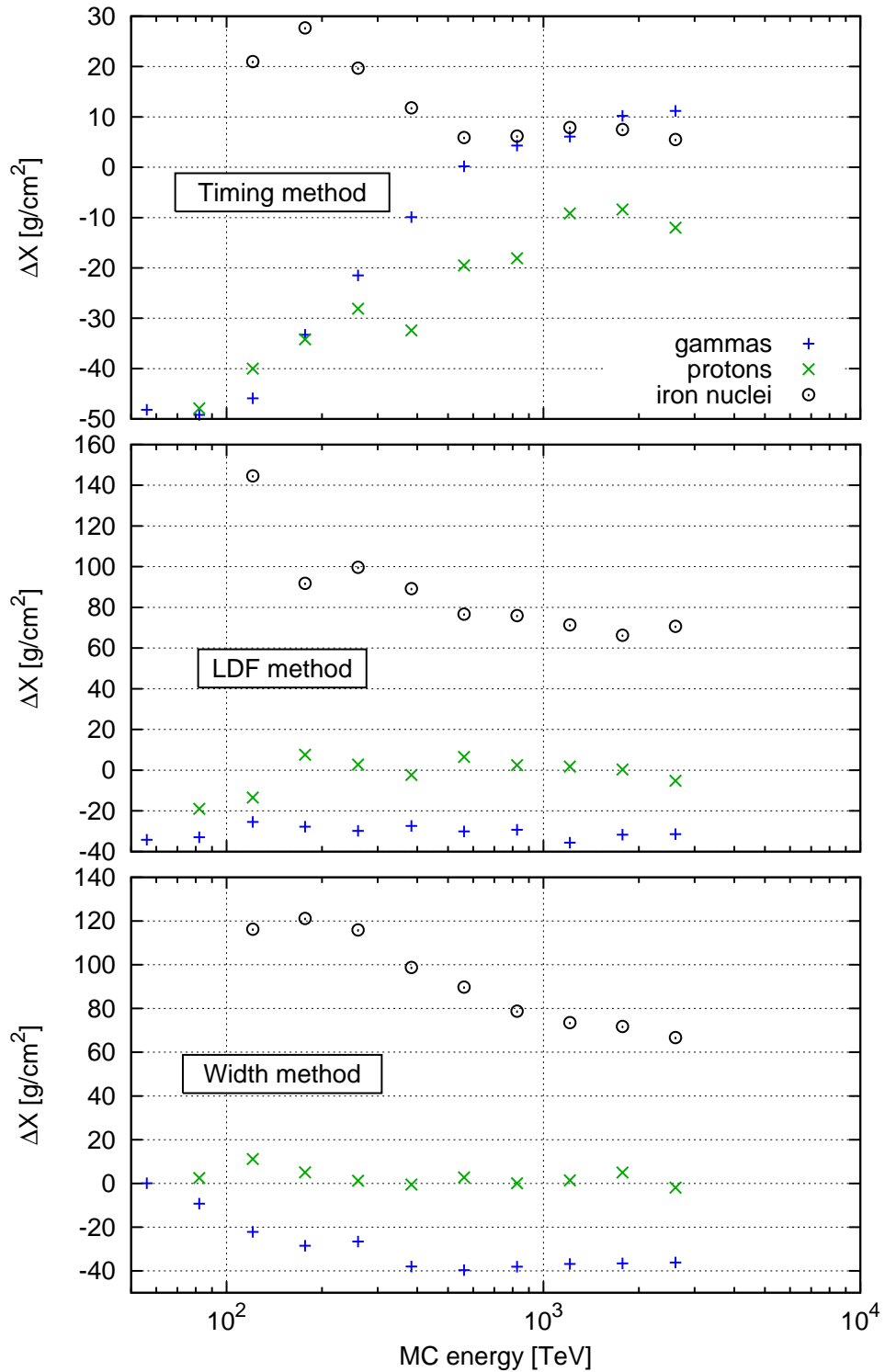


Figure 5.33: Systematic bias in the depth reconstruction for gammas, protons and iron nuclei for the timing method (top panel), the LDF method (centre) and width method (bottom). The deviations are given as  $\Delta X = X_{reco} - X_{MC}$ . Only data points generated with more than 100 events are shown.

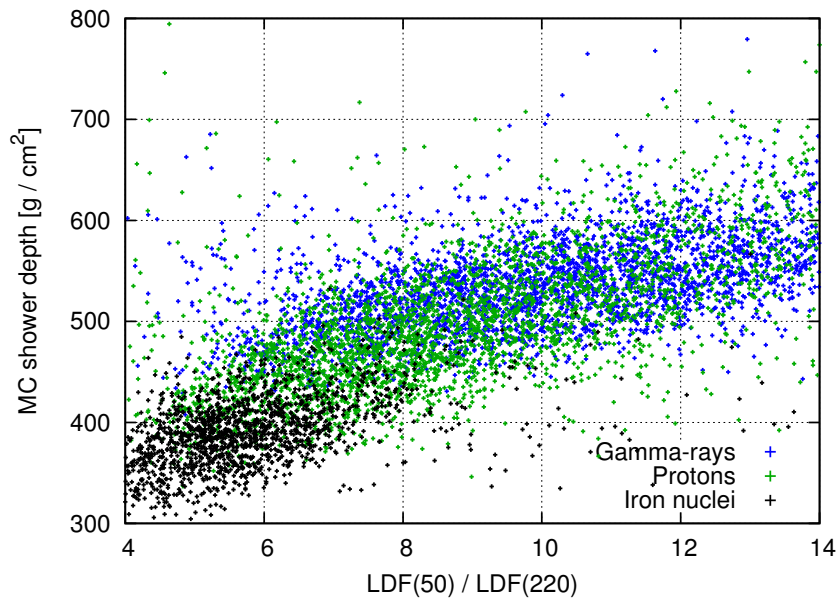


Figure 5.34: Correlation of the ratio  $LDF(50)/LDF(220)$  and the MC shower depth for gammas, protons and iron nuclei with the detector at an altitude of 2000m.

It is remarkable that the systematic shifts between the particles seen here in the LDF and width methods do not appear in other simulation studies or experiments such as BLANCA [Fowler *et al.*, 2001] or TUNKA [Korostelev *et al.*, 2009]. One reason might be the different energy and thus depth range of these experiments combined with a higher altitude, which makes the shower development below the maximum less important. Another reason might be the coarser sampling of the LDF in  $H_i$ SCORE, which leads to the inner part of the LDF often being defined by one or very few data points. It also means that the innermost part, below 30m from the core, cannot be systematically excluded as it was done in the BLANCA analysis. Inclusion of these points adds a strong sensitivity of the last part of the shower development to the LDF method.

To check the effect of these differences, additional simulations are carried out for a detector with a station spacing of only 20m. To eliminate effects of the detector acceptance, all photons arriving at the detector were used in the analysis, i.e. the Winston cone and PMT acceptances were not used. Both the ratio  $LDF(50)/LDF(220)$  and the slope of the inner region were tried as parameters, and the inner 30m were excluded from the fit. In all cases, the offsets between the particles remained, sometimes even more pronounced than in the standard configuration.

In another set of simulations, the standard layout detector was elevated to an altitude of 2000m above sea level. In this case, the reconstructed depths show almost no offsets between particles, no matter which parameter is used. In figure 5.34, this is illustrated for the correlation between the LDF ratio and the MC depth. This shows that the main reason for this offset to remain undetected in other studies was indeed the higher altitude looked at. The only other simulation study for a sea level detector, by Patterson and Hillas [1983b], contained only proton primaries, so that no offsets between particles could be detected.

In conclusion, this means that a low altitude is not ideal for a wide angle Cherenkov detector, if the depth of the shower maximum is of primary interest. On the other hand, the observed offsets can be used for particle discrimination, which is of great importance for the use of  $H_i$ SCORE as a gamma-ray observatory (see section 5.5). As the main focus of  $H_i$ SCORE is on gamma-ray astronomy, a low altitude seems to be suitable under this aspect. However, the present work did not study the potential for gamma hadron separation at a high altitude, so that no quantitative comparison can be made.

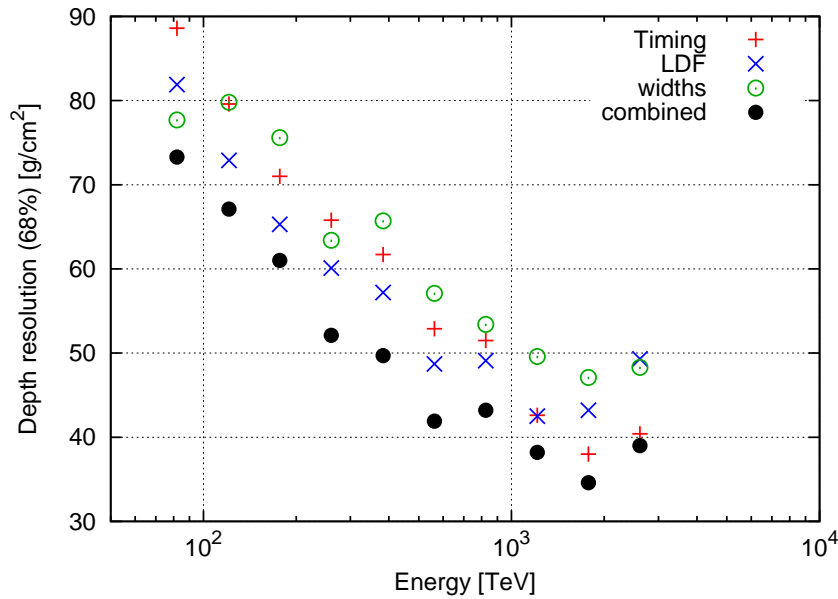


Figure 5.35: Resolution of the different depths methods described in the text, given as 68% containment region, for proton events. The statistical uncertainties amount to about  $\pm 5\%$ .

**Reconstruction accuracy** To judge the accuracy of the different methods in the depth reconstruction, the resolution of the depth reconstruction for protons is shown in figure 5.35. It should be noted that at low energies the resolution of the timing method is slightly better than it appears here, as the error originating from the systematic bias is not subtracted. The plot also contains a combined depth value, which is obtained by averaging over all available depth estimations for each individual event. This method turns out to produce slightly better results than the individual methods alone. Compared to the previous performance plots (core and direction resolution, energy resolution) the calculated depth resolution shows larger fluctuations. This is due to the low statistics in some bins of the two-dimensional lookup tables used in the reconstruction: To obtain a reasonable coverage, all bins with at least thirty events are used.

All individual methods achieve roughly the same accuracy, and all improve significantly with energy due to the better accuracy of the signal parameters at higher energies. This energy dependence is more pronounced here than it is for e.g. core position or direction reconstruction, as the most sensitive parameters for the depth reconstruction are obtained at large core distances where only little Cherenkov light is available. At larger energies than simulated here, a further improvement of the depth reconstruction is anticipated from the trend of the shown data. Additionally, at higher energies the fits to the time structure and the signal widths could be extended to core distances beyond 400 m, yielding more sensitive parameters (e.g. signal width at 500 m), which should additionally improve the depth reconstruction.

## 5.5 Particle separation

In general, the particle separation, especially the identification of gamma events against the large background of cosmic rays, is always a complicated task for indirect, ground-based experiments. The type of primary particle imprints a signature on the development of the air shower, however the differences are hard to measure and partly lost in event to event fluctuations. Two general approaches exist: First, the use of the lateral development of the shower, which exploits the fact that secondary particles show a larger transversal momentum in hadronic showers. This goes back to methods developed by Hillas [1985] for the Whipple telescope and is used to great success in atmospheric Cherenkov telescopes today (see e.g. Aharonian *et al.*

## 5 $H_i$ SCORE simulations and event reconstruction

[2006c]; de Naurois and Rolland [2009]; Lemoine-Goumard *et al.* [2006]). Essentially, the larger transversal spread of particles appears as a broader, sometimes patchy image in the telescope cameras (see also image 3.4 in section 3.2). Second, the longitudinal development of the shower can be used, i.e. the shower depth and the shape of the cascades below the maximum. This is the main information available in wide-angle Cherenkov detectors, as the longitudinal development is mapped to the LDF and the width distribution.

In general, wide-angle detectors do not achieve the same performance in gamma hadron separation as Cherenkov telescopes, which constitutes one of their major drawbacks. In the analysis of the wide-angle Cherenkov detector AIROBICC it was tried to overcome this weakness by using additional information from the HEGRA particle detectors [Arqueros *et al.*, 1996; Lindner, 1998]. Another method tested there uses a change of slope within the inner 120 m of the core position as parameter. Both strategies are not available for the  $H_i$ SCORE detector in the version currently planned. Additional muon detectors or denser array regions may be installed in the final set-up, however these measures are expensive and effectively reduce the size of the detector achievable at a given budget. Therefore, it will be tried here to develop a particle separation scheme which relies purely on the Cherenkov light signals sampled by the regular  $H_i$ SCORE set-up.

The main parameters used here to experimentally determine the differences in the longitudinal development are the reconstructed depth and energy, and the rise time of the Cherenkov light signal. Other methods that have been found to be not as effective will be sketched out briefly. Finally, two methods to combine the different parameters into a single cut are introduced and tested with respect to their separation power.

### 5.5.1 Separation using depth reconstruction bias

As can be seen from figure 5.33, the different depth reconstruction methods produce different systematic biases for different particles. While the offsets are similar in the LDF method and the width method, the shifts from both these methods differ significantly from the (rather small) bias in the timing method. Therefore it can be expected that for an individual event the difference in the reconstructed depth values can be used to estimate the primary species. Here, the parameter  $X_{width} - X_{timing}$  is tested, which is expected to be larger for hadrons than for gamma-rays.

Figure 5.36 shows the distribution of this parameter for gamma, proton and iron induced events between 100 TeV and 1 PeV. It shows that the parameter is indeed larger on average for protons than for gammas, and even larger for iron nuclei. The overlap between the distributions is considerable, especially between gammas and protons, nevertheless this parameter enables a separation to a certain extent. The shape of the distributions implies that this parameter is especially useful for a rather loose cut, i.e. one that retains most of the gammas while cutting out some of the hadrons.

### 5.5.2 Separation using depth versus energy

As shown in figure 5.25 (page 118), the average depth of a shower depends on the type of the primary particle and its energy. If energy and depth are reconstructed with a sufficient accuracy, they can be used to distinguish between the particles. While the overlap between gammas and protons is rather large, the discrimination of heavier particles should be rather good.

In practice, the separation is complicated by the systematic shifts in both the energy and the depth reconstruction. The bias in the energy reconstruction shifts the heavy particles to smaller energies, the bias in the depth reconstruction to larger depths, thereby increasing the overlap of the distributions. To keep the latter effect as small as possible, only the timing depth is used here, as it shows the smallest bias (see figure 5.33).

Figure 5.37 shows the reconstructed depth versus the reconstructed energy for gammas, protons and iron together with their fluctuations (indicated by the error bars). It can be seen that the energy dependent bias distorts the linear dependence on  $\log(E)$  seen for the MC values. Nevertheless, a clear difference between gammas and iron nuclei exists. To use that difference for particle separation, the depth expected for gamma-

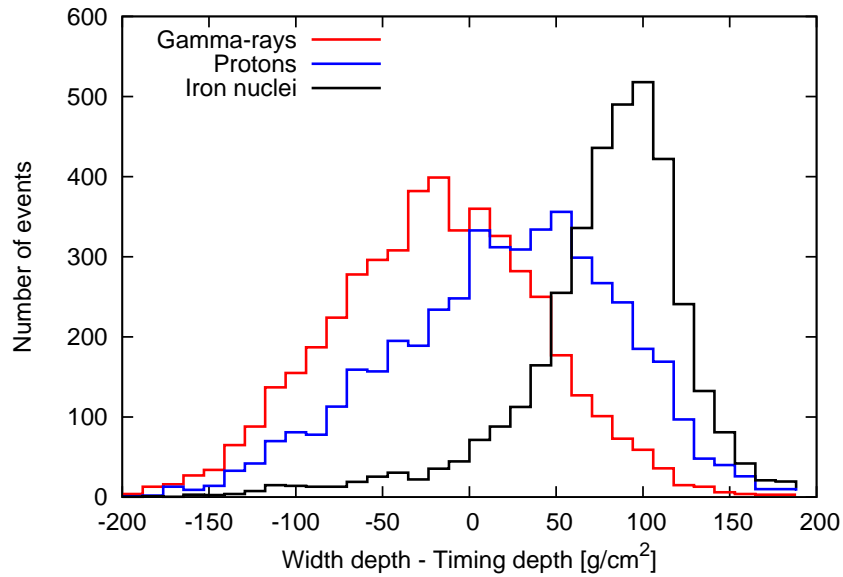


Figure 5.36: Distribution of the difference  $X_{width} - X_{timing}$ , i.e. the depths reconstructed using the width method and the timing method. The events used have passed acceptance cuts and have MC energies between 100 TeV and 1 PeV.

rays is parametrised by the best fit line (blue dashed line in the plot):

$$\frac{X_{exp}(E)}{[\text{g/cm}^2]} = 212 + 131 \log_{10} \left( \frac{E}{[\text{TeV}]} \right) \quad (5.26)$$

The cut parameter is then given by the difference between this expected depth and the depth reconstructed by the timing method. Figure 5.38 shows the distribution of this parameter for gammas, protons and iron nuclei with MC energies between 100 TeV and 1 PeV. The distributions are shifted against each other but have a large overlap, similar to the distributions of the previously introduced parameter.

### 5.5.3 Separation using signal rise times

The long tail of a hadron cascade is due to the larger content of both muons and hadrons in the shower. Muons are produced relatively high in the atmosphere and propagate largely unaffected to the observation level, emitting Cherenkov light at all stages. Hadrons propagate a certain distance through air which is determined by their mean free path (which is also energy-dependent), and initiate further sub-shower cascades at lower altitudes. As both muons and secondary hadrons they are still in the Cherenkov regime, i.e. travel faster than light in the surrounding medium, the light they produce low in the atmosphere (either directly or through sub-showers) arrives at the detector *earlier* than the light from the shower maximum.

The large fraction of muons and hadrons typical of a hadronic shower should therefore be detectable by light arriving before the main Cherenkov light peak. From the height of a typical air shower maximum a particle with speed  $c$  gains a few nanoseconds against light with speed  $c/n$ . With a perfect time resolution, this may well manifest in a pre-peak before the main peak, but with the time response assumed in the  $H_i$ SCORE simulations the effect is reduced to differences in the rise time (20% to 80%) of the signals.

The impact is most noticeable near the shower core, since especially the muons travel very close to the shower axis. Also, at larger core distances the longer geometric distance of light emitted at low altitudes makes up and finally overcompensates the faster velocity of muons and hadrons. Therefore, the parameter

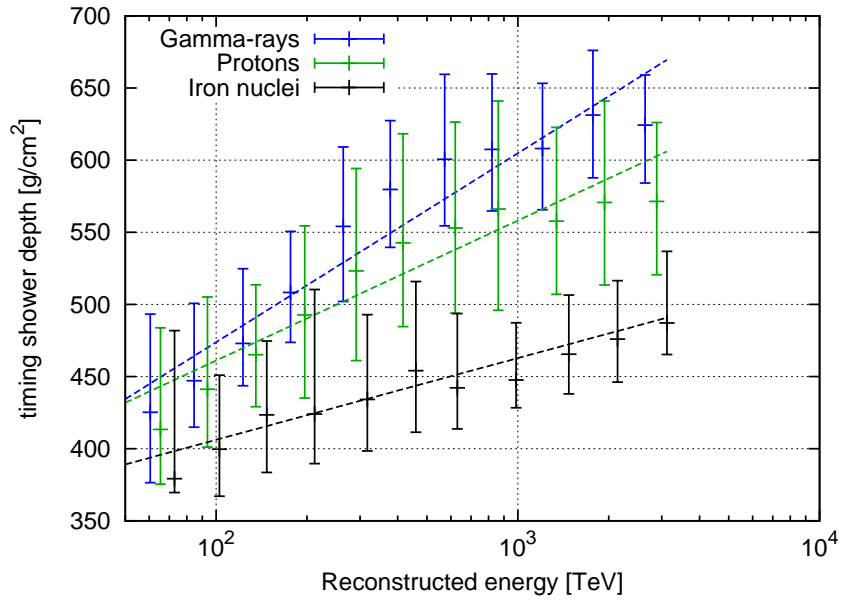


Figure 5.37: The median reconstructed depth (timing method) versus the reconstructed energy for gammas, protons and iron nuclei. The error bars indicate the fluctuations (68% region). Values for protons are shown at 10%, for iron nuclei at 20% higher energies for clarity.

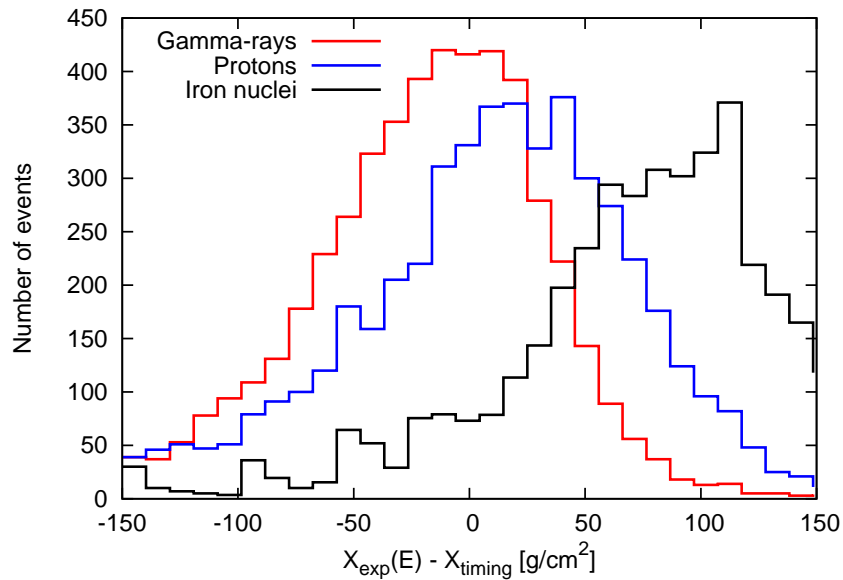


Figure 5.38: Distribution of the difference  $X_{exp} - X_{timing}$ , i.e. the difference between the depth expected for gammas and actual depth reconstructed by the timing method, for events with energies between 100TeV and 1PeV.

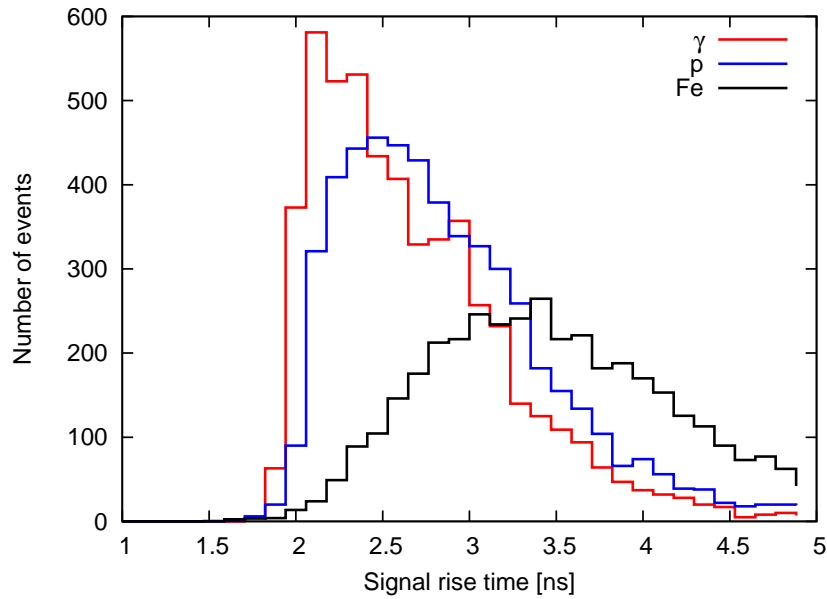


Figure 5.39: Distribution of the signal rise time of the central detector station for different particles for gammas, protons and iron nuclei with MC energies between 100 TeV and 1 PeV.

chosen here is the signal rise time of the central detector station, which is the station closest to the reconstructed shower core. If the core position is right in the middle of four stations, the nearest station(s) may be as far away as hundred metres, where the rise time effect is not as pronounced. It is therefore anticipated that this method would work even better if a closer station spacing was used.

Nevertheless, a significant difference in the central rise time is found in the simulations, with distributions of different particles again overlapping strongly (figure 5.39). The separation power seems to be roughly of the same order of magnitude as for the previously introduced parameters. This parameter seems to be especially effective to apply a strong cut that throws away almost all hadrons while retaining a sufficient number of gammas (using a cut value close to 2).

The use of the rise time as particle separation parameter has been suggested previously for the use in Cherenkov telescopes (see e.g. Razdan *et al.* [2002]), but due to its close correlation with the image shape recorded in the telescopes it was considered not useful [Aharonian *et al.*, 1997]. It seems however that in non-imaging detectors that do not see the wealth of information available in Cherenkov telescopes, the rise time can be a useful parameter for gamma hadron separation.

#### 5.5.4 Other methods

**The Cherenkov light spectrum** Looking back at figure 5.31, it can be seen that light in the UV regime, around 250 nm, can only arrive at the detector level if it is emitted at very low altitudes. It therefore seems that the UV light content of a Cherenkov flash should contain information about the latest stages of the shower development. Especially, it is expected that the light emitted at low altitudes by muons and secondary hadrons in cosmic ray events should lead to a higher amount of UV light for these events. The light in V band (around 550 nm) is usually used to normalise the UV light intensity to the total amount of light.

This connection has been noted and suggested as a method for gamma hadron separation by several groups, usually in the connection with Cherenkov telescopes. Stepanian *et al.* [1983] report a suppression of the background of two orders of magnitude and an improvement in sensitivity by a factor of two. In simulations by Aharonian *et al.* [1991] it was found that the UV to V ratio is a suitable parameter for background rejection in Cherenkov telescopes, however it is strongly correlated with the standard image

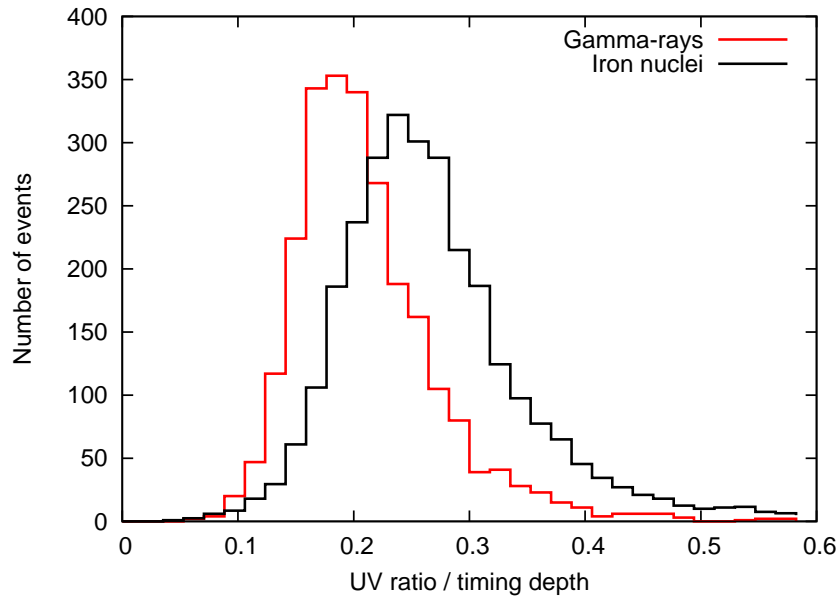


Figure 5.40: Distribution of the spectrum parameter obtained by dividing the UV to V light ratio in the central detector station by the reconstructed shower depth (timing method). Shown are gamma and iron events between 100TeV and 1 PeV.

parameters and leads to no additional improvement. Razdan *et al.* [2002] also reported that their simulations of the TACTIC Cherenkov telescope show a slight difference in the UV to V ratio between particles, but expressed doubt whether this difference is sufficient to benefit the particle separation.

As for the rise time, the case is slightly different for wide-angle Cherenkov detectors. Without the image shape parameters, the UV to V ratio itself might be a useful parameter for the particle identification. This was tested in the simulation by adding an additional UV channel to the *H<sub>i</sub>SCORE* detector stations which is sensitive to light between 200nm to 300nm. The signal from this channel is then used in the event reconstruction to calculate the UV to V ratio. Since the general amount of UV light is rather low, only the UV to V ratio in the central detector, where the light intensity is largest, is used. An additional complication arises as the UV to V ratio partly reflects the shower depth: If the altitude of the shower maximum is low, the cascade propagates to distances closer to the detector, which enhances the UV content of the spectrum regardless of the type of particle. Therefore, the UV to V ratio is divided by the reconstructed shower depth to obtain the particle separation parameter.

The distribution of this parameter is shown in figure 5.40 for gammas and iron nuclei in the energy range from 100TeV to 1 PeV. The proton distribution is not plotted since it is essentially identical to the distribution for gammas. While some difference between the distributions is visible, the overlap is larger than for the previously discussed parameters. The potential for gamma hadron separation seems too small to justify the additional experimental effort of a UV measurement.

**Fluctuations of signal parameters** Since hadronic showers show a larger transversal spread and contain numerous sub-showers, it is expected that the Cherenkov light on the ground should be distributed less smoothly than for gamma-rays. Therefore, the fluctuations of the signal parameters intensity and arrival time around the best fit – in other words, the (reduced)  $\chi^2$  of the LDF and arrival time fit – should be correlated with the type of primary particle. With the simulation presented here it was however not possible to achieve a particle separation based on these parameters, as all possible differences are lost in much larger event to event fluctuations.

### 5.5.5 Performance of gamma hadron separation

**Calculation of performance** The performance of a gamma hadron cut is usually measured by its quality factor, which is defined as

$$Q = \frac{\epsilon_{\text{gamma}}}{\sqrt{\epsilon_{bg}}} \quad (5.27)$$

In this,  $\epsilon_{\text{gamma}}$  and  $\epsilon_{bg}$  are the probabilities for gamma-ray events and background events to survive the cut. As will be discussed in section 5.6.4, the quality factor has a linear impact on the instrument sensitivity. A value above one increases the sensitivity, while a value below one would decrease the sensitivity (by throwing away too many gammas while retaining too much background).

To properly calculate  $\epsilon_{bg}$  for a given cut, the composition of the background must be known. As shown in the previous sections, all separation schemes work better for heavier hadronic particles than for protons, therefore a composition with more heavy particles will result in a lower  $\epsilon_{bg}$  and thus a better quality factor. For the calculation presented here, the cosmic ray composition suggested by the polygonato model [Hörandel, 2003] is used, which gives individual spectra for all nuclei from hydrogen ( $Z = 1$ ) to lead ( $Z = 92$ ). Each particle spectrum is characterised by a power law with a smooth spectral break:

$$\frac{d\Phi_Z}{dE_0}(E_0) = \Phi_Z^0 E_0^{\gamma_Z} \left[ 1 + \left( \frac{E_0}{E_Z^c} \right)^{\epsilon_c} \right]^{-\Delta\gamma/\epsilon_c} \quad (5.28)$$

The power law part is quantified by the absolute flux  $\Phi_Z^0$  and the spectral index  $\gamma_Z$ . The energy of the spectral break is given by  $E_Z^c$ , while  $\epsilon_c$  defines the sharpness of the cut-off. Finally,  $\Delta\gamma$  gives the change of spectral indices from before to after the break. Three different options for the cut-off energy  $E_Z^c$  are discussed in Hörandel [2003]: It may be constant for all particles, proportional to  $Z$ , or proportional to the mass number of the particle  $A$ . Here, it is assumed to be proportional to  $Z$ , i.e.  $E_Z^c = E_p Z$ , which is motivated best by astrophysical considerations [Hörandel, 2004]. According to Hörandel [2003], the best fit to all available data then gives  $E_p = 4.49$  PeV,  $\Delta\gamma = 2.1$  and  $\epsilon_c = 1.9$ . The values for  $\Phi_Z^0$  and the spectral index  $\gamma_Z$  are given for all particles up to  $Z = 92$ . Values for  $\gamma_Z$  range from almost  $-3$  (for lighter elements) to about  $-2$  for the heaviest elements. The errors on the fit parameters are given in the paper but ignored here.

Using these values, the measured all-particle cosmic ray spectrum can be reproduced as the sum of the individual spectra. In the calculation done here, the spectra for all particles are first determined individually. Then the spectra of particles with similar charge number  $Z$  are added up and assigned to heavy (for  $Z \geq 25$ ), medium ( $6 \leq Z \leq 24$ ), and light ( $2 \leq Z \leq 5$ ) nuclei, and protons ( $Z = 1$ ). For the simulations, these four groups are represented by iron, nitrogen, helium and hydrogen.

Figure 5.41 shows spectra of the four element groups and the resulting sum spectrum. Below 1 PeV, the light and medium groups and the protons contribute roughly the same amount to the total cosmic ray flux, while elements with  $Z \geq 25$  are less abundant by about a factor of two. Between 1 PeV and 10 PeV protons and helium nuclei reach their spectral break, which reproduces the experimentally observed steepening of the all-particle spectrum at about 4 PeV (“the knee”). Above 10 PeV, heavy particles become the most dominant group, and their spectral break produces the “second knee”. Around and beyond the second knee the accuracy of this model is not as good as at lower energies, since the influence of extra-galactic cosmic rays (which are not considered in the model) becomes important. This however not a problem: As will be seen in section 5.6.4, the background for the H<sub>i</sub>SCORE gamma-ray observations becomes negligible at energies of about a few PeV, and the exact cosmic ray numbers are not needed beyond that energy.

Before the calculated numbers can be used for the background calculation, the impact of the non-ideal H<sub>i</sub>SCORE energy reconstruction must be taken into account. As shown in section 5.4.4, the energy of cosmic rays, especially heavy ones, is significantly underestimated by the event reconstruction. This means that at a given energy  $E_{\text{reco}}$  the H<sub>i</sub>SCORE detector will see the cosmic ray flux from a higher energy  $E_{\text{true}}$ , which is lower than at the energy  $E_{\text{reco}}$ . This decreases the background by about a factor of two to three, while the composition becomes slightly lighter (since heavy particles show a larger bias in the energy reconstruction).

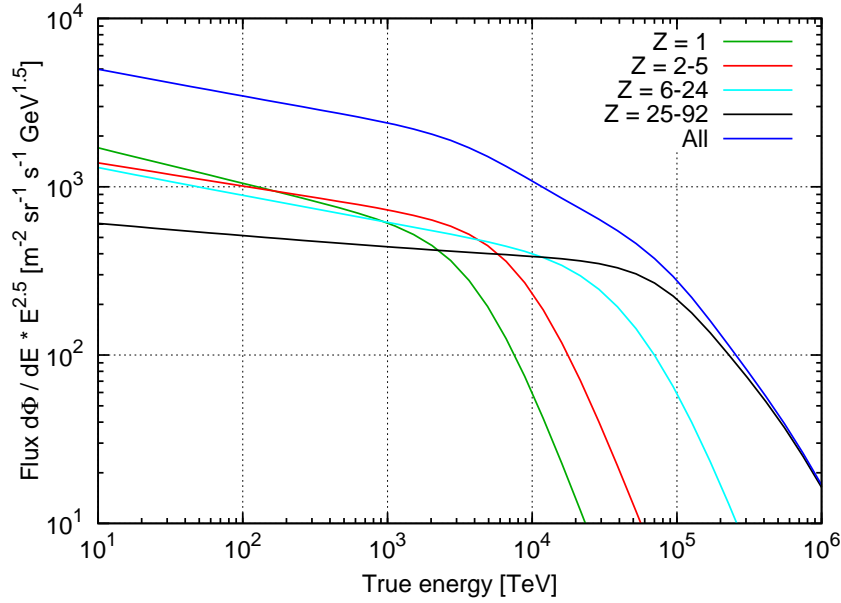


Figure 5.41: The cosmic ray spectra for element groups of similar charge number  $Z$  calculated by the polygonato model.

Knowing the relative abundances of the individual particle groups at a given reconstructed energy, the survival probability for cosmic ray particles  $\epsilon_{bg}$  can be calculated for different cut parameters and cut values. First, the survival probability  $\epsilon_x$  for each simulated particle species  $x$  (protons, helium, nitrogen and iron nuclei) is calculated using the simulated dataset. The probability  $\epsilon_{bg}$  is then calculated as the weighted average of the individual  $\epsilon_x$ , using their relative abundances  $N_x$  at the respective energy as weighting parameter:

$$\epsilon_{bg}(E, cut) = \frac{\sum N_x(E) \times \epsilon_x(E, cut)}{\sum N_x(E)} \quad (5.29)$$

**Combination of cut parameters** Three suitable parameters for gamma hadron separation have been found in the previous sections, which will be called  $P_1$  to  $P_3$  from now on for simplicity:

$$\begin{aligned} P_1 &= X_{width} - X_{timing} \\ P_2 &= X_{exp} - X_{timing} \\ P_3 &= rise.time \end{aligned} \quad (5.30)$$

Figure 5.42 shows – qualitatively – the correlations of  $P_1$  with  $P_2$  and of  $P_1$  with  $P_3$ . Parameters  $P_1$  and  $P_2$  are correlated strongly, nevertheless the spread is still large enough to justify the inclusion of both parameters in the particle separation algorithm. The correlation is much weaker with the rise time  $P_3$ , which is – in contrast to the other two – especially sensitive to the shower development at very low altitudes and close to the shower core.

The most effective way to combine these three parameters for the gamma hadron separation would be a multivariate analysis, similar for example to the analysis developed by Ohm *et al.* [2009] for the H.E.S.S. experiment. Such an analysis is however far beyond the scope of the present work, and two simpler approaches will be tested here:

- **Combination 1:** Individual cut values are chosen for the three parameters by defining a desired fraction of surviving gamma-rays. Events that survive all three cuts are considered as gammas.

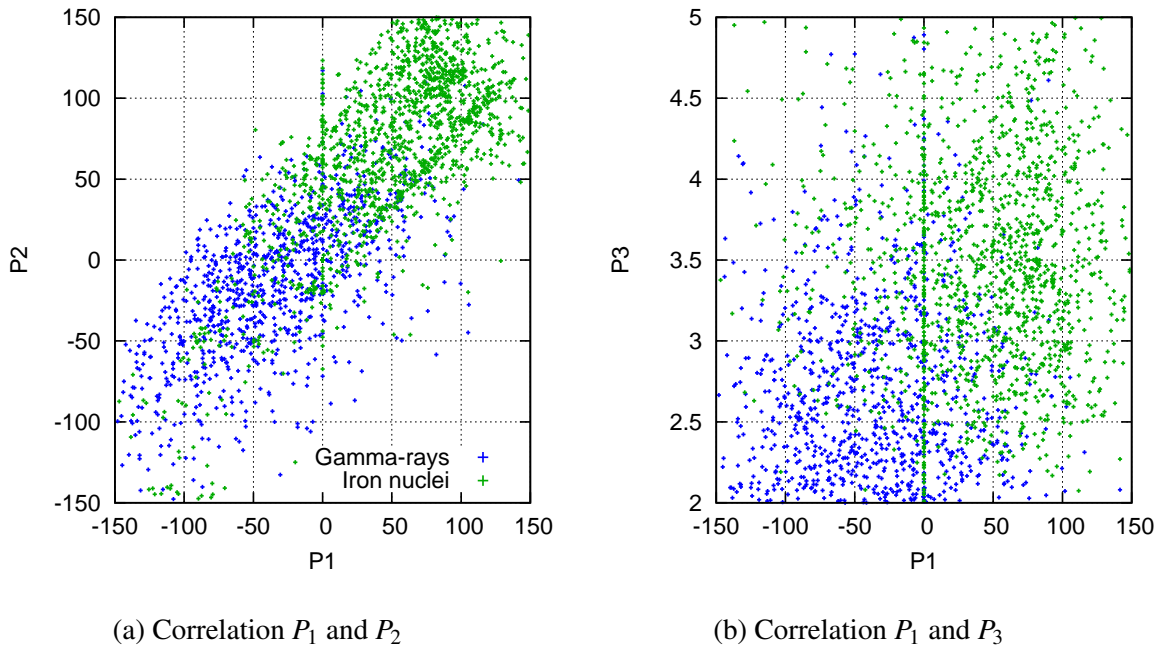


Figure 5.42: Correlation of the gamma hadron separation parameters. Shown are gamma and iron events in the energy range 100TeV to 1 PeV. The accumulation of events near  $P_1 = 0$  is due to events for which the depth reconstruction failed.

- **Combination 2:** The distributions of the three parameters are mapped onto the range 0 to 1, with higher values characterising hadron-like, lower values gamma-like events. The three parameters are multiplied to obtain a fourth parameter  $P_4$ . The optimal cut value on this parameter is found by maximising the quality factor.

In both variants, the optimal cut values will be energy dependent, because e.g. the biases in the energy and depth reconstruction, but also the composition of cosmic rays change with energy. In the following, the performance of these two methods will be evaluated using the quality factor defined in equation 5.27.

**Testing parameter combination 1** The cuts on the three individual parameters are adjusted to retain 80% of the gamma events at every energy. The corresponding cut values are found empirically by testing a range of cut values. Typical numbers for the cut values are -20 to 40 for  $P_1$ , 0 to 30 for  $P_2$  and 2.8 to 3.5 for  $P_3$ .

Figure 5.44 (page 139) shows the gamma and cosmic ray survival probabilities and the resulting quality factor versus the reconstructed energy. If the cut parameters were not correlated, about 50% of the gammas were expected to survive, which turns out to be the case up to energies of about 200TeV. Above that energy, the probability for gamma detections increases gradually to about 60%. The survival rate for cosmic rays starts at about 30% near the threshold and decreases to about 10% at PeV energies. The quality factor shows a constant increase with energy and reaches almost 2 at PeV energies. At energies below 100TeV, the quality factor is below one, which means that the sensitivity of the instrument cannot be improved by the application of this separation algorithm.

There are various approaches to improve this method. For a start, cut values achieving other gamma survival rates could be tested. The different shapes of the individual parameter distributions imply also that it might be beneficial to test different gamma survival rates for the three parameters, e.g. a high survival rate at  $P_1$  and  $P_2$  and a low survival rate at  $P_3$ . To that end, one could do simulations varying all three cut values

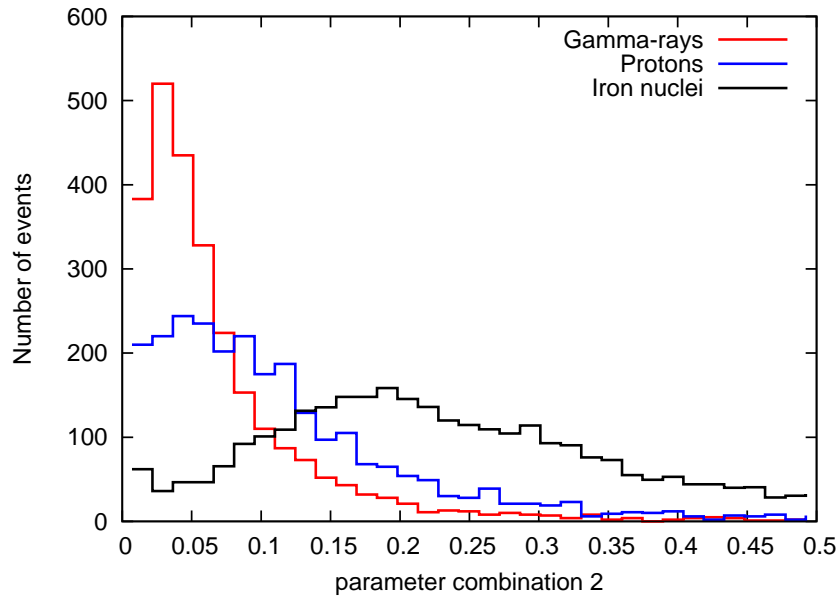


Figure 5.43: Distribution of the cut combination 2 (product of  $P_1$  to  $P_3$ ) for gammas, protons and iron nuclei in the energy range from 100 TeV to 1 PeV.

and scanning for a maximum of the quality factor in the resulting dataset. None of this is pursued further here.

**Testing parameter combination 2** Each of the distributions of the three parameters is linearly mapped to a range from 0 to 1 and then multiplied. Figure 5.43 shows the distribution of the resulting parameter. Due to the influence of  $P_3$ , the rise time, the gamma and proton distributions are strongly asymmetrical.

The best cut value on this distribution is found empirically for each energy by maximising the quality factor. Figure 5.45 shows the resulting gamma and hadron efficiencies and quality factor. The quality factor shows about the same behaviour as in the previous combination method, but reaches slightly higher values. The gamma efficiencies vary randomly between 60 and 80%, which is mostly higher than in the previous case.

Below 100 TeV, no separation can be achieved by this method either. The reason for the problems at low energies is the very poor reconstruction of the depth values needed for parameters  $P_1$  and  $P_2$ , which is in turn due to the low light intensities at large core distances where the depth sensitive parameters are measured. It turns out however that parameter  $P_3$  alone, which only needs one proper signal near the shower core, can achieve a moderate quality factor of 1.2 to 1.3 between 50 TeV and 100 TeV. At energies above 100 TeV, its quality factor remains well below the values achieved by the parameter combinations. This suggests that the analysis should use the rise time alone at low energies, and either one of the parameter combinations at higher energies.

Note that the quality factors are given – in contrast to the resolutions of the reconstructed values up to here – with only five bins per decade and only up to 2 PeV, to keep the errors small. Since the survival probabilities incorporate a lot of information from different reconstructed values that all have their own errors attached, e.g. the depth reconstruction by different methods or the rise time measurement, their errors are larger than for the individual reconstructed values shown so far. It seems therefore more reasonable to use a coarser binning and a limited energy range, and to inter- or extrapolate the values when needed.

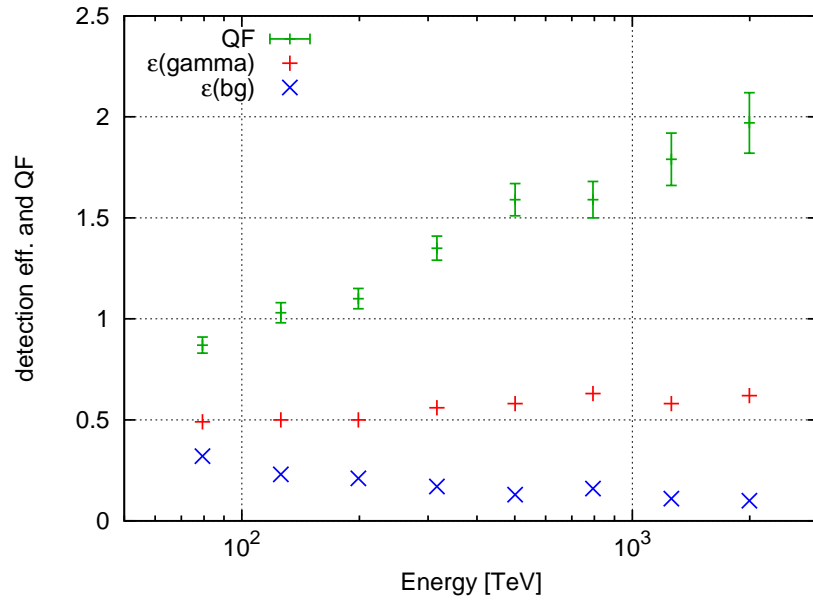


Figure 5.44: Gamma-ray and cosmic ray (background) survival probabilities after the application of the cut combination 1, versus the reconstructed energy. The uncertainties of the survival probabilities are about the size of the markers or smaller.

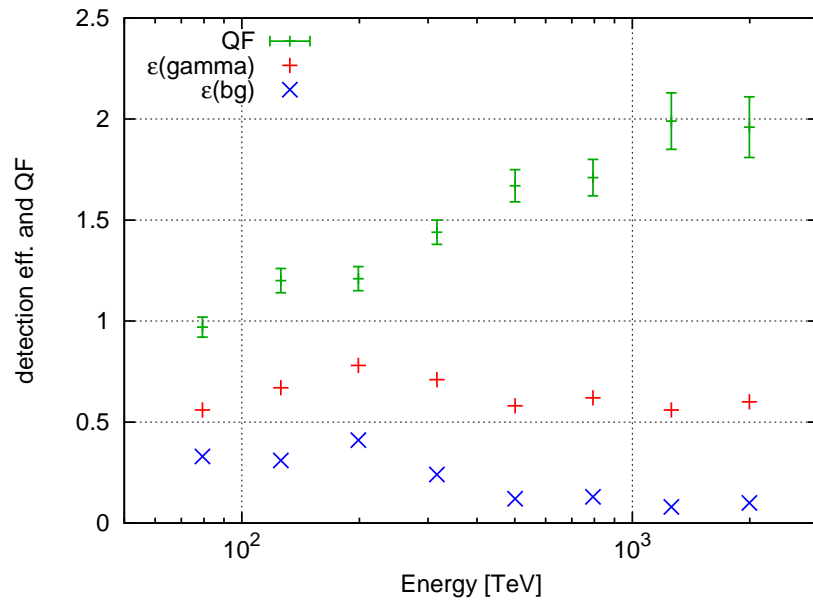


Figure 5.45: Gamma-ray and cosmic ray (background) survival probabilities after the application of the cut combination 2, versus the reconstructed energy. The uncertainties of the survival probabilities are about the size of the markers or smaller.

## 5 $H_i$ SCORE simulations and event reconstruction

	Sel. 90% p	Sel. 50% p	Sel. 90% iron	Sel. 50% iron
Protons	0.91	0.51	0.45	0.07
Helium	0.84	0.29	0.64	0.13
Nitrogen	0.68	0.16	0.80	0.26
Iron	0.42	0.08	0.90	0.51

Table 5.1: Fraction of surviving events after selection of 90% or 50% of protons or iron nuclei. The cuts are done using parameter  $P_4$ . Events are pre-selected to pass acceptance cuts and to have reconstructed energies around 300 TeV.

### 5.5.6 Determination of hadron mass

The second key science project of the  $H_i$ SCORE detector, besides UHE gamma-ray astronomy, is the measurement of the energy spectrum and, if possible, the composition of cosmic rays. While air shower detectors cannot identify individual particle species, they are sensitive to the mean mass of detected cosmic rays, which gives at least hints about their composition (e.g. proton or iron dominated). Typically, the mean mass is derived via the mean shower depth, which is lower for heavier particles at a given energy (for a collection of recent data, see Blümer *et al.* [2009]). For  $H_i$ SCORE, such an analysis will not be straightforward, since – according to the simulations – the reconstructed depth itself depends on the type of particle. If the timing method is used, this bias is however not too large, and the depth may be used to derive the mean mass (see also figure 5.37).

Apart from that, the presented gamma hadron separation parameters can be used as well for a measurement of the cosmic ray composition, as they all show significant differences between protons and iron primaries. If, for example, parameter  $P_4$  is used to select either a proton-rich or an iron-rich sample, the other particles are reasonably well suppressed. Table 5.1 shows the fraction of surviving events of all simulated particles for different cuts on  $P_4$ . The cut values are chosen to select 90% or 50% of the wanted species. Comparing to the corresponding values for the HEGRA AIROBICC experiment [Lindner, 1998], it can be seen that the separation power of the  $H_i$ SCORE experiment is significantly worse with the current analysis. This is not unexpected, since the AIROBICC detector could gather much more data on each event due to the closer station spacing and the existence of the HEGRA particle detectors. Nevertheless the separation scheme presented here should enable the distinction between a proton or an iron dominated composition.

## 5.6 Detector acceptance and sensitivity to gamma-ray sources

### 5.6.1 Angular and spatial acceptance

The angular acceptance of the simulated detector is roughly flat up to a zenith angle of  $25^\circ$ , which is the standard angular cut in the reconstruction. Only in events with energies close to the threshold the impact of the angular dependence of the light transmission through the Winston cone becomes apparent: At larger zenith angles, a slightly higher amount of light (and therefore energy) is needed to trigger the detector. At energies well above 100 TeV, on the other hand, it would be possible to loosen the standard zenith angle cut to include more events. Due to the increasing phase space even a moderate increase to  $28^\circ$  would have a significant impact on the event statistics. Since the impact of such a change on the reconstruction accuracy has not yet been studied in detail, only the standard cut is used for the following calculations.

The energy dependent angular acceptance, defined here as probability to trigger three detector stations, is shown in figure 5.46 for gamma events that have a reconstructed core position inside the array. Zenith angles up to  $10^\circ$  are not shown, as they have low statistics and the acceptance is generally flat there.

The spatial acceptance is also rather homogeneous within the array. Even at low energies no clustering

## 5.6 Detector acceptance and sensitivity to gamma-ray sources

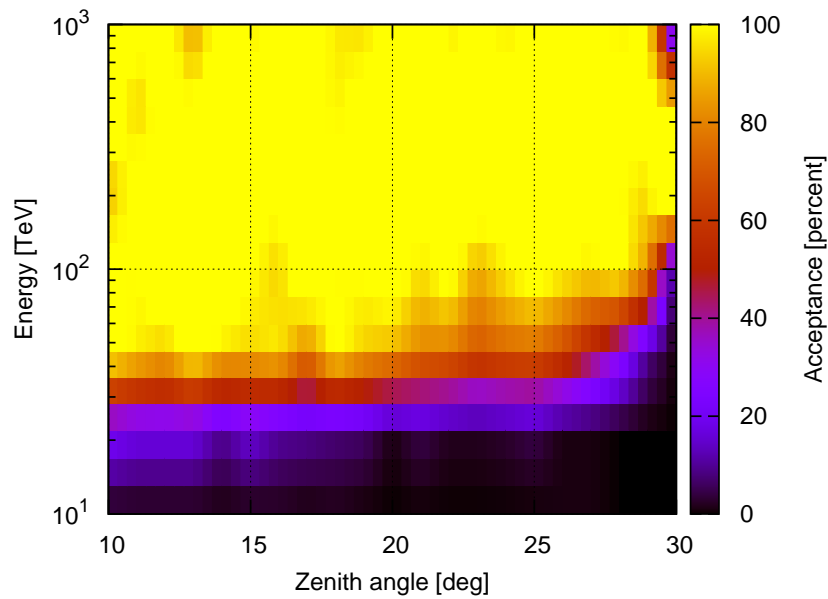


Figure 5.46: Energy dependent angular acceptance to gamma-ray events with reconstructed core positions inside of the detector array. The events are registered as accepted if at least three detector stations have triggered. Energy and zenith angle are MC values.

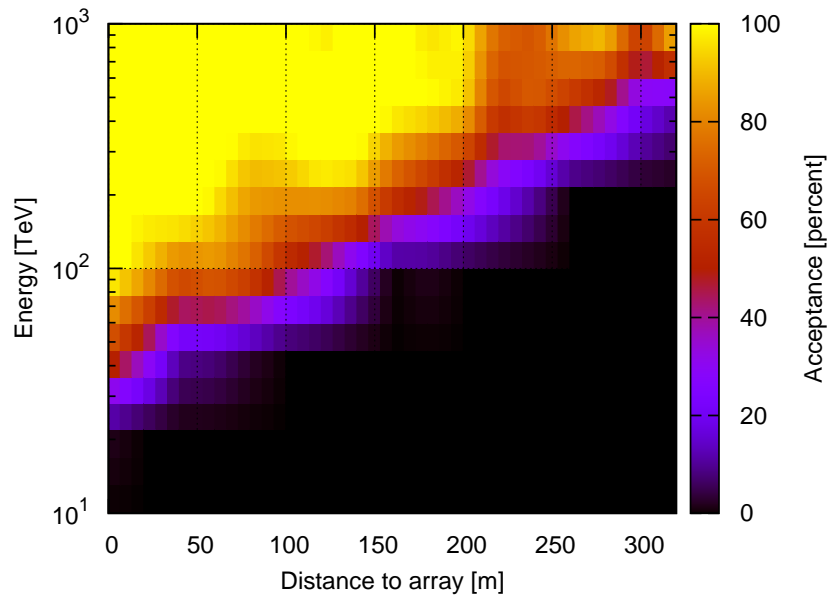


Figure 5.47: Acceptance of events outside of the array boundaries, for gamma-rays with reconstructed zenith angles up to  $25^\circ$ . Energy and distance to array boundary are MC values.

## 5 $H_i$ SCORE simulations and event reconstruction

at certain grid points is apparent, if three triggered stations are requested. The acceptance to events with core locations *outside* of the array boundaries is highly energy dependent, as events with higher energies produce enough light to trigger three stations even at large core distances. Figure 5.47 shows the acceptance of gamma-rays versus the distance to the array boundary (from MC data) and the MC energy. While below 100 TeV only events within 150m distance from the array can trigger the detector, at higher energies even events with core locations further than 300m away still trigger.

For the same reason as above, events outside of the array are not used at all so far, but may be included in the future to increase the event statistics. Especially at higher energies, and for a smaller detector array (with a higher perimeter to area ratio) this can substantially improve the event rate: For a 1 km<sup>2</sup> array the inclusion of events up to 300m distance would more than double the effective area.

### 5.6.2 Effective areas

The effective area of a detector is defined as

$$A_{eff} = \int_A \epsilon(\vec{r}) dA \quad (5.31)$$

In this,  $\epsilon$  is the acceptance or detection probability for an event at the point  $\vec{r}$ , and the integration area  $A$  is an (arbitrary) area which extends well beyond the maximum distance at which events can be detected. Like the detection probability  $\epsilon$ , the effective area depends on the energy, the zenith angle, the type of primary particle and the event cuts applied (one or three triggered stations, restrictions on the zenith angle, gamma cuts, etc.).

Here, the effective areas will be given as function of energy and particle after acceptance cuts (three triggered stations, reconstructed zenith angle up to 25°, and reconstructed core position inside the detector boundaries) and after gamma cuts. The mild zenith angle dependence, which is implied by figure 5.46, is ignored for simplicity. Since the arrival directions were randomised in the simulations, the resulting effective areas should give a realistic average value for zenith angles up to the cut at 25°.

The integration region is defined by the region for which events were simulated, which extends 325m beyond the size of the detector array. As seen in figure 5.47, this is not quite large enough to incorporate all events that trigger the detector at higher energies. However, it seems safe to assume that events that are further away are very rarely reconstructed to be inside the detector array, and that the effective area after acceptance cuts should therefore not be influenced significantly.

The detection probability is calculated as the ratio of events in a given energy bin that survive the respective cuts to the total number of simulated events with zenith angles up to 25°. Therefore, it can also become greater than one, if some events survive the zenith angle cut only because the angle is underestimated in the reconstruction. Similarly, events with core positions outside of the array may be erroneously reconstructed to lie within the array. As result, the calculated effective area can become slightly greater than the actual geometric area of the simulated detector.

Figure 5.48 shows the effective areas after acceptance cuts versus the true (MC) energy. All particles eventually reach a level slightly above the geometrical size of the detector, but the threshold is significantly higher for heavier particles as they produce less Cherenkov light at the same energy. Figure 5.49 shows the effective areas after the gamma cut (using combination method 1). In accordance with the gamma event survival rate shown in figure 5.44 the area for gamma-rays is decreased to 50 to 60% of the detector area. The effective areas for the other particles reflect the power of the gamma hadron separation, which becomes better for heavier nuclei and higher energies.

The calculated effective areas use the same binning and energy range as the gamma and hadron efficiencies presented in figures 5.44 and 5.45. For the following calculations the effective areas are linearly interpolated between the given data points, and extrapolated to higher energies. The extrapolation assumes that the areas remain constant from 2 PeV on, which seems to be a conservative assumption given the general

### 5.6 Detector acceptance and sensitivity to gamma-ray sources

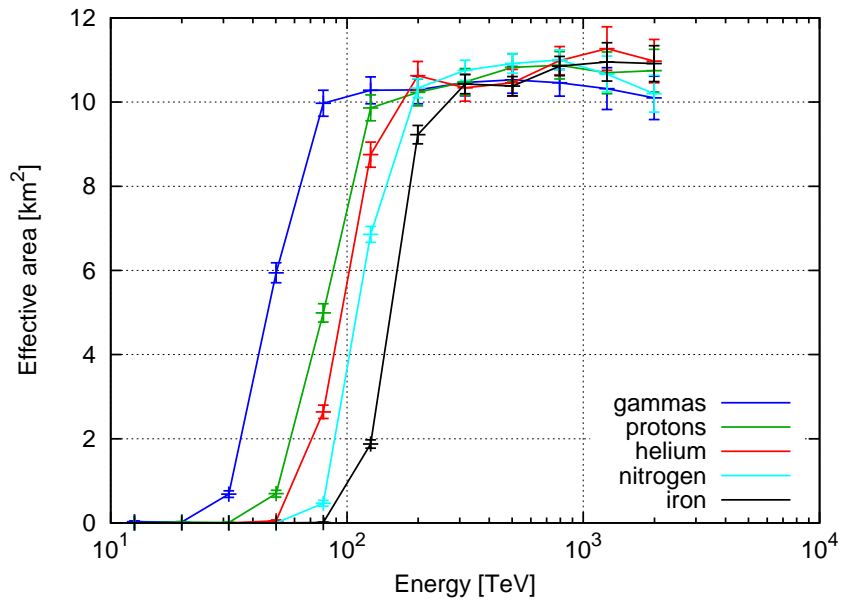


Figure 5.48: Effective areas of the simulated detector for all five simulated particle species versus MC energy, after acceptance cuts. Error bars indicate statistical uncertainties.

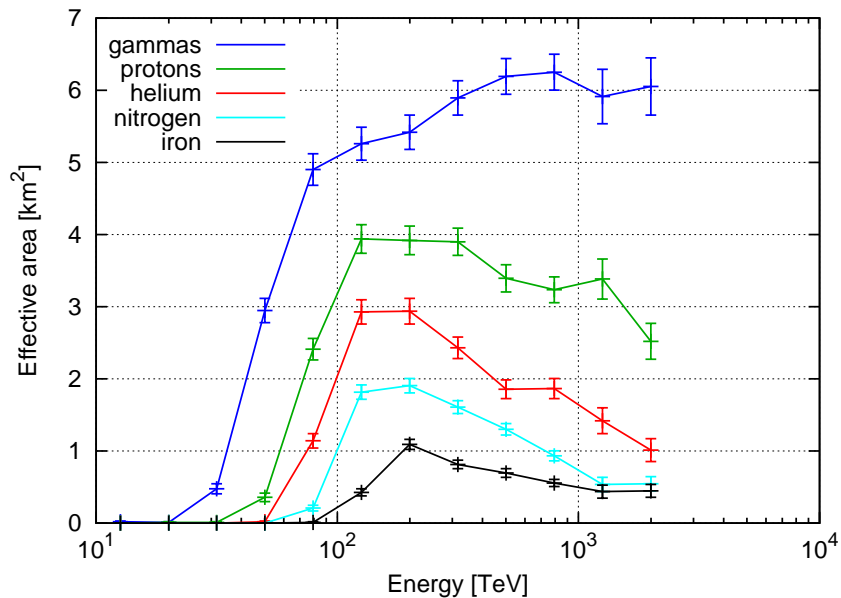


Figure 5.49: Effective areas of the simulated detector for all five simulated particle species versus MC energy, after gamma cuts (combination method 1). Error bars indicate statistical uncertainties.

## 5 $H_i$ SCORE simulations and event reconstruction

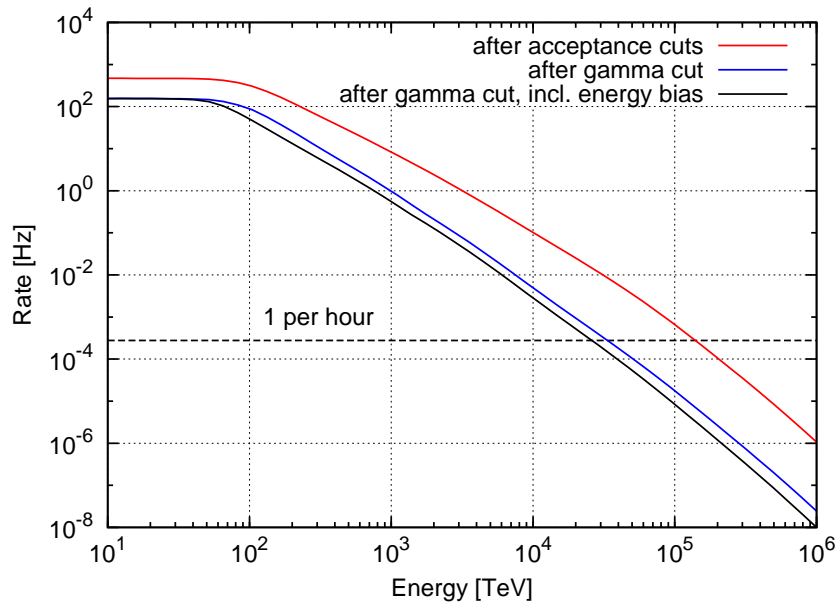


Figure 5.50: Integrated cosmic ray rates (i.e. number of particles with  $E > E_0$ ) seen by a  $10\text{km}^2$   $H_i$ SCORE detector array. The rates are given after acceptance cuts and after the gamma-ray cut. The third line additionally includes the bias of the energy reconstruction, which leads to an effective reduction of the seen cosmic ray rates at a given energy.

trend in the data: Realistically, the gamma area might still increase slightly while the cosmic rays become better suppressed.

### 5.6.3 Event rates

Using the cosmic ray rates calculated in section 5.5.5 and the effective areas of the instrument, the expected event rates can be estimated. Figure 5.50 shows the integrated all-particle cosmic ray rates for the  $10\text{km}^2$  detector array after acceptance cuts and after the gamma-ray cut. The gamma cut reduces the rate by about a factor of three at lower energies, and by more than a factor of 30 at the highest energies where the composition is dominated by heavy particles. As discussed in section 5.5.5, the rate actually seen as background at a certain energy is additionally reduced by the bias in the energy reconstruction. This effective background rate is shown by the third line in the plot.

All rates show approximately the expected form of a power law with indices between  $-1.7$  and  $-2$ . At energies below  $100\text{TeV}$ , the effect of the rapidly decreasing effective areas leads to a flat spectrum. Since events with energies below  $10\text{TeV}$  will virtually never trigger the detector, the rates at  $10\text{TeV}$  can be a good indication of the total data rate that is recorded by the instrument. For the  $10\text{km}^2$  array, the single station trigger rate amounts to about  $1.5\text{kHz}$ , the three station trigger rate to about  $600\text{Hz}$  (both not shown). The rate after acceptance cuts is a good indication of the potential of the detector for cosmic ray physics: At  $10\text{TeV}$  the integrated rate is  $470\text{Hz}$ , while around the knee region it is about  $0.6\text{Hz}$ , which leads to more than  $2.3 \times 10^6$  events per year (assuming 1,000 hours of observation per year). At  $10^{18}\text{eV}$ , still about four events per year are expected.

The rate including gamma cut and energy bias is indicative of the background for gamma-ray observations. However, the actual rate seen when analysing a gamma-ray source is much lower, since only cosmic rays with a similar direction of origin must be taken into account. This will be discussed in more detail in the following section.

### 5.6.4 Sensitivity

One of the most important performance figures of a gamma-ray observatory is its point source sensitivity, which means its potential to see a weak gamma-ray source over a large background of cosmic rays. It is defined as the minimal integral flux  $\Phi_\gamma(E > E_0)$  above a given energy  $E_0$  that must arrive from a source in order to be detected by the instrument. A source is classified as detected if the signal in the source region exceeds the homogeneous background level from cosmic rays by at least five standard deviations, i.e. if the significance  $S \geq 5$ . This way, the probability for a false detection caused by a large fluctuation of the background is below  $10^{-6}$  (for the case of no trial factors<sup>10</sup>). Additionally, a minimum of 50 gamma-ray events is required, which usually limits the detectable flux at the highest energies (the “background-free” regime).

The significance of the source detection is approximated here by

$$S = \frac{N_{on} - N_{off}}{\sqrt{N_{on} + N_{off}}} \quad (5.32)$$

where  $N_{on}$  is the number of events in the source region, and  $N_{off}$  the number of events in a background region of equal area (Li and Ma [1983], equation 9). Assuming that the number of events in the source region is made up of background events ( $N_{bg}$ ) and signal events ( $N_\gamma$ ), one can set  $N_{on} = N_\gamma + N_{bg}$  and  $N_{off} = N_{bg}$ , resulting in

$$S = \frac{N_\gamma}{\sqrt{N_\gamma + 2N_{bg}}} \quad (5.33)$$

The significance can be improved if the background is averaged over a larger sky region or observation time, which is commonly expressed by the introduction of an  $\alpha$  factor (see also equation 3.12). This however causes some complications in the correct calculation of the significance, and is not done here<sup>11</sup>. The minimal number of gammas needed is calculated by

$$N_\gamma(E > E_0) = 12.5 + \sqrt{156.25 + 50N_{bg}(E > E_0)} \quad (5.34)$$

The background  $N_{bg}(E_0)$  is calculated using the integrated cosmic ray rates shown in figure 5.50, multiplied by the observation time  $T$  and reduced to the solid angle of the source region. For a point source, this source region is usually a small circle around the nominal source position. Here, it is assumed to be energy dependent and equal to the angular resolution shown in figure 5.18 (assuming 1 ns jitter). This way, about 68% of the gamma photons are included at all energies, while the background level is kept relatively small.

The gamma-ray flux needed to detect  $N_\gamma$  photons is calculated using a gamma-ray source spectrum with  $\frac{dN}{dE} \propto E^{-\Gamma}$  (no cut-off), the effective area for gamma-rays, and the observation time:

$$\Phi_\gamma(E > E_0) = \frac{N_\gamma(E > E_0)}{T} \times \frac{\int_{E_0}^{\infty} E^{-\Gamma} dE}{\int_{E_0}^{\infty} E^{-\Gamma} A_{eff}(E) dE} \quad (5.35)$$

The index of the gamma-ray spectrum is set to  $\Gamma = 2.6$  for the calculation.

The sensitivity improves (i.e.  $\Phi_\gamma$  decreases) with the square root of the sensitive area of the detector, since the background fluctuations increase only with  $\sqrt{A}$ , the signal on the other hand with  $A$ . In fact,  $\Phi_\gamma$  is proportional to  $\sqrt{A_{eff}(bg)}/A_{eff}(\gamma)$ , which motivates the definition of the quality factor as given in equation 5.27.

<sup>10</sup>Trial factors must be included if a signal is searched for at many positions simultaneously, since the chance probability for a false detection increases in this case.

<sup>11</sup>This way, the obtained sensitivity is a rather conservative estimate. Due to the detector’s large field of view, homogeneous acceptance and constant survey operation the  $\alpha$  factor can probably improve the sensitivity by up to a factor of  $\sqrt{2}$ .

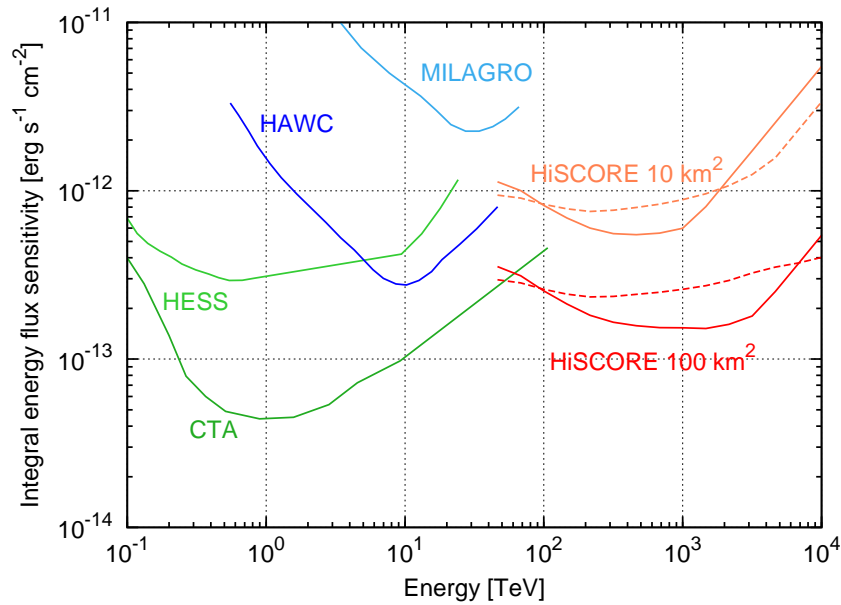


Figure 5.51: Sensitivity of the simulated  $H_i$ SCORE detector for  $10\text{km}^2$  and  $100\text{km}^2$  instrumented area. The dashed lines indicate the sensitivity without gamma hadron separation. The sensitivities of other observatories are plotted for comparison (see also figure 2.14 on page 34).

Similarly, the sensitivity of an instrument also improves with the square root of the observation time. For a pointed instrument such as a Cherenkov telescope, it is usually given for 50 hours, which is a realistic amount of observation time usually devoted to a single object<sup>12</sup>. For an instrument constantly in survey mode, such as the Fermi gamma-ray satellite (see section 2.4.1) or wide-angle Cherenkov detectors, it is usually given for a continuous operation of five years, the expected minimum lifetime of the fully operational system. For a ground-based wide-angle detector such as  $H_i$ SCORE the yearly exposure time of an individual source depends on its position on the sky relative to the location of the detector system on Earth. This is examined in some detail in section 6.3, where exposure times for different sky regions, a range of known gamma-ray sources and two detector locations are calculated. Supported by the results presented there, an average source exposure time of 200 hours per year, or 1,000 hours in total, will be assumed here.

Figure 5.51 shows the calculated point source sensitivity, represented by the minimal required gamma-ray energy flux, for a  $10\text{km}^2$   $H_i$ SCORE detector array (as simulated) and for a  $100\text{km}^2$  array. The latter is derived by multiplying the effective areas by ten, and using the performance figures (angular resolution, gamma hadron separation, etc.) obtained from the simulation of the  $10\text{km}^2$  array, which is a conservative estimate. As the larger array has a smaller perimeter to area ratio, the edge effects (reduced reconstruction accuracy due to only partially contained events) are less important, and the larger detector should have a (slightly) better resolution. The plot additionally shows the sensitivities before gamma hadron separation, which are slightly worse for the main energy region. At low energies they produce a slightly better result, in agreement with the development of the quality factor shown in figure 5.44. For comparison, the sensitivities of selected other current and planned gamma-ray observatories are shown as well in the plot.

Towards high energies, all detectors are limited by the requirement of 50 gamma events during the total observation time. For most detectors, the required gamma-ray flux is constant in this regime (being essentially a function of the effective area and the observation time), resulting in a straight rising line in the energy flux plot. The sensitivity of H.E.S.S. shows a steeper rise in its background-free regime, as the effective area

<sup>12</sup>For current, “third-generation“ Cherenkov telescopes. Early systems needed much more observation time in order to detect the first sources.

decreases slightly towards multi-TeV energies due to its limited field of view (see also section 3.5). For H<sub>i</sub>SCORE, the sensitivity before gamma-ray cuts is better than after cuts in the background-free regime, as the effective area for gammas is larger before the cuts. In practice, this means that the cuts would not be applied at these energies. Additionally, the angular cut could be loosened in this regime, thereby including more than the usual 68% of the gammas and improving the sensitivity by another factor of 1.5 (if *all* gammas are contained in the source region).

The sensitivity is shown only down to an energy of 50 TeV, since below that energy the reconstruction accuracy becomes considerably worse. However, this does not mean that it is not possible to detect gamma-rays below that energy: As shown in figure 5.49, gamma-rays have a substantial detection probability down to 25 TeV. The poor reconstruction quality results however in a sensitivity considerably worse than above 50 TeV.

It should be emphasised here that the point source sensitivity depends linearly on the angular resolution, which in turn depends on the accuracy of the time synchronisation between the detector stations. If this accuracy can be improved to below the 1 ns assumed here, another improvement in the sensitivity of up to a factor of 1.5 to 2 is possible.

The sensitivity to an extended source is determined by the source radius  $r_s$  relative to the angular resolution of the instrument  $\sigma_{ang}$ . The size of the source region in the analysis, and therefore the amount of background events, is increased by a factor of  $(r_s/\sigma_{ang})^2$  compared to the point source scenario. As result, the minimal flux needed to detect an extended source, i.e. the extended source sensitivity, is by a factor of  $(r_s/\sigma_{ang})$  higher than the point source sensitivity<sup>13</sup>. This is a common feature of all background dominated instruments (i.e. also all ground-based gamma-ray observatories), which means that for an extended source all sensitivities shown in figure 5.51 would increase by the same factor (assuming a similar angular resolution). However, very large sources with a radius of more than one degree are challenging in the analysis of Cherenkov telescopes, as it can be difficult to find appropriate background regions in the observed field of view. For wide-angle detectors this is less of a problem, which makes them better suited for the study of very extended sources, or large scale gamma-ray emission regions.

In conclusion, it can be seen that a 100 km<sup>2</sup> H<sub>i</sub>SCORE detector can achieve an energy flux sensitivity in the UHE gamma-ray regime better than the sensitivity in the VHE regime achieved by current Cherenkov telescope systems. Therefore, H<sub>i</sub>SCORE is well suited to extend the range of current gamma-ray observations to higher energies, and it is anticipated that many sources currently detected in the VHE regime will be visible by H<sub>i</sub>SCORE. An extrapolation of currently known H.E.S.S. source with hard spectra to the UHE regime is shown in Tluczykont *et al.* [2012b]. A more detailed study of the expected event rates from known VHE sources will be presented in Einhaus [2012].

## 5.7 Options to lower the energy threshold<sup>14</sup>

For several reasons, the energy threshold is a very important performance figure of the H<sub>i</sub>SCORE detector: Since current VHE instruments are sensitive only up to a few ten TeV, a low energy threshold is necessary to assure an overlap between these detectors and H<sub>i</sub>SCORE. This is not only important for cross-calibration, but also to obtain continuous spectra from the low VHE regime ( $\sim 100$  GeV) up to ultra high energies. Furthermore, cut-offs have been observed for many spectra in the VHE regime, while for other spectra hints of a cut-off are seen in the 10 to 100 TeV regime. To detect as many sources as possible, and to properly resolve the cut-offs in the multi-TeV regime, a threshold as close to 10 TeV as possible is desirable.

For the following discussion, the energy threshold will be defined as the energy at which the effective area for gamma-rays after acceptance cuts reaches 50% of the geometrical detector area. For the standard

<sup>13</sup>In the background-free regime this is not an issue, and the sensitivity to extended sources is equal to the point source sensitivity

<sup>14</sup>Note: Some of the results presented in this section have been published previously by the author and collaborators in Hampf *et al.* [2011b].

## 5 $H_i$ SCORE simulations and event reconstruction

Spacing	sea level	2000 m a.s.l.
100 m	38	27
125 m	-	36
150 m	47	53
200 m	98	-

Table 5.2: Energy thresholds (in TeV) of various detector configurations, defined as the energy where the effective area for gammas after acceptance cuts reaches 50% of the geometric detector area. Configurations marked with a dash have not been simulated.

Spacing	sea level	2000 m a.s.l.
100 m	32	17
125 m	-	18
150 m	33	20
200 m	37	-

Table 5.3: Energy thresholds (in TeV) for the 2x2 sub-array configuration, derived from the single station effective areas. Configurations marked with a dash have not been simulated.

configuration, this threshold is at 47 TeV. Several other configurations have been simulated to study how the threshold can be reduced: The detector spacing is varied between 100 m and 200 m, and the observation altitude has been changed from sea level to 2000 m. Finally, a concept with small sub-arrays instead of integrated four-channel detector stations has been tested.

Table 5.2 shows the change of the energy threshold with detector station spacing and observation altitude. At 2000 metres altitude, the Cherenkov light pool (i.e. the inner, roughly flat part of the LDF) is considerably (20 to 30%) smaller than at sea level. Therefore, the same amount of light is concentrated on a smaller area, and less energy is needed to reach the trigger threshold in this area. Additionally, less light is absorbed by the atmosphere between the shower maximum and the detector, which leads to another 10 to 20% increase in the light levels (see also figure 5.31). Therefore, the detector should have a lower energy threshold at a higher elevation. The simulations show that this is indeed the case for a spacing of 100 m. At 150 m, the threshold is however higher than at sea level, probably because, on average, less detector stations are contained in the Cherenkov light pool. At both altitudes, a denser array always leads to a lower threshold, since on average the nearest three detector stations are closer to the shower core position.

These results show that a low observation altitude is ideal for the  $H_i$ SCORE standard layout. If a lower threshold is envisaged, the most effective approach will be to change to a denser spacing while at the same time going to a higher observation altitude. It should however be kept in mind that a denser spacing leads to more channels per area, and therefore a smaller total instrumented area at a given budget. Therefore, a trade-off between a low energy threshold and the overall sensitivity must be found.

Another option to reach a low threshold is splitting up the four channels of each detector station to four largely independent detectors, positioned about five to ten metres apart. The four channels can then be used to achieve a basic event reconstruction (direction, possibly a rough guess of the core position and energy) for low energy events that trigger only this sub-array. At higher energies, the signals from the four detectors are added up and treated as a single signal for the standard event reconstruction. No dedicated simulations have been conducted yet for this approach, but the energy threshold achievable can be estimated by using the effective area for single station triggers in the standard layout.

Table 5.3 shows the energy thresholds for this set-up. Here, the influence of the detector spacing is rather weak, since close to the threshold most events will only be detected by a single sub-array. A higher altitude leads to a significant drop in the thresholds at all spacings due to the higher light levels. These thresholds are low enough to achieve a substantial overlap with current VHE instruments. Two drawbacks must be mentioned though: First, the reconstruction accuracy and thus the gamma-ray source sensitivity near the threshold will probably be considerably worse compared to the figures shown for the standard configuration. Further simulations are necessary to determine whether such a system can really see the currently known VHE gamma-ray sources and thus provide an overlap. Second, the use of sub-arrays significantly increases

	H <sub>i</sub> SCORE	H.E.S.S.
Effective area	100 km <sup>2</sup>	up to 1 km <sup>2</sup>
Energy range	50 TeV to 10 PeV	100 GeV to ~ 30 TeV
Field of view	0.59 sr	0.006 sr
Angular resolution	0.1° to 0.25°	0.1°
Energy resolution	10% to 15%	15%
Point source sensitivity	$2 \times 10^{-13}$ ergs s <sup>-1</sup> cm <sup>-2</sup>	$4 \times 10^{-13}$ ergs s <sup>-1</sup> cm <sup>-2</sup>

Table 5.4: Comparison of key performance figures for gamma-ray astronomy between H<sub>i</sub>SCORE (100 km<sup>2</sup> array), and H.E.S.S. as an example of a typical, third generation Cherenkov telescope system. For H<sub>i</sub>SCORE, resolutions and sensitivity are given for energies between 100 TeV and 1 PeV. The figures for H.E.S.S. are taken from Aharonian *et al.* [2006c] and Aharonian *et al.* [2008b]

the cost per station, since four (largely) independent control and readout systems are needed.

In any case, it should be kept in mind that the quoted thresholds are not the minimum energy at which gamma-rays can be seen. As can be seen from the effective areas in figure 5.48, gamma-rays can be detected down to energies several ten TeV below the 50% threshold.

## 5.8 Concluding remarks

In this chapter, the detector simulation and event reconstruction for the H<sub>i</sub>SCORE detector have been presented. The event reconstruction is based on concepts developed for previous wide-angle detector systems, but the strong focus on gamma-ray astronomy, the large station spacing and the low observation altitude required a number of adaptations. The use of an arrival time model on basis of the work by Stamatescu *et al.* [2011] results in an angular resolution comparable to the one achieved with Cherenkov telescopes, a key factor for a good gamma-ray point source sensitivity. The time structure of the Cherenkov light signals is exploited in several ways (signal edge times, signal durations, signal rise times) to determine the shower depth and to separate gamma-rays from cosmic rays. It was shown that despite the low number of channels per square kilometre and the simple and inexpensive set-up, the detector can achieve a performance (measured in angular and energy resolution and in point source sensitivity) comparable to Cherenkov telescopes in its main energy range above 100 TeV. As such, it is the ideal extension of existing gamma-ray observatories to higher energies (see also table 5.4). It has also been shown that it is a powerful cosmic ray detector with an expected event rate of about 470 Hz at the threshold and still around 4 events per year at 1 EeV (10 km<sup>2</sup> version).

Some possibilities to improve the performance of the detector have been pointed out and may be examined in future studies. At energies above 100 TeV the event statistics may be increased by relaxing the acceptance cuts to include events with zenith angles above 25°, and events with core positions outside of the array. The impact of such new cuts on the reconstruction performance has not yet been studied in detail, and the reconstruction may need to be adapted to be better suited for these events (e.g. using the signal widths to reconstruct core positions outside of the array).

The energy, depth, and particle type reconstructions depend on a number of partially correlated parameters. A sophisticated multivariate analysis should be able to account better for these correlations and improve the energy and depth resolution, and the particle separation.

The detector layout simulated here, i.e. a regular grid with a square perimeter, is not optimal. Edge effects that degrade the reconstruction accuracy can be minimised if a circular perimeter is used. Additionally, an array with changing inter-station spacings may be a good compromise to combine a low energy threshold with a large total area. This can be achieved by denser clusters scattered throughout the array, or a graded

## 5 $H_i$ SCORE simulations and event reconstruction

array with a dense core and large spacings towards the edges. It is however not straightforward to predict the improvement (or deterioration) of performance achieved by such a non-regular grid pattern, and more simulations with different layouts are needed to evaluate this (first results for this will be presented in Spitschan [2013]). It seems however that no single *optimal* configuration exists, and that in the end a compromise between a low energy threshold (which means smaller inter-station spacings, more dense sub-arrays etc.) and a good point source sensitivity (which means large instrumented area) must be found. Ultimately, this is a decision which must be taken in view of the scientific goals of the experiment.

One of the most challenging demands on the hardware is the need for fast communication between the detector stations, necessary to implement an n-station trigger ( $n \in [2, 3]$ ) and the readout of non-triggered stations. It was shown in section 5.2 that the n-station trigger is not needed if the bandwidth of the station readout can handle rates up to a few hundred events per second, or if the trigger threshold can be increased slightly. It turns out however that the non-triggered stations are rather important for the event reconstruction, especially at smaller energies where only few signals are available. If only triggered stations are used for the event reconstruction, the core and angular resolution around 100 TeV deteriorate by 40% and 25%, respectively, while above 1 PeV no significant difference is found. This may be counteracted by a lower trigger threshold to include weaker signals, which would however produce even higher NSB trigger rates and therefore quite certainly require a n-station trigger. In conclusion, this shows that either way a real-time communication between the stations cannot be avoided unless a significant deterioration in the event reconstruction is accepted.

While there still seems to be potential for improvement of the event reconstruction, it should also be pointed out that some effects expected in the real detector have not yet been included in the simulation, and that these issues may deteriorate the reconstruction accuracy and ultimately the detector sensitivity. Some examples are (temporarily) defunct detector stations, the non-ideal gain calibration (in each channel as well as in between stations) and additional noise factors (e.g. electronic noise). The greatest impact however may come from a time response function slower than the one assumed here. In this case, the power of the signal width and rise time for the event reconstruction may significantly diminish. This needs to be re-evaluated once the characteristics of the electronic set-up are known better.

It should also be noted that the results are subject to certain systematic uncertainties that have not been discussed so far: The air shower simulations depend on elaborate models of the reactions (especially the hadronic interactions) in the shower, which may be not entirely accurate. Various inputs to the detector simulation, e.g. the model for the atmospheric absorption or the quantum efficiency of the PMT, may deviate from the conditions found in the real experiment (in fact, such values usually change during the lifetime of the experiment). Also, the polygonato model used to quantify the individual components of the cosmic ray flux adds a systematic uncertainty to the final results, especially the sensitivity.

Finally, it is mentioned again that the key results presented in this chapter are available in tabulated form in appendix B.

## 6 Site evaluation

In this chapter the question of a suitable detector site for the H<sub>i</sub>SCORE detector will be discussed. In section 6.1 a set of criteria will be compiled upon which possible sites should be evaluated. In section 6.2 some possible sites are introduced, with a focus on the Fowler's Gap research station in Australia that has also been visited for site evaluation.

One important criterion is the sky region visible from the site, which is the focus of section 6.3. Skymaps of expected exposure times for two different sites have been simulated and will be discussed in terms of the potential for ultra high energy gamma-ray astronomy.

Another important aspect is the darkness of the site, and a measurement of the residual night sky brightness at the Fowler's Gap station is presented in section 6.4.

### 6.1 Criteria for a suitable detector site

#### 6.1.1 Field of view and potential gamma-ray sources

In contrast to Cherenkov telescopes, the H<sub>i</sub>SCORE detector cannot be pointed at targets of interest, instead it continuously monitors a large portion of the sky. As described in chapter 5, all events with zenith angles up to 25° are accepted, which results in an effective solid angle of 0.59 sr (4.7% of the total sky). Due to the revolution of the Earth around the sun, the detector looks at different parts of the sky during the year. The sky regions observed by the detector depend only on the latitude of the detector location on Earth.

To evaluate the potential for the discovery of UHE gamma-ray sources, the visible sky region can be compared with the distribution of known VHE gamma-ray sources, as many VHE sources may also be visible at ultra high energies. However it should be kept in mind that the currently known distribution of sources is not unbiased, as current gamma-ray detectors have only scanned small fractions of the sky, or targeted specific sources. Also, some source classes are better candidates for UHE gamma-ray emission than others, e.g. many extra-galactic sources will be difficult to detect in the UHE regime due to their soft energy spectra (see also section 2.3.2).

A calculation of the field of view for two possible detector sites is presented in section 6.3, the potential for detections of UHE sources is also discussed there.

#### 6.1.2 Weather conditions

The H<sub>i</sub>SCORE detector will only be operational in clear nights, since a large amount of the Cherenkov light is generated high up in the atmosphere above the usual height of clouds, therefore a low average nightly cloud coverage at the site is most important. Also, the distribution of nightly cloud coverage over the year should be taken into consideration, if a rather uniform exposure over the field of view is desired. At many locations, especially in tropical regions, there is typically a wet and a dry season, and sky regions visible mainly during the wet season may get a much lower than average exposure.

The actual amount of rainfall is, on the other hand, not an important factor. However, potential dangers to the detector infrastructure from flooding due to heavy rainfalls, or other catastrophic events (storms, bushfires, volcano eruptions etc.), should be examined carefully. This may be complicated by the fact that most interesting locations are very remote and not used intensively so far, and long time weather hazard records may be sparse. An established research or observation site is therefore preferable under this aspect.

## 6 Site evaluation

For a clear view of the sky it is also important to look at the aerosol concentration of the air, and its possible variation. As many interesting sites are located in desert-like areas, dust or sand in the air can become a serious problem. The best possibility to rate the quality of the site in that respect is to evaluate long-term extinction measurements, if available.

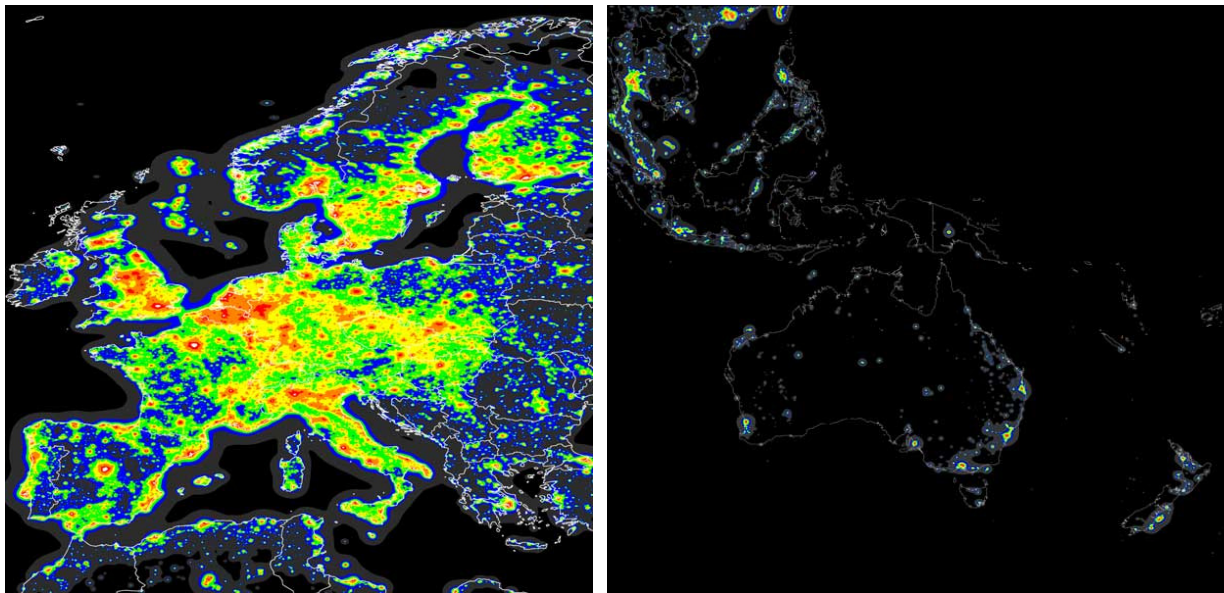
It is generally possible to operate the H<sub>i</sub>SCORE detector at all temperatures, however, some modifications to the standard design may be necessary to ensure safe and reliable operation at extreme temperatures. If temperatures below zero are expected during winter nights, the detector stations need to be sealed with a transparent entry window and heated inside to keep the temperature range within the specifications of the electronic components and to prevent ice cover on optical surfaces (Winston cone mirror surface, PMT entry window). If, on the other hand, very high temperatures are expected during the day, cooling is necessary in order to prevent damage to the electronics.

### 6.1.3 Darkness

Due to the large light sensitive area and optical field of view of the individual detector channels, the night sky brightness poses a considerable source of noise for the H<sub>i</sub>SCORE detector. This noise induces false triggers on the detector near the threshold (see section 5.2) and deteriorates the event reconstruction at low energies, therefore effectively determines the energy threshold of the instrument. The detector site should therefore be as dark as possible, especially without any man-made light pollution. Light pollution generated by cities, but also isolated structures like large mining sites, increases the night sky brightness level up to distances of more than hundred kilometres. The first World Atlas of artificial night sky brightness [Cinzano *et al.*, 2001] provides data on the amount of light pollution for all regions of the world, as obtained by satellite data. Figure 6.1 presents maps from two very different regions of the world: In western Europe, the general level of light pollution is very high due to the high population density, while there are many desolated areas in Oceania, especially in central and western Australia, that show no sign of any light pollution. A magnified version of the light pollution map for southern Australia is shown in figure 6.3 in section 6.2.1.

In the absence of light pollution (and the moon), the remaining night sky brightness in the visible wavelength regime is dominated by air-glow, direct and scattered star light and zodiacal light. It is a function of time on time scales from years (due to the solar cycle which influences the amount of air-glow) down to hours (as the air-glow decreases during the night). It also varies with the sky region looked at due to different densities of brighter stars, e.g. it is usually stronger towards the Galactic plane than towards other regions.

The night sky brightness has been measured in various spectral bands by many experiments, an overview of which can be found in Leinert *et al.* [1998]. A comparison of the darkness of different known observatory sites can be found in Garstang [1989]. Measurements with a focus on Cherenkov astronomy have been conducted by Mirzoyan and Lorenz [1994] at the HEGRA site at La Palma and by Preuß *et al.* [2002], again at the HEGRA site and in Namibia, at the site at which later the H.E.S.S. telescopes were built. Almost all measurements focused on high altitude sites, as these are in general better suited both for optical as well as ground-based gamma-ray observations with a low energy threshold. However, in the UHE regime a high altitude may not be necessary (see also section 5.7), and a low altitude site may be used for the H<sub>i</sub>SCORE system. One of the possible sites is the research station Fowler's Gap in Australia (see section 6.2.1), which has an average altitude of about 180m above sea level. It is however not a priori clear how the night sky brightness varies with altitude. Therefore, a measurement of the night sky brightness in the visible light regime was conducted at Fowler's Gap in February and August 2010, and the results are presented in section 6.4.



(a) Europe

(b) Oceania

Figure 6.1: Level of artificial light pollution for Europe and Oceania, reproduced from Cinzano *et al.* [2001]. The light pollution is given in the astronomical V band, and towards zenith. Colours indicate the ratio of artificial sky brightness to total night sky brightness: Below 0.01: black; 0.01-0.11: grey; 0.11-0.33: blue; 0.33-1: green; 1-3: yellow; 3-9: orange; 9-27: red; above 27: white.

#### 6.1.4 Infrastructure and geographical conditions

The set-up and operation of a detector system like  $H_i$ SCORE requires a certain amount of infrastructure, which may not be readily available in remote areas with low light pollution. Important points are:

- **Road:** The detector site must be accessible by a reliable road to transport the detector hardware onto the site and to allow for later maintenance. In the case of  $H_i$ SCORE, it is expected that heavy building machines or cranes are not needed for construction, thus relaxing the demand on the road to the site.
- **Power supply:** For the operation of the detector stations and the central data acquisition electricity is needed. This power may be partially or completely generated on site. The detector stations are planned to be powered independently, e.g. by solar power, in order to avoid the need for extensive cabling.
- **Data transfer:** In order to remote control the detector operation, update software, run tests or to read out data, a data transfer link from the detector site to the internet is very valuable. In a remote area a slow and expensive satellite link may be the only option, however, the expanding coverage of mobile phone networks may provide an additional, cheaper and faster option.

If the operation of the detector needs to be supervised permanently by a shift crew, a control room and accommodation for the shifters is needed additionally. For this accommodation electricity and water supply is needed, of which the latter may be challenging to achieve in remote, possibly desert-like areas. Also, a possibility for food supply as well as the option for medical treatment in case of an emergency must be available, e.g. by a town that can be reached within a reasonable time.

Apart from the infrastructure, the landscape must be suitable to deploy the  $H_i$ SCORE detector. Most important is the availability of a sufficiently flat area of at least  $100\text{ km}^2$ . The ground must be solid enough

## 6 Site evaluation

Location	Detector	Latitude	Longitude	Altitude [m]
<b>Fowler's Gap, Australia</b>	–	<b>31° 05' S</b>	<b>141° 43' E</b>	<b>180</b>
Pampa Amarilla, Argentina	Pierre Auger Obs.	35° 28' S	69° 35' W	1400
Khomas highlands, Namibia	H.E.S.S.	23° 16' S	16° 30' E	1800
Western Australia	(SKA)	26° 42' S	116° 40' E	390
<b>Tunka Valley, Russia</b>	<b>TUNKA</b>	<b>51° 49' N</b>	<b>103° 04' E</b>	<b>675</b>
Tibet, China	Tibet AS array	30° 06' N	90° 31' E	4300
Central Mexico	HAWC	19° 00' N	97° 18' W	4100

Table 6.1: Coordinates of current or future detector sites. Altitude is given in meters above sea level. Printed in bold are locations for which the H<sub>i</sub>SCORE field of view was simulated (see section 6.3). References are (in this order): Hampf *et al.* [2011a], The Auger Collaboration [1997], Aharonian *et al.* [2006c], MRO website [2011], TUNKA website [2011], Amenomori *et al.* [2011] and Sandoval *et al.* [2008]

to allow secure set-up of the detector modules. Rivers or strong vegetation pose obstacles for the set-up and maintenance of the detector and also increase the danger of natural disasters that can destroy the detector, such as flooding or bush fires. If the site is threatened by flooding, possibly also by occasional intense rainfall, or by extensive snowfall, the design of the detector stations must take this into account.

As discussed in section 5.7, a low altitude site is well suited for the H<sub>i</sub>SCORE detector in the standard configuration. However, if another set-up, especially a denser station spacing, is used in order to decrease the energy threshold, it will be beneficial to deploy the detector at a higher altitude.

### 6.1.5 Safety and sustainability

In order to ensure a safe operation of the detector for the whole duration of the project (at least ten years), the possible development of the site must be taken into account. Apart from the natural hazards mentioned in section 6.1.4, the operation can be endangered by new constructions nearby that produce strong light pollution, e.g. new mining sites or military structures. For example, the CANGAROO Cherenkov telescope system has suffered from light pollution from search lights installed on a nearby detention centre for illegal immigrants for some time of its operation [Itoh *et al.*, 2003]. While such development can never be ruled out completely, this danger can be minimised by discussions and agreements with the landowners of the surrounding area and the responsible governmental departments prior to the final selection of the site.

A careful evaluation of the political stability of the host country is also important with respect to the safety of the staff on site and the guaranteed access to the site. For the success of the project, support from the local authorities, companies and scientific community is also highly beneficial.

## 6.2 Possible detector sites

In this section, a few possible sites for the H<sub>i</sub>SCORE detector will be introduced. It should be noted that this list is far from exhaustive and only takes into account a few of the currently discussed options. A special focus is on the Fowler's Gap research station, the only location visited so far specifically for site evaluation (section 6.2.1). The other sites covered in this section are the TUNKA site in Siberia, Russia (section 6.2.2) and the Pampa Amarilla, site of the Pierre Auger observatory in Argentina (section 6.2.3). In section 6.2.4, a few other options are discussed briefly.

The coordinates and altitudes of all discussed sites are summarised in table 6.1 along with the sites of some other currently existing or planned detectors. All detectors mentioned in the table, besides SKA, are introduced in section 2.4. SKA is a new large radio telescope array, and the site mentioned in the table is

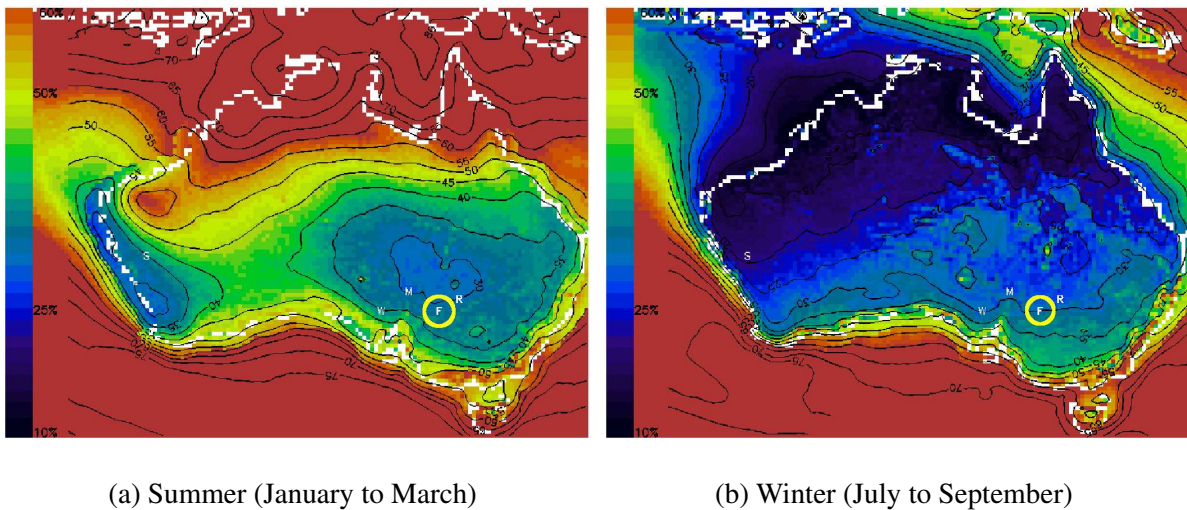


Figure 6.2: Percentage of cloudy nights over Australia for the period 1985 to 2006, defined as the time the given pixel is recorded as cloudy in [ISCCP, 2010]. The pixel size is  $30\text{ km}^2$ , contours are smoothed. The location of Fowler's Gap is indicated by the yellow circle in the south east of Australia [Thornton, 2010].

one of the two options currently considered for the detector, the other being in South Africa [SKA website, 2011].

### 6.2.1 Fowler's Gap research station

This 38,888 hectares research station is located in southern Australia in the state of New South Wales, about 110 km north of Broken Hill, a town of about 20,000 inhabitants which is served by regular airlines and can also be reached by car (via the Sydney-Adelaide highway) or the Transaustralian train service. The road to Fowler's Gap is well maintained and partly sealed. The nearest other settlement is the Packsaddle Roadhouse about 60 km north of Fowler's Gap.

The station is maintained by the University of New South Wales (Sydney) and is used mainly for arid zone vegetation and animal studies. A well maintained infrastructure for research exists, including a workshop, a range of heavy vehicles, a lab, a small library, a conference area and a computer room with internet connection. The station is run by a team of three to six permanent staff members, and research is being conducted by up to two dozen visiting scientists [University of New South Wales, 2011].

Fowler's Gap has been identified in an Australian wide survey [Thornton, 2010] as a location with very low cloud coverage, with only about 10% more cloud coverage than the best spots in Australia. Furthermore, the percentage of cloudy nights is roughly constant throughout the year, in contrast to many other tropical locations that have pronounced dry and wet seasons, thus making observations of all theoretically accessible regions of the sky equally feasible (see figure 6.2).

In the World Atlas of artificial night sky brightness [Cinzano *et al.*, 2001] the area around Fowler's Gap is classified in the lowest light pollution class, which means that the contribution of artificial sources to the total night sky brightness is less than 1% towards zenith (see figures 6.1b and 6.3). A more detailed study of the night sky brightness on site is presented in section 6.4.

Due to the continuous research activity at Fowler's Gap both long-term weather conditions as well as possible hazards by extreme weather conditions are well documented. In case of strong rainfall, the small rivers on the property can cause flooding. While the flooding area is rather small as the rivers run in deep valleys, and widespread damage is not expected, flooding can however affect the access for normal cars to the station. Bush fires are not expected to be a danger, as the vegetation is mostly very sparse.

## 6 Site evaluation

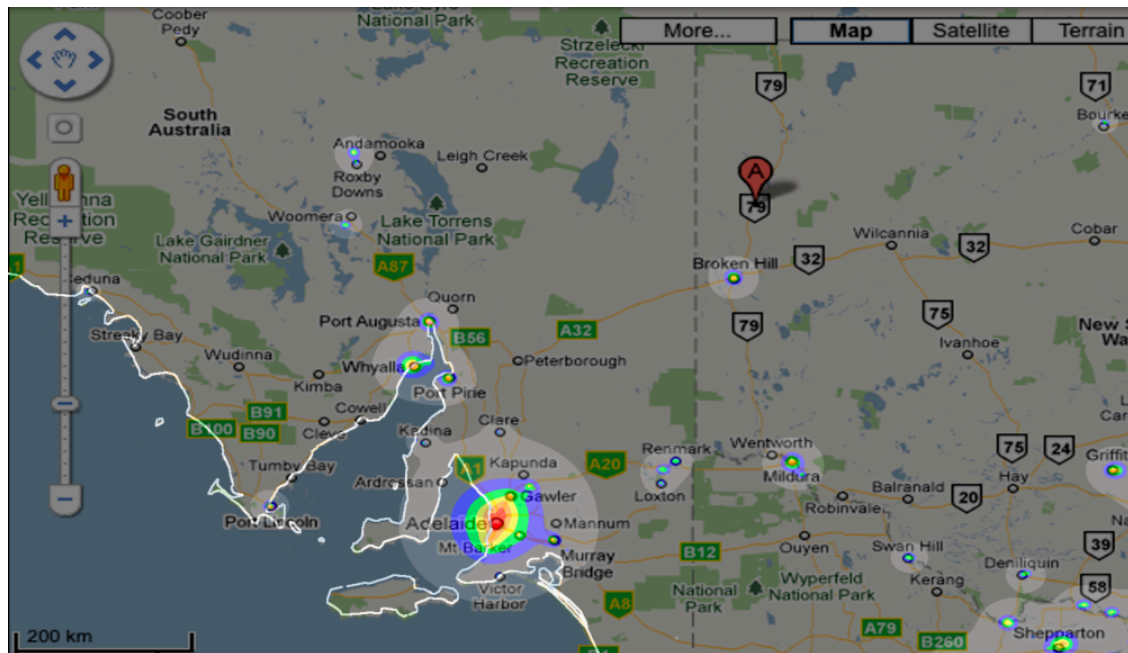


Figure 6.3: This overlay shows the light pollution levels in South Australia and the western parts of New South Wales. The location of Fowler's Gap is indicated by the "A" north of Broken Hill. Colour coding for brightness levels is the same as in figure 6.1. From Cinzano *et al.* [2001] and googlemaps [2010].

So far, the long term viewing quality has not been examined at Fowler's Gap, and it seems possible that dust from nearby sandy plains can increase the aerosol concentration in the air, leading to a strong light absorption. A light extinction measurement, ideally over a longer period, is still necessary to evaluate the quality of the site for astronomical observations.

The station homestead is located at an altitude of 180m above sea level, and most of the property is relatively even, except for a few hills that rise up to about 230m. Figure 6.4 shows two images of the location. For more information about Fowler's Gap, refer to appendix C.

### 6.2.2 TUNKA site

The TUNKA experiment is located in Tunka valley near lake Baikal in Siberia, Russia. The next biggest city is Irkutsk, a city of 500,000 inhabitants that can be reached by car, train and national airlines. Due to the operation of the TUNKA detector at the site all necessary infrastructure is available, including electricity, data transfer links and cabling to the detector stations. As the TUNKA detector operates at an energy threshold of about 1 PeV [Budnev *et al.*, 2008], a large overlap with  $H_i$ SCORE is possible that can be used for tests and calibration. For firsts tests it may also be possible to connect  $H_i$ SCORE detector stations to the TUNKA electronics to use the same trigger and readout. The effective operation time for the TUNKA detector is about 400 hours per year [Kuzmichev, 2011].

### 6.2.3 Pierre Auger Observatory site

The Pierre Auger Observatory (PAO) is set up at the Pampa Amarilla in Argentina at an altitude of 1400 metres above sea level. The slope of the area is less than 0.5% over the whole area covered by the detector of 3000km<sup>2</sup> [The Auger Collaboration, 1997]. Due to the ongoing research activity on the site a complete infrastructure is available, including electricity, water supply, data transfer links and roads. Even though the



(a) Fowler's Gap station from above [University of New South Wales, 2011]

(b) Typical landscape at Fowler's Gap

Figure 6.4: Impressions of Fowler's Gap research station.

focus of the PAO is on energies above the energy range of  $H_i$ SCORE, a small overlap exists around  $10^{17}$  eV to  $10^{18}$  eV, offering valuable options for cross-checks and calibration. The overlap in energy range will become better with the planned low energy extension of the PAO, AMIGA [Platino and The Pierre Auger Collaboration, 2009]. The experience from members of the PAO collaboration could also be very beneficial for the development and operation of  $H_i$ SCORE in the case of a joint project. The major drawback of this site is possibly its relatively high cloud coverage of 35%, with peak values exceeding 50% in the Argentinian winter [The Auger Collaboration, 1997].

#### 6.2.4 Other options

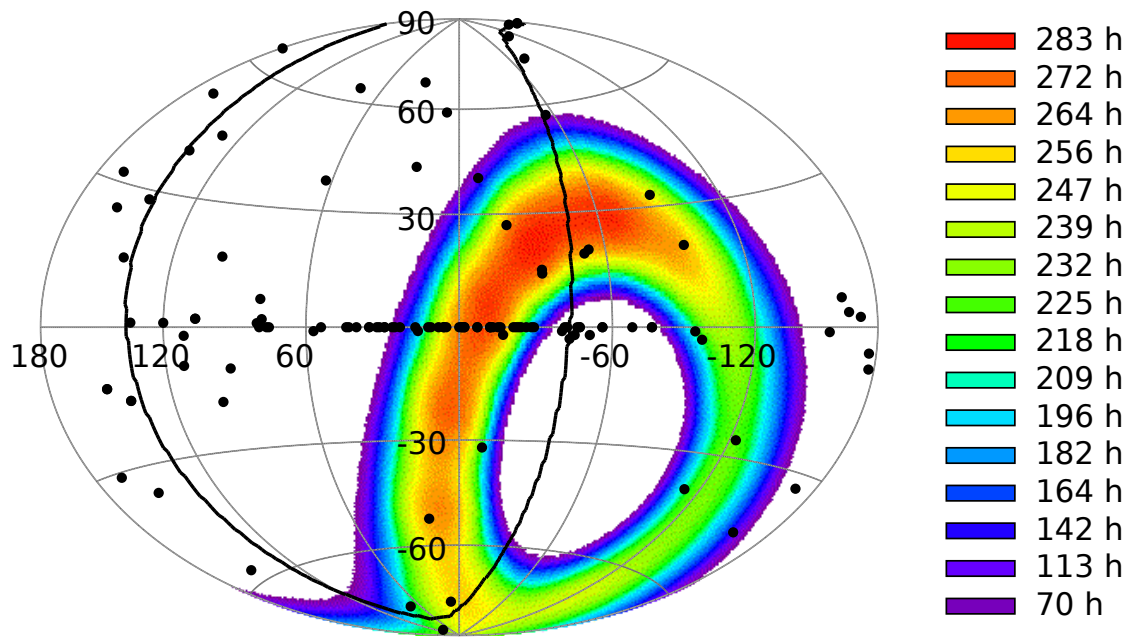
As mentioned above, this list is far from complete, and no systematic study for possible detector locations world-wide has yet been undertaken. In general, a site on the southern hemisphere seems to be preferable due to the field of view towards the inner Galaxy (see also section 6.3). Considering the criteria listed in section 6.1, many sites in Australia, southern Africa and South America are suited in principal.

### 6.3 Simulated field of view

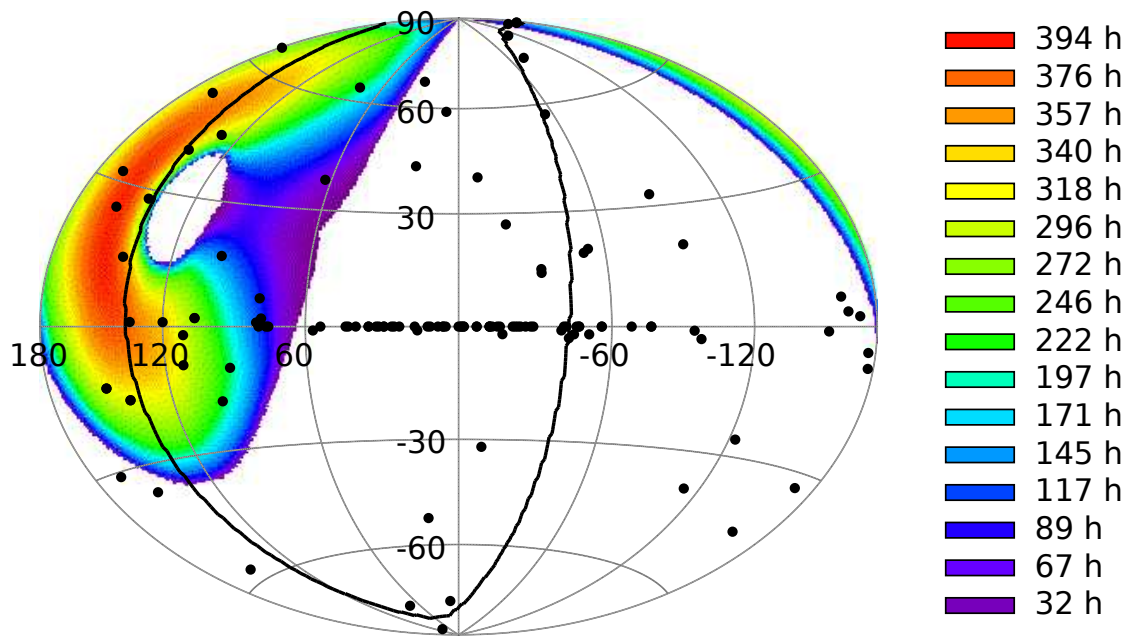
To determine the visible regions for different detector locations, a simulation to calculate the sky exposure for a detector at a given site has been developed (for technical details, see appendix A). It assumes that the detector is operating when the sun is at least  $18^\circ$ , and the moon at least  $2^\circ$  below the horizon. Other influences, like detector maintenance shut-downs or bad weather times are not considered at this stage. The simulation assumes that the detector has a uniform acceptance up to  $25^\circ$  zenith angle, which is supported by the detector acceptance derived in section 5.6.1. If events with higher zenith angle could be taken into account additionally (e.g. by modifying the Winston cones or relaxing the zenith angle cut), this would lead not only to a larger total field of view, but also to a longer exposure in the areas already covered.

The results of the simulation for two different locations are presented here: The Fowler's Gap research station in southern Australia on  $31^\circ$  southern latitude, and the site of the TUNKA experiment in Siberia, Russia at a latitude of  $52^\circ$  north (as mentioned in section 6.1.1, the field of view depends only on the detector latitude). The results for these two sites may be seen as examples for typical southern and northern hemisphere sites.

6 Site evaluation



(a) Fowler's Gap (31° south)



(b) TUNKA site (52° north)

Figure 6.5: Simulated one-year exposure times for H<sub>1</sub>SCORE at Fowler's Gap (top) and at the TUNKA site (bottom) in Galactic coordinates. No correction for bad weather has been included. Black dots are known VHE gamma-ray sources extracted from TeVCat [Wakely and Horan, 2011]. The thick black line indicates the supergalactic plane.

### 6.3 Simulated field of view

Name	long.	lat.	Exp.	Name	long.	lat.	Exp.
1ES 0347-121	-159°	-45°	130 h	HESS J1718-385	-12°	0°	274 h
PKS 0447-439	-112°	-39°	215 h	PKS 2005-489	-10°	-32°	208 h
PKS 0548-322	-123°	-26°	226 h	PKS 1510-089	-9°	40°	127 h
Vela X	-97°	-3°	216 h	HESS J1729-345	-7°	0°	277 h
RX J0852 h-4622	-94°	-1°	215 h	HESS J1731-347	-7°	0°	277 h
TeV J1010-313	-94°	20°	259 h	HESS J1741-302	-2°	0°	273 h
1ES 1101-232	-87°	33°	247 h	HESS J1745-303	-2°	0°	273 h
1ES 1312-423	-53°	20°	264 h	Galactic Centre	-1°	0°	270 h
Centaurus A	-51°	19°	262 h	G0.9+0.1	0°	0°	269 h
SN 1006	-33°	15°	272 h	HESS J1800-240B	5°	0°	253 h
HESS J1614-518	-29°	0°	178 h	HESS J1800-240A	6°	0°	249 h
HESS J1616-508	-28°	0°	188 h	HESS J1804-216	8°	0°	240 h
HESS J1626-490	-26°	0°	207 h	HESS J1809-193	11°	0°	224 h
HESS J1632-478	-24°	0°	224 h	HESS J1813-178	12°	0°	219 h
HESS J1634-472	-23°	0°	231 h	HESS J1825-137	17°	0°	183 h
HESS J1640-465	-22°	0°	238 h	LS 5039	16°	-1°	197 h
Westerlund 1	-21°	0°	245 h	HESS J1834-087	23°	0°	116 h
AP Lib	-20°	27°	265 h	HESS J1837-069	25°	0°	74 h
HESS J1702-420	-16°	0°	266 h	HESS J1841-055	26°	0°	30 h
HESS J1708-443	-17°	-2°	257 h	H 2356-309	12°	-78°	253 h
HESS J1708-410	-15°	0°	269 h	PKS 2155-304	17°	-52°	264 h
RX J1713.7-3946	-13°	0°	273 h	TeV J0013-189	74°	-78°	209 h
CTB 37A / B	-12°	0°	274 h	NGC 253	97°	-87°	232 h

Table 6.2: One year exposure times (no bad weather correction) for known VHE gamma-ray sources from Fowler's Gap (see also figure 6.5a). Positions are given in Galactic coordinates.

Name	long.	lat.	Exp.	Name	long.	lat.	Exp.
1ES 1218+304	-174°	82°	137 h	Cassiopeia A	111°	-2°	312 h
1ES 1215+303	-172°	82°	131 h	1ES 2344+514	112°	-9°	312 h
W Comae	-159°	83°	83 h	Tycho	120°	1°	342 h
Markarian 501	63°	38°	57 h	Markarian 180	131°	45°	305 h
MGRO J2019+37	75°	0°	97 h	LSI +61 303	135°	1°	377 h
MilagroDiffuse	76°	0°	103 h	3C66A	140°	-16°	307 h
H 1426+428	77°	64°	210 h	MAGIC J0223+403	140°	-16°	307 h
VER J2019+407	78°	2°	112 h	M82	141°	40°	332 h
MGRO J2031+41	79°	0°	121 h	1ES 0502+675	143°	15°	367 h
MAGIC J2001+435	79°	7°	107 h	S5 0716+714	143°	28°	307 h
TeV J2032+4130	80°	1°	126 h	IC 310	150°	-13°	308 h
BL Lacertae	92°	-10°	209 h	NGC 1275	150°	-13°	308 h
B3 2247+381	98°	-18°	213 h	RGB J0710+591	157°	25°	394 h
1ES 1959+650	98°	17°	136 h	1ES 1011+496	165°	52°	348 h
G106.3+2.7	106°	2°	275 h	1ES 0806+524	166°	32°	373 h
Boomerang	106°	2°	275 h	Markarian 421	179°	65°	255 h

Table 6.3: One year exposure times (no bad weather correction) for known VHE gamma-ray sources from the TUNKA site (see also figure 6.5b). Positions are given in Galactic coordinates.

## 6 Site evaluation

**Fowler’s Gap** Figure 6.5a shows the visible regions for a H<sub>i</sub>SCORE detector at the location of the Fowler’s Gap research station, colour-coded for the one-year exposure times. The sky visible during the Australian winter, i.e. the Galactic Centre region up to Centaurus A, receives nominal exposure times up to 250 hours and more. Assuming an experiment down-time of about 30% due to bad weather (which seems realistic, see figure 6.2), this leads to an exposure of 175 hours per year for sources in this region. During the summer, the Galactic plane is crossed again at a Galactic longitude of about  $-110^\circ$ , covering well-known VHE gamma-ray sources such as Vela X and RX J0852. The simulation has also been used to estimate the yearly exposure times of all currently known VHE gamma-ray sources, to evaluate the ”guaranteed” science output (source list taken from TeVCat in June 2011 [Wakely and Horan, 2011]). The results can be found in table 6.2, which contains 46 sources, many of them Galactic sources found during the H.E.S.S. Galactic plane survey. A study of this potential source list which compares the so-far measured spectrum of each source with the simulated sensitivity of the H<sub>i</sub>SCORE detector will be presented in Einhaus [2012]. As discussed in section 2.3.2, it is anticipated that many of these Galactic sources will be visible also in the UHE regime, as no cut-off is seen with VHE gamma-ray instruments, or the cut-off appears at sufficiently high energies to make the end of the spectrum visible to H<sub>i</sub>SCORE. It should also be emphasised that the continuous, unbiased survey operation of H<sub>i</sub>SCORE offers a great potential to discover new sources, especially in the inner Galactic region. A part of the supergalactic plane, which has been proposed to be a potential emitter of UHE gamma-rays [Kneiske *et al.*, 2009], also receives a high nominal exposure of more than 250 hours. In total, almost one quarter of the sky is seen with a nominal exposure of more than 200 hours per year, and 33% of the sky with more than 100 hours per year. The total darktime, which is relevant for calculating cosmic ray event numbers, is about 1500 hours (nominal) at this site.

**TUNKA site** In figure 6.5b the one-year exposure times for a detector at the TUNKA site are shown. During the Russian winter, the exposure exceeds 350 hours in some regions, covering the area around the Galactic longitudes of  $120^\circ$  to  $180^\circ$  at latitudes from zero to  $60^\circ$ . Prominent sources covered in this region are Markarian 180 and the starburst galaxy M82. During the summer the exposure is low due to short nights, and sources seen in this season, such as Markarian 501 or the Milagro TeV source MGRO J2019+37 receive less than hundred hours nominal exposure per year. The complete source list with exposure times can be found in table 6.3. As many of the extra-galactic sources seen from this location have been found to have a very steep (”soft”) spectrum in the VHE regime, it may be difficult to detect most of them (see also argument in section 2.3.2). It seems also reasonable to assume that the loss of observation time due to bad weather is relatively high at this location, since the operation time of the TUNKA experiment is given with 400 hours per year, while the total darktime given by the simulation is about 1200 hours. Due to the high latitude, the total covered area is smaller than for the Fowler’s Gap location, namely 21% of the sky above 100 hours, and only 15% above 200 hours per year.

### 6.4 Night sky brightness measurement at Fowler’s Gap<sup>1</sup>

As outlined in section 6.1.3, the residual night sky brightness (NSB) present even during moonless nights is the most important source of noise in the H<sub>i</sub>SCORE detector channels. Therefore, the site evaluation campaign at Fowler’s Gap was also used for a measurement of the NSB at the site, including a measurement of the spectrum and the variation of NSB between different regions of the sky. To cover both the summer and the winter sky, measurements were carried out during February and August 2010. In this section, these measurements and their results are presented.

In subsection 6.4.1 the portable instrument developed and built specifically for this campaign is described. The data from the instrument is processed as described in subsection 6.4.2. In subsection 6.4.3 the measured

---

<sup>1</sup>Note: The results presented in this section have been published previously by the author and collaborators in Hampf *et al.* [2011a].

brightness levels from several dark and brighter sky regions are presented, including scans across the Galactic plane. In subsection 6.4.4, these values are used to estimate the noise level induced in the H<sub>i</sub>SCORE detector stations by night sky brightness. The measured NSB spectrum is presented in subsection 6.4.5 and compared to measurements by other groups at other sites. Since the spectral measurements show significant differences in the NSB spectrum from the Cherenkov light spectrum, using band-pass filters to improve the signal to noise ratio may be an option, as discussed in section 6.4.6.

All sky positions in this section are given in equatorial coordinates by right ascension (RA) and declination (Dec) in the J2000 epoch.

#### 6.4.1 The instrument and its calibration

**Instrument set-up** The instrument design follows the concept presented in Preuß *et al.* [2002] with a few modifications for better calibration and a wider spectral coverage. Its main component is the photon counting photomultiplier module Hamamatsu HC124-3 that incorporates the photomultiplier tube (PMT) R268P, a Cockcroft-Walton high voltage generator, an amplifier and a discriminator into a single, rugged metal casing. The module requires only a 12 V supply and a control voltage to set the high voltage. Its discriminator threshold is preset to distinguish effectively between noise and single photon events. The resulting dark count rate is about 200 Hz, while the maximum signal rate is 1 MHz. The module is connected via an analogue-digital-converter (National Instruments USB-6008) to a laptop and controlled by a LabView programme (virtual instrument, VI), which was developed specifically for this application (see also appendix A). The VI is used to set the PMT high voltage, read out the signal rate and record the ambient temperature. All data is logged into an ASCII file together with user comments for later evaluation.

The PMT is installed in a metal tube on a standard hobby astronomer telescope mount (Meade LX D55). The telescope mount can be controlled via a handheld control pad or over a serial connection with the laptop. Either way, the telescope position is always recorded by the LabView VI and stored together with the other data in the log file. A small finderscope is installed in parallel to the viewing direction of the PMT in order to calibrate the telescope mount.

A long black plastic tube (length 580 mm, inner diameter 17 mm) is positioned in front of the PMT to reduce the photon rate to a level manageable by the PMT and the readout electronics, usually between 50 kHz and several 100 kHz at a dark site. This range is selected in order to achieve a high signal to noise ratio against the dark count rate of 200 Hz but keep away safely from the non-linear regime above 1 MHz. A sketch of the instrument is shown in figure 6.6, and a picture of the whole set-up in figure 6.7.

All supply voltages needed for the PMT and the telescope mount are generated from rechargeable 12 V lead batteries.

**Effective solid angle** In order to convert the measured rates into a flux, it is important to know light sensitive area and solid angle of the instrument. The inner diameter of the black plastic tube is measured to be  $(16.76 \pm 0.04)$  mm, which gives an area of

$$A = ((8.38 \pm 0.02) \text{ mm})^2 \times \pi = (2.21 \pm 0.01) \times 10^{-4} \text{ m}^2 \quad (6.1)$$

The effective solid angle  $\Omega$  can be calculated from the angular acceptance  $\varepsilon(\theta)$  using

$$\Omega = 2\pi \int \varepsilon(\theta) \sin(\theta) d\theta \quad (6.2)$$

The angular acceptance  $\varepsilon(\theta)$  is defined as the transmittance of light with an incident angle of  $\theta$ , normalised to the transmittance at an incident angle of zero. It is simulated using the ray tracing algorithm introduced in section 4.2.2, with the unknown reflectivity of the black tube as free parameter. The ray tracing encompasses the plastic tube, the metal box connecting to the PMT, and PMT entry window (see figure 6.6). However,

## 6 Site evaluation

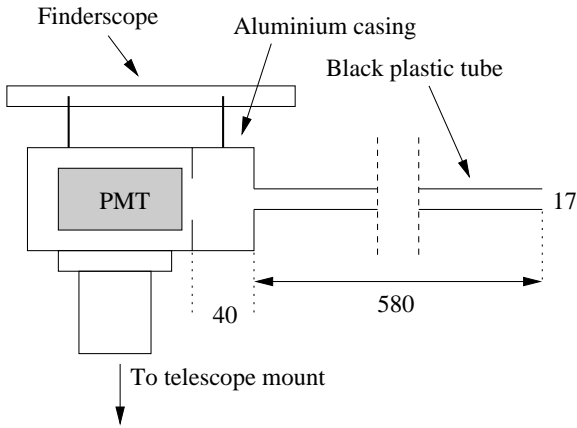


Figure 6.6: Sketch of the NSB instrument set-up.



Figure 6.7: The set-up during the measurements at Fowler's Gap.

a comparison with a simulation that contains only the plastic tube shows that the metal box and the PMT entry window do not influence the angular acceptance of the instrument (as planned in the design).

A cross-check of the simulation with an analytical calculation of  $\epsilon(\theta)$  (see appendix D), both for the case of no reflection, shows good agreement (see figure 6.8). To determine the reflectivity of the tube and to confirm the ray tracing results also for the case of non-zero reflectivity, a measurement of  $\epsilon(\theta)$  has been conducted. For this, the instrument was directed towards a point-like, isotropic light source at about 20m distance in a dark indoor corridor. From this distance, the light rays have a maximum angle of 3 arcminutes between them and can be treated as parallel in the view of the overall accuracy of the measurement. Using the telescope mount controls, the instrument was pointed to various angles away from the light source and the count rate was recorded by the LabView VI. Normalising the count rates to the rate at the centre position yields the angular acceptance. Comparing the measurement with simulations with different reflectivities, it is found that a simulation with a reflectivity of 11% fits the measured values best (figure 6.8).

Despite the good agreement between measurement and simulation, the measured acceptance is slightly above the simulated values at larger angles and at small angles. The deviation at larger angles is caused by stray light from the corridor walls, and the simulated values are believed to be more reliable in this regime. At small angles, the deviation is not understood, however, these values contribute only weakly to the effective solid angle: If only the simulation results are used for  $\epsilon(\theta)$ , the solid angle is found to be  $\Omega = 1.24 \times 10^{-3}$  sr, if the slightly higher measured values are used in the inner  $1.5^\circ$  instead, the solid angle increases to  $\Omega = 1.29 \times 10^{-3}$  sr. For all following calculations a value of

$$\Omega = (1.29 \pm 0.05) \times 10^{-3} \text{ sr} \quad (6.3)$$

is used.

**Systematic checks of the device** The rate measurement with the analogue-digital-converter and the LabView VI has been cross-checked with a stand-alone scaler module. The output of the PMT is split up to drive both the computer counter and the scaler module simultaneously, and the PMT is illuminated by an LED with various intensities. No discrepancy between the rates measured by the scaler and the LabView VI is found up to 200kHz (see figure 6.9).

The linearity of the brightness measurement is checked while the device is pointed towards a bright region of the sky. The photon intensity is reduced by putting neutral density filters with known transmittances into the optical path, and the reduction in the observed rate is compared to the expected reduction of photon intensity. The deviations from linearity are found to be below 4% (not shown).

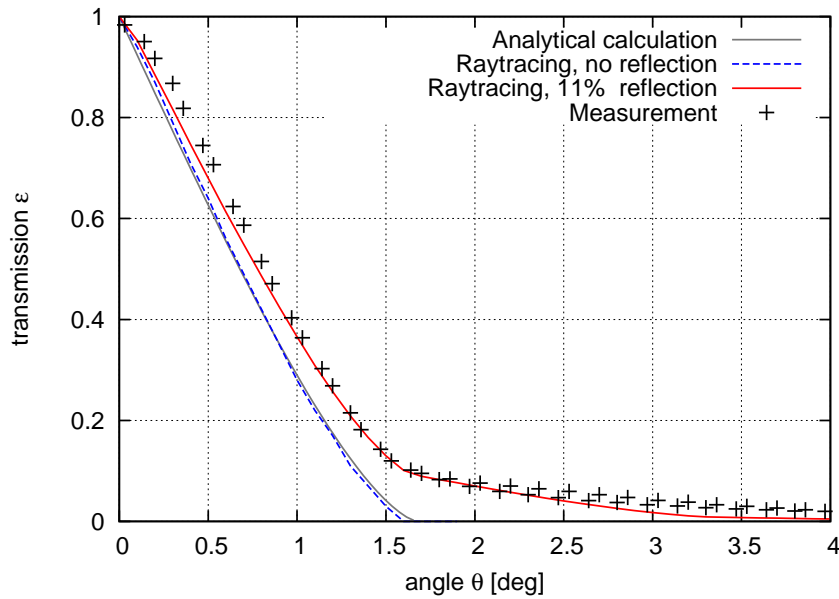


Figure 6.8: Angular acceptance of the NSB instrument, comparing analytical calculation and simulation for the case of zero reflectivity, and the measured values with a simulation using a reflectivity of 11%

The long-term stability of the device is checked in several long runs (24 to 48 hours) in a dark room by illuminating the detector by an LED that is automatically switched to various intensities in regular intervals, and monitoring the resultant count rates. Figure 6.10 shows the frequency measured with the highest setting of the LED in a 13 hour excerpt from one of the long runs. Deviations within this and other runs are below 1%, and deviations between different runs are below 2%.

#### 6.4.2 Data evaluation

The night sky brightness levels measured during this project are reported using the following quantities:

- **Count rate** at PMT: This is the raw count rate that was recorded with the device during the measurements. It is given in order to allow direct comparison of results of future campaigns using the same device and settings.
- **Photoelectron intensity** at PMT: This value gives the above count rate in units of  $(\text{s sr m}^2)^{-1}$ , using the area and the solid angle given in equation 6.1 and 6.3. This can be used directly as input for detector simulations, assuming that the PMT used here and the ones used in the experiments have sufficiently similar spectral response and peak quantum efficiency. The systematic uncertainty of this value is caused by uncertainties in the solid angle, the effective area of the tube and slight changes in the dark count rate, and is estimated to be about 5%.
- **Integral photon intensity** between 300nm and 650nm: This value gives the intensity of photons incident at the PMT cathode in units of  $\text{photons}/(\text{s sr m}^2)$ . It is obtained by dividing the photoelectron intensity by the effective quantum efficiency of the PMT over the relevant wavelength regime. The effective quantum efficiency is computed by convolving the wavelength dependent quantum efficiency

## 6 Site evaluation

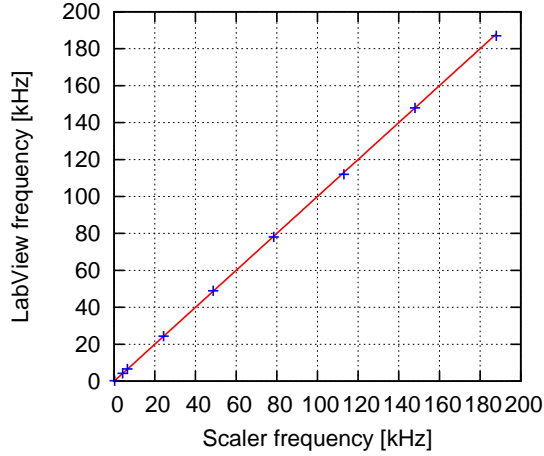


Figure 6.9: Frequency measured with a stand-alone scaler module and with the LabView VI, for various settings of the LED brightness. The statistical uncertainties on the data points are smaller than the markers.

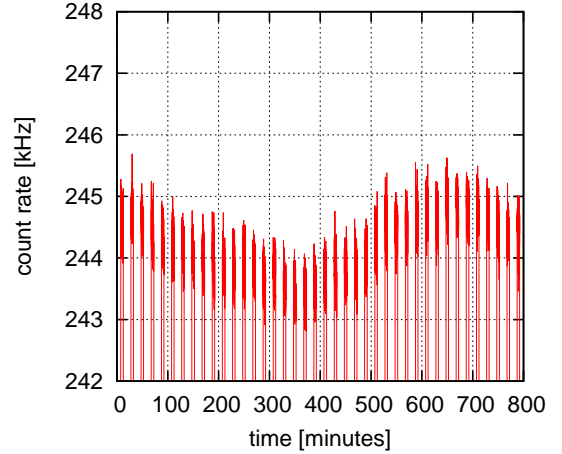


Figure 6.10: Frequency measured for the highest setting of the LED in one of the long-term stability checks. During the check, the LED was switched to a four different brightness settings in five minute steps. The rate was measured every 3 s.

$\epsilon_{\text{PMT}}(\lambda)$  with a normalised spectrum of the night sky brightness  $S(\lambda)$ :

$$\langle \epsilon_{\text{PMT}} \rangle = \int_{\lambda_1}^{\lambda_2} \epsilon_{\text{PMT}}(\lambda) S(\lambda) d\lambda \quad (6.4)$$

The PMT quantum efficiency is taken from the manufacturer's datasheet (see appendix E). For the night sky brightness, the spectrum measured by Benn and Ellison [1998] at the Isaac Newton and Jacobus Kapteyn telescopes on La Palma is used, shown in figure 6.11 before and after the convolution with the PMT quantum efficiency. Integration over the folded spectrum gives an effective quantum efficiency of

$$\langle \epsilon_{\text{PMT}} \rangle = 0.0935 \text{ p.e./photon} \quad (6.5)$$

It is estimated that this value has an uncertainty of about 10%, due to uncertainties in the PMT quantum efficiency, which may e.g. degrade with age, and the shape of the assumed night sky brightness spectrum, which may be different at the time and location of the measurement. The systematic uncertainty of the integral photon intensity is therefore estimated to be 15%, much higher than for the photoelectron intensity. However, the integral photon intensity allows the easiest comparison to other studies taken with different instruments, e.g. CCD cameras at telescopes.

The spectral measurements presented in section 6.4.5 were done using a set of four astronomical Johnson filters (U, B, V, and R). To obtain the spectra, the recorded count rates  $R$  have to be corrected for the different total transmission of the filters and the wavelength dependency of the PMT quantum efficiency, resulting in a differential photon intensity (unit: photons/(s sr m<sup>2</sup> nm)):

$$\Phi = \frac{R}{A \Omega w_x} \quad (6.6)$$

## 6.4 Night sky brightness measurement at Fowler's Gap

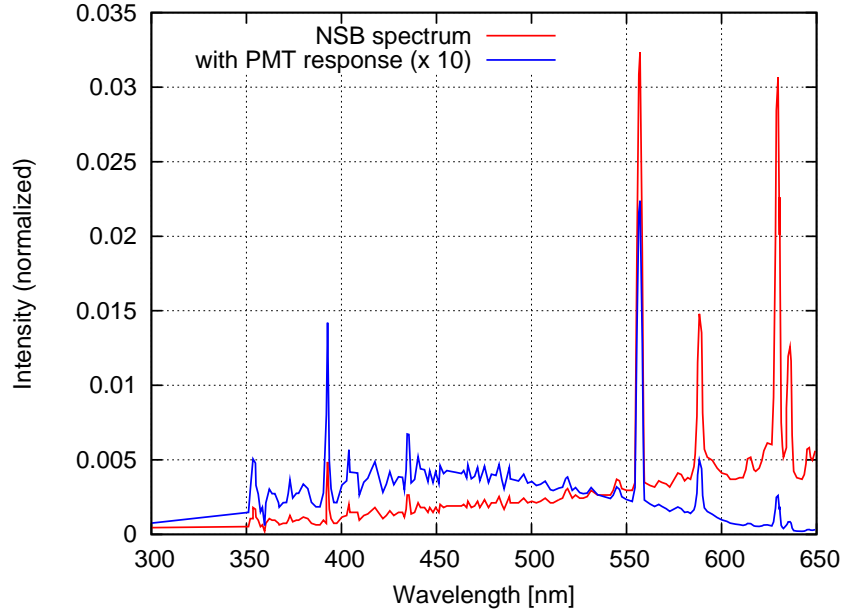


Figure 6.11: Normalised spectrum of the night sky brightness at La Palma [Benn and Ellison, 1998], and the same spectrum after taking into account the response of the PMT R268P used in the NSB measurement.

Filter	Eff. wavelength midpoint	$w_x$
U	365 nm	9.00 nm
B	445 nm	15.4 nm
V	551 nm	5.44 nm
R	658 nm	1.40 nm

Table 6.4: The effective wavelength window size  $w_x$  for the four Johnson filters that were used during the spectral measurements, calculated by equation 6.7. The effective wavelength midpoints are taken from Binney and Merrifield [1998].

In this,  $A$  and  $\Omega$  are the area and the effective solid angle of the tube as defined in equations 6.1 and 6.3, while  $w_x$  is the effective wavelength window size of the filter  $x$ , defined as

$$w_x = \int \epsilon_{\text{PMT}}(\lambda) T_x(\lambda) d\lambda \quad (6.7)$$

with the PMT quantum efficiency  $\epsilon_{\text{PMT}}(\lambda)$  and the transmission function of the filter  $T_x(\lambda)$ . For the filter transmission functions the values given by the manufacturer [Omega Optical, 2010] are used. The calculated values of  $w_x$  are shown in table 6.4.

A commonly used unit for the brightness of the night sky is *magnitudes per arcsec<sup>2</sup>* in the B and V band. The differential photon intensity can be converted to this unit using equations from Leinert *et al.* [1998]:

$$\text{B band: } 4.81 \times 10^7 \frac{\text{photons}}{\text{s sr m}^2 \text{ nm}} = 1 \text{ S}_{10} \text{ unit} \quad (6.8)$$

$$\text{V band: } 3.27 \times 10^7 \frac{\text{photons}}{\text{s sr m}^2 \text{ nm}} = 1 \text{ S}_{10} \text{ unit} \quad (6.9)$$

$$1 \text{ S}_{10} \text{ unit} = 27.28 \frac{\text{mag}}{\text{arcsec}^2} \quad (6.10)$$

## 6 Site evaluation

Name	Constellation	RA	Dec	count rate [kHz]	p.e. int. [ $10^{11}$ Hz] $\pm 5\%$	photon int. [ $10^{12}$ Hz] $\pm 15\%$
Dark region 1 (F)	Hydra	$8^h 25^m$	$0^\circ 00'$	55	1.9	2.1
Dark region 2 (F)	Antlia	$10^h 46^m$	$-25^\circ 37'$	48	1.7	1.8
Dark region 3 (F)	Lepus	$5^h 25^m$	$-26^\circ 16'$	47	1.7	1.8
Dark region 4 (F)	Corvus	$12^h 42^m$	$-16^\circ 50'$	56	2.0	2.1
Dark region 5 (A)	Sculptor	$23^h 30^m$	$-32^\circ 29'$	57	2.0	2.1
Dark region 6 (A)	Piscis Austr.	$22^h 20^m$	$-24^\circ 00'$	54	1.9	2.0
Dark region 7 (A)	Virgo	$13^h 40^m$	$-8^\circ 50'$	76	2.7	2.9
Dark region 8 (A)	Libra	$14^h 30^m$	$-17^\circ 50'$	71	2.5	2.7
From [1]	- - - various - - -			n / a	2.3	2.4
From [2]	- - - various - - -			n / a	n / a	1.8
Bright region 1 (F)	Monoceros	$7^h 25^m$	$-10^\circ 36'$	83	2.9	3.1
$\eta$ -Carinae area (F)	Carina	$10^h 44^m$	$-59^\circ 52'$	97	3.4	3.7
LMC (F)	Dorado	$5^h 23^m$	$-64^\circ 44'$	100	3.5	3.8
Crux region (F)	Crux	$11^h 22^m$	$-64^\circ 34'$	138	4.9	5.2
GC region (A)	Sagittarius	$17^h 20^m$	$-30^\circ 00'$	189	6.6	7.1

Table 6.5: Night sky brightness levels observed in February (F) and August (A) 2010 from Fowler’s Gap, and references from Preuß *et al.* [2002] ([1], Namibia and La Palma) and Mirzoyan and Lorenz [1994] ([2], La Palma). The upper part of the table contains selected dark regions, the lower part brighter regions of the sky. The photoelectron and photon intensities are given per sr and  $m^2$  (see section 6.4.2 for definition of these numbers). LMC denotes the Large Magellanic Cloud and GC the Galactic Centre.

### 6.4.3 Brightness levels at Fowler’s Gap

**Dark regions** During the measurements in Fowler’s Gap, the device was pointed at several selected dark regions in the sky. Each region was measured several times each night, and the results were averaged. The differences between the measurements were less than 5%, and probably mostly due to the different zenith angles of the individual measurements (unfortunately, not enough data could be collected during this campaign to evaluate the zenith angle dependence systematically).

The upper part of table 6.5 gives the coordinates and the measured brightness levels at several dark sky regions that were observed during the two campaigns in February and August 2010. For most of the regions the average level of brightness is about  $2 \times 10^{12}$  photons/(s sr  $m^2$ ) over the sensitive range of the PMT. This is slightly lower than the value given in Preuß *et al.* [2002] and higher than the one from Mirzoyan and Lorenz [1994], but consistent with both within the systematic uncertainties. Further comparisons with other measurements, which were taken in certain photometric bands, are presented in section 6.4.5.

The dark regions 7 and 8 (Virgo and Libra constellations) are significantly brighter than the rest of the dark regions, even though they are well away from the Galactic plane and other bright regions. However, since they were close to the horizon during the time of observation and their position on the sky is coincident with the ecliptic, it is possible that the higher photon intensity is at least partly due to zodiacal light. Bernstein *et al.* [2002] have measured the intensity of zodiacal light to be  $1.1 \times 10^{-7}$  ergs  $s^{-1}$   $cm^{-2}$   $sr^{-1}$   $\text{\AA}^{-1}$  at 465 nm, which converts to  $2.5 \times 10^9$  photons/(s sr  $m^2$  nm) at this wavelength. If one assumes an approximately flat spectrum over the sensitive wavelength range of the photomultiplier, it seems reasonable that the zodiacal light can increase the total measured flux by up to  $0.5 \times 10^{12}$  photons/(s sr  $m^2$ ), roughly in the right order of magnitude to explain the increased flux at these two regions.

**Bright regions** As many known and potential gamma-ray sources are located in brighter regions of the sky like the Galactic plane, the night sky brightness levels in these regions are of particular interest for this study. Therefore, several pointed measurements were done towards these regions, and the results are shown in the lower part of table 6.5. The  $\eta$ -Carinae area and the Large Magellanic cloud, which contains several interesting targets for UHE gamma-ray observations such as the SN 1987A or 30 Doradus, are about twice as bright as the darkest regions of the sky. The Galactic Centre region, also a very interesting VHE and potential UHE gamma-ray source, is about three times brighter than the darkest regions. To estimate the impact of this higher brightness on a wide-angle detector it is also important to know the extension of the high brightness levels. For this, the brightness profile of the Galactic plane was examined with several scans across different regions.

Figure 6.12 shows two scans across the plane in the Canis Major region, one of the darker regions of the Galactic plane. The two scans, which were taken along a declination of  $-22^\circ$  in two successive nights during the February campaign, are in reasonable agreement. The maximum photon intensity in this scan is about  $3.5 \times 10^{12}$  photons/(s sr m<sup>2</sup>), almost twice as bright as in the darkest regions of the sky.

Figure 6.13 shows a scan across the Galactic Centre / Sagittarius region, one of the brightest regions in the sky. The very bright outlier at 17.8 hours is probably due to a single bright star, while the actual peak of the scan is found at 17.3 hours with a brightness of  $7 \times 10^{12}$  photons/(s sr m<sup>2</sup>). This is about twice as high as in the Canis Major area and four times higher than in the darkest regions in the sky, in agreement with the measurement by Preuß *et al.* [2002]. A scan across the southern cross region, along a right ascension of  $11^h 30^m$ , shows a similar brightness profile.

It can be seen from all scans that the brightness level drops to values considerably below the peak within the field of view of the H<sub>i</sub>SCORE detector of  $\pm 25^\circ$ . A calculation of the night sky levels expected in the detector is presented in the following subsection.

The statistical errors in the data points of figures 6.12 and 6.13 are negligible. The systematic error is assumed to be 15%, mainly due to uncertainties in the instrument calibration (see section 6.4.2).

#### 6.4.4 Expected noise level in the H<sub>i</sub>SCORE detector channels

**Dark regions** If the NSB is assumed to be roughly constant across the field of view of the H<sub>i</sub>SCORE detector, the average brightness level in one H<sub>i</sub>SCORE detector channel can be calculated using the upper area of the Winston cone,  $A = 0.125 \text{ m}^2$ , and its effective solid angle,  $\Omega = 0.59 \text{ sr}$  (see section 4.2.2). This assumption seems reasonable for most of the dark regions in sky. Using the average dark region NSB level of  $2 \times 10^{12}$  photons/(s sr m<sup>2</sup>), the average brightness level  $N$  on the PMT becomes

$$N_{\text{dark}} = 1.5 \times 10^{11} \text{ photons/s} \quad (6.11)$$

If the PMTs used in the detector are assumed to have roughly the same quantum efficiency as the detector used in this NSB measurement (see equation 6.5), the resulting photoelectron rate in the PMT would be about  $1.4 \times 10^{10}$  Hz, or 14 photoelectrons per nanosecond.

**Bright regions** To obtain the noise level for regions with strong variations of the NSB over the H<sub>i</sub>SCORE field of view, such as the Galactic plane, an assumed NSB distribution in the sky is convoluted with the acceptance of the Winston Cone in two dimensions. For the NSB distribution, the profile from the scan across the Galactic Centre region shown in figure 6.13 is used, with the very bright outlier at 17.8 hours removed. For a conservative estimate, i.e. to obtain the highest possible noise level, the centre of the Winston cone is pointed towards the peak of the NSB profile at the right ascension of 17.3 hours. This places some part of the Winston cone field of view outside the scanned region, this region is filled up with a constant NSB level equal to the last scan point at  $RA = 16.5$ , namely  $3.7 \times 10^{12}$  photons/(s sr m<sup>2</sup>). From the shape of the scan it seems that this is also a conservative assumption, i.e. rather overestimating the actual NSB level,

## 6 Site evaluation

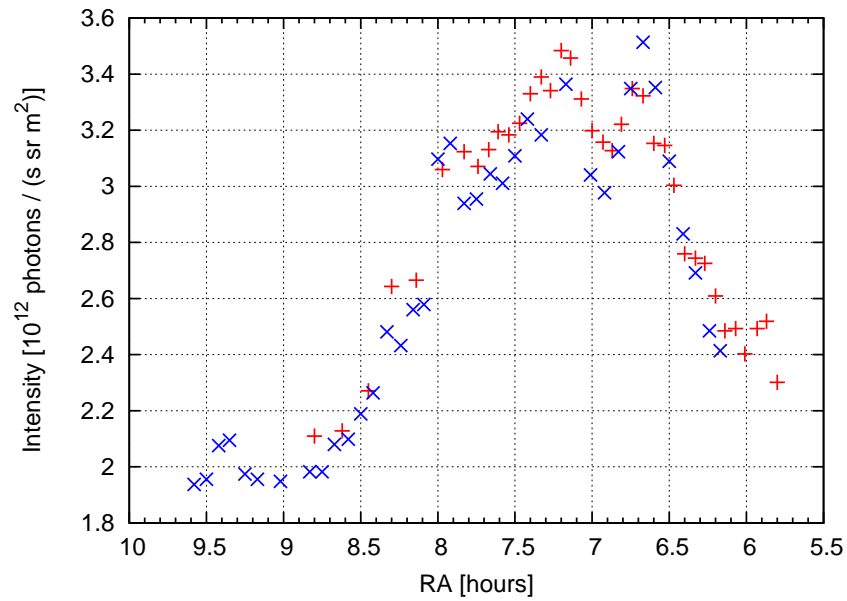


Figure 6.12: Scan of NSB levels along a declination of  $-22^\circ$  through the Canis Major region. The different markers indicate measurements from two different nights in February 2010.

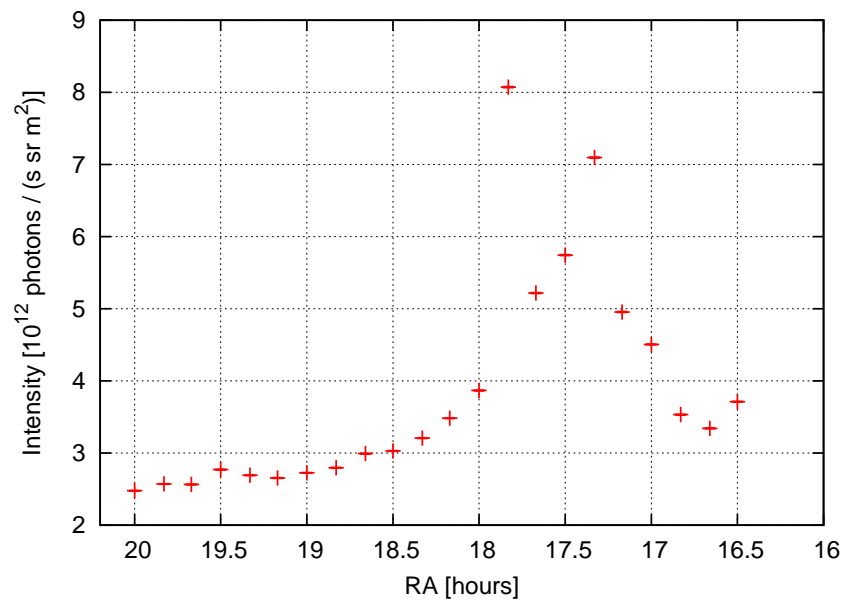


Figure 6.13: Scan of NSB levels along the declination of  $-30^\circ$  through the Galactic Centre region, taken in August 2010.

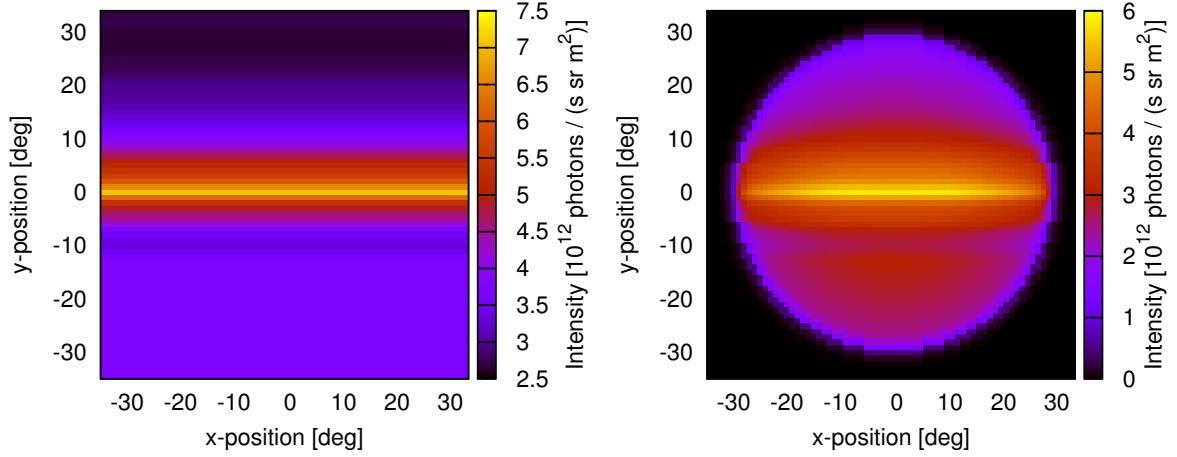


Figure 6.14: The brightness profile of the Galactic plane as derived from the scan across the Galactic Centre region (figure 6.13) before (left) and after (right) convolving with the Winston cone acceptance.

since towards the other direction the brightness eventually drops to a much lower level. For the Winston cone acceptance, 80% reflectivity and a uniform PMT acceptance is assumed (see figure 4.5 on page 80).

Figure 6.14 shows the obtained brightness profile of the Galactic plane before and after convolution with the Winston cone acceptance. In the inner region, the NSB level is reduced to about 80%, and at about  $28^\circ$  from the centre the brightness level drops to zero, which is consistent with figure 4.5. The average photon level seen through the Winston cone is calculated by integrating over the convoluted skymap to be  $2.5 \times 10^{12}$  photons/(s m<sup>2</sup>), which results – by taking into account the Winston cone area of  $A = 0.125$  m<sup>2</sup> – in a photon rate of about

$$N_{\text{bright}} = 3.1 \times 10^{11} \text{ photons/s} \quad (6.12)$$

This is about twice as high as the brightness seen towards the darkest regions of the sky. The corresponding photoelectron rate is  $2.9 \times 10^{10}$  Hz, or 29 photoelectrons per nanosecond.

In the simulation presented in chapter 5, an average NSB level of

$$N_{\text{simulation}} = 2.3 \times 10^{11} \text{ photons/s} \quad (6.13)$$

is used, with a corresponding photoelectron rate of  $2.15 \times 10^{10}$  Hz, or 21.5 photoelectrons per nanosecond.

**Impact of bright stars** These numbers are derived from observations without bright stars in the field of view, however, a number of bright stars will usually be in the field of view of the H<sub>i</sub>SCORE detector. A star with visible magnitude zero ( $m_V = 0$ ) appears with a brightness of  $2.54 \times 10^{-6}$  lumen/m<sup>2</sup> outside of the atmosphere [Schlyter, 2010]. The brightness of one lumen is equivalent to a power of 1.464 mW at a wavelength of 555 nm, therefore light from this star corresponds to  $3.7 \times 10^{-9}$  W/m<sup>2</sup>. At this wavelength, a flux of  $10^{10}$  photons/(s m<sup>2</sup>) is needed to generate this power. Assuming an atmospheric transmission of 80% and taking into account the effective area of the Winston cone, the photon rate on the PMT from a single bright star is expected to be about

$$N_{\text{star}} = 10^9 \text{ photons/s} \quad (6.14)$$

i.e. at least two orders of magnitude below the average level of NSB. The brightness levels from stars with higher magnitude  $m_V$  are lower by a factor of  $2.512^{m_V}$ . From the total numbers of stars with a given magnitude [Hoffleit and Warren, 1995], and assuming a homogeneous distribution over the sky, on average

## 6 Site evaluation

about one star with a  $m_V < 1$  and about two stars with  $m_V < 2$  are expected in the field of view. Therefore, the contribution by single bright stars to the overall noise level is negligible for H<sub>i</sub>SCORE.

**Impact on H<sub>i</sub>SCORE operation** The impact of NSB on the detector is two-fold:

1. The NSB causes a constant current through the anode of the PMTs, which must be kept below the respective maximum ratings for the PMT. For the ET 9352KB PMTs introduced in section 4.2.3, the maximum current is 100  $\mu\text{A}$  (see datasheet in appendix E), which converts to  $6.24 \times 10^5$  photoelectrons per nanosecond. Comparing to the photoelectron flux seen towards bright regions, this imposes a PMT gain limit of about 21,500. With the nominal gain of the PMTs of  $10^4$  the anode current remains at about 46  $\mu\text{A}$ , well below the maximum rating.
2. The NSB also introduces noise fluctuations into the recorded PMT signals. These can cause false triggers (see section 5.2) and generally deteriorate the signal quality and thereby the accuracy of the event reconstruction. According to the Poisson distribution the noise in the signal is given by  $\sqrt{N}$ , i.e. between  $3.7 \sqrt{\text{p.e./ns}}$  for dark regions and up to  $5.4 \sqrt{\text{p.e./ns}}$  for bright regions. The average NSB level used for the simulation has a noise of  $4.6 \sqrt{\text{p.e./ns}}$  (all numbers for one detector channel).

### 6.4.5 Spectral composition of the night sky brightness

The spectral composition of the NSB over the visible region was examined using astronomical Johnson filters for the U, B, V and R band. The measured rates are converted to differential photon intensities at the filter wavelength midpoints as described in section 6.4.2. No significant differences were found in the shape of the spectra from different regions.

Figure 6.15 shows an average spectrum of the dark regions 1, 2, 3, 6 and 7 (see table 6.5 for their locations), along with results from measurements by other groups at the later H.E.S.S. site in Namibia and on La Palma. While the measurement by Preuß *et al.* [2002] was done with a similar instrument as the one used in this study (however with narrow bandpass filters instead of Johnson filters), the measurement by Benn and Ellison [1998] used a CCD camera and a spectrometer at a large optical telescope. A high resolution spectrum from the latter measurement, as shown in figure 6.11, was used to calibrate the instrument used here.

All spectra show an clear increase of the NSB towards longer wavelengths and are generally consistent with each other. Compared to the spectra from La Palma and Namibia, the photon intensity at Fowler's Gap is slightly lower at short wavelengths. This may be due to the stronger absorption by the increased air-mass above the observation level, which would be most pronounced at short wavelengths. This may, in fact, also be the reason for the slightly lower flux measured in Namibia (at 1800m a. s. l.) compared to La Palma (at 2200m a. s. l.) at the lowest wavelength data point by Preuß *et al.* [2002]. At longer wavelengths, the data from Fowler's Gap shows a slightly higher photon flux than the CCD measurement by Benn and Ellison [1998], the reason for which is unknown. It should be noted however that all differences between the spectra hardly exceed the systematic uncertainties of the measurements.

The photoelectron intensities seen in the different bands are shown in figure 6.16 for the same dark regions used in the previous plot, and for an average of bright regions (Crux, Monoceros and LMC regions as defined in table 6.5). Due to the low PMT quantum efficiency at long wavelengths the noise is dominated by wavelengths in the B and V band. Despite the high photon flux in the R band, it contributes only about 8% to the photoelectron flux at the PMT.

Using equations 6.8 to 6.10, the measured photon flux levels can be converted from the differential photon flux to the more commonly used unit of  $\text{mag/arcsec}^2$  in B or V band. The results are shown in table 6.6. The magnitude in V band is often used to quantify the darkness on an astronomical site, and a NSB level of  $21.6 \text{ mag/arcsec}^2$  can be considered typical for a good astronomical site [Garstang, 1989]. Measured values at large optical observatories are in the same order of magnitude, e.g. 21.69 to 21.91  $\text{mag/arcsec}^2$  for the

### 6.4 Night sky brightness measurement at Fowler's Gap

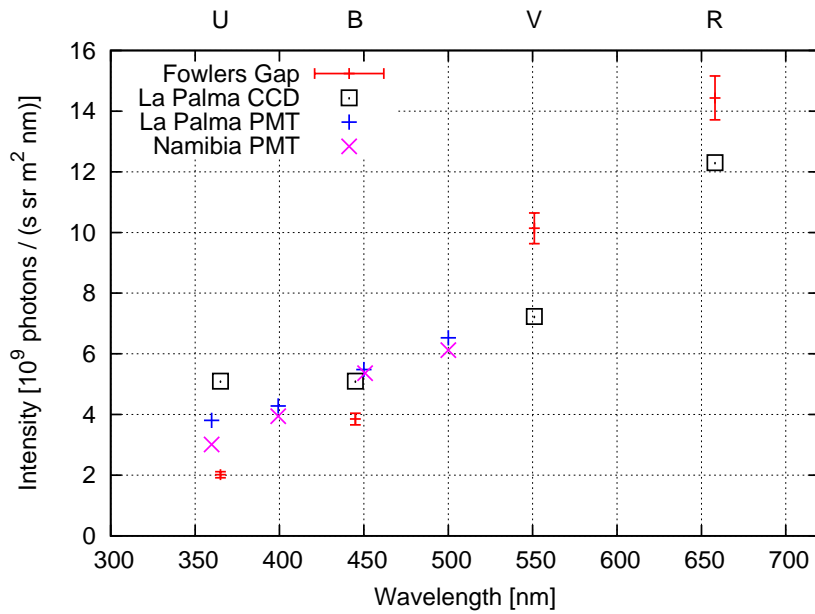


Figure 6.15: Averaged spectra of dark regions 1, 2, 3, 6, and 7 as measured from Fowler's Gap with astronomical Johnson filters (U, B, V, and R bands) and measurements from Preuß *et al.* [2002] ("PMT") and Benn and Ellison [1998] ("La Palma CCD"). Statistical uncertainties are indicated by errorbars, systematic uncertainty is 15% (see section 6.4.2).

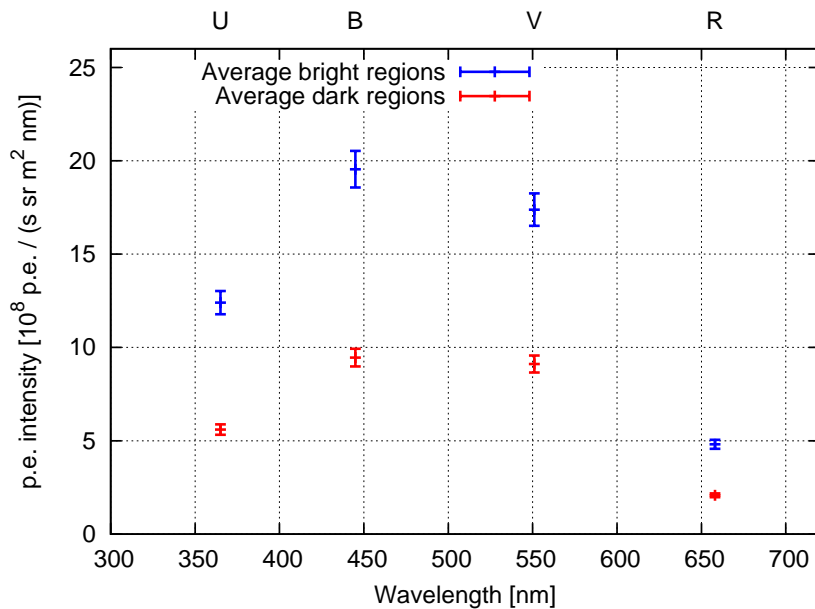


Figure 6.16: Spectra of dark and bright regions as measured in Fowler's Gap, without unfolding the PMT response (i.e., the intensities actually seen by the PMT). Statistical uncertainties are indicated by errorbars, systematic uncertainty is 5% (see section 6.4.2).

## 6 Site evaluation

	diff. photon intensity $10^9$ photons / (s sr m <sup>2</sup> nm)	$S_{10}$ units	brightness mag/arcsec <sup>2</sup>
Dark regions, B band	3.85	80	23.0
Dark regions, V band	10.1	310	21.6
Bright regions, B band	7.97	166	22.2
Bright regions, V band	19.4	592	20.9

Table 6.6: Measured NSB levels at Fowler’s Gap in B and V band in different units.

Included	Blocked	signal	NSB	$S / \sqrt{\text{NSB}}$
U	B, V, R	0.55	0.21	1.20
U, B	V, R	0.92	0.57	1.21
U, B, V	R	1.00	0.92	1.04
U, B, V, R	-	1.00	1.00	1.00

Table 6.7: Fraction of Cherenkov light and NSB present upon application of an ideal low-pass filter with a threshold between the ”included“ and ”blocked“ filter bands (using the same numbers as the plot in figure 6.17). The last column shows the gain in the signal to noise ratio achieved by the filter. Shown are the numbers for dark regions as measured at Fowler’s Gap; however, the numbers for bright regions are almost identical.

European Southern Observatory in Chile or 21.54 to 21.92 mag/arcsec<sup>2</sup> for the McDonald Observatory in the United States [Leinert *et al.*, 1998]. In those measurements all stars brighter than magnitude 13 were excluded, while the measurement presented here excluded only the brightest stars, which should lead to a (small) overestimation of the NSB level.

### 6.4.6 The use of filters to suppress night sky brightness

While the noise from NSB is dominated by longer wavelengths, the Cherenkov spectrum after atmospheric absorption peaks at about 320nm and falls off towards longer wavelengths (see figure 2.12 on page 31). Figure 6.17 shows a comparison of the normalised NSB and Cherenkov spectra, as seen by the photomultiplier in the four previously used wavelength bands. Due to the different shape of the spectra it seems promising to use low-pass filters to block a large fraction of the unwanted NSB while keeping most of the Cherenkov light.

To estimate the potential, the effect of an ideal low-pass filter (with 100% transmission below and no transmission above the threshold) was calculated. Table 6.7 shows the transmitted fraction of NSB and Cherenkov light for all four possible positions of the threshold, and the gain in the signal to noise ratio. The largest gain, a factor of about 1.2, can be achieved including only wavelengths from U or from U and B bands. Of those two options, the second is preferable as it keeps more than 90% of the Cherenkov light and therefore reduces the relative effect of any other noise source. For a non-ideal filter with only 90% transmission above the threshold, the maximum gain is 1.15.

The same test has been done with the continuous spectrum measured by Benn and Ellison [1998] at La Palma (see figure 6.11), and a continuous simulated Cherenkov spectrum. The maximum gain for an ideal filter is 1.17 in this case, similar to the previous result, however the optimal cut-off wavelength is at only 430nm, while the discrete calculation suggested a cut-off at about 500nm. At 430nm, only about 70% of the Cherenkov light pass the filter.

While this gain in the signal to noise ratio is only moderate, it would help to improve the event recon-

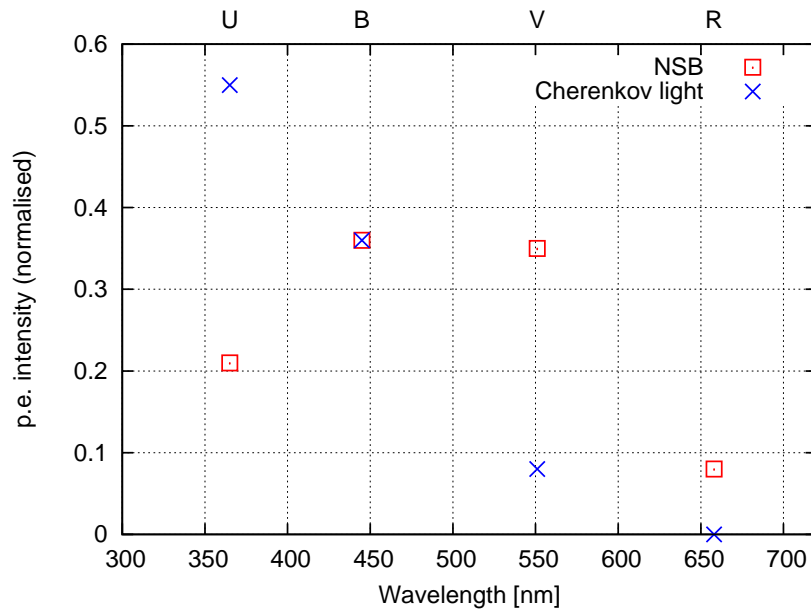


Figure 6.17: Normalised spectrum of the dark regions (the same as in figure 6.15), and simulated Cherenkov light intensities in the four used bands (U, B, V, R). Both spectra contain atmospheric absorption and the photomultiplier response function.

struction of low energy events with heavily distorted Cherenkov light signals. Additionally, it would reduce the rate of false noise triggers or allow to reduce the trigger threshold while keeping the same rate of false triggers (see also the discussion in section 5.2). In the latter case, the energy threshold of the detector is decreased accordingly, however additional simulations would be necessary to quantify the effect.

## 6.5 Concluding remarks

In this chapter, several promising sites for the set-up of the  $H_i$ SCORE detector have been introduced, with a focus on the research station Fowler's Gap in New South Wales, Australia. This station has been found to be an excellent astronomical location with respect to a low average cloud coverage and a low night sky brightness level. Also, it offers an excellent view on the inner Galactic region, the most promising part of the sky for the discovery of UHE gamma-ray sources. Large flat areas are available, however, the full  $H_i$ SCORE detector may need to extend to neighbouring properties. The possibility for this extension, and the willingness of the respective landowners for cooperation, has not yet been assessed. The most important task that still needs to be addressed, however, is a long-term measurement of the atmospheric absorption at the site. Since the surrounding region contains also sandy, desert-like areas, a high aerosol concentration may be present in the atmosphere, increasing the extinction of Cherenkov light. Measurements of the extinction are underway, and first results are presented in Sudholz [2011].

The TUNKA site is currently foreseen as site for a small test array of  $H_i$ SCORE stations. For this, the available infrastructure and the experience and support of the TUNKA collaboration are very beneficial. For the set-up of the full-scale detector, this site seems to be not well suited, mainly due to the field of view and the relatively short possible observation time per year of only 400 hours.

The site of the PAO in Argentina may be a very good site for the  $H_i$ SCORE detector. It has proven to be a high quality site for astronomical observations during the recent years and offers a more than sufficiently large flat area. The cooperation with the PAO collaboration seems very promising due to their experience

## 6 Site evaluation

with a similar detector concept. The main drawback of this site may be the apparently high percentage of cloudy nights.

Generally, a southern hemisphere site at latitudes of about  $-35^\circ$  south is well suited for observations in the UHE regime, as it offers a good coverage of the inner Galactic region and a relatively large part of the Galactic plane. As several other projects that aim at UHE observations are located in the northern hemisphere, e.g. HAWC or Tibet AS-gamma experiment, with its planned extension to LHAASO [Cao and The LHAASO Collaboration, 2009], a southern site seems especially recommendable for a new UHE gamma-ray observatory for a good overall sky coverage.

The night sky brightness measurements at Fowler's Gap have resulted in valuable data for the simulation and design of the H<sub>i</sub>SCORE detector. The NSB levels have been found to vary by up to a factor of four between different regions of the sky. However, the brightest regions in the sky have only a small extension, and the noise rate on the detector has been calculated to vary only by a factor of two, between 14 and 29 photoelectrons per nanosecond (per detector channel). In the simulation a value of 21.5 p.e./ns is used.

The spectrum of the NSB at Fowler's Gap has been found to be dominated by longer wavelengths, similar to spectra measured at other sites. However, due to the wavelength dependency of the PMT quantum efficiency, the strongest noise contributions are from light in the blue and green region. Filters can be employed to suppress long wavelengths and to improve the signal to noise ratio, however, the expected gain has been found to be only between 1.15 and up to 1.2.

## 7 Conclusion & Outlook

In this thesis, two different approaches towards improving the observation capabilities of gamma-rays at ultra high energies have been examined. In both cases, this involved the development of new event reconstruction techniques that make particular use of the time structure of the Cherenkov light from extensive air showers.

### 7.1 Time gradient event reconstruction for the H.E.S.S. experiment

**Conclusions** It has been shown in simulations that the standard event reconstruction of the H.E.S.S. Cherenkov telescope array can be improved at primary energies above 1 TeV by using the *time gradient* of the telescope images. This time gradient essentially reflects the differences in the photon arrival times at different parts of the image, and is known to depend on the core position distance. The correlation between the time gradient and the core distance is used to improve the core position and subsequently the direction reconstruction for events with core positions far away from the telescopes, which are otherwise difficult to reconstruct. The time gradient reconstruction in its current implementation has been found to be most effective at energies between 3 TeV and 20 TeV, where the resolution of both the core position and the direction are improved by up to a factor of two. It has also been shown that the time gradient reconstruction is rather robust against camera edge effects. In principle, this makes it possible to relax the event quality cuts, which leads to a substantial increase in the effective area.

Both effects can improve the sensitivity of H.E.S.S.: A better angular resolution can be used to reduce the size of the source region in the analysis, thus decreasing the amount of background events. A larger effective area leads to higher event statistics, which is particularly valuable at high energies where the sensitivity is limited by the low number of detected gamma photons.

The new event reconstruction has been tested on data taken by the H.E.S.S. experiment in October 2009 in dedicated sampling mode runs. The observations were pointed towards the Crab Nebula, a prominent bright VHE gamma-ray source. Quality checks on the data revealed that the increased data rate in sampling mode caused problems in the H.E.S.S. readout system, which resulted in a substantial increase of the dead time. Nevertheless, the sampling mode data could be used successfully to detect the gamma-ray flux from the Crab Nebula. Above energies of about 3 TeV, the time gradient reconstruction results in more gamma-ray events in the source region, although the low number of gamma-ray events detected at these energies limits the significance of this result.

**Outlook** The time gradient analysis presented in this thesis can be seen as a first feasibility study for the H.E.S.S. experiment, which has shown that a gain in sensitivity can be expected. The software tools written for that study lack however many important features of the standard analysis framework. The next sensible step to make use of the time gradient analysis is therefore its incorporation into the standard H.E.S.S. software tools. This seems also important in view of the upcoming commissioning of the H.E.S.S. II telescope that is planned to make regular use of the time gradient to improve its monoscopic event reconstruction. Before further data is taken with H.E.S.S. in sampling mode, the described issues concerning the system dead time should be addressed and resolved.

The analysis presented here uses the distance prediction from the time gradient in a rather simple way. It is expected that its performance will improve further if it is used in connection with a more sophisticated event

## 7 Conclusion & Outlook

reconstruction algorithm like algorithm 3 [Hofmann *et al.*, 1999; Stamatescu *et al.*, 2011] or the model++ analysis [de Naurois and Rolland, 2009].

It seems also possible that the sampling mode data can be used to derive more information than only the time gradient, e.g. the evolution of the image shape in time or the movement of the image centre of gravity. The time structure may also be used as additional input in the image cleaning process to lower the threshold.

The further development of a stereoscopic time based analysis will be particularly interesting for the planned Cherenkov telescope array CTA.

## 7.2 The wide-angle, non-imaging air Cherenkov detector H<sub>i</sub>SCORE

**Summary** Dedicated observations of gamma-rays at ultra high energies are difficult with current instruments due to the low event numbers achievable with the available effective areas and require the development of new experiments. One approach, the H<sub>i</sub>SCORE wide-angle air Cherenkov detector array, has been introduced in this thesis. The experiment will consist of an array of small, non-imaging detector stations that are used to sample the Cherenkov light signal of extensive air showers. The design is optimised for UHE gamma-rays: As each event produces relatively strong Cherenkov light (about  $10^4$  photons/m<sup>2</sup> at 100 TeV), a light sensitive area of 0.5 m<sup>2</sup> per station is found to be sufficient (compared to light sensitive areas of  $\sim 100$  m<sup>2</sup> in Cherenkov telescopes used in the VHE regime). On the other hand, a large effective area of 10 km<sup>2</sup> to 100 km<sup>2</sup> is needed to gather enough events despite the very low gamma-ray flux. The instrumentation of such a large area becomes feasible by using a large inter-station distance of 150 m (resulting in  $\sim 49$  stations per km<sup>2</sup>), and a simple and inexpensive design of the detector stations. As one part of this thesis, the design of such a detector station has been sketched out, and two prototype stations have been constructed.

To examine the potential of the detector concept for UHE gamma-ray observations, the air shower simulation CORSIKA and the detector simulation `sim_score` are used in combination with a newly developed event reconstruction software. The low number of data channels, needed to facilitate the instrumentation of a large area, poses a significant challenge for the event reconstruction. The newly developed H<sub>i</sub>SCORE event reconstruction framework adapts some methods used previously for other detectors and introduces new methods which have not been used in non-imaging Cherenkov detectors so far. It was shown that the reconstruction of the core position, direction and energy achieves an accuracy comparable with that of Cherenkov telescopes in the VHE regime.

A special emphasis is put on the identification of gamma photons against the dominant background of cosmic ray particles. Several methods for the gamma-ray identification have been tested, and three of them are combined to a single gamma hadron separation parameter: The signal rise time in the central detector station, the shower depth relative to the particle energy, and the systematic biases in the different methods of the shower depth reconstruction. It has been shown that the gamma hadron separation has a noticeable impact on the detector sensitivity, with a quality factor rising from 1 (no improvement) near the energy threshold to about 1.7 at an energy of 1 PeV.

The sensitivity, i.e. the minimal detectable gamma-ray energy flux, for a 100 km<sup>2</sup> H<sub>i</sub>SCORE array is found to be about  $2 \times 10^{-13}$  ergs s<sup>-1</sup> cm<sup>-2</sup> in the energy range from 50 TeV to about 10 PeV. With this sensitivity, a detailed study of the continuation of energy spectra of currently known sources into the ultra high energy regime should be possible. This can help to shed light on several open questions of the non-thermal universe, most notably the origin of the Galactic cosmic rays seen at Earth.

The H<sub>i</sub>SCORE detector is by design in constant survey operation and offers a largely unbiased view of the sky region in its field of view. This is useful to examine source class abundances and distributions, but also a powerful way to detect new, unexpected gamma-ray sources. Its large field of view and its rather uniform acceptance are beneficial for the detection of extended sources or even large emission regions. It was also shown that due to its large effective area H<sub>i</sub>SCORE can be a powerful cosmic ray detector for energies from  $10^{14}$  eV to  $10^{18}$  eV. All these features make H<sub>i</sub>SCORE the ideal extension of the existing and planned suite

## 7.2 The wide-angle, non-imaging air Cherenkov detector $H_i$ SCORE

of gamma-ray observatories.

Finally, the question of a suitable detector site is discussed in this thesis, with a special emphasis on the visible sky region and the night sky brightness at site, which poses a major source of noise for a wide-angle Cherenkov detector like  $H_i$ SCORE. It was shown that a southern hemisphere site at latitudes of  $-30^\circ$  is ideally suited to study the inner region of our Galaxy, a promising site for sources of ultra high energy gamma-ray emission. Exposure times of almost 200 hours per year can be achieved for sources in the central field of view. The research station Fowler's Gap in New South Wales, Australia, has been visited for a closer examination, and a measurement of the night sky brightness at site has been conducted. It was found to be an excellent site for astronomical observations in respect to its darkness, which is comparable to established astronomical sites around the world. Various surveys of the night sky brightness revealed that it varies up to a factor of four between the darkest regions of the sky and bright regions such as the central Milky Way. Simulations show that the brightness observed by  $H_i$ SCORE will increase only by about a factor of two due to the averaging effect of its wide field of view. The numbers obtained here have been used to model the noise in the detector simulation `sim_score`. It was also shown that the spectrum of the night sky brightness is dominated by longer wavelengths, in contrast to Cherenkov light which peaks in the blue. The effect of bandpass filters to improve the signal to noise ratio is discussed, and a gain of a factor of up to 1.2 is anticipated. It has however not yet been decided whether this moderate improvement justifies the installation of filters in the detector stations.

**Outlook** Using the simulations presented in this work the  $H_i$ SCORE concept could be established as a promising approach for UHE gamma-ray observations. Therefore, the focus for the  $H_i$ SCORE project should now be on the development of the hardware and the deployment of the detector. In a first step, the mechanical and electronic design of the prototype station must be improved further using the experience gathered with the first two prototypes. Long term and extreme condition tests of the materials as well as the complete station are needed to ensure reliable operations. Additionally, the software for the slow control and the data readout and processing must be developed beyond the level described in Eichler [2011]. A very important and challenging task ahead is the development of a nanosecond time synchronisation between the detector stations.

It is foreseen to install first prototype stations and eventually a small engineering array at the site of the TUNKA detector in Siberia. Cooperation with the TUNKA collaboration as well as the Pierre Auger collaboration for the further development of the detector system is planned.

In terms of the software, more detailed studies of the impact of detector parameters (inter-station distance, light sensitive area, altitude) on the sensitivity may be done using the software introduced here. Further studies might address the potential of coupling the non-imaging Cherenkov measurements with other air shower detection mechanisms, such as particle detectors, Cherenkov telescopes, radio wave detectors etc.

The performance of the reconstruction, especially of the energy, and the gamma hadron separation is expected to improve by a multivariate analysis. This may however be a lower priority in comparison with the tasks currently at hand to realise the set-up of the detector.

Concerning the detector site, further studies are needed. More locations must be examined carefully with respect to the criteria lined out in this thesis to ensure a well-grounded decision. Unless a well-established observation site is envisaged for  $H_i$ SCORE, long term measurements of various atmospheric parameters, such as the night sky brightness and the atmospheric extinction, are crucial. If a site is decided upon, the infrastructure needs to be developed to prepare the site for the detector operation.

Finally, upon its completion, the  $H_i$ SCORE detector will be able to contribute significantly to our understanding of the non-thermal universe and has the potential to add a large piece in the puzzle of the origin of Galactic cosmic rays. The author would like to express his best wishes for success to all members of the  $H_i$ SCORE collaboration and is looking forward to hear exciting news from the project in the future.

## *7 Conclusion & Outlook*

# Appendices



## A Software developed for this work

This chapter contains a reference to all software that was developed by the author during the work on this thesis. Each one is described briefly, lining out the main features and directions for usage. It should be noted that detailed documentations of the codes are not possible here due to their large size. However, it should be possible to understand the code with the comments given here and in the code.

Since some of the programmes may be useful for future work on the described projects, they are made available at the following locations:

- Uni Hamburg astroparticle group subversion repository (SVN): The directories where the programmes can be found are given in the respective sections, relative to the base address <https://svnsrv.desy.de/desy/astrohh/>. The software versions used in this thesis are stored in revision 3683. The repository is only accessible for members of the astroparticle group.
- On the author's personal website: [www.desy.de/~dhampf](http://www.desy.de/~dhampf) (publicly accessible)

All software (except the NSB measurement framework) is written in python version 2.x (with  $x \geq 4$ ). For most programmes additional python modules are needed, as described in the respective sections. A reference list for the less common modules is given towards the end of this chapter, in section A.8.

Note that the detector simulation `sim_score` was written mainly by Martin Tluczykont and is therefore not described here. For reference, see Tluczykont *et al.* [2012a].

### A.1 H.E.S.S. event reconstruction

used in:	sections 3.2 to 3.7, see 3.4 for an overview of the software
SVN directory:	dhampf/HESS_timing/
Required python modules:	numpy, scipy, Tkinter, ephem, sidereal
Classes and functions:	HESS_classes.py, HESS_timing_functions.py, HESS_timing_constants.py
Main scripts (reconstruction):	treetime_ascii.C, merger.py, reco.py, start_reko.py, join_parts.py
Main scripts (organisation):	datenbank.py, HESS_timing.py
Main scripts (evaluation):	evaluate.py, core_res.py, eff_area.py, check_energy. py, make_event_list.py, make_width_lookup.py, show_ skymap.py

**Data structure** All data needed for the analysis is stored in python objects of the custom classes *event*, *telescope* and *pixel*, which are implemented in `HESS_classes.py`. The classes also contain all methods necessary for the reconstruction. Typical functions of the event class would be the core and direction reconstruction using algorithm 1 or the time gradient algorithm, or the energy reconstruction, while typical functions of the telescope class would be the image cleaning, the calculation of the time gradient or of the Hillas parameters. The pixel class is used mainly for data storage and has only a few minor functions.

## A Software developed for this work

**Additional functions and constants** The script `HESS_timing_functions.py` contains functions needed during different steps of the reconstruction, e.g. for file IO or coordinate transformations. In `HESS_timing_constants.py` important constants needed for the reconstruction are defined, e.g. the image cleaning thresholds or the ADC to photoelectron conversion factors for high and low gain channels.

**Data processing** Before the simulated data can be used, it must be converted from the native `sim_telarray` output format into a ROOT file. This is done using the `montecarloreader/eventio` programme supplied with the H.E.S.S. software (using release hap-10-06 with ROOT 5.18). In its standard version, the programme does not accept sampling mode data, however the underlying functions are capable of handling the different data structure. In order to activate the sampling mode data processing, the call to `Sash::EventioReader` must be done with a "16" (instead of "0") as second argument, which can be changed in line 85 of `eventio.C`.

The ROOT file is then processed using the script `treetime_ascii.C`, which calculates the pixel pedestals, identifies broken (dead) pixels and writes the signals of good pixels into a plain text file. This text file is read in by `merger.py`, which fills the python event class objects used for the further processing. It also adds information from other sources (hence its name), which is lost during the ROOT to ASCII conversion: The pixel coordinates in the telescope are read in from `pixelpositions.dat` or `pixelpositions2.dat` (simulated data and real data files use different pixel ordering), and the Monte Carlo values of events (core position, energy, etc.) are read in from the log output of `sim_telarray`. Because of the differences between simulated and real data, this script requires the manual setting of the boolean variable `real_data`.

The signal parameters, such as the peak time or the pixel amplitude are filled during the process. The merger script also takes over the time-consuming task of image cleaning. In order to allow parallel processing in the following steps and to avoid overly large files, the output is split into files with 50 events.

**Reconstruction** The reconstruction is done using functions of the telescope and event classes, which are called from `reco.py`. It calls the core position and direction reconstruction for both the extended and the standard nominal distance cut and stores the results. After that, the energy is reconstructed and the mean scaled width is calculated for later use in the gamma hadron separation. The results are stored into `summary` files, which contain only the event and telescope level information without the individual pixels, which yields a substantial decrease in file size.

The script `start_reco.py` is used for batch processing of a large number of files. Finally, `join_parts.py` is used to merge all files of 50 events each into one summary file containing all events of a run.

**Organisation and visualisation** To keep a record of all simulated data, the script `datenbank.py` is used. It can also be used to call all scripts of the evaluation level using a selection of runs. The script `HESS_timing.py` provides a powerful event display with camera images showing the pixel amplitudes and peak times, and the reconstruction parameters. It also displays a "ground view" of the four telescopes with their reconstructed Hillas axes along with the reconstructed and MC core positions for a visualisation of the core reconstruction. The displays can be written out into `svg`-files for reproduction. The programme also contains functions to call individual reconstruction steps for testing, e.g. to visually inspect the effect of different image cleaning algorithms.

**Evaluation level** Different scripts are available to evaluate the accuracy of the reconstruction (using simulated data), to check the data quality and to produce the high level results like skymaps and spectra (using real data).

The scripts `eff_area.py`, `check_energy.py` and `core_res.py` are used to generate the effective areas, to check the energy reconstruction and to calculate the resolution of the core position and direction reconstruction from the simulated data. Also using simulated data, the lookup tables for the mean scaled

width and the energy reconstruction are generated in `make_width_lookup.py`. The script `evaluate.py` works both with simulated and real data and displays an assorted variety of information about the data, such as telescope performance figures, distributions of the mean scaled width, the core distances, the nominal distance or the image size and information about the effectiveness of various quality cuts.

Finally, `make_event_list.py` is used to generate eventlists in FITS format from real data for subsequent use with the `pyfact` tools [Raue, 2011]. On this level, the mode of reconstruction used for the analysis (algorithm 1, time gradient, mixed algorithm, different nominal distance cuts) is chosen. Also, the conversion from telescope to sky coordinates is called at this stage (see also next paragraph). The `pyfact` tools are used then to generate the skymaps and spectra. The script `show_skymap.py` displays the skymaps generated by `pyfact/pfmap.py` (cannot be used directly on the eventlist).

**Coordinate transformations** Since the transformation from telescope to sky coordinates is a non-trivial exercise, the used method will be described briefly. The conversion relies on the coordinate transformation routines from the python package `sidereal`, and is implemented in the event class method `radec_of`, which makes use of the function `alt_az`.

In a first step, the pointing of the telescopes, which is given in equatorial coordinates (right ascension / declination) in the run log file, must be converted into horizontal coordinates (azimuth / altitude). This task is performed by the function `alt_az` using the geographic location of the H.E.S.S. array and the exact time of the event. The result gives the horizontal coordinates of the camera centre.

Subsequently, the direction of the event, given in camera coordinates, is added to these coordinates. Care must be taken to include the cosine correction for the azimuth angle to take into account that the azimuthal field of view of the camera can be larger than its nominal  $5^\circ$  opening angle, depending on the altitude. Finally, the resulting horizontal coordinates are transformed back into equatorial coordinates, using again the event time and the telescope location.

## A.2 Ray tracing algorithm

used in: sections 4.2.2 (Winston cone) and 6.4.1 (NSB measuring device)  
 SVN directory: `dhampf/python/raytracing/`  
 Main script: `winston.py`

This script simulates the propagation of light rays through a spherically symmetric object. It can be used to calculate the angular acceptance of the object and to study the properties of the light rays at the bottom, e.g. their spatial or angular distribution. The shape of the object is given by the function  $r(z)$ , which contains default functions for Winston cones (using equation 4.4), approximated Winston cones (not used in this thesis) and straight cones (including straight tubes).

If `display` is set to true, the object and the simulated light rays are shown on a graphical interface, which is valuable for debugging but should be turned off for large statistics runs. The reflectivity of the surfaces is set by `reflectivity`, the size of the cone or tube by  $R1$  (upper, larger opening),  $R2$  (lower opening) and `default_length` (height). For Winston cones, the height is calculated from  $R1$  and  $R2$  and `default_length` is ignored. All sizes are in pixels and can represent any scale needed for the actual problem (e.g. for the Winston cone calculation usually one pixel  $\hat{=}$  1 mm is used).

The loop over the events (simulated light rays) is done in the function `draw`, the actual ray tracing in function `startStrahl`. Each time a light ray collides with a surface, `startStrahl` is called recursively with a new direction vector (representing the direction of the light ray after reflection) until the light ray either arrives at the bottom, is reflected back to the upper opening, or is attenuated to an intensity less than 0.01% by the reflections. The light rays are implemented as objects of type `lichtstrahl`, using the `vector` class for their origin and direction information. The results are stored in an object of the `Statistik` class.

### A.3 NSB simulation and trigger rate calculation

used in: section 5.2  
SVN directory: dhampf/python/nsb/  
Required python modules: numpy  
Main scripts: produce\_nsb.py, calculate\_rates.py, array\_trigger.py

**Noise generation** The samples of NSB induced noise are generated by `produce_nsb.py`. The noise is generated for *no\_of\_modules* modules simultaneously. The average noise level can be set in the first lines of the code. The result is written to the file *nsb\_file\_name*, which will contain *no\_of\_modules* columns. The length of the file, i.e. the length of the simulated noise signal, is given by  $signal\_length \times no\_of\_loops$ . The signal is generated in portions to save memory – the signal is written to file at the end of each loop. The signal shape is read in from a file and stored in *pmt\_pulse*, the amplitude distribution is given by the function  $p(x)$ .

**Station trigger rate** The script `calculate_rates.py` calculates the station trigger rates for the three considered systems: Coincidence trigger (type A), sum trigger (type B) and clipped sum trigger (type C). The trigger schemes are applied to a noise file generated by `produce_nsb.py`. Again, the file is not processed at once, but in loops with size *signal\_length* (in ns). The characteristics of the trigger systems, such as the coincidence window or the dead time after a trigger, are set by a few variables at the beginning of the code. The most important number is *threshold*, which means the level denoted by  $L_T$  in this thesis. For the clipped sum trigger, the *clipping\_level* is set at  $1.05/4 \times threshold$ .

**Two and three station trigger rates** The script `array_trigger.py` takes the station trigger rate as input and calculates the rates of coincidence between two and three neighbouring stations. Station triggers are distributed within a time window of *signal\_length* for a set of five stations (which stand for a central station and its four direct neighbours in a square grid). Triggers which are closer to each other than the dead time are eliminated, which results in a slightly lower station trigger rate than requested (the actual trigger rate is calculated, printed and used for the plots). Coincidences between the stations are found by comparing the individual lists of trigger times, looking for times which are no more than *coincidence\_window* nanoseconds apart. Triggers are issued if the centre station and one (two station trigger) or two (three station trigger) of the neighbouring stations have a local trigger.

### A.4 H<sub>i</sub>SCORE event reconstruction

used in: sections 5.4 to 5.7  
SVN directory: score/software/reco\_score/  
Required python modules: numpy, scipy, Tkinter  
Classes and functions: class\_event.py, reco\_constants.py, reco\_functions.py, score\_io\_ascii.py  
Main scripts (reconstruction): reco\_B1.py, reco\_B2.py, start\_reko.py  
Main scripts (organisation): datenbank.py, eventdisplay.py  
Main scripts (calibration): depth\_calibration.py, energy\_calibration.py, test\_theta\_new.py  
Main scripts (evaluation): all\_res.py, ang\_res.py, angular\_acceptance.py, core\_res.py, depth\_histo.py, depth\_res.py, effective\_areas.py, energy\_res.py, g\_h\_sep.py, show\_spectrum.py

The software framework presented here contains not only the event reconstruction algorithm itself, but also many helper scripts that are used to organise the simulated data, to obtain lookup tables for the calibration, and to evaluate the accuracy of the performance of the simulated detector.

**Reconstruction** The reconstruction is done in the scripts `reco_B1.py` and `reco_B2.py`, of which the first takes over the time consuming work with the full detector data, e.g. extracting the signal parameters and fitting parameter distributions, while the second one applies the calibration lookup tables to the extracted quantities to obtain the physical parameters of the event like energy or shower depth.

The events are stored in event class objects, which are filled with data from the air shower and detector simulations using functions implemented in `score_io_ascii.py`. They contain event level data as well as a list of detector objects, which in turn contain the detector signals and the detector / signal parameters. During the course of the reconstruction, newly calculated values are filled into the appropriate property variables of the event class.

The scripts `reco_B1.py` and `reco_B2.py` do not contain any of the actual reconstruction procedure, but only call the reconstruction methods of the event class. The event class, and the detector class, are implemented in `class_event.py`.

At the end of level B1, the results are stored by saving the event list to the file `reko_04m.dat` using the python serialising function. The detector signals are deleted before that to save memory, and to reduce the time needed to write and later on read this file. At the end of level B2, the results are saved to `reko_B2_04m.dat`, this time without any detector data at all. This file contains only event level data, which is sufficient for almost all tasks on the evaluation level. If the detector data is needed again, it can be retrieved from the `reko_04m.dat`. The suffix `_04m` indicates the detector station configuration and may be used to keep data from other configurations in parallel. Currently, however, no other configuration is readily implemented in `sim_score`.

The gamma hadron separation is not done during the reconstruction. Instead, the event class method `gamma_cut` can be called by any script to find out whether the event passes certain cuts. The type of cut is supplied as argument to the function, the cut "B" corresponds to the standard acceptance cuts (at least three triggered stations, core position inside the array, zenith angle below  $25^\circ$ ), the cut "C" incorporates the actual gamma cuts. The type of gamma cut combination (method 1 or 2 as described in the main text) can be selected in this function (hard coded).

The file `reco_constants.py` contains many parameters of the event reconstruction, such as signal thresholds for certain reconstruction steps or the size of parameter distribution fits. Additionally, various debug flags can be set to display fitted distributions. The variable `make_only` can be used to limit the reconstruction to one or a few events for debugging, which is highly recommended if plots are to be displayed.

For the reconstruction of a large number of runs, the use of the (fairly simple) script `start_reko.py` is recommended. Note that it is possible to select whether both reconstruction steps ("B1" and "B2") should be called or only one of them.

**Organisation** The script `datenbank.py` implements a graphical user interface for organising the simulated air shower data. It scans all subfolders of the directory set in the configuration file `settings/datenbank.ini` on startup, i.e. it does not need an actual database to keep track of the simulations. The runs are ordered by particle type, energy range and azimuth and zenith angle ranges. The logged screen outputs from CORSIKA, `sim_score` and the two reconstruction steps can be accessed easily via the menu. The reconstruction can be started here for single runs for testing (note that the screen printout is not logged in this case, and it is generally preferable to use the script `start_reko.py` to start the reconstruction).

The primary use of this GUI is the calculation of calibration parameters, and the evaluation of the reconstruction accuracy. All important scripts from the evaluation section (see below) can be called via the menu, and a list of the selected runs is passed on to the scripts. This way, an evaluation can easily be done for all

## A Software developed for this work

events of a certain particles type or in a certain energy range. Parameters of the evaluation (e.g. the type of depth reconstruction used) are usually set in the respective scripts, and not supplied by the GUI. It should be noted that not all menu items may work with all data, as some scripts may be outdated. However, all main scripts mentioned under “calibration” and “evaluation” in the header of this section are functional.

The button “event display” starts the script `eventdisplay.py`. It features an interactive display of all events of the current run (only one run can be selected for this) with colour coding for station intensities or peak times (can be selected in the script). Information about each detector can be retrieved by left-clicking on a station. A right click displays the station signal.

**Calibration** The script `energy_calibration.py` is used to derive a relation between the light level at 220m from the core position, LDF(220) or Q220, and the energy of the primary particle in TeV (MC energy). In each bin of MC energy (usually six bins per decade are used) the median light level is calculated. The result is stored in `calibration/energy_calibration.dat` in plain text format.

The script `depth_calibration.py` is used for the calibration of the shower depth. The used parameter (timing, LDF steepness, signal widths, spectrum, etc.) can be selected with `par_name`. Since the depth calibration is energy dependent, the relation is derived using the median parameter of bins in MC energy and MC depth. For this, the bin class implemented in `reco_functions.py` is used. The results are stored in `calibration/{LDF}{timing}{width}_depth_calibration_2D.dat` for the three used methods.

The scripts `test_theta_new.py` and `test_parameters.py` are used to calculate the small empirical correction to the geometrically reconstructed zenith angle. Essentially, the difference between the reconstructed and the actual MC zenith angle is recorded, and the medians are calculated for different zenith angle bins. The result is stored in `calibration/theta_correction3.dat`.

The results from the calibration are used in `reco_B2.py` for the reconstruction of energy and depth, and to correct the zenith angle.

Note that all these scripts should be started by using `datenbank.py`.

**Evaluation** The resolution of the different reconstruction steps can be evaluated with the scripts `ang_res.py`, `core_res.py`, `depth_res.py` and `energy_res.py`. Essentially all scripts use the errors calculated in reconstruction step B2 and display them in bins of energy or zenith angle. The script `all_res.py` gives an overview over the most important resolution numbers and may be used for a quick check of the effect of a change in the reconstruction algorithm or of reconstruction parameters. The results are displayed on the screen and additionally stored in plain text files for later evaluation.

A few of the scripts output additional information, e.g. the `ang_res.py` additionally calculates the point spread function, and `energy_res.py` generates a complete energy response matrix, e.g. histograms of reconstructed energies in different energy bins.

The script `angular_acceptance.py` is used to calculate either the angular or the spatial acceptance of the detector for different energies, as shown in section 5.6.1. The effective areas after the different cuts are generated by `effective_areas.py` and stored in text files for later use. The script `depth_histo.py` is used to display the shower depth versus energy, and `show_spectrum.py` is used to read out and display the simulated Cherenkov light spectra (used in sections 5.4.5 and 5.5.4).

The script `g_h_sep.py` is used to test various methods of gamma hadron separation, generate parameter distributions, and calculate the quality factor for given cuts. It is also used to determine the energy dependent cut values for the parameter combinations 1 and 2. These cut values are stored in `calibration/chosen_cut_PX.dat`. The files with  $X \in [1, 2, 3]$  are used for the combination method 1 and contain the respective cut values for the parameters  $P_1$  to  $P_3$  that give an efficiency of 80% at each cut. The file with  $X = 4$  contains the cut values for the combined parameter  $P_4$ , which are optimised for a high quality factor.

## A.5 $H_i$ SCORE sensitivity calculation

used in: section 5.6.4  
 SVN directory: score/software/sensitivity\_score/sensitivity\_dh\_score/  
 Required python modules: numpy, scipy, matplotlib, Tkinter  
 Main scripts: make\_sensitivity.py, show\_sensitivities.py

The script `make_sensitivity.py` is used to calculate the expected point source sensitivity of the  $H_i$ SCORE detector. For this, it uses the effective areas for the different simulated particles, the energy reconstruction bias, the cosmic ray flux parametrisations from Hörandel [2003] and the expected angular resolution of the experiment. All these values are read in from ASCII files.

The sensitivity is calculated as minimal integrated flux above an energy  $E_0$  that is needed to see the source with  $5\sigma$ . At each energy point  $E_0$ , the calculation starts with the determination of the background. The event numbers of each particle species are calculated individually by the function `corr_flux_num`. This function integrates over the differential flux of cosmic rays given by the function `diff_CR_flux` (which implements equation 5.28), and takes into account the effective areas and the size of the source region (assumed to be identical to the angular resolution). The total number of cosmic rays is stored in  $N_{CR}$ .

From this, the number of required gamma-rays is calculated using equation 5.34. The required flux is then calculated according to equation 5.35, using the functions `integrate_gamma_spectrum` and `integrate_pevatron_spectrum`.

The sensitivity plots shown in the thesis are generated with the script `show_sensitivities.py`, which reads in the results from the previous script, and tabulated sensitivities of other experiments from the ASCII files in the directory `sensi_data`. The plot can be displayed either directly, using `matplotlib`, or via `gnuplot`.

## A.6 $H_i$ SCORE source exposure calculation and display

used in: section 6.3  
 SVN directory: dhampf/python/astro\_py/  
 Required python modules: pyephem, healpy and matplotlib or PIL  
 Main scripts: exposure\_b.py, anzeige\_new.py

**Exposure calculation** The script `exposure_b.py` calculates the amount of time each position in the sky is seen by the detector during the course of one year. The time is stored in the two-dimensional array `stats`, which gives the exposure time in minutes as function of galactic longitude and latitude. The position is quantised to full degrees, resulting in an array of  $180 \times 360$  entries. At the end of the programme, this array is written to file and used later for display and evaluation.

The terrestrial location of the detector is given by `base` as a `pyephem` observer object. The `direction` is usually set to the same position, but can be set to a different (virtual) position to account for a tilted detector array.

The year is simulated in 20 minute steps. At each step, the conditions for astronomical darkness are checked: The sun must be at least  $18^\circ$ , the moon at least  $2^\circ$  below the horizon. If this is the case, observations can take place, and the astronomic altitude angle of each Galactic position bin is calculated taking into account the time and location of the observer. The equatorial coordinates of each Galactic position bin, which are needed for the computation, are pre-calculated at the start of the programme, as this step is relatively time consuming. If the altitude angle is larger than the cut-off angle defined by the acceptance cuts in the reconstruction (by default  $25^\circ$ ), 20 minutes of exposure are added to this position. All coordinate transformations are done using the `pyephem` framework.

## A Software developed for this work

**Exposure display** The script `anzeige_new.py` displays the calculated exposure as colour map in Galactic coordinates, and prints out some statistical figures such as the sky area covered or the average exposure. Known VHE gamma-ray sources are read in from the file `sources.dat` and displayed in the exposure plot, optionally coloured for the discovering instrument or the source type (shell-type supernova remnant, pulsar wind nebula, etc.). Additionally, a table is produced that gives the exposure time for each of the sources – see tables 6.5a and 6.5b.

The plot is produced in two file formats:

- First, a `svg` file with the lines, labels and source markers is produced. The colour map of the exposure is generated as `png` file using the PIL, and embedded into the `svg` file. The `svg` file can later be converted to other formats, e.g. `eps`, by various freeware tools (e.g. `inkscape`). This method uses the Hammer projection for the skymap.
- A `matplotlib` figure using `healpy`. This figure can be saved directly in various image formats. By default, this method uses the Mollweide projection.

One of the two formats can be selected to account for available modules. The results are nearly identical.

The calculation of the covered sky area towards the end of the script must take into account that the simulated position bins are different in area. This can be done most efficiently by using the `healpy` framework. If it is not available, the displayed sky area is calculated without taking the different areas into account, and is therefore slightly off. The error is however not very large as long as the exposure covers roughly the same amount of pixels at high and low Galactic latitudes.

## A.7 LabView VI for NSB measurement

used in: section 6.4  
SVN directory: `score/software/nsb_measurement/`  
Main script: `NSB_messung_v5.vi`

For the NSB measurement, the National Instruments analogue-digital-converter USB 6008 is used to control and read out the photomultiplier and the telescope mount. The corresponding software is implemented in LabView as a VI (virtual instrument). Versions for LabView 7.1, 8.0 and 8.5 exist in the respective subfolders. The user interface is loaded with the file `NSB_messung_v5.vi`, which in turn imports all other necessary VIs. A detailed manual for the use of the software can be found in the programme directory.

## A.8 Reference list of needed python modules

The python modules needed for the software described in this section can be found at the following websites:

- `healpy` (astronomical map generation): <https://github.com/healpy/healpy>
- `matplotlib` (plotting): <http://matplotlib.sourceforge.net/>
- `numpy`: <http://numpy.scipy.org/>
- `PIL` (python imaging library): <http://www.pythonware.com/products/pil/>
- `pyephem` (astronomical calculations): <http://rhodesmill.org/pyephem/>
- `scipy`: <http://www.scipy.org/>
- `sidereal` (astronomic coordinate transformations): <http://infohost.nmt.edu/tcc/help/lang/python/examples/sidereal/>

## B Tabulated results of H<sub>i</sub>SCORE event reconstruction

The following table contains the key results of the H<sub>i</sub>SCORE simulation, to enable further use of the data without the need to manually scan the plots shown in chapter 5.

$E_{low}$ (TeV)	$E_{mid}$ (TeV)	$N_{sim}$	$N_{acc}$	Core res. (m)	Ang. res. (deg)	E res. (percent)	E shift (percent)	Sensitivity ( $\times 10^{13}$ ) (erg s <sup>-1</sup> cm <sup>-2</sup> )
10	12	1769	3	44.9	14.68	648.1	648.1	40.3
15	18	1845	0	0.0	0.0	0.0	0.0	27.1
22	26	1781	12	47.6	11.78	55.5	51.1	11.9
32	38	1817	187	44.4	2.25	39.5	4.8	5.60
46	56	1741	640	34.2	0.39	33.7	-2.5	3.54
68	83	1847	914	24.3	0.29	22.5	-0.5	3.13
100	121	1707	855	18.4	0.24	15.8	-0.7	2.54
147	178	1657	846	13.5	0.18	12.0	-0.4	2.12
215	261	1738	891	10.9	0.14	10.3	0.5	1.82
316	383	1717	872	8.1	0.13	9.3	-0.1	1.65
464	562	1736	940	6.7	0.12	8.4	0.8	1.58
681	825	1695	881	5.5	0.11	8.3	0.2	1.54
1000	1212	696	362	4.7	0.10	8.0	1.2	1.53
1468	1778	676	331	4.3	0.09	7.4	1.6	1.52
2154	2610	697	348	3.9	0.09	7.1	0.9	1.61
3162	3831	695	353	3.9	0.10	6.7	0.1	1.80
4642	5623	146	72	3.8	0.11	3.6	-1.9	2.52

Table B.1: Overview of the simulated gamma-ray events (standard layout) and the resolutions of the reconstructed values.  $E_{low}$  and  $E_{mid}$  are the low edge and the logarithmic mean energy of the bin (the last bin goes up to 6813 TeV).  $N_{sim}$  and  $N_{acc}$  are the number of simulated events and events surviving the acceptance cuts defined at the beginning of section 5.4. The resolution of the core position, the direction and the energy reconstruction are given for the best algorithm presented in the respective section. The energy shift is defined as  $(E_{reco} - E_{MC})/E_{MC}$ . The resolutions and the energy shift are calculated only for events passing the acceptance cuts. The sensitivity is given for a 100km<sup>2</sup> H<sub>i</sub>SCORE array including gamma hadron cuts.

*B Tabulated results of  $H_i$ SCORE event reconstruction*

## C Additional information on Fowler's Gap

Additional information on Fowler's Gap can be found on the station's website on <http://www.fowlersgap.unsw.edu.au/>, listing among other things up-to-date contact information and the latest research reports. A compact overview can be found in the information brochure which can be downloaded directly as <http://www.fowlersgap.unsw.edu.au/pdf/fg%20brochure.pdf>

A four-minute video clip for public outreach, which gives an impression of the landscape at Fowler's Gap, can be found at YouTube at <http://www.youtube.com/watch?v=b8m1wUfQSZU>

Figure C.1 shows a map of the research station property. The site of the station buildings is marked as "homestead", near the bottom left corner. The areas east of the Silver City Highway are mostly flat, sandy plains, while towards the west, the landscape is slightly more hilly and the ground consists of hard soil and stones. Despite the hills, the western areas (Bald Hills, Sandstone, South Sandstone, South Ridge) seem to be more appropriate for the deployment of the detector as the stony ground offers reliable mounting and operation of the stations. Additionally, the fine sand found at the eastern side may be whirled up by wind and thereby significantly decrease the visibility.

The area west to the station's property continues to look suitable for the detector deployment, and it may be possible to extend the detector to that area, if more space is needed. The land there is owned by several private sheep and cattle stations.

C Additional information on Fowler's Gap

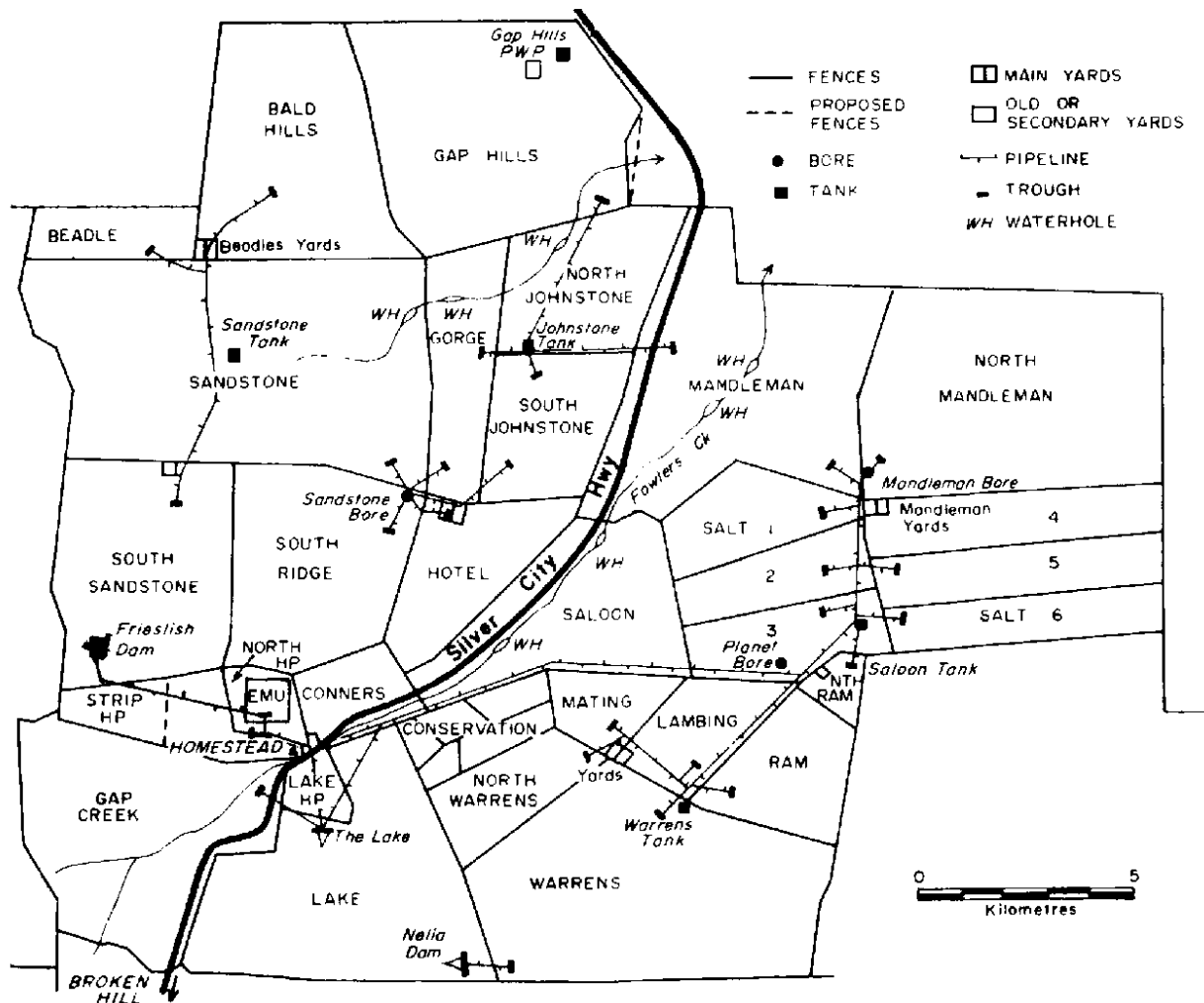


Figure C.1: Schematic map of the Fowler's Gap research station property.

## D Angular acceptance of a tube

In section 6.4.1, the angular acceptance  $\varepsilon(\theta)$  of a long black plastic tube is needed to derive its effective solid angle. The ray tracing simulation used to obtain  $\varepsilon(\theta)$  is cross-checked with an analytical calculation for the case of no internal reflection in the tube. This calculation is presented here.

The basic idea is to calculate the overlapping area  $A$  of the front and rear tube opening when seen from an angle  $\theta$  (see figure D.1). This is done by integrating a sphere function between  $x_s$  and the radius of the opening  $r$  (see figure D.2):

$$A = 4 \int_{x_s}^r \sqrt{r^2 - x^2} dx \quad (\text{D.1})$$

$$= 2 \left[ x\sqrt{r^2 - x^2} + r^2 \sin^{-1} \left( \frac{x}{r} \right) \right]_{x_s}^r \quad (\text{D.2})$$

$$= 2 \left[ r^2 \frac{\pi}{2} - x_s \sqrt{r^2 - x_s^2} - r^2 \sin^{-1} \left( \frac{x_s}{r} \right) \right] \quad (\text{D.3})$$

$$= 2 \left[ r^2 \left( \frac{\pi}{2} - \sin^{-1} \left( \frac{x_s}{r} \right) \right) - x_s \sqrt{r^2 - x_s^2} \right] \quad (\text{D.4})$$

The value  $x_s$  can be expressed in terms of the tube length  $L$  and the angle  $\theta$ :

$$x_s(\theta) = \frac{d}{2} = \frac{L \sin(\theta)}{2} \quad (\text{D.5})$$

Since the transmittance is proportional to the overlapping area, it can be calculated by

$$\varepsilon(\theta) = \frac{A(\theta)}{A(0)} = \frac{r^2 \left( \pi - 2 \sin^{-1} \left( \frac{x_s(\theta)}{r} \right) \right) - 2x_s(\theta) \sqrt{r^2 - x_s^2(\theta)}}{\pi r^2} \quad (\text{D.6})$$

using equation D.5 for  $x_s(\theta)$ . Equation D.6 is used for the comparison in plot 6.8.

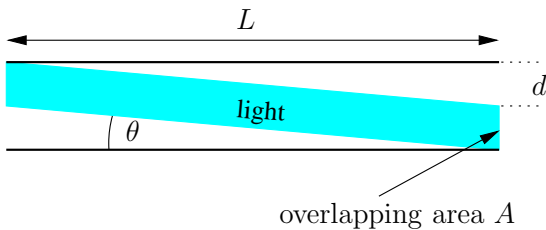


Figure D.1: Cross-section view of the tube

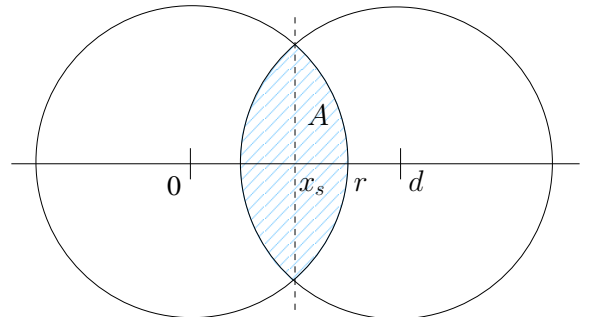


Figure D.2: Quantities needed in the calculation of the overlap between front and rear tube opening.

*D Angular acceptance of a tube*

## E Datasheets

This appendix chapter contains the following datasheets of devices or materials used or referred to in this thesis:

- ALANOD 4300UP (page 196): Reflective material for the Winston cones, see section 4.2.2
- ET PMT 9352KB (page 197): Photomultiplier candidate for H<sub>i</sub>SCORE detector station, see section 4.2.3
- PHQ 9352 (page 199): High voltage supply for the above PMT, see section 4.2.3
- M12M Timing GPS module (page 200): GPS module used in time stamp generation, see section 4.3. The full version of this datasheet can be found on [www.ilotus.com.sg/m12m\\_timing\\_oncore](http://www.ilotus.com.sg/m12m_timing_oncore)
- Hamamatsu R6095 (page 201): Photon counting photomultiplier used for the NSB measurement, see section 6.4

# Qualitätsdatenblatt

**4300UP**

**Miro - UV**

**Qualität:** 4300UP MIRO-3, Hochglanz

**Zusatzinformationen**

4300UP / 01

31.05.2001

**Liefermöglichkeiten**

Dicke von bis [mm] 0,30 - 0,80

Breite bis max. [mm] 1250,00

**Werkstoff/Legierung:**<sup>1</sup> Al 99,85

**Härte:**<sup>2</sup> Hart

**Mechanische Eigenschaften:**

Zugfestigkeit [MPa] 160 - 200

Streckgrenze [MPa] 140 - 180

Dehnung (A50) [%]  $\geq 2$

Verformung/Abkantung: Biegeradius  $\geq 1,5$  fache Materialdicke

Bearbeitung Vorderseite: (S1) Elektrolytisch gegläntzt, eloxiert und PVD-beschichtet

Irisierungsbeurteilung: (S1) Absolut Interferenzfarbenfrei

**Toleranzen:** Band, Spaltband, Tafeln, Zuschnitte

Materialdicke: [mm] 0,30 - 0,50  $\pm 0,04$  0,61 - 0,80  $\pm 0,06$

[mm] 0,51 - 0,60  $\pm 0,05$

Breite/Coil: [mm] +3,00 /-0,00

Breite Spaltband: [mm]  $\pm 0,20$  Standard  $\pm 0,05$  Spezial

Säbelförmigkeit: [mm]  $\leq 1,00$  auf eine Messlänge von 1000mm

Tafelware: [mm] 0 - 600 +1,0/-0,00

[mm] 600 - 1500 +1,5/-0,00

[mm] 1500 - 2500 +2,5/-0,00

[mm] 2500 - 3500 +3,5/-0,00

Planheit: 1% der Wellenlänge jedoch maximal 8 [mm]

Diagonalabweichung: [mm]  $\leq 1,50$  (D1-D2)

**Optische Eigenschaften:**

**Schutzfolie:** PE - Folie

Dicke 50 - 60  $\mu\text{m}$

**Besonderheit:**

<sup>1</sup> nach DIN EN 573-3 bzw. Werknorm

<sup>2</sup> nach DIN EN 485-2 bzw. Werknorm

# 200 mm (8") photomultiplier 9352KB series data sheet

## 1 description

The 9352KB is a 200mm (8") diameter end window photomultiplier with blue-green sensitive bialkali photocathode on a hemispherical window, and 6 BeCu dynodes of linear focused design for good linearity and timing. Metal fingers extend over the active area to ensure satisfactory operation at high ambient light levels.

## 2 applications

- high energy physics studies with high light levels (e.g. Cosmic Ray Shower studies in the night sky)

## 3 features

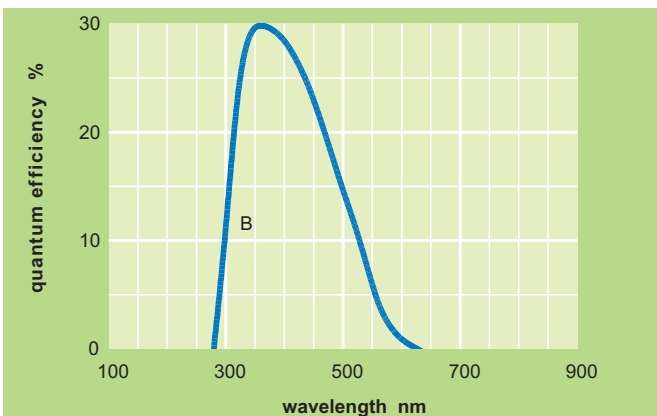
- $2\pi$  detection
- large active area
- internal collection efficiency optimised
- high light level capability
- fast time response
- low background glass envelope

## 4 window characteristics

		9352KB borosilicate
spectral range*(nm)		290 - 630
refractive index ( $n_d$ )		1.49
K (ppm)		300
Th (ppb)		250
U (ppb)		100

\* wavelength range over which quantum efficiency exceeds 1% of peak

## 5 typical spectral response curves

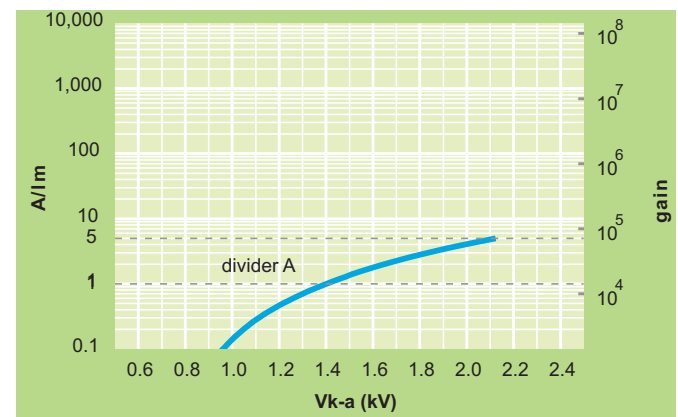


## 6 characteristics

	unit	min	typ	max
<b>photocathode: bialkali</b>				
active diameter	mm		195	
active surface area	cm <sup>2</sup>		480	
quantum efficiency at peak	%		30	
luminous sensitivity	μA/lm		70	
with CB filter		8	12	
with CR filter			1	
<b>dynodes: 6LFBcCu</b>				
<b>anode sensitivity in divider A:</b>				
nominal anode sensitivity	A/lm		1	
max. rated anode sensitivity	A/lm		5	
overall V for nominal A/lm	V		1400	2300
overall V for max. rated A/lm	V		2000	
gain at nominal A/lm	x 10 <sup>6</sup>		0.01	
<b>dark current at 20 °C:</b>				
dc at nominal A/lm	nA		0.2	5
dc at max. rated A/lm	nA		1	
<b>pulsed linearity (-5% deviation):</b>				
divider A	mA		50	
<b>rate effect (I<sub>a</sub> for Δg/g=1%):</b>				
	μA		1	
<b>magnetic field sensitivity:</b>				
the field for which the output decreases by 50 %				
most sensitive direction	T x 10 <sup>-4</sup>		0.4	
<b>temperature coefficient:</b>				
	% °C <sup>-1</sup>		± 0.5	
<b>timing:</b>				
multi electron rise time	ns		5	
multi electron fwhm	ns		8	
transit time	ns		50	
<b>weight:</b>				
	g		650	
<b>maximum ratings:</b>				
anode current	μA			100
cathode current	nA			5000
gain	x 10 <sup>6</sup>			0.07
sensitivity	A/lm			5
temperature	°C	-30		60
V (k-a) <sup>(1)</sup>	V			2400
V (k-d1)	V			600
V (d-d) <sup>(2)</sup>	V			300
ambient pressure (absolute)	kPa			202

<sup>(1)</sup> subject to not exceeding max. rated sensitivity <sup>(2)</sup> subject to not exceeding max rated V(k-a)

## 7 typical voltage gain characteristics



## 8 voltage divider distribution

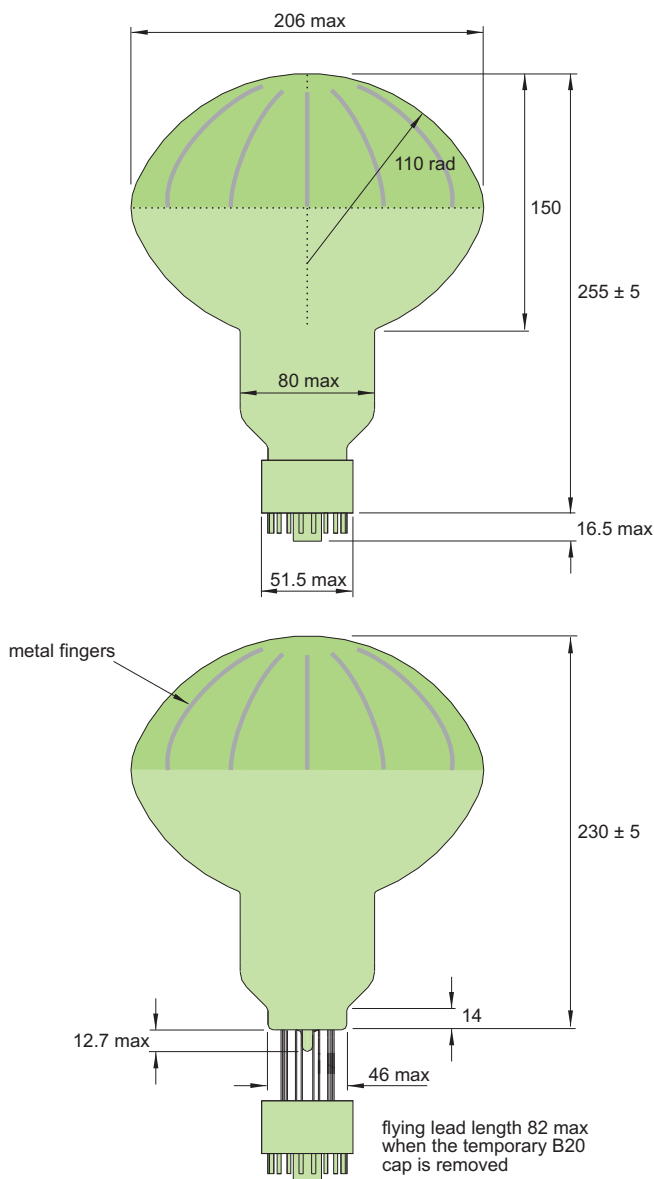
k	d <sub>1</sub>	d <sub>2</sub>	d <sub>3</sub>	d <sub>4</sub>	d <sub>5</sub>	d <sub>6</sub>	a	
A	600V	R	R	R	R	R	R	Standard

note: focus connected to d<sub>1</sub>

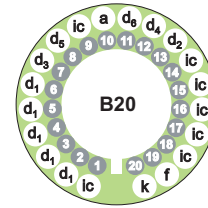
Characteristics contained in this data sheet refer to divider A unless stated otherwise.

## 9 external dimensions mm

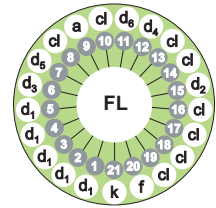
The drawings below show the 9352KB with the B20 cap fitted, and the 9352KFLB in flying lead format with a temporary B20 cap fitted. This temporary cap is attached as agreed with the customer.



## 10 base configuration (viewed from below)



B20 cap  
(for 9352KB & 9352KFLB)  
'ic' indicates an internal connection



flying lead base  
(for 9352FLB  
after removal of  
temporary cap)  
'cl' indicates cut lead

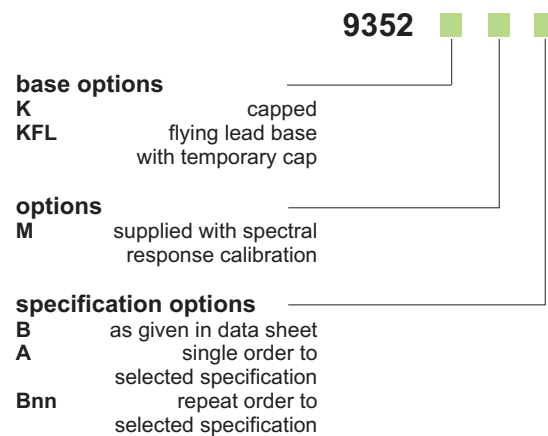
note: connect focus to d<sub>1</sub>

note: connect focus to d<sub>1</sub>

Our range of B20 sockets is available to suit the B20 cap. The socket range includes versions with or without a mounting flange, and versions with contacts for mounting directly onto printed circuit boards.

## 11 ordering information

The 9352KB meets the specification given in this data sheet. You may order **variants** by adding a suffix to the type number. You may also order **options** by adding a suffix to the type number. You may order product with **specification options** by discussing your requirements with us. If your selection option is for one-off order, then the product will be referred to as 9352KA. For a repeat order, Electron Tubes will give the product a two digit suffix after the letter B, for example B21. This identifies your specific requirement.



## 12 voltage dividers

Voltage dividers for this type are available to special order. Please discuss your requirements with us.

**ET Enterprises Limited**  
45 Riverside Way  
Uxbridge UB8 2YF  
United Kingdom  
tel: +44 (0) 1895 200880  
fax: +44 (0) 1895 270873  
e-mail: sales@et-enterprises.com  
web site: www.et-enterprises.com

**Electron Tubes**  
100 Forge Way Unit F  
Rockaway NJ 07866 USA  
tel: (973) 586 9594  
toll free: (800) 521 8382  
fax: (973) 586 9771  
e-mail: sales@electron tubes.com  
web site: www.electrontubes.com

choose accessories for this pmt on our website

an ISO 9001 registered company

The company reserves the right to modify these designs and specifications without notice. Developmental devices are intended for evaluation and no obligation is assumed for future manufacture. While every effort is made to ensure accuracy of published information the company cannot be held responsible for errors or consequences arising therefrom.

**ET Enterprises**  
electron tubes

© ET Enterprises Ltd, 2009  
DS\_9352KB Issue 4 (10/09/09)

## PHQ 9352 (SCORE)

### Integrierte Hochspannungsquelle für PMT electron tubes 9352 KB

Das Modell PHQ 9352 ist eine Hochspannungsquelle, die direkt am Röhrensockel des Photomultipliers ETL 9352 KB angeschlossen werden kann. Sie stellt alle benötigten Spannungen für die Kathode und die Dynoden zur Verfügung. Die Dynodenspannungen werden entsprechend Dynodenspannungsteiler Typ A (laut Datenblatt) aus der Kathodenspannung erzeugt. Die letzten 2 Dynoden (5 und 6) sind dabei aktiv stabilisiert. Die Spannung an diesen Dynoden bleibt deshalb auch unter dynamischen Belastungen stabil. Die Signalauskopplung erfolgt entsprechend der angegebenen Schaltung an Dynode 5 und Anode über Koaxstecker MMCX (LP-Befestigung, gerade, Kabelanschluss RF178 mit abgewinkelter Buchse MMCX).

#### Technische Daten:

Katodenspannung $V_{OUT}$	0 ... - 2500 V										
Anodenstrom $I_A$	max. 200 $\mu$ A										
Stabilität $\Delta V_{OUT}$	$< 1 * 10^{-4}$										
Restwelligkeit	$< 10$ mV <sub>ss</sub>										
Betriebstemperaturbereich	0 bis +40 °C										
Versorgungsspannung	+ 12 V										
analoge Steuerspannung $V_{SET}$	0 ... 5 V	( $V_{OUT} \Rightarrow 0 \dots - 2500$ V)									
Monitorspannung $V_{OUT}$ $V_{MON}$	0 ... 5 V	( $V_{OUT} \Rightarrow 0 \dots - 2500$ V)									
Monitorspannung $I_A$ $I_{MON}$	0 ... 5 V	( $I_A \Rightarrow 0 \dots 200$ $\mu$ A)									
Digitale Steuerung HV-off	TTL-Pegel: Low = HV-off High oder offen = HV-on										
Regelstatus HVstat	TTL-Pegel: High = $V_{OUT}$ entsprechend $V_{SET}$ Low = Regelfehler										
Schutzschaltungen	Abschaltung $V_{OUT}$ für Anodenstrom $> 200$ $\mu$ A										
Anschluss	Bez.	nc	HV-off	$V_{SET}$	GND	$V_{MON}$	$I_{MON}$	HVstat	GND	+12V	nc
X4	PIN-LP	1	2	3	4	5	6	7	8	9	10

File: PHQ9352\_SCORE\_deu, Version: Proto\_17.09.2010

# 1 M12M Timing Oncore™ Receiver Overview

## 1.1 Description

M12M Timing Oncore™ Receiver is a 12 channel precise GPS timing module that gives you up to nano seconds accuracy of time synchronization. Features included precise, programmable, one-pulse-per-second (1PPS) or 100 pulse-per-second (100PPS) outputs. Built with cost effective in mind, you can equip your stationary applications with precise GPS or UTC time synchronization at an affordable cost.

M12M Timing also incorporates the Timing RAIM (Receiver autonomous integrity monitoring) algorithm to ensure validity and reliable GPS measurements.

Design to work in tough conditions, M12M undergoes various drop and temperature test before rolling out into the market.

### >> **Accurate Timing**

Extensive testing of M12M Timing Oncore™ ensures a high level of performance accuracy of 2 nano seconds.

### >> **Automatic Site Survey Mode**

Averages a total of 10,000 valid 2D and 3D position fixes to determine precise position, simplifies system installation for static timing applications.

### >> **Fast Timing Update**

Using position-hold Modes, M12M enables fast time resolution rather than positioning update.

### >> **RF Jamming Immunity**

Provide up to 10dBm of immunity, utilizing the Adaptive Tracking Loops algorithm built in the firmware.

### >> **Clock Granularity Message**

Utilizing M12M Timing Oncore's™ clock granularity software output, 1 PPS output can be resolved within only 2 nano seconds of UTC time immediately, reducing noise and accelerating host clock disciplining process.

Features	Benefits
12 Channel receiver	M12M Timing Oncore™ is able to track up to 12 satellites <ul style="list-style-type: none"> <li>• More satellites aid tracking during intermittent visibility</li> <li>• Improved Urban Canyon performance</li> </ul>
3 Volt technology	2.85 – 3.15v Power Supply <ul style="list-style-type: none"> <li>• Direct connection to latest micro-controllers</li> <li>• Saving power</li> <li>• Saving board space</li> </ul>
Low power	<155mW at 3V without Antenna <ul style="list-style-type: none"> <li>• Lowest in its class</li> <li>• Half of previous Oncore generations</li> </ul>
Tiny Footprint	60x40x13mm footprint <ul style="list-style-type: none"> <li>• Space efficient board</li> <li>• Low Volume</li> </ul>
Fast Acquisition	Performance: <ul style="list-style-type: none"> <li>• TTFF Cold – 150 seconds</li> <li>• TTFF Warm – 40 seconds</li> <li>• TTFF Hot – 15 seconds</li> <li>• Re-acquisition - &lt;1 sec</li> </ul>
Accurate Timing	Performance using clock granularity message: <ul style="list-style-type: none"> <li>• &lt; 2 ns, 1-sigma</li> <li>• &lt; 6 ns, 6-sigma</li> </ul> Performance not using clock granularity message: <ul style="list-style-type: none"> <li>• &lt; 10 ns, 1-sigma</li> <li>• &lt; 20 ns, 6-sigma</li> </ul>

### 28mm(1-1/8 Inch) Diameter, 11-stage, Bialkali Photocathode, Head-On Type, Low Dark Current, High Stability, Low Profile (R6094)

#### GENERAL

Parameter		Description/Value	Unit
Spectral Response		300 to 650	nm
Wavelength of Maximum Response		420	nm
Photocathode	Material	Bialkali	-
	Minimum Effective Area	25	mm dia.
Window Material		Borosilicate glass	-
Dynode	Structure	Box and Line	-
	Number of Stages	11	-
Base		14-pin glass base	-
Suitable Socket		E678-14C (supplied)	-

#### MAXIMUM RATINGS (Absolute Maximum Values)

Parameter		Value	Unit
Supply Voltage	Between Anode and Cathode	1500	Vdc
	Between Anode and Last Dynode	250	Vdc
Average Anode Current		0.1	mA
Ambient Temperature		-80 to +50	°C

#### CHARACTERISTICS (at 25°C)

Parameter		Min.	Typ.	Max.	Unit
Cathode Sensitivity	Luminous (2856K)	60	95	-	$\mu$ A/lm
	Radiant at 420nm	-	88	-	mA/W
	Blue (CS-5-58 filter)	-	11	-	$\mu$ A/lm-b
Anode Sensitivity	Luminous (2856K)	50	200	-	A/lm
	Radiant at 420nm	-	$1.8 \times 10^5$	-	A/W
Gain		-	$2.1 \times 10^6$	-	-
Anode Dark Current (after 30min. storage in darkness)		-	2	10	nA
Time Response	Anode Pulse Rise Time	-	4	-	ns
	Electron Transit Time	-	30	-	ns
	Transit Time Spread (FWHM)	-	3	-	ns

**NOTE:** Anode characteristics are measured with the voltage distribution ratio shown below.

#### VOLTAGE DISTRIBUTION RATIO AND SUPPLY VOLTAGE

Electrodes	K	Dy1	Dy2	Dy3	Dy4	Dy5	Dy6	Dy7	Dy8	Dy9	Dy10	Dy11	P
Ratio	1	1	1	1	1	1	1	1	1	1	1	1	1

Supply Voltage : 1000Vdc, K : Cathode, Dy : Dynode, P : Anode

# PHOTOMULTIPLIER TUBES R6094, R6095

Figure 1: Typical Spectral Response

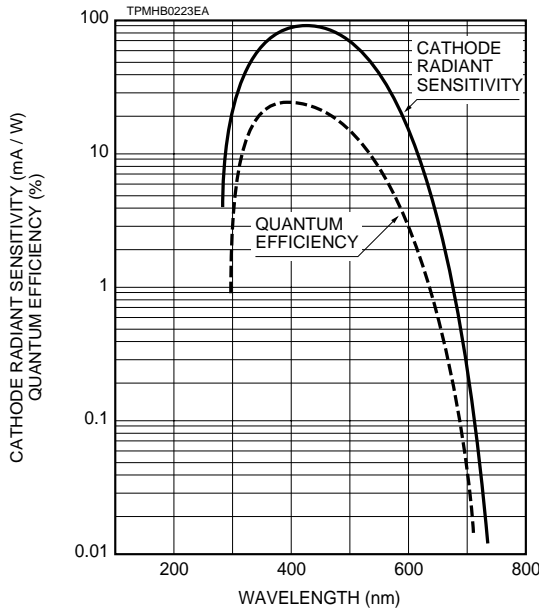


Figure 2: Typical Gain

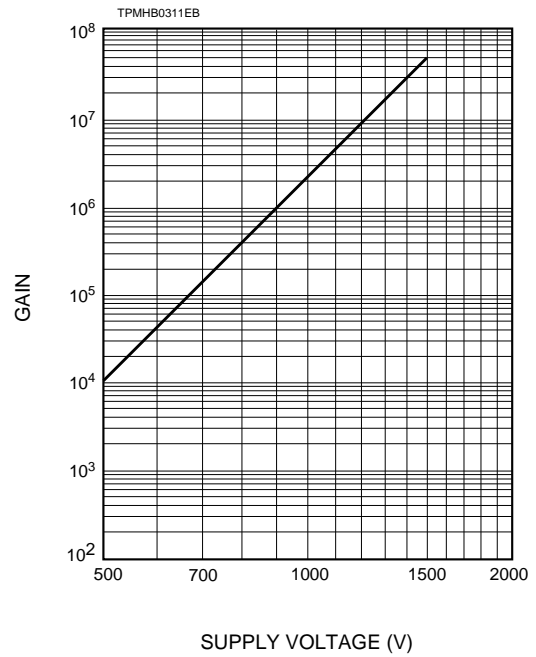
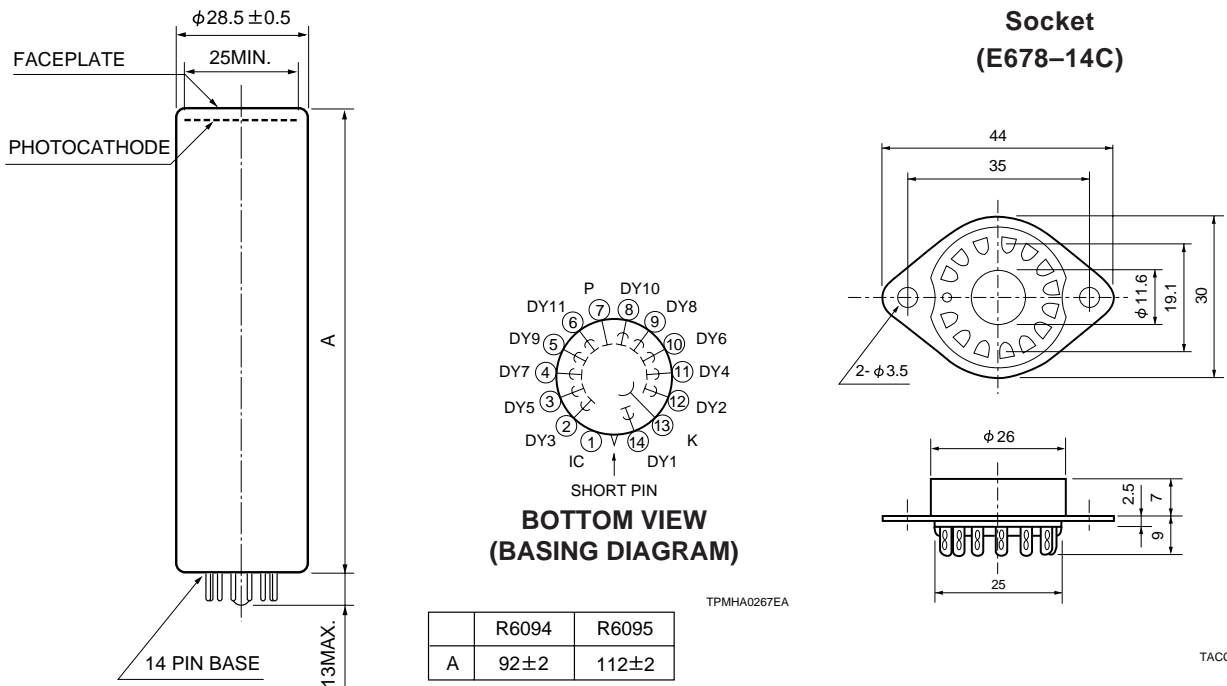


Figure 3: Dimensional Outline and Basing Diagram (Unit : mm)



# HAMAMATSU

HAMAMATSU PHOTONICS K.K., Electoron Tube Center

314-5, Shimokanzo, Toyooka-village, Iwata-gun, Shizuoka-ken, 438-0193, Japan, Telephone: (81)539/62-5248, Fax: (81)539/62-2205

U.S.A.: Hamamatsu Corporation: 360 Foothill Road, Bridgewater, N.J. 08807-0910, U.S.A., Telephone: (1)908-231-0960, Fax: (1)908-231-1218

Germany: Hamamatsu Photonics Deutschland GmbH: Arzbergerstr. 10, D-82211 Herrsching am Ammersee, Germany, Telephone: (49)8152-375-0, Fax: (49)8152-2658

France: Hamamatsu Photonics France S.A.R.L.: 8, Rue du Saule Trapu, Parc du Moulin de Massy, 91882 Massy Cedex, France, Telephone: (33)1 69 53 71 00, Fax: (33)1 69 53 71 10

United Kingdom: Hamamatsu Photonics UK Limited: Lough Point, 2 Gladbeck Way, Windmill Hill, Enfield, Middlesex EN2 7JA, United Kingdom, Telephone: (44)181-367-3560, Fax: (44)181-367-6384

North Europe: Hamamatsu Photonics Norden AB: Färögatan 7, S-164-40 Kista Sweden, Telephone: (46)8-703-29-50, Fax: (46)8-750-58-95

Italy: Hamamatsu Photonics Italia: S.R.L.: Via Della Moia, 1/E, 20020 Arese, (Milano), Italy, Telephone: (39)2-935 81 733, Fax: (39)2-935 81 741

TPMH1103E02  
AUG. 1996

## Bibliography

- [Abbasi *et al.*, 2010a] R. U. Abbasi, Y. Abdou, T. Abu-Zayyad *et al.* Measurement of the Anisotropy of Cosmic-Ray Arrival Directions with IceCube. *Astrophys. J. Letters*, 718:L194–L198, 2010a.
- [Abbasi *et al.*, 2010b] R. U. Abbasi, T. Abu-Zayyad, M. Al-Seady *et al.* Indications of Proton-Dominated Cosmic-Ray Composition above 1.6 EeV. *Physical Review Letters*, 104(16):161101–+, 2010b.
- [Abbasi *et al.*, 2011] R. U. Abbasi, Y. Abdou, T. Abu-Zayyad *et al.* Time-integrated Searches for Point-like Sources of Neutrinos with the 40-string IceCube Detector. *Astrophys. J.*, 732:18–+, 2011.
- [Abdo *et al.*, 2007] A. A. Abdo, B. Allen, D. Berley *et al.* Discovery of TeV Gamma-Ray Emission from the Cygnus Region of the Galaxy. *Astrophys. J. Letters*, 658:L33–L36, 2007.
- [Abdo *et al.*, 2008] A. A. Abdo, B. Allen, T. Aune *et al.* Discovery of Localized Regions of Excess 10-TeV Cosmic Rays. *Physical Review Letters*, 101(22):221101–+, 2008.
- [Abdo *et al.*, 2009] A. A. Abdo, B. T. Allen, T. Aune *et al.* Milagro Observations of Multi-TeV Emission from Galactic Sources in the Fermi Bright Source List. *Astrophys. J. Letters*, 700:L127–L131, 2009.
- [Abdo *et al.*, 2011a] A. A. Abdo, M. Ackermann, M. Ajello *et al.* Observations of the Young Supernova Remnant RX J1713.7-3946 with the Fermi Large Area Telescope. *Astrophys. J.*, 734:28–+, 2011a.
- [Abdo *et al.*, 2011b] A. A. Abdo, M. Ackermann, M. Ajello *et al.* Gamma-Ray Flares from the Crab Nebula. *Science*, 331:739–, 2011b.
- [Abraham *et al.*, 2004] J. Abraham, M. Aglietta, I. C. Aguirre *et al.* Properties and performance of the prototype instrument for the Pierre Auger Observatory. *Nuclear Instruments and Methods in Physics Research A*, 523:50–95, 2004.
- [Abraham *et al.*, 2009] J. Abraham, P. Abreu, M. Aglietta *et al.* Upper limit on the cosmic-ray photon fraction at EeV energies from the Pierre Auger Observatory. *Astroparticle Physics*, 31:399–406, 2009.
- [Abraham *et al.*, 2010a] J. Abraham, P. Abreu, M. Aglietta *et al.* Measurement of the Depth of Maximum of Extensive Air Showers above  $10^{18}$  eV. *Physical Review Letters*, 104(9):091101–+, 2010a.
- [Abraham *et al.*, 2010b] J. Abraham, P. Abreu, M. Aglietta *et al.* Measurement of the energy spectrum of cosmic rays above  $10^{18}$  eV using the Pierre Auger Observatory. *Physics Letters B*, 685:239–246, 2010b.
- [Abreu *et al.*, 2010] P. Abreu, M. Aglietta, E. J. Ahn *et al.* Update on the correlation of the highest energy cosmic rays with nearby extragalactic matter. *Astroparticle Physics*, 34:314–326, 2010.
- [Acero *et al.*, 2010a] F. Acero, F. Aharonian, A. G. Akhperjanian *et al.* First detection of VHE  $\gamma$ -rays from SN 1006 by HESS. *Astr. Astrophys.*, 516:A62+, 2010a.
- [Acero *et al.*, 2010b] F. Acero, F. Aharonian, A. G. Akhperjanian *et al.* Localizing the VHE  $\gamma$ -ray source at the Galactic Centre. *Month. Not. Roy. Astr. Soc.*, 402:1877–1882, 2010b.

## Bibliography

- [Actis *et al.*, 2011] M. Actis, G. Agnetta, F. Aharonian *et al.* Design concepts for the Cherenkov Telescope Array CTA: an advanced facility for ground-based high-energy gamma-ray astronomy. *Experimental Astronomy*, 32:193–316, 2011.
- [Adriani *et al.*, 2009] O. Adriani, G. C. Barbarino, G. A. Bazilevskaya *et al.* An anomalous positron abundance in cosmic rays with energies 1.5-100 GeV. *Nature*, 458:607–609, 2009.
- [Adriani *et al.*, 2010] O. Adriani, G. C. Barbarino, G. A. Bazilevskaya *et al.* PAMELA Results on the Cosmic-Ray Antiproton Flux from 60 MeV to 180 GeV in Kinetic Energy. *Physical Review Letters*, 105(12):121101–+, 2010.
- [Agasa Collaboration, 2006] Agasa Collaboration. AGASA results. *Nuclear Physics B Proceedings Supplements*, 151:3–10, 2006.
- [Aguilar *et al.*, 2010] M. Aguilar, J. Alcaraz, J. Allaby *et al.* Relative Composition and Energy Spectra of Light Nuclei in Cosmic Rays: Results from AMS-01. *Astrophys. J.*, 724:329–340, 2010.
- [Aharonian, 2004] F. Aharonian. *Very High Energy Cosmic Gamma Radiation: A crucial Window on the Extreme Universe*. World Scientific Publishing Co. Pte. Ltd., 2004.
- [Aharonian *et al.*, 2004] F. Aharonian, A. Akhperjanian, M. Beilicke *et al.* The Crab Nebula and Pulsar between 500 GeV and 80 TeV: Observations with the HEGRA Stereoscopic Air Cerenkov Telescopes. *Astrophys. J.*, 614:897–913, 2004.
- [Aharonian *et al.*, 2005a] F. Aharonian, A. G. Akhperjanian, K.-M. Aye *et al.* Discovery of extended VHE gamma-ray emission from the asymmetric pulsar wind nebula in MSH 15-52 with HESS. *Astr. Astrophys.*, 435:L17–L20, 2005a.
- [Aharonian *et al.*, 2005b] F. Aharonian, A. G. Akhperjanian, K.-M. Aye *et al.* A New Population of Very High Energy Gamma-Ray Sources in the Milky Way. *Science*, 307:1938–1942, 2005b.
- [Aharonian *et al.*, 2005c] F. Aharonian, A. G. Akhperjanian, A. R. Bazer-Bachi *et al.* Detection of TeV  $\gamma$ -ray emission from the shell-type supernova remnant RX J0852.0-4622 with HESS. *Astr. Astrophys.*, 437:L7–L10, 2005c.
- [Aharonian *et al.*, 2006a] F. Aharonian, A. G. Akhperjanian, A. R. Bazer-Bachi *et al.* A detailed spectral and morphological study of the gamma-ray supernova remnant RX J1713.7-3946 with HESS. *Astr. Astrophys.*, 449:223–242, 2006a.
- [Aharonian *et al.*, 2006b] F. Aharonian, A. G. Akhperjanian, A. R. Bazer-Bachi *et al.* First detection of a VHE gamma-ray spectral maximum from a cosmic source: HESS discovery of the Vela X nebula. *Astr. Astrophys.*, 448:L43–L47, 2006b.
- [Aharonian *et al.*, 2006c] F. Aharonian, A. G. Akhperjanian, A. R. Bazer-Bachi *et al.* Observations of the Crab nebula with HESS. *Astr. Astrophys.*, 457:899–915, 2006c.
- [Aharonian *et al.*, 2007] F. Aharonian, A. G. Akhperjanian, A. R. Bazer-Bachi *et al.* H.E.S.S. Observations of the Supernova Remnant RX J0852.0-4622: Shell-Type Morphology and Spectrum of a Widely Extended Very High Energy Gamma-Ray Source. *Astrophys. J.*, 661:236–249, 2007.
- [Aharonian *et al.*, 2008a] F. Aharonian, A. G. Akhperjanian, U. Barres de Almeida *et al.* HESS very-high-energy gamma-ray sources without identified counterparts. *Astr. Astrophys.*, 477:353–363, 2008a.
- [Aharonian *et al.*, 2008b] F. Aharonian, J. Buckley, T. Kifune *et al.* High energy astrophysics with ground-based gamma ray detectors. *Reports on Progress in Physics*, 71(9):096901–+, 2008b.

- [Aharonian *et al.*, 1991] F. A. Aharonian, A. A. Chilingarian, A. K. Konopelko *et al.* A multidimensional analysis of the Cherenkov images of air showers induced by very high energy  $\gamma$ -rays and protons. *Nuclear Instruments and Methods in Physics Research A*, 302:522–528, 1991.
- [Aharonian *et al.*, 1997] F. A. Aharonian, W. Hofmann, A. K. Konopelko *et al.* The potential of ground based arrays of imaging atmospheric Cherenkov telescopes. I. Determination of shower parameters. *Astroparticle Physics*, 6:343–368, 1997.
- [Aharonian *et al.*, 2000] F. A. Aharonian, A. G. Akhperjanian, J. A. Barrio *et al.* Optimizing the angular resolution of the HEGRA telescope system to study the emission region of VHE gamma rays in the Crab Nebula. *Astr. Astrophys.*, 361:1073–1078, 2000.
- [Aharonian *et al.*, 2001] F. A. Aharonian, A. K. Konopelko, H. J. Völk *et al.* 5@5 - a 5 GeV energy threshold array of imaging atmospheric Cherenkov telescopes at 5 km altitude. *Astroparticle Physics*, 15:335–356, 2001.
- [Aielli *et al.*, 2006] G. Aielli, R. Assiro, C. Bacci *et al.* Layout and performance of RPCs used in the Argo-YBJ experiment. *Nuclear Instruments and Methods in Physics Research Section A: Accelerators, Spectrometers, Detectors and Associated Equipment*, 562(1):92 – 96, 2006. ISSN 0168-9002.
- [ALANOD customer service, 2009] ALANOD customer service. S. Hauck, personal communication. 2009.
- [Albert *et al.*, 2008] J. Albert, E. Aliu, H. Anderhub *et al.* Very-High-Energy gamma rays from a Distant Quasar: How Transparent Is the Universe? *Science*, 320:1752–, 2008.
- [Aliu *et al.*, 2008] E. Aliu, H. Anderhub, L. A. Antonelli *et al.* Observation of Pulsed  $\gamma$ -Rays Above 25 GeV from the Crab Pulsar with MAGIC. *Science*, 322:1221–, 2008.
- [Aliu *et al.*, 2009] E. Aliu, H. Anderhub, L. A. Antonelli *et al.* Improving the performance of the single-dish Cherenkov telescope MAGIC through the use of signal timing. *Astroparticle Physics*, 30:293–305, 2009.
- [Amenomori *et al.*, 2006] M. Amenomori, S. Ayabe, X. J. Bi *et al.* Anisotropy and Corotation of Galactic Cosmic Rays. *Science*, 314:439–443, 2006.
- [Amenomori *et al.*, 2010] M. Amenomori, X. J. Bi, D. Chen *et al.* Observation of TeV Gamma Rays from the Fermi Bright Galactic Sources with the Tibet Air Shower Array. *Astrophys. J. Letters*, 709:L6–L10, 2010.
- [Amenomori *et al.*, 2011] M. Amenomori, X. J. Bi, D. Chen *et al.* Observation of the Fermi pulsar catalog at TeV energies with the Tibet air shower experiment. *Astrophysics and Space Sciences Transactions*, 7:211–215, 2011.
- [Anderhub *et al.*, 2011] H. Anderhub, M. Backes, A. Biland *et al.* FACT — The first Cherenkov telescope using a G-APD camera for TeV gamma-ray astronomy. *Nuclear Instruments and Methods in Physics Research A*, 639:58–61, 2011.
- [Antoni *et al.*, 2004] T. Antoni, W. D. Apel, A. F. Badea *et al.* Search for Cosmic-Ray Point Sources with KASCADE. *Astrophys. J.*, 608:865–871, 2004.
- [Apel *et al.*, 2011] W. D. Apel, J. C. Arteaga-Velázquez, K. Bekk *et al.* Kneelike Structure in the Spectrum of the Heavy Component of Cosmic Rays Observed with KASCADE-Grande. *Physical Review Letters*, 107(17):171104, 2011.
- [Arqueros, 2003] F. Arqueros. The GRAAL experiment. *Nuclear Physics B Proceedings Supplements*, 114:253–257, 2003.

## Bibliography

- [Arqueros *et al.*, 1996] F. Arqueros, A. Karle, E. Lorenz *et al.* Separation of gamma and hadron initiated air showers with energies between 20 and 500 TeV. *Astroparticle Physics*, 4:309–332, 1996.
- [Atkins *et al.*, 2005] R. Atkins, W. Benbow, D. Berley *et al.* Evidence for TeV Gamma-Ray Emission from a Region of the Galactic Plane. *Physical Review Letters*, 95(25):251103–+, 2005.
- [Atoyan and Aharonian, 1996] A. M. Atoyan and F. A. Aharonian. On the mechanisms of gamma radiation in the Crab Nebula. *Month. Not. Roy. Astr. Soc.*, 278:525–541, 1996.
- [Atwood *et al.*, 2009] W. B. Atwood, A. A. Abdo, M. Ackermann *et al.* The Large Area Telescope on the Fermi Gamma-Ray Space Telescope Mission. *Astrophys. J.*, 697:1071–1102, 2009.
- [Backes *et al.*, 2009] M. Backes, A. Biland, A. Boller *et al.* Long-term monitoring of blazars — the DWARF network. *Proceedings of the 31<sup>st</sup> ICRC, Łódź*, 2009.
- [Balzer, 2010] A. Balzer. Systematic studies of the H.E.S.S. camera calibration. 2010. Diploma thesis, University of Erlangen-Nürnberg.
- [Battaner *et al.*, 2009] E. Battaner, J. Castellano, and M. Masip. Galactic Magnetic Fields and the Large-Scale Anisotropy at Milagro. *Astrophys. J. Letters*, 703:L90–L93, 2009.
- [Bednarek and Idec, 2011] W. Bednarek and W. Idec. On the variability of the GeV and multi-TeV gamma-ray emission from the Crab nebula. *Month. Not. Roy. Astr. Soc.*, 414:2229–2234, 2011.
- [Benn and Ellison, 1998] C. R. Benn and S. L. Ellison. Brightness of the night sky over La Palma. *New Astronomy Reviews*, 42:503–507, 1998.
- [Berge *et al.*, 2007] D. Berge, S. Funk, and J. Hinton. Background modelling in very-high-energy  $\gamma$ -ray astronomy. *Astr. Astrophys.*, 466:1219–1229, 2007.
- [Berger and Seltzer, 1964] M. J. Berger and S. M. Seltzer. Tables of Energy Losses and Ranges of Electrons and Positrons. NASA SP-3012. *NASA Special Publication*, 3012, 1964.
- [Bergström *et al.*, 2009] L. Bergström, J. Edsjö, and G. Zaharijas. Dark Matter Interpretation of Recent Electron and Positron Data. *Physical Review Letters*, 103(3):031103, 2009.
- [Bernlöhr, 2008] K. Bernlöhr. Simulation of imaging atmospheric Cherenkov telescopes with CORSIKA and sim\_telarray. *Astroparticle Physics*, 30:149–158, 2008.
- [Bernlöhr *et al.*, 2003] K. Bernlöhr, O. Carrol, R. Cornils *et al.* The optical system of the H.E.S.S. imaging atmospheric Cherenkov telescopes. Part I: layout and components of the system. *Astroparticle Physics*, 20:111–128, 2003.
- [Bernstein *et al.*, 2002] R. A. Bernstein, W. L. Freedman, and B. F. Madore. The First Detections of the Extragalactic Background Light at 3000, 5500, and 8000 Å. II. Measurement of Foreground Zodiacal Light. *Astrophys. J.*, 571:85–106, 2002.
- [Binney and Merrifield, 1998] J. Binney and M. Merrifield. *Galactic astronomy*. 1998.
- [Bird *et al.*, 1994] D. J. Bird, S. C. Corbato, H. Y. Dai *et al.* The cosmic-ray energy spectrum observed by the Fly’s Eye. *Astrophys. J.*, 424:491–502, 1994.
- [Blandford and Eichler, 1987] R. Blandford and D. Eichler. Particle acceleration at astrophysical shocks: A theory of cosmic ray origin. *Physical reports*, 154:1–75, 1987.

- [Blasi, 2010] P. Blasi. On the origin of high energy cosmic rays. *Journal of Physics Conference Series*, 203(1):012017–+, 2010.
- [Blümer *et al.*, 2009] J. Blümer, R. Engel, and J. R. Hörandel. Cosmic rays from the knee to the highest energies. *Progress in Particle and Nuclear Physics*, 63:293–338, 2009.
- [Britto *et al.*, 2011] R. J. Britto, B. S. Acharya, G. C. Anupama *et al.* Observations with the High Altitude GAMMA-Ray (HAGAR) telescope array in the Indian Himalayas. *Astrophysics and Space Sciences Transactions*, 7:501–505, 2011.
- [Budnev *et al.*, 2005] N. M. Budnev, D. V. Chernov, O. A. Gress *et al.* Cosmic Ray Energy Spectrum and Mass Composition from  $10^{15}$  to  $10^{17}$  eV by Data of the Tunka EAS Cherenkov Array. In *International Cosmic Ray Conference*, volume 6 of *International Cosmic Ray Conference*, pages 257–+. 2005.
- [Budnev *et al.*, 2008] N. M. Budnev, O. B. Chvalaev, O. A. Gress *et al.* Data Acquisition System for the TUNKA-133 Array. In M. Barone, A. Gaddi, C. Leroy, L. Price, P.-G. Rancoita, & R. Ruchti, editor, *Astroparticle, Particle and Space Physics, Detectors and Medical Physics Applications*, pages 287–291. 2008.
- [Budnev *et al.*, 2009] N. M. Budnev, D. Besson, O. A. Chvalaev *et al.* The Tunka-133 EAS Chrenkov array - status, first results and plans. *Proceedings of the 31<sup>st</sup> ICRC, Łódź, 2009*. ArXiv 1003.0089 (2010).
- [Butt, 2009] Y. Butt. Beyond the myth of the supernova-remnant origin of cosmic rays. *Nature*, 460:701–704, 2009.
- [Büker, 2012] M. Büker. 2012. Diploma thesis, University of Hamburg.
- [Cao and The LHAASO Collaboration, 2009] Z. Cao and The LHAASO Collaboration. A Future Project at Tibet: The Large High Altitude Air Shower Observatory (LHAASO). *Proceedings of the 31<sup>st</sup> ICRC, Łódź, 2009*.
- [Cao *et al.*, 2011] Z. Cao, S. Z. Chen, and for the ARGO-YBJ collaboration. TeV gamma-ray survey of the northern sky using the ARGO-YBJ experiment. *ArXiv e-prints*, 1110.1809, 2011.
- [Chaves and the H.E.S.S. Collaboration, 2009] R. C. G. Chaves and the H.E.S.S. Collaboration. Extending the H.E.S.S. Galactic Plane Survey. *ArXiv e-prints*, 0907.0768, 2009.
- [Cinzano *et al.*, 2001] P. Cinzano, F. Falchi, and C. D. Elvidge. The first World Atlas of the artificial night sky brightness. *Month. Not. Roy. Astr. Soc.*, 328:689–707, 2001.
- [Clay and Dawson, 1997] R. Clay and B. Dawson. *Cosmic Bullets: High Energy Particles in Astrophysics*. Allen & Unwin, 1997.
- [Cornils *et al.*, 2003] R. Cornils, S. Gillessen, I. Jung *et al.* The optical system of the H.E.S.S. imaging atmospheric Cherenkov telescopes. Part II: mirror alignment and point spread function. *Astroparticle Physics*, 20:129–143, 2003.
- [CTA Consortium, 2010] CTA Consortium. Design Concepts for the Cherenkov Telescope Array. *ArXiv e-prints*, 1008.3703, 2010.
- [Daum *et al.*, 1997] A. Daum, G. Hermann, M. Hess *et al.* First results on the performance of the HEGRA IACT array. *Astroparticle Physics*, 8:1–11, 1997.
- [Dawson *et al.*, 1989] B. R. Dawson, R. W. Clay, J. R. Patterson *et al.* The lateral distribution of Cerenkov light from extensive air showers. *Journal of Physics G Nuclear Physics*, 15:893–908, 1989.

## Bibliography

- [de La Calle Pérez and Biller, 2006] I. de La Calle Pérez and S. D. Biller. Extending the sensitivity of air Čerenkov telescopes. *Astroparticle Physics*, 26:69–90, 2006.
- [de Naurois and Rolland, 2009] M. de Naurois and L. Rolland. A high performance likelihood reconstruction of  $\gamma$ -rays for imaging atmospheric Cherenkov telescopes. *Astroparticle Physics*, 32:231–252, 2009.
- [de Naurois *et al.*, 2002] M. de Naurois, J. Holder, R. Bazer-Bachi *et al.* Measurement of the Crab Flux above 60 GeV with the CELESTE Cerenkov Telescope. *Astrophys. J.*, 566:343–357, 2002.
- [Dixit *et al.*, 2010] A. Dixit, P. Jain, D. W. McKay *et al.* New physics, the cosmic ray spectrum knee, and pp cross section measurements. *European Physical Journal C*, 68:573–580, 2010.
- [Doro *et al.*, 2008] M. Doro, D. Bastieri, A. Biland *et al.* The reflective surface of the MAGIC telescope. *Nuclear Instruments and Methods in Physics Research A*, 595:200–203, 2008.
- [Drury and Aharonian, 2008] L. O. . Drury and F. A. Aharonian. The puzzling MILAGRO hot spots. *Astroparticle Physics*, 29:420–423, 2008.
- [Drury *et al.*, 1994] L. O. Drury, F. A. Aharonian, and H. J. Voelk. The gamma-ray visibility of supernova remnants. A test of cosmic ray origin. *Astr. Astrophys.*, 287:959–971, 1994.
- [Dyakonov *et al.*, 1973] M. N. Dyakonov, S. P. Knurenko, V. A. Kolosov *et al.* The Results of the First Stage Observations at the Yakutsk EAS Complex Array. II. The Lateral Distribution of EAS Čerenkov Light of Large Sizes at Sea Level. In *International Cosmic Ray Conference*, volume 4 of *International Cosmic Ray Conference*, pages 2389–+. 1973.
- [Edlén, 1966] B. Edlén. The refractive index of air. *Metrologia*, 2(2):71, 1966.
- [Egberts and H.E.S.S. Collaboration, 2011] K. Egberts and H.E.S.S. Collaboration. The spectrum of cosmic-ray electrons measured with H.E.S.S. *Nuclear Instruments and Methods in Physics Research A*, 630:36–39, 2011.
- [Eichler, 2011] R. Eichler. Slow Control und Datenauslese für den HiSCORE-Detektor. 2011. Diploma thesis, University of Hamburg.  
URL [http://wwwiexp.desy.de/groups/astroparticle/de/forschung/eichler\\_diplom.pdf](http://wwwiexp.desy.de/groups/astroparticle/de/forschung/eichler_diplom.pdf)
- [Einhaus, 2012] U. Einhaus. 2012. Master thesis, University of Hamburg.
- [Ellison *et al.*, 2010] D. C. Ellison, D. J. Patnaude, P. Slane *et al.* Efficient Cosmic Ray Acceleration, Hydrodynamics, and Self-Consistent Thermal X-Ray Emission Applied to Supernova Remnant RX J1713.7-3946. *Astrophys. J.*, 712:287–293, 2010.
- [Erlykin and Wolfendale, 1997] A. D. Erlykin and A. W. Wolfendale. A single source of cosmic rays in the range  $10^{15}$  -  $10^{16}$  eV. *Journal of Physics G Nuclear Physics*, 23:979–989, 1997.
- [Evonik Industries, 2000] Evonik Industries. Lichttechnik: Richtwerte und Anwendungen. Technical report, 2000.
- [Fermi, 1949] E. Fermi. On the Origin of the Cosmic Radiation. *Physical Review*, 75:1169–1174, 1949.
- [Fesefeldt, 1985] H. Fesefeldt. 1985. Report PITHA-85/02, RWTH Aachen.
- [Fowler *et al.*, 2001] J. W. Fowler, L. F. Fortson, C. C. H. Jui *et al.* A measurement of the cosmic ray spectrum and composition at the knee. *Astroparticle Physics*, 15:49–64, 2001.

- [Funk *et al.*, 2004] S. Funk, G. Hermann, J. Hinton *et al.* The trigger system of the H.E.S.S. telescope array. *Astroparticle Physics*, 22:285–296, 2004.
- [Gabici and Aharonian, 2007] S. Gabici and F. A. Aharonian. Searching for Galactic Cosmic-Ray Pevatrons with Multi-TeV Gamma Rays and Neutrinos. *Astrophys. J. Letters*, 665:L131–L134, 2007.
- [Gallant and Arons, 1994] Y. A. Gallant and J. Arons. Structure of relativistic shocks in pulsar winds: A model of the wisps in the Crab Nebula. *Astrophys. J.*, 435:230–260, 1994.
- [Garstang, 1989] R. H. Garstang. Night-sky brightness at observatories and sites. *Astronomical Society of the Pacific*, 101:306–329, 1989.
- [Giacinti *et al.*, 2011] G. Giacinti, M. Kachelriess, D. V. Semikoz *et al.* Ultrahigh Energy Nuclei in the Turbulent Galactic Magnetic Field. *ArXiv e-prints*, 1104.1141, 2011.
- [Gillesen, 2004] S. Gillesen. *Sub-Bogenminuten-genaue Positionen von TeV-Quellen mit H.E.S.S.* Ph.D. thesis, University of Heidelberg, 2004.  
URL [http://www.mpi-hd.mpg.de/hfm/HESS/public/phdtheses/gillesen\\_phd.pdf](http://www.mpi-hd.mpg.de/hfm/HESS/public/phdtheses/gillesen_phd.pdf)
- [Gingrich *et al.*, 2005] D. M. Gingrich, L. M. Boone, D. Bramel *et al.* The STACEE Ground-Based Gamma-Ray Detector. *IEEE Transactions on Nuclear Science*, 52:2977–2985, 2005.
- [Goodman and HAWC Collaboration, 2010] J. A. Goodman and HAWC Collaboration. Physics with HAWC. In D. B. Kieda & P. Gondolo, editor, *2009 Snowbird Particle Astrophysics and Cosmology Workshop (SNOWPAC 2009)*, volume 426 of *Astronomical Society of the Pacific Conference Series*, pages 19–+. 2010.
- [googlemaps, 2010] googlemaps. 2010.  
URL <http://maps.google.com.au/>
- [Gosse, 2001] J. Gosse. Terrestrial in situ cosmogenic nuclides: theory and application. *Quaternary Science Reviews*, 20:1475–1560, 2001.
- [Greisen, 1966] K. Greisen. End to the cosmic-ray spectrum? *Phys. Rev. Lett.*, 16(17):748–750, 1966.
- [Grieder, 2001] P. K. F. Grieder. *Cosmic Rays at Earth*. Elsevier, 2001.
- [Hampf *et al.*, 2011a] D. Hampf, G. Rowell, N. Wild *et al.* Measurement of night sky brightness in southern Australia. *Advances in Space Research*, 48(6):1017 – 1025, 2011a.
- [Hampf *et al.*, 2011b] D. Hampf, M. Tluczykont, and D. Horns. Simulation of the expected performance for the proposed gamma-ray detector HiSCORE. *Proceedings of Science*, 2011b.
- [Hara *et al.*, 1993] T. Hara, T. Kifune, Y. Matsubara *et al.* A 3.8 m imaging Cherenkov telescope for the TeV gamma-ray astronomy collaboration between Japan and Australia. *Nuclear Instruments and Methods in Physics Research A*, 332:300–309, 1993.
- [Hauser and Dwek, 2001] M. G. Hauser and E. Dwek. The Cosmic Infrared Background: Measurements and Implications. *Annu. Rev. Astron. Astrophys.*, 39:249–307, 2001.
- [Haustein, 1996] V. Haustein. *Messung der Ankunftszeitverteilung von Luft-Cerenkovphotonen mit einem Flash-ADC-System zur Bestimmung der Energie und der Komposition der primären kosmischen Strahlung im Energiebereich von  $10^{14}$  –  $10^{16}$  eV*. Ph.D. thesis, University of Hamburg, 1996.

## Bibliography

- [Haustein *et al.*, 1995] V. Haustein, V. Henke, A. Lindner *et al.* Arrival Time Distribution of Cerenkov Photons and the Elemental Composition of Primary Cosmic Rays Around  $10^{15}$ eV. In *International Cosmic Ray Conference*, volume 1 of *International Cosmic Ray Conference*, pages 418–+. 1995.
- [Heck *et al.*, 1998] D. Heck, J. Knapp, J. N. Capdevielle *et al.* CORSIKA – an Air Shower Simulation Program. 1998.  
URL <http://www-ik.fzk.de/corsika/>
- [Heitler, 1944] W. Heitler. *Quantum Theory of Radiation*. Oxford University Press, 2 edition, 1944.
- [Henke, 1994] V. Henke. Studie zur Auswertung der Ankunftszeitverteilung des Cerenkov-Lichts ausgedehnter Luftschaer. 1994. Diploma thesis, University of Hamburg.
- [Heß *et al.*, 1999] M. Heß, K. Bernlöhr, A. Daum *et al.* The time structure of Cherenkov images generated by TeV gamma-rays and by cosmic rays. *Astroparticle Physics*, 11:363–377, 1999.
- [Hess, 1912] V. F. Hess. Über Beobachtungen der durchdringenden Strahlung bei sieben Freiballonfahrten. *Physikalische Zeitschrift*, 13:1084–1091, 1912.
- [H.E.S.S. website, 2011] H.E.S.S. website. 2011.  
URL <http://www.mpi-hd.mpg.de/hfm/HESS/>
- [Hester, 2008] J. J. Hester. The Crab Nebula: An Astrophysical Chimera. *Annu. Rev. Astron. Astrophys.*, 46:127–155, 2008.
- [Hester *et al.*, 2002] J. J. Hester, K. Mori, D. Burrows *et al.* Hubble Space Telescope and Chandra Monitoring of the Crab Synchrotron Nebula. *Astrophys. J. Letters*, 577:L49–L52, 2002.
- [Hillas, 1985] A. M. Hillas. Cerenkov light images of EAS produced by primary gamma. In F. C. Jones, editor, *International Cosmic Ray Conference*, volume 3 of *International Cosmic Ray Conference*, pages 445–448. 1985.
- [Hillas, 1996] A. M. Hillas. Differences between Gamma-Ray and Hadronic Showers. *Space Science Reviews*, 75:17–30, 1996.
- [Hillas, 2005] A. M. Hillas. TOPICAL REVIEW: Can diffusive shock acceleration in supernova remnants account for high-energy galactic cosmic rays? *Journal of Physics G Nuclear Physics*, 31:95–+, 2005.
- [Hillas, 2006] A. M. Hillas. Cosmic Rays: Recent Progress and some Current Questions. *ArXiv Astrophysics e-prints*, 0607109, 2006.
- [Hillas *et al.*, 1998] A. M. Hillas, C. W. Akerlof, S. D. Biller *et al.* The Spectrum of TeV Gamma Rays from the Crab Nebula. *Astrophys. J.*, 503:744, 1998.
- [Hinton, 2009] J. Hinton. Ground-based gamma-ray astronomy with Cherenkov telescopes. *New Journal of Physics*, 11(5):055005–+, 2009.
- [Hinton, 2004] J. A. Hinton. The status of the HESS project. *New Astronomy Reviews*, 48:331–337, 2004.
- [Hoffleit and Warren, 1995] D. Hoffleit and W. H. Warren, Jr. Bright Star Catalogue, 5th Revised Ed. (Hoffleit+, 1991). *VizieR Online Data Catalog*, 5050:0–+, 1995.
- [Hofmann *et al.*, 1999] W. Hofmann, I. Jung, A. Konopelko *et al.* Comparison of techniques to reconstruct VHE gamma-ray showers from multiple stereoscopic Cherenkov images. *Astroparticle Physics*, 12:135–143, 1999.

- [Holder, 2005] J. Holder. Exploiting VERITAS Timing Information. In *International Cosmic Ray Conference*, volume 5 of *International Cosmic Ray Conference*, pages 383–+. 2005.
- [Hörandel, 2003] J. R. Hörandel. On the knee in the energy spectrum of cosmic rays. *Astroparticle Physics*, 19:193–220, 2003.
- [Hörandel, 2004] J. R. Hörandel. Models of the knee in the energy spectrum of cosmic rays. *Astroparticle Physics*, 21:241–265, 2004.
- [Hörandel *et al.*, 2006] J. R. Hörandel, W. D. Apel, F. Badea *et al.* Results from the KASCADE, KASCADE-Grande, and LOPES experiments. *Journal of Physics Conference Series*, 39:463–470, 2006.
- [Hörandel *et al.*, 2011] J. R. Hörandel, W. D. Apel, J. C. Arteaga *et al.* Measurement of radio emission from extensive air showers with LOPES. *Nuclear Instruments and Methods in Physics Research A*, 630:171–176, 2011.
- [Horns, 2008] D. Horns. High-(Energy)-Lights - The Very High Energy Gamma-Ray Sky (With 9 Figures). In S. Röser, editor, *Reviews in Modern Astronomy*, volume 20 of *Reviews in Modern Astronomy*, pages 167–+. 2008.
- [Horns and Aharonian, 2004] D. Horns and F. A. Aharonian. The Crab Nebula: Linking MeV Synchrotron and 50 TeV Inverse Compton Photons. In V. Schoenfelder, G. Lichti, & C. Winkler, editor, *5th INTEGRAL Workshop on the INTEGRAL Universe*, volume 552 of *ESA Special Publication*, page 439. 2004.
- [Horns and Meyer, 2012] D. Horns and M. Meyer. Indications for a pair-production anomaly from the propagation of VHE gamma-rays. *ArXiv e-prints*, 1201.4711, 2012.
- [Hüntemeyer and Milagro Calibration, 2010] P. Hütemeyer and Milagro Calibration. Galactic TeV Gamma Ray Sources and Diffuse Emission - Results from Milagro. In *25th Texas Symposium on Relativistic Astrophysics*. 2010.
- [ISCCP, 2010] ISCCP. 2010.  
URL <http://isccp.giss.nasa.gov/>
- [Itoh *et al.*, 2003] C. Itoh, R. Enomoto, S. Yanagita *et al.* Evidence of TeV gamma-ray emission from the nearby starburst galaxy NGC 253. *Astr. Astrophys.*, 402:443–455, 2003.
- [Jordan and Krennrich, 2004] P. Jordan and F. Krennrich. The Design of Light Concentrators for a 12 m Cherenkov telescope. 2004.  
URL <http://www.eecs.umich.edu/~prjordan/papers/lightcollector.pdf>
- [Just *et al.*, 1993] F. Just, S. Hartmann, F. Aharonian *et al.* Measurement of the Muon Content of Extensive Air Showers With The Hegra Detector. In *International Cosmic Ray Conference*, volume 4 of *International Cosmic Ray Conference*, pages 203–+. 1993.
- [Kalmykov *et al.*, 1997] N. Kalmykov, S. Ostapchenko, and A. Pavlov. Quark-gluon-string model and EAS simulation problems at ultra-high energies. *Nuclear Physics B - Proceedings Supplements*, 52(3):17 – 28, 1997.
- [Kalmykov *et al.*, 1977] N. N. Kalmykov, G. B. Christiansen, I. A. Nechin *et al.* The further studies of the shape of the EAS Cerenkov radiation pulse with the Yakutsk array. In *International Cosmic Ray Conference*, volume 8 of *International Cosmic Ray Conference*, pages 244–250. 1977.

## Bibliography

- [Kalmykov *et al.*, 1979] N. N. Kalmykov, Y. A. Nechin, V. V. Prosin *et al.* The Results Obtained in Studying the Position of  $e0 > 2 \times 10^{16}$  eV EAS Maxima by the Method of Cerenkov Pulse Detection. In *International Cosmic Ray Conference*, volume 9 of *International Cosmic Ray Conference*, pages 73–+. 1979.
- [Karle *et al.*, 1995] A. Karle, M. Merck, R. Plaga *et al.* Design and performance of the angle integrating Cerenkov array AIROBICC. *Astroparticle Physics*, 3:321–347, 1995.
- [Kennel and Coroniti, 1984] C. F. Kennel and F. V. Coroniti. Confinement of the Crab pulsar’s wind by its supernova remnant. *Astrophys. J.*, 283:694–709, 1984.
- [Kneiske and Dole, 2008] T. M. Kneiske and H. Dole. A strict lower-limit EBL Applications on gamma-ray absorption. In F. A. Aharonian, W. Hofmann, & F. Rieger, editor, *American Institute of Physics Conference Series*, volume 1085 of *American Institute of Physics Conference Series*, pages 620–623. 2008.
- [Kneiske *et al.*, 2009] T. M. Kneiske, J. Kulbartz, D. Horns *et al.* Diffuse Gamma-Ray and Neutrino Emission from the Local Supercluster. *Proceedings of the 31<sup>st</sup> ICRC, Łódź, 2009*.
- [Kneizys *et al.*, 1996] F. X. Kneizys, L. W. Abreu, G. P. Anderson *et al.* The modtran 2/3 report and lowtran 7 model. Technical report, Ontar Corporation, 1996.
- [Kobayashi *et al.*, 2004] T. Kobayashi, Y. Komori, K. Yoshida *et al.* The Most Likely Sources of High-Energy Cosmic-Ray Electrons in Supernova Remnants. *Astrophys. J.*, 601:340–351, 2004.
- [Kohnle *et al.*, 1996] A. Kohnle, F. Aharonian, A. Akhperjanian *et al.* Stereoscopic imaging of air showers with the first two HEGRA Cherenkov telescopes. *Astroparticle Physics*, 5:119–131, 1996.
- [Korostelev *et al.*, 2009] E. E. Korostelev, L. A. Kuzmichev, V. V. Prosin *et al.* The New Method of EAS Parameters Reconstruction Using the FWHM of Cherenkov Light Pulses. *Proceedings of the 31<sup>st</sup> ICRC, Łódź, 2009*.
- [Krennrich *et al.*, 2011] F. Krennrich, M. Bautista, M. Beilicke *et al.* Results from the first two years of VERITAS observations. *Nuclear Instruments and Methods in Physics Research A*, 630:16–21, 2011.
- [Krivosheina, 2004] I. V. Krivosheina. Sn 1987A - Historical View about Registration of the Neutrino Signal with Baksan, KAMIOKANDE II and IMB Detectors. *International Journal of Modern Physics D*, 13:2085–2105, 2004.
- [Kuhlmann *et al.*, 1977] J. D. Kuhlmann, R. W. Clay, P. C. Crouch *et al.* Cerenkov light from EAS at sea-level. In *International Cosmic Ray Conference*, volume 8 of *International Cosmic Ray Conference*, pages 239–243. 1977.
- [Kunnas, 2012] M. Kunnas. 2012. Diploma thesis, University of Hamburg.
- [Kuzmichev, 2011] L. Kuzmichev. personal communication. 2011.
- [Lagage and Cesarsky, 1983] P. O. Lagage and C. J. Cesarsky. The maximum energy of cosmic rays accelerated by supernova shocks. *Astr. Astrophys.*, 125:249–257, 1983.
- [Leinert *et al.*, 1998] C. Leinert, S. Bowyer, L. K. Haikala *et al.* The 1997 reference of diffuse night sky brightness. *Astr. Astrophys. Suppl.*, 127:1–99, 1998.
- [Lemoine-Goumard *et al.*, 2006] M. Lemoine-Goumard, B. Degrange, and M. Tluczykont. Selection and 3D-reconstruction of gamma-ray-induced air showers with a stereoscopic system of atmospheric Cherenkov telescopes. *Astroparticle Physics*, 25:195–211, 2006.

- [Li and Ma, 1983] T.-P. Li and Y.-Q. Ma. Analysis methods for results in gamma-ray astronomy. *Astrophys. J.*, 272:317–324, 1983.
- [Lindner, 1998] A. Lindner. A new method to reconstruct the energy and determine the composition of cosmic rays from the measurement of Cherenkov light and particle densities in extensive air showers. *Astroparticle Physics*, 8:235–252, 1998.
- [Liner0s, 2011] R. Lineros. Galactic positrons and electrons from dark matter and astrophysical sources. *Nuclear Instruments and Methods in Physics Research A*, 630:70–73, 2011.
- [Lobanov *et al.*, 2011] A. P. Lobanov, D. Horns, and T. W. B. Muxlow. VLBI imaging of a flare in the Crab nebula: more than just a spot. *Astr. Astrophys.*, 533:A10, 2011.
- [Lucek and Bell, 2000] S. G. Lucek and A. R. Bell. Non-linear amplification of a magnetic field driven by cosmic ray streaming. *Month. Not. Roy. Astr. Soc.*, 314:65–74, 2000.
- [Masbou *et al.*, 2009] J. Masbou, G. Lamanna, S. Rosier-Lees *et al.* HESS-II expected performance in the tens of GeV. *Proceedings of the 31<sup>st</sup> ICRC, Łódź*, 2009.
- [Meyer *et al.*, 2010] M. Meyer, D. Horns, and H.-S. Zechlin. The Crab Nebula as a standard candle in very high-energy astrophysics. *Astr. Astrophys.*, 523:A2, 2010.
- [Middelberg and Bach, 2008] E. Middelberg and U. Bach. High resolution radio astronomy using very long baseline interferometry. *Reports on Progress in Physics*, 71(6):066901–+, 2008.
- [Mirizzi and Montanino, 2009] A. Mirizzi and D. Montanino. Stochastic conversions of TeV photons into axion-like particles in extragalactic magnetic fields. *J. Cosmol. Astropart. Phys.*, 12:4, 2009.
- [Mirzoyan and Lorenz, 1994] R. Mirzoyan and E. Lorenz. Measurement of the night sky light background at La Palma. Technical report, Max-Planck-Institut für Physik, München, 1994.
- [Moskalenko *et al.*, 2006] I. V. Moskalenko, T. A. Porter, and A. W. Strong. Attenuation of Very High Energy Gamma Rays by the Milky Way Interstellar Radiation Field. *Astrophys. J. Letters*, 640:L155–L158, 2006.
- [MRO website, 2011] MRO website. The Murchison Radio-Astronomy Observatory. 2011.  
URL <http://www.astro.uwa.edu.au/ska/mro/>
- [Nachtigall, 2011] R. Nachtigall. Charakterisierung von Photomultipliern und Beiträge zur Entwicklung eines Prototypen für Luftcherenkovmessungen. 2011. Diploma thesis, University of Hamburg.  
URL [http://wwiexp.desy.de/groups/astroparticle/de/forschung/nachtigall\\_diplom.pdf](http://wwiexp.desy.de/groups/astroparticle/de/forschung/nachtigall_diplom.pdf)
- [NOAA, 2005] NOAA. National Geophysical Data Center (USA). 2005.  
URL [ftp://ftp.ngdc.noaa.gov/geomag/images/F\\_map\\_mf\\_2005\\_large.jpeg](ftp://ftp.ngdc.noaa.gov/geomag/images/F_map_mf_2005_large.jpeg)
- [Ogio *et al.*, 2005] S. Ogio, M. Fukushima, F. Kakimoto *et al.* Telescope Array; Progress of Fluorescence Detector. In *International Cosmic Ray Conference*, volume 8 of *International Cosmic Ray Conference*, pages 173–+. 2005.
- [Ohm *et al.*, 2009] S. Ohm, C. van Eldik, and K. Egberts.  $\gamma$ /hadron separation in very-high-energy  $\gamma$ -ray astronomy using a multivariate analysis method. *Astroparticle Physics*, 31:383–391, 2009.
- [Omega Optical, 2010] Omega Optical. 2010.  
URL [https://www.omegafilters.com/index.php?page=prod\\_astro\\_index](https://www.omegafilters.com/index.php?page=prod_astro_index)

## Bibliography

- [Paré *et al.*, 2002] E. Paré, B. Balauge, R. Bazer-Bachi *et al.* CELESTE: an atmospheric Cherenkov telescope for high energy gamma astrophysics. *Nuclear Instruments and Methods in Physics Research A*, 490:71–89, 2002.
- [Patterson and Hillas, 1983a] J. R. Patterson and A. M. Hillas. The relation of Cerenkov time profile widths to the distance to maximum of air showers. *Journal of Physics G Nuclear Physics*, 9:323–337, 1983a.
- [Patterson and Hillas, 1983b] J. R. Patterson and A. M. Hillas. The relation of the lateral distribution of Cerenkov light from cosmic-ray showers to the distance of maximum development. *Journal of Physics G Nuclear Physics*, 9:1433–1452, 1983b.
- [Plailly, 2006] P. Plailly. Eurelios / Science Photo Library. 2006.  
URL <http://www.sciencephoto.com/media/323186/enlarge>
- [Platino and The Pierre Auger Collaboration, 2009] M. Platino and The Pierre Auger Collaboration. AMIGA - Auger Muons and Infill for the Ground Array of the Pierre Auger Observatory. *Proceedings of the 31<sup>st</sup> ICRC, Łódź*, 2009.
- [Preuß *et al.*, 2002] S. Preuß, G. Hermann, W. Hofmann *et al.* Study of the photon flux from the night sky at La Palma and Namibia, in the wavelength region relevant for imaging atmospheric Cherenkov telescopes. *Nuclear Instruments and Methods in Physics Research A*, 481:229–240, 2002.
- [Prosin *et al.*, 2009] V. V. Prosin, N. M. Budnev, O. A. Chvalaiev *et al.* The Cosmic Ray Mass Composition in the Energy Range  $10^{15}$ - $10^{18}$  eV measured with the Tunka Array: Results and Perspectives. *Nuclear Physics B Proceedings Supplements*, 190:247–252, 2009.
- [Pryke and Lloyd-Evans, 1995] C. L. Pryke and J. Lloyd-Evans. A high performance GPS based autonomous event time-tagging system with application in a next generation Extensive Air Shower array. *Nuclear Instruments and Methods in Physics Research A*, 354:560–566, 1995.
- [Raue, 2011] M. Raue. PyFACT: Python FITS Analysis for Cherenkov Telescopes. 2011. V 0.0.3.  
URL <https://github.com/mraue/pyfact>
- [Raue and Mazin, 2010] M. Raue and D. Mazin. Potential of the next generation VHE instruments to probe the EBL (I): The low- and mid-VHE. *Astroparticle Physics*, 34:245–256, 2010.
- [Razdan *et al.*, 2002] A. Razdan, A. Haungs, H. Rebel *et al.* Image and non-image parameters of atmospheric Cherenkov events: a comparative study of their  $\gamma$ -ray/hadron classification potential in ultrahigh energy regime. *Astroparticle Physics*, 17:497–508, 2002.
- [Ritt, 2011] S. Ritt. DRS 4 discussion forum. 2011.  
URL <https://midas.psi.ch/eLogs/DRS4+Forum/133>
- [Rowell, 2011] G. Rowell. Working group website. 2011.  
URL <http://www.physics.adelaide.edu.au/astrophysics/gpr/research.html>
- [Rowell *et al.*, 2008] G. P. Rowell, V. Stamatescu, R. W. Clay *et al.* TenTen: A new IACT array for multi-TeV  $\gamma$ -ray astronomy. *Nuclear Instruments and Methods in Physics Research A*, 588:48–51, 2008.
- [Sandoval *et al.*, 2008] A. Sandoval, M. M. González, and A. Carramiñana. Construction of the HAWC observatory at Volcán Sierra Negra. In F. A. Aharonian, W. Hofmann, & F. Rieger, editor, *American Institute of Physics Conference Series*, volume 1085 of *American Institute of Physics Conference Series*, pages 854–857. 2008.

- [Scherini and the Pierre Auger Collaboration, 2011] V. Scherini and the Pierre Auger Collaboration. Search for ultra-high energy photons with the Pierre Auger Observatory. *Nuclear Instruments and Methods in Physics Research A*, 630:226–229, 2011.
- [Schlyter, 2010] P. Schlyter. Radiometry and photometry in astronomy. 2010.  
URL <http://stjarnhimlen.se/comp/radfaq.html>
- [Schröder *et al.*, 2010] F. G. Schröder, T. Asch, L. Bähren *et al.* New method for the time calibration of an interferometric radio antenna array. *Nuclear Instruments and Methods in Physics Research A*, 615:277–284, 2010.
- [SKA website, 2011] SKA website. 2011.  
URL <http://www.skatelescope.org/the-sites/>
- [Spitschan, 2013] D. Spitschan. 2013. Diploma thesis, University of Hamburg.
- [Stamatescu, 2010] V. Stamatescu. *New timing analysis techniques in multi-TeV gamma-ray astronomy*. Ph.D. thesis, University of Adelaide, School of Chemistry and Physics, 2010.  
URL <http://www.physics.adelaide.edu.au/astrophysics/multitev/VStamatescu.pdf>
- [Stamatescu *et al.*, 2011] V. Stamatescu, G. P. Rowell, J. Denman *et al.* Timing analysis techniques at large core distances for multi-TeV gamma ray astronomy. *Astroparticle Physics*, 34:886–896, 2011.
- [Stepanian *et al.*, 1983] A. A. Stepanian, V. P. Fomin, and B. M. Vladimirkii. A method of distinguishing Cerenkov gamma-ray flashes from the proton component of cosmic rays. *Izvestiya Ordena Trudovogo Krasnogo Znameni Krymskoj Astrofizicheskoj Observatorii*, 66:234–241, 1983.
- [Striani *et al.*, 2011] E. Striani, M. Tavani, G. Piano *et al.* The Crab Nebula Super-flare in 2011 April: Extremely Fast Particle Acceleration and Gamma-Ray Emission. *Astrophys. J. Letters*, 741:L5, 2011.
- [Sudholz, 2011] T. Sudholz. 2011. Master thesis, School of Chemistry and Physics, University of Adelaide.
- [Tavani *et al.*, 2009] M. Tavani, G. Barbiellini, A. Argan *et al.* The AGILE Mission. *Astr. Astrophys.*, 502:995–1013, 2009.
- [Tavani *et al.*, 2011] M. Tavani, A. Bulgarelli, V. Vittorini *et al.* Discovery of Powerful Gamma-Ray Flares from the Crab Nebula. *Science*, 331:736–, 2011.
- [The Auger Collaboration, 1997] The Auger Collaboration. The Pierre Auger Observatory Design Report. 1997.  
URL [http://www.auger.org/technical\\_info/design\\_report.html](http://www.auger.org/technical_info/design_report.html)
- [The High Resolution Fly’s Eye Collaboration, 2009] The High Resolution Fly’s Eye Collaboration. Measurement of the flux of ultra high energy cosmic rays by the stereo technique. *Astroparticle Physics*, 32:53–60, 2009.
- [Thornton, 2010] G. Thornton. 2010. Personal communication.
- [Thornton and Clay, 1978] G. J. Thornton and R. W. Clay. The dependence of the duration of atmospheric Cerenkov pulses on cosmic-ray shower parameters. *Journal of Physics G: Nuclear Physics*, 4(9):L251, 1978.
- [Tibolla *et al.*, 2009] O. Tibolla, R. C. G. Chaves, W. Domainko *et al.* New unidentified Galactic H.E.S.S. sources. *ArXiv e-prints*, 0912.3811, 2009.

## Bibliography

- [Tluczykont *et al.*, 2009a] M. Tluczykont, D. Hampf, D. Horns *et al.* Proposal for High-Energy Crab Nebula Observations using Sampling mode, 2009a. Internal H.E.S.S. observation proposal (61/2009).
- [Tluczykont *et al.*, 2009b] M. Tluczykont, T. Kneiske, D. Hampf *et al.* Gamma-ray and Cosmic Ray Astrophysics from 10 TeV to 1 EeV with a large-area ( $> 10\text{km}^2$ ) air-shower detector. *Proceedings of the 31<sup>st</sup> ICRC, Łódź*, 2009b.
- [Tluczykont *et al.*, 2011] M. Tluczykont, D. Hampf, D. Horns *et al.* The ground-based large-area wide-angle gamma-ray and cosmic-ray experiment HiSCORE. *Advances in Space Research*, 48(12):1935 – 1941, 2011.
- [Tluczykont *et al.*, 2012a] M. Tluczykont, D. Hampf, D. Horns *et al.* The HiSCORE detector for Gamma-ray and cosmic ray astrophysics beyond 10 TeV, 2012a. To be published.
- [Tluczykont *et al.*, 2012b] M. Tluczykont, D. Horns, D. Hampf *et al.* HiSCORE: A new detector for astroparticle and particle physics beyond 10 TeV. *Nuclear Instruments and Methods in Physics Research A*, 2012b. ISSN 0168-9002.
- [Tridon *et al.*, 2010] D. B. Tridon, T. Schweizer, F. Goebel *et al.* The MAGIC-II gamma-ray stereoscopic telescope system. *Nuclear Instruments and Methods in Physics Research A*, 623:437–439, 2010.
- [Trimble, 1973] V. Trimble. The Distance to the Crab Nebula and NP 0532. *Astronomical Society of the Pacific*, 85:579, 1973.
- [Tsunesada *et al.*, 2009] Y. Tsunesada, F. Kakimoto, H. Matsumoto *et al.* A Cherenkov light detection experiment at Mount Chacaltaya to study nuclear composition of cosmic rays. *Proceedings of the 31<sup>st</sup> ICRC, Łódź*, 2009.
- [TUNKA website, 2011] TUNKA website. 2011.  
URL <http://www.dbserv.sinp.msu.ru/tunka/>
- [Uchiyama *et al.*, 2007] Y. Uchiyama, F. A. Aharonian, T. Tanaka *et al.* Extremely fast acceleration of cosmic rays in a supernova remnant. *Nature*, 449:576–578, 2007.
- [University of New South Wales, 2011] University of New South Wales. Fowler’s Gap information brochure. 2011.  
URL <http://www.fowlersgap.unsw.edu.au/pdf/fg%20brochure.pdf>
- [US Standard Atmosphere, 1976] US Standard Atmosphere. National Atmospheric And Oceanic Administration, National Aeronautics and Space Administration, United States Air Force. 1976.  
URL [http://ntrs.nasa.gov/archive/nasa/casi.ntrs.nasa.gov/19770009539\\_1977009539.pdf](http://ntrs.nasa.gov/archive/nasa/casi.ntrs.nasa.gov/19770009539_1977009539.pdf)
- [Véron-Cetty and Véron, 2006] M.-P. Véron-Cetty and P. Véron. A catalogue of quasars and active nuclei: 12th edition. *Astr. Astrophys.*, 455:773–777, 2006.
- [Vincent *et al.*, 2003] P. Vincent, J.-P. Denanca, J.-F. Huppert *et al.* Performance of the H.E.S.S. Cameras. In *International Cosmic Ray Conference*, volume 5 of *International Cosmic Ray Conference*, pages 2887–+. 2003.
- [Völk and Zirakashvili, 2004] H. J. Völk and V. N. Zirakashvili. Cosmic ray acceleration by spiral shocks in the galactic wind. *Astr. Astrophys.*, 417(3):807–817, 2004.
- [Wakely and Horan, 2011] S. Wakely and D. Horan. TeVcat. 2011.  
URL <http://tevcat.uchicago.edu/>

- [Weekes *et al.*, 1989] T. C. Weekes, M. F. Cawley, D. J. Fegan *et al.* Observation of TeV gamma rays from the Crab nebula using the atmospheric Cerenkov imaging technique. *Astrophys. J.*, 342:379–395, 1989.
- [Wibig and Wolfendale, 2008] T. Wibig and A. W. Wolfendale. The Ankle in the UHE Cosmic Ray Spectrum. In *International Cosmic Ray Conference*, volume 4 of *International Cosmic Ray Conference*, pages 269–272. 2008.
- [Winston, 1970] R. Winston. Light Collection within the Framework of Geometrical Optics. *J. Opt. Soc. Amer.*, 60:245–247, 1970.
- [Zatsepin and Kuz'min, 1966] G. T. Zatsepin and V. A. Kuz'min. Upper limit of the spectrum of cosmic rays. *JETP Letters*, 4(3):78, 1966.
- [Zavrtanik and Pierre Auger Collaboration, 2011] D. Zavrtanik and Pierre Auger Collaboration. Results from the Pierre Auger Observatory. *Nuclear Instruments and Methods in Physics Research A*, 630:166–170, 2011.
- [Zuccon, 2009] P. Zuccon. The AMS-02 experiment on the ISS: status and perspectives. *Proceedings of the 31<sup>st</sup> ICRC, Łódź*, 2009.

## *Bibliography*

# List of publications

## First author

- Refereed paper D. Hampf, G. Rowell, N. Wild et al.. Measurement of night sky brightness in southern Australia. *Advances in Space Research*, 48(6):1017 – 1025, 2011
- Rev. Conf. proc. D. Hampf, M. Tluczykont, and D. Horns. Simulation of the expected performance for the proposed gamma-ray detector HiSCORE. *Proceedings of Science*, 2011
- Conf. proc. D. Hampf, M. Tluczykont, and D. Horns. Event reconstruction with the proposed large area Cherenkov air shower detector SCORE. *Proceedings of the 31<sup>st</sup> ICRC, Łódź*, 2009

## Co-author

- Refereed paper M. Tluczykont, D. Horns, D. Hampf et al.. HiSCORE: A new detector for Astroparticle and Particle Physics beyond 10 TeV. *Nuclear Instruments and Methods in Physics Research A*, 2012 (in press)
- Refereed paper M. Tluczykont, D. Hampf, D. Horns et al.. The ground-based large-area wide-angle gamma-ray and cosmic-ray experiment HiSCORE. *Advances in Space Research*, 48(12):1935 - 1941, 2011
- Conf. proc. M. Tluczykont, T. Kneiske, D. Hampf, D. Horns. Gamma-ray and Cosmic Ray Astrophysics from 10 TeV to 1 EeV with a large-area ( $> 10\text{km}^2$ ) air-shower detector. *Proceedings of the 31<sup>st</sup> ICRC, Łódź*, 2009
- Refereed paper R. Jöhren, R. Berendes, W. Buglak, D. Hampf, V. Hannen, J. Mader, W. Nörtershäuser, R. Sánchez, C. Weinheimer. APDs as single-photon detectors for visible and near-infrared wavelenghts down to Hz rates. *JINST*, 7(2):2015, 2012

Co-author of 18 refereed H.E.S.S. collaboration papers from 2009 to 2012.

Extended lists including talks and poster presentations can be found on the HiSCORE website, [wwwiexp.desy.de/groups/astroparticle/score/](http://wwwiexp.desy.de/groups/astroparticle/score/) and on [www.desy.de/~dhampf/](http://www.desy.de/~dhampf/).